Stony Brook University

OFFICIAL COPY

The official electronic file of this thesis or dissertation is maintained by the University Libraries on behalf of The Graduate School at Stony Brook University.

© All Rights Reserved by Author.

Experimental Investigation of Magnetohydrodynamic Flow for An Intense Proton Target

A Dissertation Presented

by

Hee Jin Park

to

The Graduate School

in Partial Fulfillment of the

Requirements

for the Degree of

Doctor of Philosophy

in

Mechanical Engineering

Stony Brook University

December 2009

Stony Brook University

The Graduate School

Hee Jin Park

We, the dissertation committee for the above candidate for the

Doctor of Philosophy degree,

hereby recommend acceptance of this dissertation.

Foluso Ladeinde, Co-Advisor,
Department of Mechanical Engineering

Harold G. Kirk, Co-Advisor,
Department of Physics, Brookhaven National Laboratory

Thomas Cubaud, Chairperson of Defense,
Department of Mechanical Engineering

Kirk T. McDonald , Outside Member,
Physics Department, Princeton University

James Glimm, Outside Member,
Department of Applied Mathematics & Statistics

This dissertation is accepted by the Graduate School.

Lawrence Martin
Dean of the Graduate School

Abstract of the Dissertation

Experimental Investigation of Magnetohydrodynamic Flow for An Intense Proton Target

by

Hee Jin Park

Doctor of Philosophy

in

Mechanical Engineering

Stony Brook University

2009

Efficient production of pions can be achieved by colliding an intense proton beam with a high-Z target. The disruption of targets from their interaction with an intense proton beam needs to be carefully investigated for optimum design of high-power targets. In this work, experiments have been carried out on mercury (Hg) jets as targets, with a focus on the interaction of the jet with an intense proton beam in the presence of an external magnetic field. The primary diagnostics in the experiment employed the technique of back-illuminated laser shadow photography to "freeze" the transient events, with several high speed cameras used to record the images. The performance of the optical diagnostic system is presented.

A magnetic field in a mercury jet flow causes induced currents, which

produce distortions of the mercury jet. The effects of the Lorentz force induced by the magnetic field and the role of joule damping were investigated for the present problem.

Statistical and qualitative analysis of the data from image processing is presented, as are experimental studies of Hg jet distortion and the dynamic of Hg flow in the magnetic field. It was observed from the experiments that the imposition of a magnetic field suppressed and stabilized the fluctuating motion in the jet when the flow was turbulent and the magnetic Reynolds number was approximately 0.26. Parallel numerical Monte Carlo simulations of energy deposition by proton beams in a similar system are being carried out elsewhere by collaborators on the project. Data on jet shape, trajectory, and proton beam spot size obtained from the present experiments have been incorporated into simulation models. Results on jet disruption, filament velocity, and energy deposition on the Hg target are reported in this work for proton beam intensities up to 30×10^{12} protons per pulse and magnetic field intensities up to 15 T. The feasibility of utilizing a Hg jet as a high-Z target for future particle acceleration is discussed.

Table of Contents

List of Figures

List of Tables

Nomenclature

$\mathbf{B}$	Magnetic induction field, T (Wb/m^2)
$\mathbf{B}_o$	Applied magnetic field, T (Wb/m^2)
$\mathbf{D}$	Electric displacement field, C/m^2
$\mathbf{E}$	Electric field, N/C (V/m); Global kinetic energy, J
$\mathbf{H}$	Magnetic field, A/m
$\mathbf{j}$	Current density, A/m^2; Jacobian matrix
$\mathbf{M}$	Magnetization density, $J/(T\ m^3)$
$\mathbf{P}$	Polarization density, C/m^2; Probability; Particle momentum, $J \cdot s/m$
$\mathbf{T}$	Maxwell stress tensor, N/m^2
$\mathbf{V}$	Electric potential, V
A	Cross sectional area, m^2
C	Contraction coefficient; Discharge coefficient; Constant; Circumference, m; Gladstone-Dale constant
D	Diameter of jet, m; Vertical jet height, m; Energy dissipation, J/s;
D_p	Dispersion function, m
E_b	Proton beam energy, eV
E_p	Energy deposition, J/g
G	Pressure ratio; Gruneisen coefficient
I_T	Initial intensity of light, cd
I_o	Intensity of light at screen, cd
K	Loss coefficient; Bulk modulus, N/m^2
L	Characteristic length, m; Pipe length, m; Disruption length, m
$L^{disruption}$	Disruption length, m

M	Mass, kg; Molar mass, g/mol
N_p	Number of protons
P	Pressure, N/m^2; Probability; Momentum, eV/c
P_p	Pressure by energy deposition, N/m^2
Q	Flow rate, m^3/s
R	Gas constant, $J/(K\ mol)$; Radius of curvature of the centerline of elbow, m
T	Temperature, °C (K)
Tp	Tera-protons, 1×10^{12} protons
U	Mean velocity in the x coordinate direction, m/s
V	Volume, m^3
α_v	Volume coefficient of thermal expansion, K^{-1}
β	Ratio of diameter, Relativistic function
γ	Ratio of specific heats, c_p/c_v; Relativistic function
Γ	Surface tension, N/m
δ	Kronecker delta; Boundary layer thickness, m
ϵ	Amplitude of a sinusoidal wave, m; Random error
ε	Electrical permittivity, F/m ($C^2/(N\ m^2)$); Emittance
ε_o	Electrical permittivity of free space, F/m ($C^2/(N\ m^2)$)
ζ	Intermittency factor
η	Absolute viscosity, $kg/(m\ s)$
θ	Angle, degree
κ	Compressibility, m^2/N
λ	Wavelength of a sinusoidal wave, m
μ	Magnetic permeability, H/m (N/A^2)
μ_o	Magnetic permeability of free space, H/m (N/A^2)

ν	Kinematic viscosity, η/ρ, m^2/s
ξ	Free surface perturbation, m
ρ	Density, kg/m^3
σ	Electrical conductivity, S/m; Standard deviation
τ	Joule damping term, s; Wall shear stress, N/m^2
ϕ	Velocity potential, m^2/s; Angle, degree
ϕ_E	Electric potential, V
χ_e	Electrical susceptibility
χ_m	Magnetic susceptibility
ψ	Stream function, m^2/s
ω	Vorticity, s^{-1}
a	Radius of circular pipe, m; Radius of jet, m
c	Local speed of sound, m/s; Distance m; Wave velocity, m/s
c_p, c_v	Specific heat capacity, $J/(g\ K)$
d	Diameter of circular pipe, m; Diameter of nozzle, m; Distance, m
e	Specific internal energy, J/kg; Surface roughness, m; Error, %
f	Focal length, m; Force, N; Friction factor
g	Gravitational constant, m/s^2
h	Head loss, m
k	Boltzmann constant; Number of parameters
n	Index of refraction; Experimental data points
p	Pressure, N/m^2; Particle momentum, $J \cdot s/m$
r	Residual; Radial coordinate
s	Position
t	Time, s

v	Directional fluid velocity, m/s; Mean velocity, m/s
x, y, z	Cartesian coordinates, m
Al	Alfvèn Number
Fr	Froude number
Ha	Hartmann number
N	Stuart number; Number of events; Augmented Jacobian matrix
Pr_m	Magnetic Prandtl number
Re	Reynolds number
Re_m	Magnetic Reynolds number
We	Weber number
Δ	Difference
$\nabla\cdot$	Divergence operator
$\nabla\times$	Curl operator
$\times$	Cross product operator
$\cdot$	Inner product operator; Multiplication

Superscripts

$'$	Differentiation with respect to variable; Perturbation; Fluctuation
$\cdot$	Differentiation with respect to time

Subscripts

I	Ion thermal
R	Reference location

T	Transpose of matrix
a	Air
b	Beam
c	Compression
e	Electron thermal
l	Liquid
o	Component mean value; Initial value at the nozzle
sc	At screen position
x, y, z	Component values in cartesian coordinates
$\perp$	Perpendicular direction

ACKNOWLEDGEMENTS

I would like to express my gratitude to all those who gave me the possibility to complete this dissertation: Philip Spampinato (ORNL), Adam Carroll (ORNL), Van Graves (ORNL), Peter Titus (MIT), Sergei Striganov (FNAL), Bill Sands (Princeton), Allan Nelson (Princeton), Ilias Efthymiopoulos (CERN), Adrian Fabich (CERN), Friedrich Haug (CERN), Hugo Pereira (CERN), Marcus Palm (CERN), Jacques Lettry (CERN), Otto Caretta (RAL), Peter Loveridge (RAL) , Goran Skoro (Sheffield), Roger Bennett (RAL), and Wurigen Bo (Stony Brook).

I would like to thank accelerator group staffs at Brookhaven National Laboratory for giving me a chance to do research for this dissertation. I am deeply indebted to my supervisor Dr. Harold Kirk (BNL), Dr. Foluso Ladeinde, and Dr. Kirk McDonald (Princeton) whose instruction, stimulating suggestions and encouragement helped me in all the time for and writing of this dissertation. Specially, I would like to thank to Dr. Kirk McDonald (Princeton) for his proof-reading of dissertation, and his solid instruction to the edition of LaTex format in dissertation. I would like to thank Dr. Thomas Tsang (BNL) whose help in guide of optical diagnostic instrumentation and encouragement. I would like to express appreciation to my committee Chairperson Dr. Thomas Cubaud, who very pleasantly accepted my request to serve on my dissertation committee. I also would like to express appreciation to my committee Dr. James Glimm and Dr. Roman Samulyak, whose valuable suggestions and contradiction pointed out misleading experimental results analysis.

Finally, I would like to acknowledge financial support for this work provided by United States Department of Energy Contract No. DE-AC02-98CH10886. The text of this dissertation in part is a reprint of the materials as it appears in Review of Scientific Instruments **79**, 045111(2008). The co-authors listed in the publication directed and supervised overall research projet that forms the basis for this dissertation.

Chapter 1

Introduction

Accelerator-based sources of exceptionally intense, tightly focused beams of X-rays and ultraviolet radiation make possible both basic and applied research in fields from physics to biology to technology that are not possible with more conventional equipment. The development of a high-intensity source of muons can be useful for the production of high-energy neutrino, thereby opening the door for a broad range of important new physics experiments such as neutrino oscillation. The concept is to use a high-intensity proton beam incident on a Hg jet to produce pions which decay to give the muons. These muons is magnetically captured, accelerated, and then inserted into a storage ring.

1.1 Neutrino Factory for High Power Neutrino Beam

1.1.1 The concept of neutrino factory

Accelerators are used to accelerate primary particle beams such as protons and electrons. The required statistics in the collision processes demand a very

high flux of primary particles. On interaction of the primary particles with a target, it is possible to produce secondary beams of elementary particles like pions, neutrons, and gammas. Primary protons pass through a linear accelerator and further through a synchrotron, bunch compressors, and accumulators to achieve a beam with a certain energy, intensity and beam structure. This beam is directed toward a target. On interaction with the target, secondary particles of different kinds are produced. A neutrino factory is the ultimate tool for producing a high-intensity neutrino beam to study neutrino oscillations. The neutrino factory is based on a new concept of an accelerator that produces a high-intensity, high-energy beam of muon and electron neutrinos. It will allow an investigation of a new domain in neutrino physics such as

- High intensity. Its flux is 10^3 times greater than conventional neutrino beams.
- High energy. It features a very high beam energy of 20 to 50 GeV.
- In a neutrino factory, the muon sign can be selected. Thus, it is possible to deliver particles and anti-particles.

The basic concept of the Neutrino Factory is the production of muon neutrinos and anti-electron neutrinos from the decay of muons that are circulating in a storage ring. An intense proton beam is delivered to a target, where pions are produced. These pions are collected in a solenoid magnetic field, which can capture both charged states of pions. The pions decay into muons in a decay channel. The muon beam has both a large energy spread and

transverse emittance. The energy spread is reduced using a phase rotation, while emittance is improved by ionization cooling. The cooled beam is accelerated to energies of 20 to 50 GeV and injected into a storage ring.

1.1.2 Neutrino physics

Muons cannot be produced directly, so pions have to be produced first. The first stage of a neutrino factory is thus a high-power proton driver that deliver protons onto a target, where pions are produced. These pions have to be collected and transported. After about 20 m, most of the pions decay into muons. A neutrino beam can be produced from the decay of high-energy muons:

- Pions from Proton + Material $\longrightarrow \pi^{\pm}+$ X
- Muons from $\pi^{\pm} \longrightarrow \mu^{\pm}\nu_{\mu}(\overline{\nu_{\mu}})$
- Neutrinos from $\mu^{\pm} \longrightarrow e^{\pm}\overline{\nu_{\mu}}\nu_{e}(\nu_{\mu}\overline{\nu_{e}})$

At this stage, the muon beam has a low phase space density and resembles more a cloud than a beam. Phase rotation as well as ionization cooling is applied to reduce the energy spread and the emittance of the muon beam.

Once the beam is cooled, it can be accelerated to a final energy of 20 to 50 GeV. In the final stage of a neutrino factory, the accelerated muons are injected into a storage ring with long straight sections.

1.2 A High Power Target for Neutrino Factory

1.2.1 Material consideration for a high power target

The intensity of muon beam is directly proportional to the power of the proton beam which initiates the process. Considering that a high intensity proton beam is required in order to generate the required muons, the choice of the target material becomes a particularly important issue. Modeling studies point to high-Z materials being more efficient at producing pions of both signs, whereas low-Z materials are better at preventing the absorption of the produced pions [66]. The pion yield per proton increases with the atomic number of the target, as shown in Fig. 1.1 from MARS calculation. A high-Z material is desirable because the pion production cross-section increases with increasing Z. However, the intense proton beam would melt a target made of a solid high-Z material. A target system using a flowing stream of Hg could recycle the spent target. Several types of target material have been proposed including copper, graphite, and Hg.

Since these targets are envisaged as being stationary, one must consider the problem of removing the energy deposited by the beam without interfering with the production of the particles.

1.2.2 Moving metallic target for pion production

While schemes for moving solid targets can be envisaged [90], a flowing liquid target is simpler, and Hg as a high Z material presents itself as the liquid metal. The liquid target should be in the form of a free jet, rather

than being confined in containment, since the beam-induced cavitation of the liquid metal can be destructive to solid walls in the immediate vicinity of the interaction region. Another issue associated with the proton beam is the effect of the energy that it deposits in the target. The temperature of the target rises almost instantaneously after the beam pulse, resulting in large internal stresses that might crack a solid target or disperse a liquid target [40]. In the case of a liquid jet target, the dispersal of the jet by the beam should not be destructive to the surrounding target system components and should not adversely affect pion production during subsequent beam pulses, either on the microsecond scale, if several micro-pulses are extracted from a proton synchrotron, or on the scale of the macro-pulse period. The operation of a liquid metal jet inside a strong magnetic field raises several magnetohydrodynamic issues such as possible deformation of the jet's shape and trajectory, as well as the effect of the magnetic field on the beam-induced dispersal of the jet.

1.2.3 Free mercury jet flow in a magnetic field for a high power target

The free Hg jet in magnetic field is proposed for a high power target to overcome the issues described in the above Chapter. The concept is to use a high intensity proton beam incident on a Hg jet to produce pions which decay to give the muons [21]. The key elements of the target system are an intense proton source, Hg jet, and capture of the generated pions in a high field solenoidal magnet [50]. The schematics of the key elements of the target

system is described in Fig. 1.2.

Previous studies [66] indicated that pion yield is maximized with a Hg target in the form of a 1 cm diameter at the interacting center, tilted by about 150 milliradian with respect to the magnetic axis. The target is tilted with respect to the axis of the capture solenoid, thus permitting the pions, whose trajectories are spirals, to leave the side of the target with a minimal probability for re-entering the target volume. The pion yield per proton increases with the atomic number of the target, as shown in Fig. 1.1 from MARS calculation. For 24 GeV protons, a high-Z target is superior in yield. As the pions emerge from the target at large angles to the beam, and follow helical paths that may intersect the target at more than one point, it is advantageous for the target to be in the form of a narrow rod, tilted at a small angle to the magnetic axis. As shown in Fig. 1.3, suitable parameters for a Hg target are a tilt angle of 150 milliradian and a target radius of 5 mm. However, jet motion in a magnetic induction field behaves differently, depending on the angle between the axis of the magnet and that of the jet, as a result of the differences in the magnitude of components of magnetic field [76]. As the crossing angle increases, the transverse component of the magnetic field increases, but with no significant change in the longitudinal component. The increase in the transverse component of the magnetic field raises the induced current on the Hg jet. Therefore, the angle of the Hg jet is launched at 33 milliradian with respect to the axis of the magnet, resulting in an interaction region about 30 cm long in case of a 1 cm diameter Hg jet. Since the proton

beam in TT2A beamline at CERN is horizontal, the Hg jet should make a 34 milliradian angle with respect to the proton beam axis, and the magnetic axis should make an angle of 67 milliradian with respect to the proton beam. The jet velocity is designed to be 15 m/s for the center of jet to intersect the center of the proton beam at the center of magnet.

Based on the previous studies described in the above, the experimental setup parameters are determined. The layout of experimental setup is more described below and optical diagnostic method for observation of Hg flow in magnetic fields is more discussed in Chapter 3. Figure 1.4 shows the detailed schematic of the overlap between key components of the experiment. The velocity of the jet is 15 m/s, where the trajectory of Hg jet overlaps with the proton beam over 30 cm. The facility is a closed piping loop, constructed primarily of 316 stainless steel, and designed to circulate liquid Hg. The parameters of the proton beam and solenoid system are determined by the required conditions of particle production rates [3]. Basic system parameters consist of proton energy 24 GeV, 14 GeV, and number of protons in one pulse $\approx 3 \times 10^{13}$, which was extracted from the CERN(European Organization for Nuclear Research) PS(Proton Synchrotron) in 2007. The solenoid length is 100 cm, inside radius is 7.5 cm, and a maximum magnetic field is 15 T. The solenoid magnet is titled at 67 milliradian angle with respect to the beam. The beam arrives at an angle 34 milliradian with respect to the jet which has a radius ≈ 0.5 cm, as schematically shown in Fig. 1.4. The angle between moving Hg jet and magnetic axis induces currents, which generates Lorentz

force with a component of magnetic field. Thus, it is expected that the optimal 150 milliradian of jet axis with respect to magnetic axis distorts jet shape [23]. Therefore, 33 milliradian of jet axis with respect to magnetic axis was designed for experiment to yield minimum distortion of jet shape. The 24 GeV proton beam is directed on to the solenoid at 67 milliradian off the solenoid axis, so that most high momentum particles do not travel straight down the beam line [22]. If there are no magnetic and gravitational effects on the Hg jet trajectory, the beam should enter at the bottom surface of Hg jet at Viewport 1, which is located at approximately 30 cm from the nozzle and the beam should exit on the top surface of Hg jet at Viewport 3, which is located at approximately 60 cm from the nozzle. The required jet velocity is determined by two conditions: 1), the need to replenish the target before the arrival of subsequent proton beam pulse, and 2), it should be high enough to overcome the deceleration force induced by Lorentz force [33].

Initial tests were performed at the BNL Alternating Gradient Synchrotron (AGS) [40], and continued at the CERN ISOLDE facility [46]. The BNL test featured a 24 GeV proton beam interacting with a free Hg jet with a nozzle diameter of 1 cm and a velocity of 2.5 m/s. The delivered proton bunch was focused to <1 mm radius, resulting in a peak energy deposition of 80 J/g, delivering 24 GeV proton beam at 15 Hz [93]. These initial tests did not have a magnetic field on the target. A parallel effort was undertaken to study the effects of high velocity Hg jets in the presence of high-magnetic fields, but with no proton beam [19].

1.2.4 Impact of the MHD mercury jet experiment for an intense proton target

The previous experiments did not perform the Hg jet in a high magnetic field interacting with an intense proton beam. In this work, we integrated the Hg jet, solenoid magnet, and intense proton beam all together. The performance and feasibility of utilizing liquid metal jet as a target for an intense proton beam is explored experimentally, which is an explicit objective of the experiment. The liquid jet target concept is recyclability otherwise the target would be destroyed. Therefore, the power of the target has to be evaluated in terms of the replacing capability and validated experimentally. In order to validate the performance of the target, the MHD jet behavior in a strong magnetic field has to be investigated. The response of the Hg jet due to the energy deposition by interacting with an intense proton beam has to be studied and the magnetic field effect to the disruption of Hg jet has to be studied, as well. The experimental results reveals that the effect of the Lorentz force to the jet stabilization as well as the deflection of jet. The experimental results provide feasibility of utilizing liquid metal jet as a target for an intense proton beam.

1.3 Mercury Target Issues

1.3.1 Mercury jet disruption by energy deposition from an intense proton beam

The production of large fluxes of particles using high energy, high intensity proton pulses impinging on solid or liquid targets presents unique problems which have not yet been entirely solved. The large amount of power deposition required in the material coupled with the short pulse duration produce large, almost instantaneous local heating. The interaction of the proton beam with the Hg target leads to very high heating rates in the target, where the heat from the beam could melt or crack a high-Z target. Sudden energy deposition into Hg jet causes increase in temperature by specific heat capacity. Increase in temperature causes volumetric changes by the volumetric thermal expansion coefficient, which results in pressure rise analogous Young's Modulus relationship between stress and strain. Thus, strain energy is built up in the Hg jet. This strain energy is released as kinetic energy such as filaments development on jet surface. The resulting sudden thermal expansion can result in damage causing stresses in solids and in the violent disruption of liquid jets. The volume expansion initiates vibrations in the material. The amplitude of these vibrations is such that stresses that exceed the strength of the material can be generated, causing mechanical failure [90].

1.3.2 Magnetohydrodynamic issues in mercury jet target

Liquid metal jets are proposed as potential target candidates because the heat energy can be removed along with the moving liquid. For Hg, heat conduction is very effective compared to convection: thermal diffusivity is dominant. In heat transfer, the Prandtl number indicates the relative thickness of the momentum and thermal boundary layers. When Prandtl number is small such as Hg, it means the heat diffuses very quickly compared to the velocity. However, there are two important problems that are associated with the use of liquid metal targets in these environments. First, as the liquid jet penetrates the magnetic field, instabilities in jet motion and deceleration may occur because of the large field gradients at the entrance and exit of the solenoid. The designed jet velocity is $\sim$ 15 m/s $\sim$ 20 m/s,considering the repetition rate of target and avoidance of bending jet trajectory in order to have 2 interaction length between proton beam and jet. Theses instabilities may change the jet shape into one that is significantly less efficient for pion production [33]. Second, during the intense pulse of energy deposition in a short time, the resultant stress could break up the target, where the liquid jet can develop surface instabilities such as filaments after beam interaction. These filaments may damage to surrounding facility under operation of target because of similar characteristics of Hg to metal.

Hg flow in a magnetic field experiences induced currents, which causes the jet to produce transverse forces normal to jet axis direction resulting deflection normal to jet axis [22, 23]. In addition, axial currents are induced if the jet axis

does not coincide with the magnetic field axis. These axial currents produce elliptical distortions of the Hg jet. Faraday's law can be used to obtain the azimuthal current density from changing the axial field in the local coordinate system of the Hg jet. The transverse component of the magnetic field normal to the jet axis also varies along the trajectory of the Hg jet. The axial current density can be related to the changing transverse component of the magnetic field normal to the jet axis. These axial currents produce a magnetic force. This force will be balanced by a restoring force from the surface tension of the Hg, and with the condition that the Hg is an incompressible liquid, will produce an elliptic deformation of the Hg jet [68].

1.3.3 Overview of experimental investigation of MHD flow and discussion

A proof-of-principle experiment performed at the CERN(European Organization for Nuclear Research) PS(Proton Synchrotron), which combined a free Hg jet target with a 15 T solenoid magnet and a 24 GeV primary proton beam. [3]. The disruption of jet could be much longer than beam-jet interaction length, which must be investigated experimentally and a key purpose of experiment. The experiment validates the liquid type of target for producing an intense secondary source of muons by showing the jet repetition rate to replace the disrupted target by the energy deposition from an intense proton beam. Also, due to the energy deposition in jet by an interaction of proton beam, the filaments development on jet surface could damage and eventually break the

facility of surrounding wall. The filament velocity could be much high, which must be investigated experimentally and another key purpose of experiment. For the investigation of feasibility, various behavior of Hg jet in magnetic fields interacting with proton beam is reported based on experimental measurement.

The PS runs in a harmonic 16 mode and can fill up to 2×10^{12} protons/bunch (2 Tp/bunch), where the term "harmonic" means sinusoidal pulse shape, the term "8(16)" means number of bunches, and the term "bunch" means sub-pulse in a pulse. Note that Tp(Tera protons) means 1×10^{12} protons. This allows up to 30×10^{12} protons per pulse on the Hg target, generating a peak energy deposition of $\sim$ 130 J/g with $\sim$ beam spot size of 5.7 mm^2 at beam energy 24 GeV, which is a key design parameter of single pulse at CERN for a target system capable of supporting proton beam with powers of 4 MW. Note that CERN could provide requirement of this key design parameter. For this experiment, a solenoid with a bore of 15 cm for a high magnetic field was designed. This magnet is capable of delivering a pulsed peak field of 15 T [91]. The pulsed solenoid incorporates a magnetic field ramp up of 9 seconds and is capable of sustaining its peak field for a duration of $\sim$ 1 second. The magnetic axis is positioned at an angle of 67 milliradian with respect to the proton beam, with the tilt provided by a common baseplate supporting all the equipment. The relationship between the measured magnetic field and the applied solenoid current was mapped to deduce the maximum magnetic field at the center of the solenoid [91]. A 5.5 MW, 700 V power supply delivers 7500 A of current to pulse the solenoid [59, 49, 42]. Figure 1.5 (a) and (b) show the

the estimated jet velocity in nozzle during Hg loop system operation and the calculated behavior of the 15 T magnet during a pulse [31, 42]. Approximately 30 MJ of energy is dissipated in the magnet, which raises its temperature from 80 to 120 K. Note that CERN could provide requirement of this key component for experiment. The magnet is cryogenically cooled by liquid nitrogen to 77 K prior to operation and warms up by 30 K during pulsing due to 30 MJ coil heating [35]. Figure 1.6 shows cryogenic process of cooling 15 T solenoid magnet. Therefore, a 30 minute cooling time is needed for each single shot. The magnetic axis is positioned at an angle of 67 milliradian with respect to the proton beam, with the tilt provided by a common baseplate supporting all the equipment (see Fig. 1.7(a)). It was found that the maximum magnetic field reached 15 T at Plasma Science and Fusion Center in Massachusetts Institute of Technology [91].

The Hg jet delivery system generates a Hg jet from 1 cm diameter nozzle with velocities up to 15 m/s [30]. The primary diagnostic of the beam-jet interaction is optical. A set of four view-ports along the interaction region is connected by imaging fiber-optic bundles to four high speed cameras. The cross-section and actual equipment for the Hg system with high field solenoid magnet is shown in Fig. 1.7. The horizontal line in Fig. 1.7(a) represents the proton beam. The Hg jet, which is ejected from right to left in Fig. 1.7(a), co-propagates with the proton beam. Four Viewports are shown within the solenoid bore, which represent viewing locations for observation of the Hg jet within its primary containment vessel. The Hg system provides for double

containment vessel of the hazardous liquid metal, and can be inserted or removed from the solenoid bore without disassembly. Figure 1.8 shows schematics of Hg loop system for experiment. A hydraulic syringe pump, with a piston velocity of 3 cm/s was used to pulse the Hg jet. This pump minimizes the heat added to Hg as opposed to a centrifugal pump. The syringe pump also reduces the discharge pressure which is the limitation of a centrifugal pump. The Hg system provides a jet duration of a $\sim$ 3 seconds of constant velocity profile. A total of 180 kg of Hg is loaded in the system. A 30 kW, 200 bar hydraulic power unit drives the syringe pump [31].

Each pulse of the proton beam delivered to this system constitutes a separate experiment. About 360 beam pulses are utilized in a beam-on-demand mode at CERN. These pulses span a range of intensities and time intervals between the multiple extracted bunches per pulse. The magnet operates over a range of field strengths of 0 $\sim$ 15 T.

In Chapter 2, the full MHD governing equation using Maxwell's equations are presented. Governing equations of conducting flow in a magnetic field are formed, where the contribution of Lorentz force to the hydrodynamic equations is discussed. The reviewed equations are employed in Frontier MHD code, whose results are referenced for comparison with experimental results.

In Chapter 3, the detailed layout of optical diagnostic setup and its installation are presented. The design of each key component for the experiment is presented. As a primary diagnostics, the scientific development of optical diagnostics employing the high speed cameras and infrared lasers to freeze the transient

motion of Hg jet is presented and the performance of the scientific instrument as well as the methodology to capture images are discussed.

In Chapter 4, 5, and 6, MHD behavior of Hg jet in various magnetic fields is discussed based on the observation from experiment. Also, the characteristics of Hg jet in magnetic fields interacting with an intense proton beam are presented, where the effect of magnetic field to suppress of disruption of jet and reducing of filament velocity are investigated to validate the performance and feasibility of utilizing Hg jet as a high power target. The key result to validate the feasibility of the high-Z liquid target is addressed based on the experimental measurements and the beam pulse structures.

To conclude, discussion based on understanding of MHD flow from various literatures and experimental results is summarized in Chapter 7.

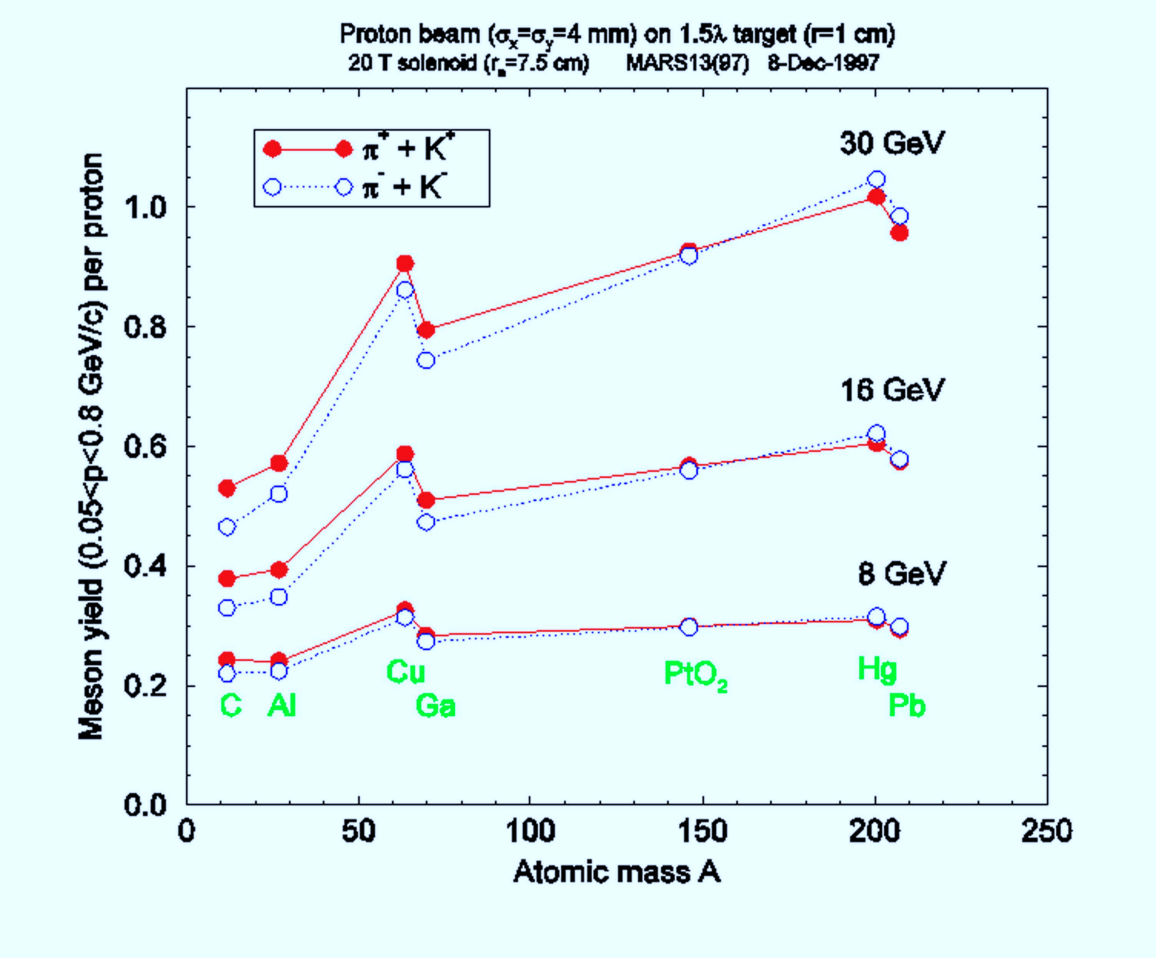

Figure 1.1: Pion yield versus atomic mass number of target at three proton beam energies [66].

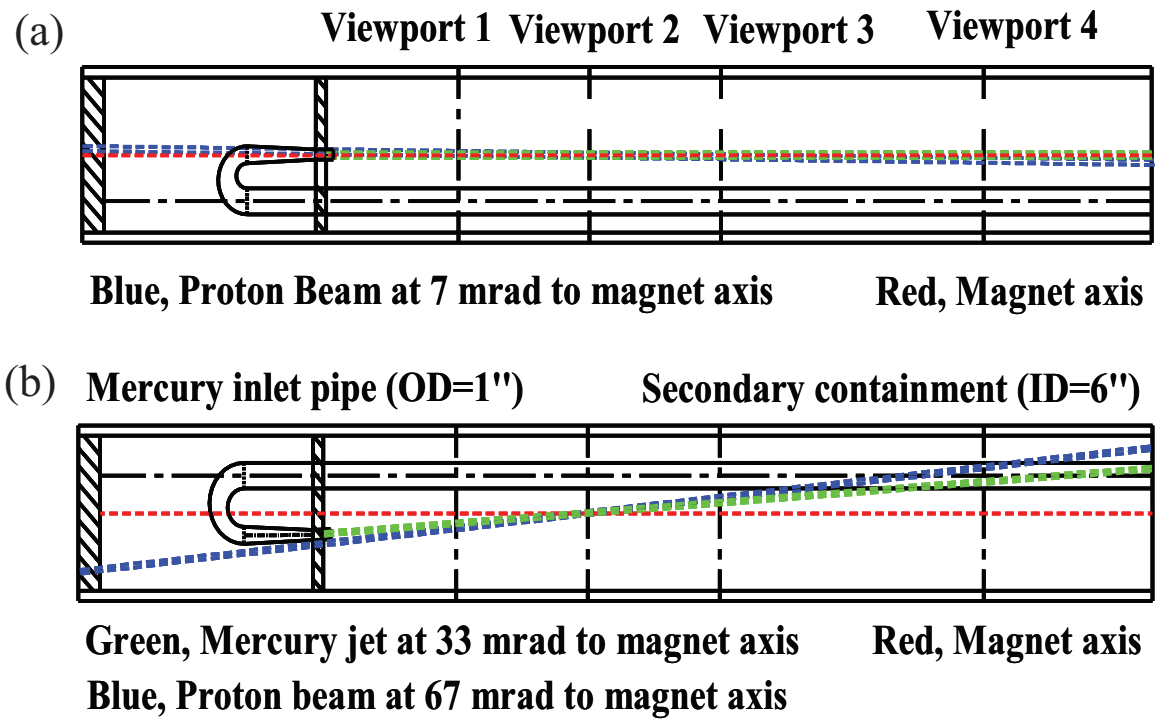

Figure 1.2: Geometry of key elements of target system and Viewports, showing the overlap between the Hg jet, magnetic axis, and the proton beam. a.) Top view. b.) Side view.

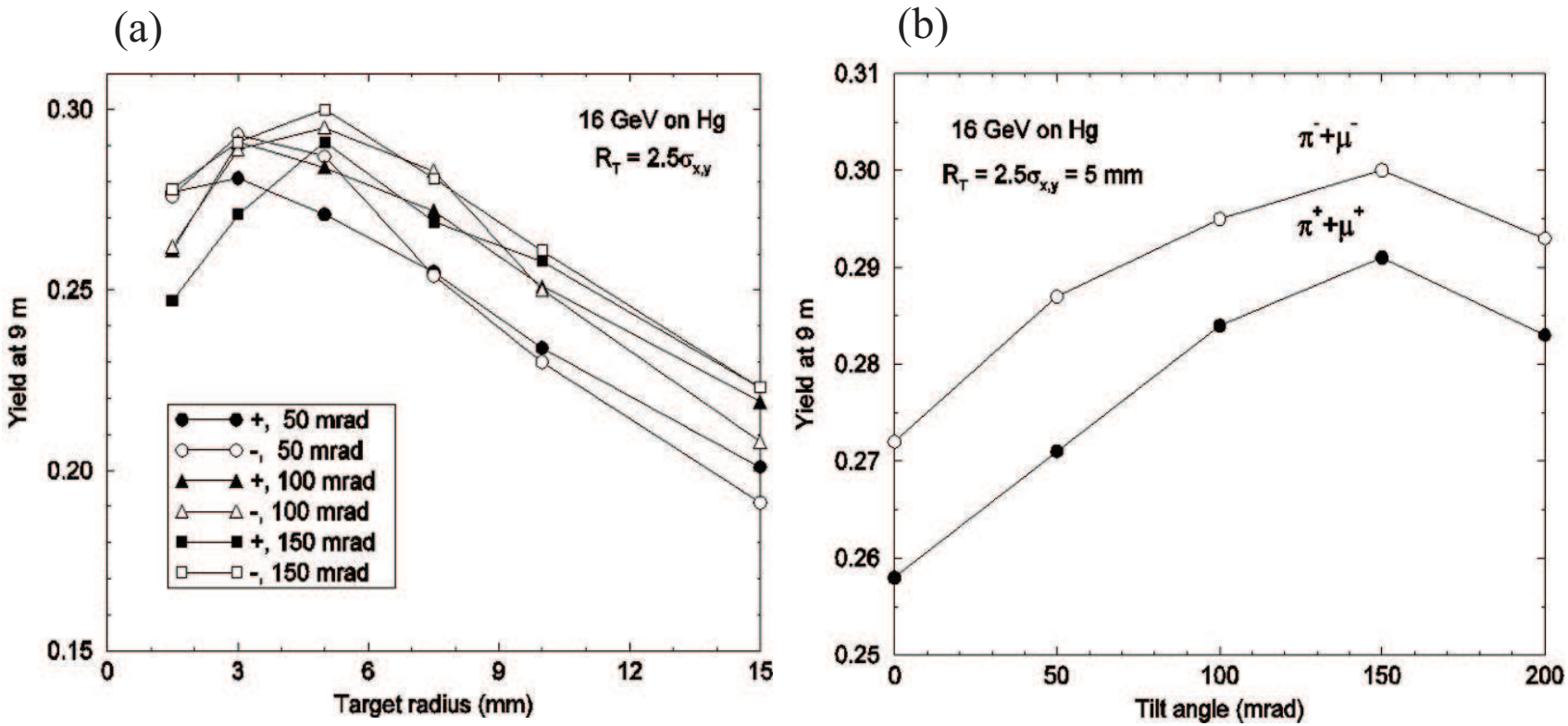

Figure 1.3: Pion yield from Hg target versus tilt angle between the target/beam axis and the solenoid axis and versus the radius of the target [66, 61]. a.) Pion yield versus target radius. b.) Pion yield versus tilt angle.

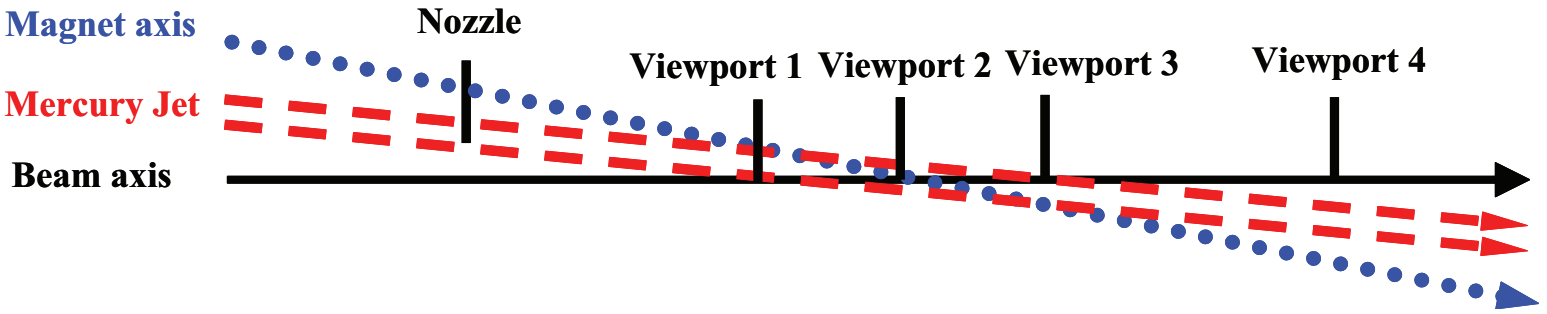

Figure 1.4: Schematics of the relative overlap between proton beam axis, Hg jet axis , and solenoid magnet axis. Viewport1, Viewport2, Viewport3, and Viewport4 are located 30 cm, 45 cm, 60 cm, 90 cm apart from nozzle exit, respectively.

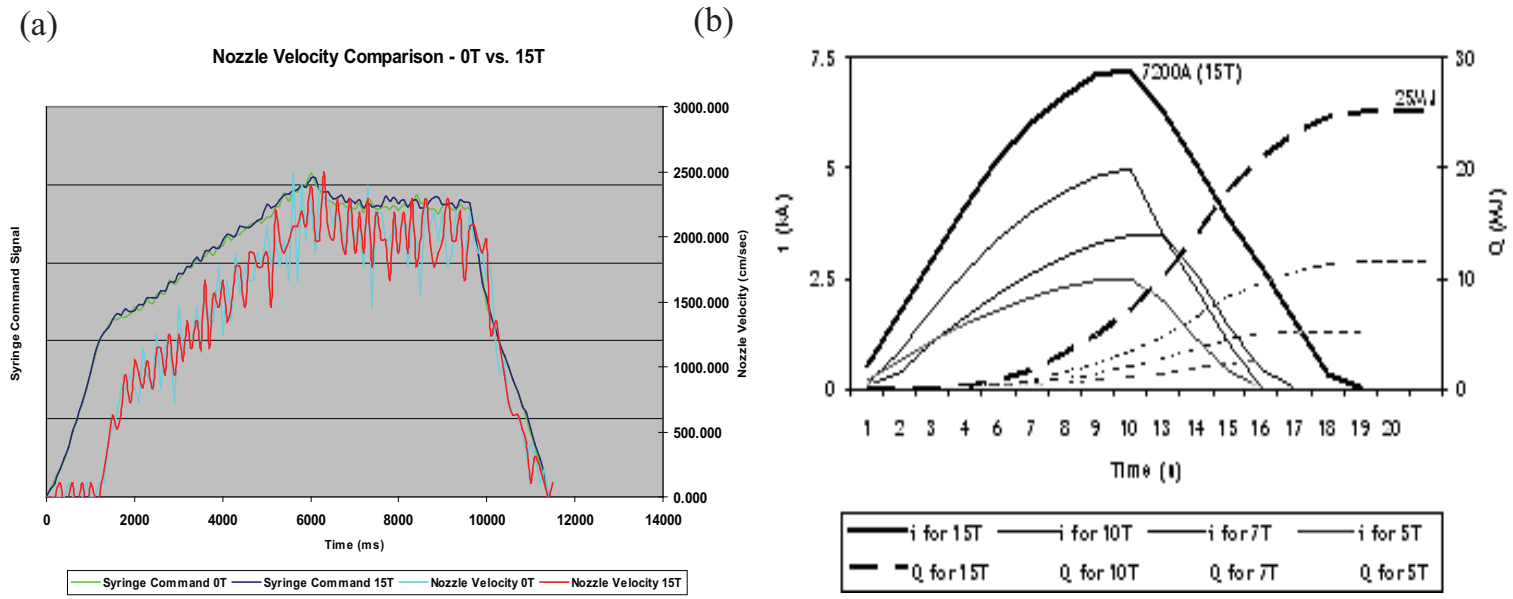

Figure 1.5: Operation of Hg loop system and pulsed 15 T solenoid magnet. a.) Hg loop system command [30]. b.) Behavior of the 15 T solenoid magnet during a pulse [42].

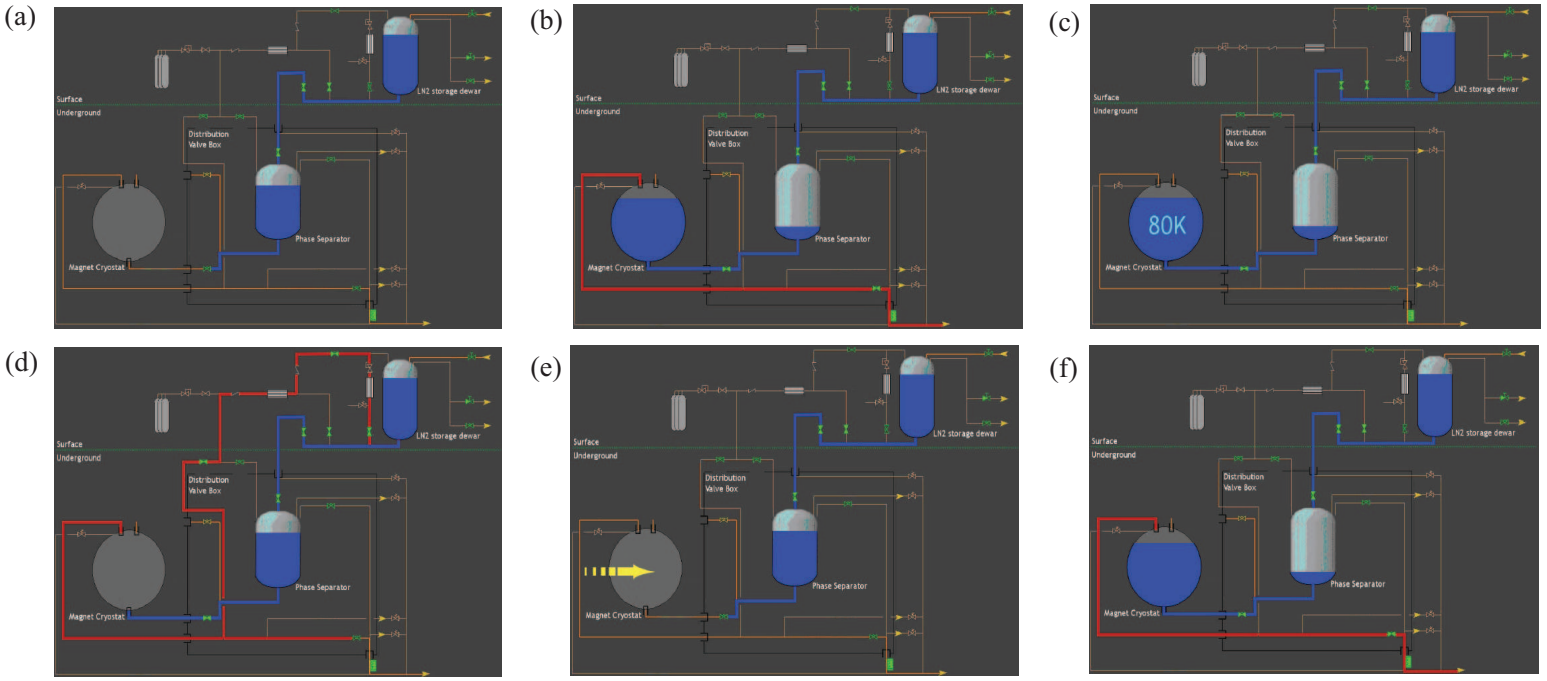

Figure 1.6: Cryogenic process of cooling 15 T solenoid magnet [35]. a.) Cooling of proximity cryogenics. b.) Magnet cooldown. c.) Magnet at 80 K. d.) Emptying of the magnet cryostat. e.) Magnet pulse. f.) Re-cooling of magnet.

(a)

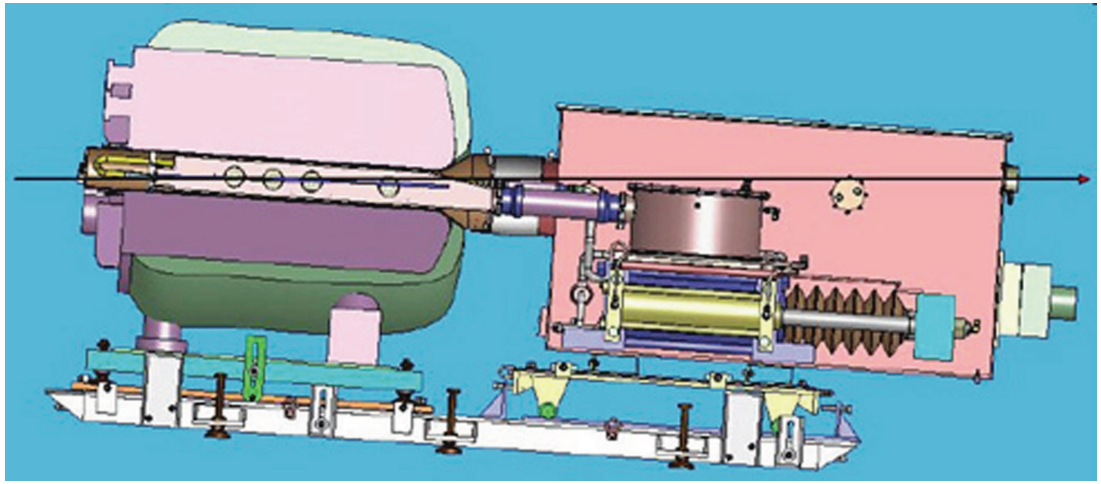

(b)

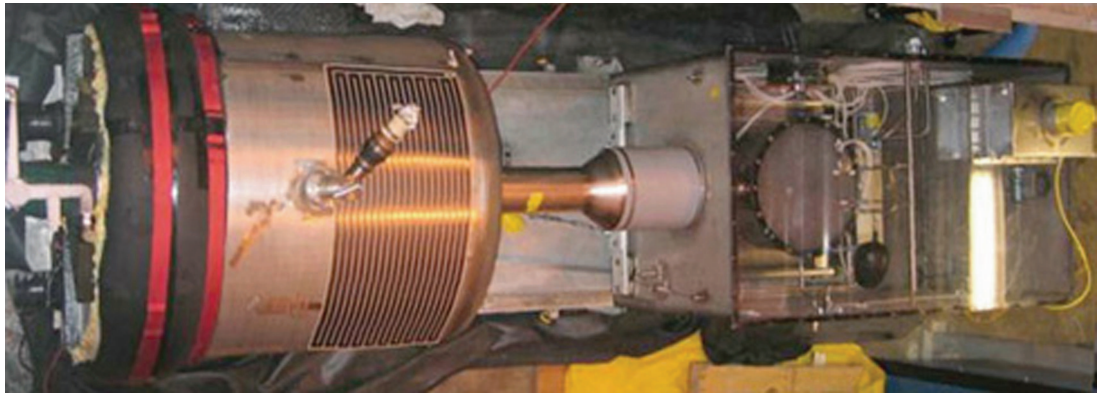

Figure 1.7: Photographs of the entire MERIT(Mercury Intense Target) experiment [31]. a.) Sectional side view of Hg loop system integrated with 15 T solenoid magnet. b.) Fabricated Hg loop system assembled with 15 T solenoid magnet (Top view).

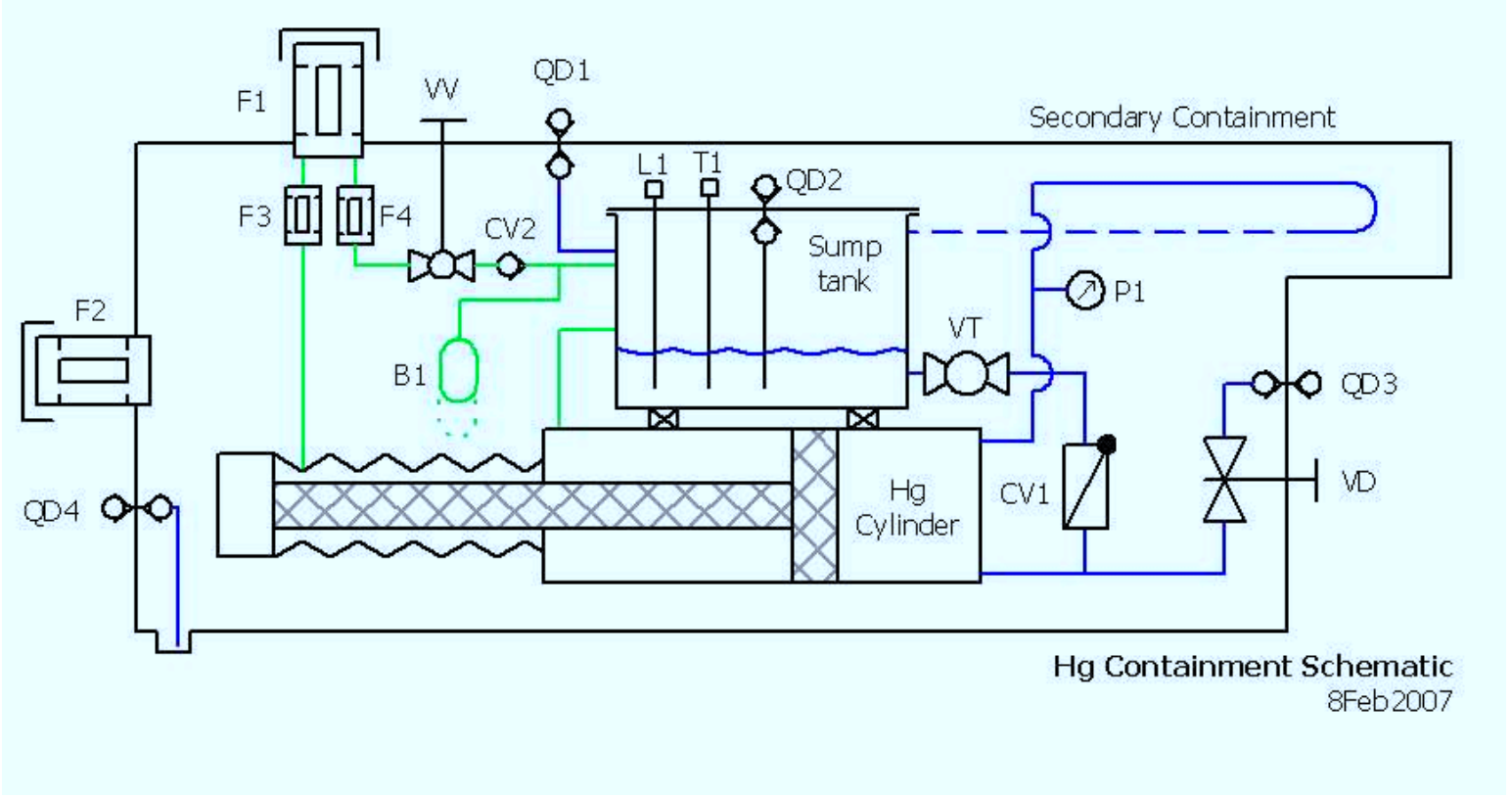

Figure 1.8: Schematics of Hg loop system for MERIT(Mercury Intense Target) experiment [31].

Chapter 2

Conducting Flow in a Magnetic Field

In this chapter, the governing equations for magnetohydrodynamics (MHD), based on electrodynamic relations of Maxwell's equation and hydrodynamic Navier-Stokes equation, are given and the effects of Lorenz force induced by magnetic field are discussed. Considering the energy equation for MHD, the roles of energy deposition induced by proton beam interaction and energy of state equation are discussed. Hartmann considered the flow between two parallel, infinite, non-conducting walls, with magnetic field applied normal to the walls [32]. An exact solution was obtained for this case. Shercliff solved the more general problem of three dimensional flow in a rectangular duct [79]. Exact solutions demonstrated the fact that for large Hartmann number, the velocity distribution consists of a uniform core with a boundary layer near the walls. This result enabled the solution of the corresponding problem for a circular pipe in an approximate manner for large Hartmann numbers, assuming walls of zero conductivities [80]. Chang [12] considered the effects

of wall conductivity for the same problem. Gold [27] considered a steady one-dimensional flow of an incompressible, viscous, electrically conducting fluid through a circular pipe in the presence of a uniform transverse field. A no-slip condition is assumed at the electrically non-conducting wall because if the walls are conducting, there is a electromagnetic force on the wall and a corresponding force on the fluid. The solution is exact and valid for all values of the Hartmann number. Conducting liquid jet under the influence of a strong magnetic field raises several MHD issues, such as the possible deformation of the jet's shape and trajectory, as well as the effect of the magnetic field on the beam-induced dispersal of the jet. The electrically conducting flow moving in a magnetic field experiences induced currents [23]. These induced currents cause the jet to experience anisotropic pressure distribution with respect to the major and minor axis of jet cross section normal to the jet axis while the jet penetrates the nonuniform magnetic field [23]. In addition, axial currents are induced if the jet axis does not coincide with the magnetic field axis. These currents in turn produce transverse elliptical distortions of the Hg jet. Finally, the liquid jet can develop surface instabilities and jet breakup during liquid motion in a inhomogeneous magnetic field and after interaction with an intense proton beam. These phenomena can change the shape of the jet to a form that is less efficient target for pion production.

2.1 Governing Equations for MHD Flow

2.1.1 Electromagnetic equations

In this section, we describe the electromagnetic relations that have been used in the derivation of the MHD governing equations. The following parameters are defined as follows:

- polarization density $\mathbf{P}$: the vector field that expresses the density of permanent or induced electric dipole moments in a dielectric material. It is defined as the dipole moment per unit volume.
- magnetization density $\mathbf{M}$: the magnetic dipole moment per unit volume.
- electrical susceptibility χ_e: a measure of how easily a dielectric material polarizes in response to an electric field. This determines the electric permittivity of the material. It is defined as the constant of proportionality when relating an electric field $\mathbf{E}$ to the induced dielectric polarization density $\mathbf{P}$.
- magnetic susceptibility χ_m: the degree of magnetization of a material in response to an applied magnetic field.
- electric displacement field $\mathbf{D}$: It accounts for the effects of bound charges within materials. It is the macroscopic field average of electric fields from charged particles that make up otherwise electrically neutral material. It can be considered the field after taking into account the response of a medium to an external field such as reorientation of electric dipoles.

- magnetic field strength **H**: A vector field that permeates space which can exert a magnetic force on a moving electric charge and on magnetic dipoles such as permanent magnets.
- electric field **E**: the electric force per unit charge. The direction of the field is taken to be the direction of the force it would exert on a positive test charge.

2.1.1.1 *electromagnetic relations in a linear material*

In a linear material, the polarization density **P**, magnetization density **M**, and the magnetic field strength are related by

$$\mathbf{P} = \chi_e \varepsilon_o \mathbf{E} \tag{2.1}$$

and

$$\mathbf{M} = \chi_m \mathbf{H} \ , \tag{2.2}$$

where χ_e is the electrical susceptibility and χ_m is the magnetic susceptibility of the material. Electric displacement field **D** and magnetic induction field **B** are related to the electric field **E** and magnetic field **H** by

$$\mathbf{D} = \varepsilon_o \mathbf{E} + \mathbf{P} = \varepsilon \mathbf{E} \tag{2.3}$$

and

$$\mathbf{B} = \mu_o (\mathbf{H} + \mathbf{M}) = \mu \mathbf{H} \ , \tag{2.4}$$

where ε is the electrical permittivity and μ is the magnetic permeability of the material.

2.1.1.2 *Maxwell's equations*

The solenoidal condition for the magnetic induction, indicating that there are no magnetic monopoles, is given by

$$\nabla \cdot \mathbf{B} = 0 \ . \tag{2.5}$$

This shows that there are no sources and sinks for magnetic field lines. Faraday's law of magnetic induction is given by

$$\nabla \times \mathbf{E} = -\partial \mathbf{B}/\partial t \ , \tag{2.6}$$

showing that a spatially varying electric field can induce a magnetic field. Charge conservation gives

$$\nabla \cdot \mathbf{E} = \rho^*/\varepsilon_o \ , \tag{2.7}$$

where $\rho^* = \varepsilon_o$ (n^+ - n^-) is the charge density, n^+ is the number of ions, and n^- is the number of electrons. Ampère's law is given by

$$\nabla \times \mathbf{B} = \mu \mathbf{j} + \mu\varepsilon \partial \mathbf{E}/\partial t \ , \tag{2.8}$$

where the last term on the right hand side is the displacement current. Introducing the fundamental units of mass M, length L, velocity v, and time t, we consider the dimensions of the displacement current in Eqn. (2.8). The

dimensions of the magnetic field B, electric field E, and the speed of light c are considered for simplicity.

$\nabla \times \mathbf{E} \sim \frac{E}{L}, \frac{\partial \mathbf{B}}{\partial t} \sim \frac{B}{t}$ gives E = v B . From the speed of light, c = $\frac{1}{\sqrt{\mu\varepsilon}}$, $\mu\varepsilon\partial\mathbf{E}/\partial t = \frac{1}{c^2}\partial\mathbf{E}/\partial t \sim \frac{1}{c^2}\frac{E}{t} = \frac{v}{c^2}\frac{B}{t} = \frac{B}{L}\frac{v^2}{c^2}$.

Therefore, the displacement current in Ampère's law can be neglected if the flow velocity is much less than the speed of light. By assuming the flow obeys charge neutrality, n^+ - n^- $\ll$ n, where n is the total number density, the charge density in Eqn. (2.7) can be neglected. Note that n includes positive, negative, and neutral charge. Thus, n^+ - n^- $\ll$ n indicates that most of charges are assumed to obey neutrality. Finally, Ohm's law without Hall effect is given by

$$\mathbf{j} = \sigma(\mathbf{E} + \mathbf{v} \times \mathbf{B}) \ . \tag{2.9}$$

This is the generalization of the relation between voltage and current in a moving conductor. It provides the link between the electromagnetic equations and the fluid equations. The electric charge is conserved, which is given by Kirchhoff's law:

$$\nabla \cdot \mathbf{j} = 0. \tag{2.10}$$

2.1.2 The Navier Stokes and magnetic induction equations in a conducting liquid flow

The motion of an electrically conducting fluid in the presence of a magnetic field obeys the equations of MHD. The fluid is treated as a continuum, and the classical results of fluid dynamics and electro-dynamics are combined in the derivation of the equations. The first equation is from mass conservation:

$$\frac{\partial \rho}{\partial t} + \nabla \cdot (\rho \mathbf{v}) = 0 \ . \tag{2.11}$$

Next, Newton's second law of motion gives

$$\rho \frac{D\mathbf{v}}{Dt} = -\nabla p + \mathbf{F} \ , \tag{2.12}$$

where the external force $\mathbf{F}$ consists of several terms, such as the Lorentz force, given by $\mathbf{j} \times \mathbf{B}$, the gravitational force $\rho \ \mathbf{g}$, and the viscous force. The viscous term is given by a kinematic viscosity of the form $\rho\nu\nabla^2 \ \mathbf{v}$ for an incompressible flow. Thus, Equation (2.12) becomes

$$\rho \frac{\partial \mathbf{v}}{\partial t} + \rho(\mathbf{v} \cdot \nabla)\mathbf{v} = -\nabla p + \rho \mathbf{g} + \eta \nabla^2 \mathbf{v} + \mathbf{j} \times \mathbf{B} \ . \tag{2.13}$$

Note that the Lorentz force couples the fluid equations to the electromagnetic equations. Equation (2.13) can be reduced to a dimensionless form.

$$\frac{\partial \mathbf{v}}{\partial t} + \mathbf{v} \cdot \nabla \mathbf{v} = -\nabla p + \frac{\mathbf{g}}{\mathrm{Fr}^2} + \frac{1}{\mathrm{Re}} \nabla^2 \mathbf{v} + \mathrm{Al}(\mathbf{j} \times \mathbf{B}) \ , \tag{2.14}$$

where Fr $= v/\sqrt{gL}$, Re$= \rho vL/\eta$, Re$_m = \mu\sigma vL$, and Al $= B_o^2/\mu\rho v^2$ denote the Froude, Reynolds, magnetic Reynolds, and Alfvén numbers, respectively. The Hartmann number, Ha $= B_o L(\sigma/\eta)^{\frac{1}{2}}$, gives the ratio of magnetic forces to viscous forces. Thus, this number is the important parameter in cases where the inertial effects are small. On the other hand, the Stuart number, N, gives the ratio of magnetic forces to inertial forces, Thus, this number is the important parameter where dealing with inviscid or turbulent flows. Ha and N are related through Ha^2 = ReRe$_m$Al and N = Re$_m$Al. Note that the ratio of Hartmann number and Reynolds number involves viscous, magnetic, and inertial forces and can be thought as the square root of the product of the viscous and magnetic forces divided by the inertial forces.

We consider components of the magnetic induction field B_x, B_y, B_z. Note that the longitudinal magnetic field along the jet axis x and the transverse magnetic field normal to the jet axis are given by $B_x = B_X cos\theta - B_Y sin\theta, B_y = -B_X sin\theta + B_Y cos\theta$ respectively, where B_X is axial magnetic field and B_Y is radial magnetic field. Also note that the jet flow uses (x, y, z) coordinate system and magnetic field uses (X, Y, Z) coordinate system in Fig. 2.1. The nondimensionalized momentum equations in the (x, y, z) coordinate system in Fig. 2.1 is represented as Eqn. (2.15) using Ohm's equation:

$$\frac{\partial v_x}{\partial t} + v_x \cdot \nabla v_x = -\nabla p + \frac{1}{\mathrm{Re}}\nabla^2 v_x - \frac{\mathrm{Ha}_y^2}{\mathrm{Re}} v_x + \frac{\mathrm{Ha}_x \mathrm{Ha}_y}{\mathrm{Re}} v_y \ ,$$
$$\frac{\partial v_y}{\partial t} + v_y \cdot \nabla v_y = -\nabla p + \frac{1}{\mathrm{Re}}\nabla^2 v_y - \frac{\mathrm{Ha}_x^2}{\mathrm{Re}} v_y + \frac{\mathrm{Ha}_x \mathrm{Ha}_y}{\mathrm{Re}} v_x \ ,$$
$$\frac{\partial v_z}{\partial t} + v_z \cdot \nabla v_z = -\nabla p + \frac{1}{\mathrm{Re}}\nabla^2 v_z - \frac{\mathrm{Ha}_x^2}{\mathrm{Re}} v_z - \frac{\mathrm{Ha}_y^2}{\mathrm{Re}} v_z \ , \qquad (2.15)$$

where $\mathrm{Ha}_x = B_x L(\sigma/\eta)^{\frac{1}{2}}$, $\mathrm{Ha}_y = B_y L(\sigma/\eta)^{\frac{1}{2}}$, and $\mathrm{Ha}_z = B_z L(\sigma/\eta)^{\frac{1}{2}}$. In MHD, to eliminate the electric field $\mathbf{E}$ and the electric current density $\mathbf{j}$, we use the Ampere's law and Ohm's law. Then, Faraday's law gives the magnetic induction equation:

$$\frac{\partial \mathbf{B}}{\partial t} = \nabla \times (\mathbf{v} \times \mathbf{B}) - \frac{1}{\mu\sigma}\nabla \times \nabla \times \mathbf{B} = \nabla \times (\mathbf{v} \times \mathbf{B}) + \frac{1}{\mu\sigma}\nabla^2 \mathbf{B} \ . \qquad (2.16)$$

2.1.2.1 *magnetic Reynolds number*

In Eqn. (2.16), the dimension of the term on the left hand side is $\frac{B}{t}$ and that of the second term on the right hand side is $\frac{B}{\sigma\mu L^2}$. Therefore, $\sigma\mu \sim \frac{t}{L^2}$. The magnetic induction equation can be written in a dimensionless form:

$$\frac{\partial \mathbf{B}}{\partial t} = \nabla \times (\mathbf{v} \times \mathbf{B}) + \frac{1}{\sigma\mu L v}\nabla^2 \mathbf{B} \ , \qquad (2.17)$$

where the quantity $\sigma\mu L v$ is the magnetic Reynolds number, Re_m, which is a measure of the size of the advection term, $\nabla \times (\mathbf{v} \times \mathbf{B})$, relative to the diffusion term, $\frac{1}{\sigma\mu L v}\nabla^2 \mathbf{B}$. Reynolds number Re measures the extent to which a convective process prevails over a diffusive one. In viscous flow, the viscosity

causes vorticity to diffuse in the face of convection and the Reynolds number measures the power of convection over diffusion of vorticity. In MHD, the conductivity causes convection to overcome diffusion of the magnetic field to a degree measured by the magnetic Reynolds number Re_m. If Re_m is large, convection dominates over diffusion and magnetic boundary layer near the magnetic field are to be expected. The magnetic Prandtl number, Pr_m, measures the ratio of viscous diffusivity and magnetic diffusivity and is defined as $\mathrm{Re}_m/\mathrm{Re}$. When it is small, magnetic fields diffuse much more rapidly than vorticity and magnetic boundary layers are much thicker than viscous layers. From Eqn. (2.18) and (2.19), the time scales with changes due to fluid motions and field diffusion can be thought of $t_{convection} = \frac{v}{L}$ and $t_{diffusion} = \sigma\mu L^2$. Thus, the time scales for magnetic Prandtl number can be $\mu\sigma vL$, which corresponds to Re_m. Therefore, if $\mathrm{Re}_m \ll 1$, the dissipation time is much smaller than characteristic time in the flow. During the characteristic time in the flow, a field disturbance diffuses $(L/\mu\sigma v)^{1/2}$. This is much larger than L if $\mathrm{Re}_m \ll 1$. This makes for simplifications such as the neglect of viscosity in the magnetic boundary layer. In any region of length scale δ where magnetic convection and diffusion are equally important, δ must be of order $1/\mu\sigma v$. Only within limited regions where B changes significantly in a distance δ can the gradients be high enough for diffusion and dissipation to matter. The characteristic time in the flow is the transit time L/v, during which a field disturbance diffuses a distance of order $(L/\mu\sigma v)^{1/2}$. This is much less than L if $\mathrm{Re}_m \gg 1$, in which case diffusion is negligible and diffuses a distance of

order $(t/\mu\sigma)^{1/2}$. This is the required criterion for the perfect conductivity approximation to be valid. At the other extreme case where diffusion is dominant is that the medium diffuses to the form it would be in stationary fluid, where no induced magnetic field would occur. The ratio of the induced magnetic field and the imposed magnetic field is of order $\mu\sigma vL$, which is Re_m. The low Re_m approximation is to ignore the induced field, to replace $\mathbf{B}$ by the known field $\mathbf{B}_o$ in all MHD equations.

2.1.2.2 *frozen-in theorem in magnetic induction equation*

If $\mathrm{Re}_m \gg 1$, the induction equation Eqn. (2.16) is approximated by

$$\frac{\partial \mathbf{B}}{\partial t} = \nabla \times (\mathbf{v} \times \mathbf{B}). \tag{2.18}$$

The timescale with changes due to the fluid motion from Eqn. (2.18) is given by $t_{motion} \sim \frac{L}{v}$. In the case $t_{motion} \ll t_{diffusion}$, which corresponds to $\mathrm{R}_m \gg 1$, the diffusion term is negligible. According to the frozen-flux theorem of Alfvén, in a perfectly conducting fluid, where $\mathrm{Re}_m \to \infty$, the magnetic field lines move with the fluid: the field lines are 'frozen' into the fluid. This theorem states that motions along the field lines do not change the field but motions transverse to the field carry the field with them.

2.1.2.3 *diffusion limit in induction equation*

If $\mathrm{Re}_m \ll 1$, the induction equation Eqn. (2.16) is approximated by

$$\frac{\partial \mathbf{B}}{\partial t} = \frac{1}{\mu\sigma}\nabla^2\mathbf{B}. \tag{2.19}$$

The timescale with changes due to field diffusion from Eqn. (2.19) is given by $t_{diffusion} \approx \sigma\mu L^2$. The diffusion equation indicates that any irregularities in an initial magnetic field will diffuse away and be smoothed out. The field will tend to be a simpler uniform field. This process of smoothing out will occur on the given diffusion timescale.

2.2 The Energy Equation in MHD

2.2.1 Energetics and effects of Lorentz force

The energy equation that contains all the various types of energy, including kinetic energy, gravitational energy, the internal energy, and the magnetic energy is obtained using the MHD governing equations. The gravitational potential Φ is defined by $-\nabla\Phi = \mathbf{g}$. By multiplying Eqn. (2.11) by $v^2/2$ and dotting Eqn. (2.12) with $\mathbf{v}$, the energy equation can be given by

$$\frac{\partial}{\partial t}(\frac{1}{2}\rho v^2) + \nabla\cdot(\frac{1}{2}\rho v^2\mathbf{v}) = -\mathbf{v}\cdot\nabla p + \mathbf{v}\cdot(\mathbf{j}\times\mathbf{B}) - \mathbf{v}\cdot\rho\nabla\Phi + \mathbf{v}\cdot\eta\nabla^2\mathbf{v}\ . \tag{2.20}$$

The gravitational term is given using Eqn. (2.11) and the fact that $\partial\Phi/\partial t = 0$ as follow:

$$\mathbf{v}\cdot\rho\nabla\Phi = \nabla\cdot(\rho\Phi\mathbf{v}) + \frac{\partial}{\partial t}(\rho\Phi)\ . \tag{2.21}$$

The Lorentz force term is given using Eqn. (2.9) as follow:

$$\mathbf{v} \cdot (\mathbf{j} \times \mathbf{B}) = -\mathbf{j} \cdot (\mathbf{v} \times \mathbf{B}) = -\frac{j^2}{\sigma} + \mathbf{j} \cdot \mathbf{E} \ . \tag{2.22}$$

Equation (2.22) is rearranged using Eqn. (2.6) as follow:

$$\mathbf{v} \cdot (\mathbf{j} \times \mathbf{B}) = -\frac{j^2}{\sigma} - \nabla \cdot (\frac{\mathbf{E} \times \mathbf{B}}{\mu}) - \frac{\partial}{\partial t}(\frac{B^2}{2\mu}) \ . \tag{2.23}$$

The pressure gradient term gives

$$-\mathbf{v} \cdot \nabla p = -\nabla \cdot (p\mathbf{v}) + p \nabla \cdot \mathbf{v} \ . \tag{2.24}$$

Equation (2.24) can also be expressed using Eqn. (2.11) as follow:

$$p \nabla \cdot \mathbf{v} = -\frac{\partial p}{\partial t} \ . \tag{2.25}$$

Substituting the foregoing relations, the full energy equation is as follow:

$$\frac{\partial}{\partial t}[\frac{1}{2}\rho v^2 + \rho\Phi + p + \frac{B^2}{2\mu}] + \nabla \cdot \{[\frac{1}{2}\rho v^2 + \rho\Phi + p]\mathbf{v} + \frac{\mathbf{E} \times \mathbf{B}}{\mu}\} = -\frac{j^2}{\sigma} - D \ , \tag{2.26}$$

where D is viscous dissipation term.

2.2.2 Proton beam induced energy deposition and equation of state

Due to the sudden energy deposition by proton beam, it is worthy to consider the components of added energy and the state of energy from compressible density variation as well as ionization to the right hand side of the full energy

equation Eqn. (2.26). It is reported [34] that the instantaneous beam energy deposition is

$$E_{beam}(r) = E_p(r) \cdot \delta(t - t_{beam}), \tag{2.27}$$

where

$$E_p(r) = E_o exp[-\frac{r}{a}] \ . \tag{2.28}$$

$E_p\ (r)$ is radial energy density distribution and the proton beam energy is assumed to be deposited as a δ function at time $t = t_{beam}$. The equation of state (EOS) is considered as the sum of compression, ion thermal, and electron thermal terms. The compressible pressure P_c and energy E_c are

$$P_c = P_{co}[(\frac{\rho}{\rho_o})^{\gamma} - 1] \tag{2.29}$$

and

$$E_c = E_{co}[(\frac{\rho}{\rho_o})^{\gamma-1} - 1]\frac{\rho}{\rho_o} + P_{co}(1 - \frac{\rho}{\rho_o}), \tag{2.30}$$

where

$$P_{co} = \frac{\rho c^2}{\gamma} \quad , \quad E_{co} = \frac{P_{co}}{\gamma - 1}. \tag{2.31}$$

Ion and electron thermal pressure and energy are

$$E_I = 3nk(T - T_o) \quad , \quad P_I = G_I E_I \tag{2.32}$$

and

$$E_e = \frac{1}{2}\beta(T - T_o)^2 \quad , \quad \beta = \beta_o(\frac{\rho_o}{\rho})^{2/3} \quad , \quad P_e = G_e E_e, \tag{2.33}$$

where $n = \frac{\rho}{M}$ and k is Boltzmann's constant. Thus, the total energy deposition and pressure are

$$E_p = E_c + E_I + E_e \quad , \quad P_p = P_c + P_I + P_e \quad , \tag{2.34}$$

where subscripts c, I, and e correspond to compression, ion thermal, and electron thermal components, respectively. G_I and G_e are the Gruneisen coefficients for the ion and electron. c is the speed of sound in the material. Initial Hg pressure P is 0 at $T = T_o$ and normal density $\rho = \rho_o$. At higher temperatures, the Hg can be ionized and the resulting energy and pressure by free-electron component is added to the EOS.

It is reported [77] that a single phase EOS for liquid Hg showed that the strength of rarefaction waves in the jet significantly exceeds the Hg cavitation threshold. The formation of cavities is believed to take place in strong rarefaction waves, and cavitation bubbles influence the wave dynamics in Hg [77]. In order to capture the formation and dynamics of the two-phase domain of bubbly Hg, a homogenized two-phase equation of state is reported [75]. EOS consists of three branches. The pure vapor and liquid branches are described by the polytropic and stiffened polytropic EOS model respectively [60]. The two branches are connected by a model for the liquid-vapor mixture. The speed of sound in an equilibrium homogeneous mixture of liquid and vapor are given:

$$\frac{1}{c^2} = (\alpha\rho_{sat,v} + (1-\alpha)\rho_{sat,l})(\frac{\alpha}{\rho_{sat,v}c^2_{sat,v}} + \frac{1-\alpha}{\rho_{sat,l}c^2_{sat,l}}) \ , \tag{2.35}$$

where $\rho_{sat,v}, \rho_{sat,l}, a_{sat,v}, a_{sat,l}$ are the density and the speed of sound of vapor and liquid in saturation point, and α is the void fraction:

$$\alpha = \frac{\rho - \rho_{sat,l}}{\rho_{sat,v} - \rho_{sat,l}} \ . \tag{2.36}$$

Integrating the sound speed with respect to the density, the pressure-density relation is given as follow:

$$P = P_{sat,l} + P_{vl} log[\frac{\rho_{sat,v}c^2_{sat,v}(\rho_{sat,l} + \alpha(\rho_{sat,v} - \rho_{sat,l}))}{\rho_{sat,l}(\rho_{sat,v}c^2_{sat,v} - \alpha(\rho_{sat,v}c^2_{sat,v} - \rho_{sat,l}c^2_{sat,l}))}] \ , \tag{2.37}$$

where $P_{sat,l}$ is the liquid pressure in the saturation point and

$$P_{vl} = \frac{\rho_{sat,v}c^2_{sat,v}\rho_{sat,l}c^2_{sat,l}(\rho_{sat,v} - \rho_{sat,l})}{\rho^2_{sat,v}c^2_{sat,v} - \rho^2_{sat,l}c^2_{sat,l}} \ . \tag{2.38}$$

Using the second law of thermodynamic at constant entropy and Eqn. (2.37), the specific internal energy of the vapor-liquid mixture is calculated [75].

2.2.3 Magnetic damping with joule dissipation

It is known that a static magnetic field can suppress motion of an electrically conducting liquid. If a conducting liquid moves through an imposed static magnetic field, electric currents are generated. These, in turn, lead to ohmic heating such as Joule dissipation. As the thermal energy of the fluid rises, there is a corresponding drop in its kinetic energy, and so the fluid decelerates. This

is to suppress the motion of liquid jets. In many applications, it is believed that the imposition of a static magnetic field is used as one means of suppressing unwanted motion. Considering the uniform perpendicularly imposed magnetic field to the flow direction for simplicity, the damping effect of Lorentz force can be quantified. If the magnetic field is uniform, the Faraday' law requires that $\nabla \times \mathbf{E} = 0$. Using Ohm's law and the fact that the current density is solenoidal, the current relationship is given by

$$\nabla \cdot \mathbf{j} = 0 \quad , \quad \nabla \times \mathbf{j} = \sigma \mathbf{B} \cdot \nabla \mathbf{v} \ . \tag{2.39}$$

Thus, $\mathbf{j}$ is zero if $\mathbf{v}$ is independent of the magnetic field direction. By doing cross product of $\mathbf{j}$ and $\mathbf{B}$ and using the vector identity, Lorentz force per unit mass is given by

$$\mathbf{F} = -\frac{\mathbf{v}_\perp}{\tau} + \frac{\sigma(\mathbf{B} \times \nabla \phi_E)}{\rho} \ , \tag{2.40}$$

where $\tau = \rho/\sigma B^2$ is Joule damping term and ϕ_E is electrical potential, which is given by the divergence of Ohm's law: $\phi_E = \nabla^{-2}(B \cdot \omega)$. The Lorentz force then simplifies to $-\mathbf{v}/\tau$ when the magnetic field and the vorticity field are mutually perpendicular. Thus, the $\mathbf{v}_\perp$ to magnetic field declines on a time scale of τ, which is the phenomenological basis of magnetic damping. The ratio of the damping time τ to the characteristic time L/v gives the interaction parameter $\mathrm{N} = \sigma B^2 L/\rho v$, which is also used for the indication of the ratio of the magnetic and inertial forces.

To investigate the role of Joule dissipation, consider the fully derived energy

equation in inviscid flow from Eqn. (2.26) is given:

$$\frac{dE}{dt} = -\frac{1}{\sigma\rho}\int j^2 dV \ , \tag{2.41}$$

where j is current density, E is global kinetic energy, and the Joule dissipation is shown as per density. $\mathbf{j}^2$ from Eqn. (2.39) was estimated [14] and is given:

$$\frac{dE}{dt} \sim -(\frac{L_{min}}{L_{\|}})^2 \frac{E}{\tau} \ , \tag{2.42}$$

from which

$$E \sim E_o \ \ exp\ (-\tau^{-1}\int_0^t (L_{min}/L_{\|})^2 dt) \ , \tag{2.43}$$

where $L_{\|}$ and L_{min} are the characteristic length scales for the flow, parallel to the magnetic field. The time constant required for energy dissipation is getting smaller as the magnetic field strength increases. Figure 2.2 (a) and (b) show the decay of energy depending on the Joule damping term with various magnetic fields and its integration with respect to time, provided $L_{\|}$ and L_{min} remain of the same order. It indicates that the flow decays on a time scale of τ. However, the Lorentz force cannot create or destroy linear momentum, nor angular momentum [14]. As long as momentum is conserved, despite the Joule dissipation, the flow will not be annihilated on a time scale of τ, and one may infer from Eqn. (2.42) that $\frac{L_{\|}}{L_{min}}$ must increase with time [14]. Therefore, it is expected that the flow will experience anisotropy, with $L_{\|}$ increasing as the flow evolves.

2.2.4 Discussion

The purpose of this Chapter is to review governing equations of conducting flow in a magnetic field and the effect of Lorentz force on flow. Important equations are as follows: Maxwell equations (Eqn. (2.5) $\sim$ Eqn. (2.10)), Navier-Stokes equation (Eqn. (2.11), Eqn. (2.14)), Induction equation (Eqn. (2.17)), Energy equation (Eqn. (2.26)), Energy deposition (Eqn. (2.27), Eqn. (2.34)), EOS equation (Eqn. (2.37)), and Magnetic damping equation (Eqn. (2.43)). These equations are employed as governing equations in Frontier MHD code using front tracking method [75, 77], whose calculated results are referenced for comparison of jet size and filament velocity with experimental measurement.

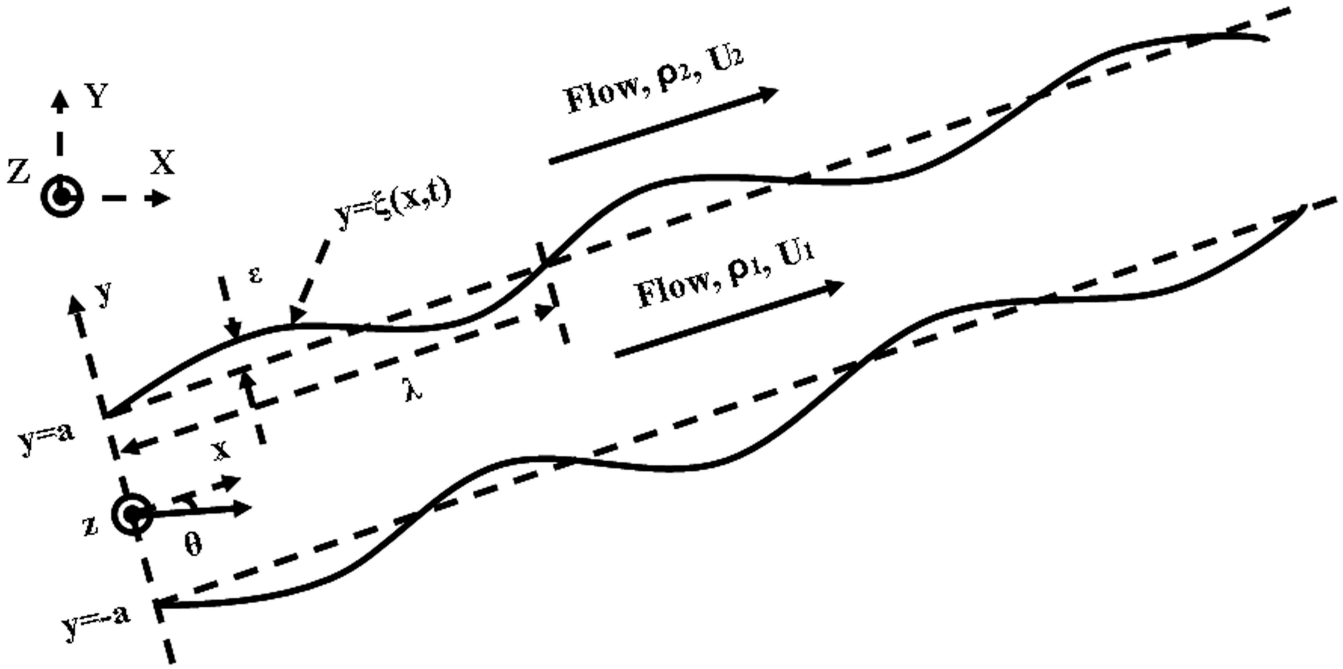

Figure 2.1: Wave-shaped interface separating two different fluids traveling at different average speeds.

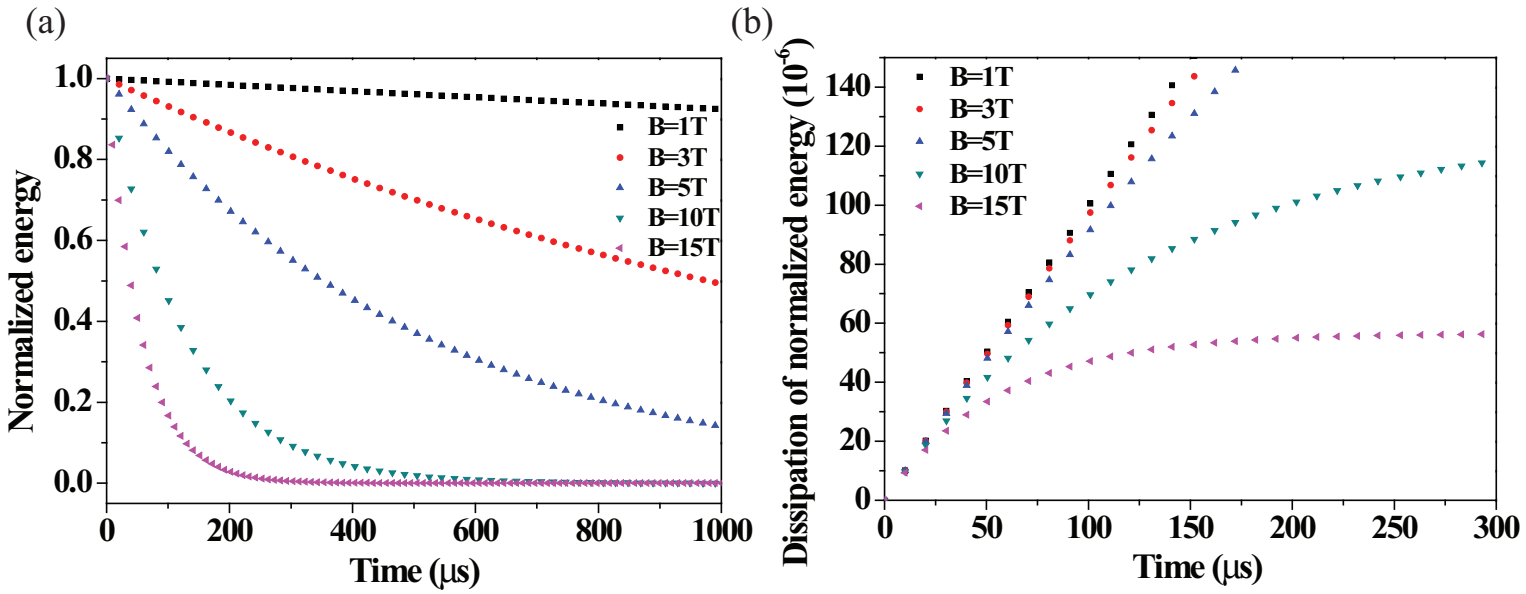

Figure 2.2: Energy decay in a magnetic field. a.) Normalized energy decay. b.) Integration of normalized energy with respect to time.

Chapter 3

Optical Diagnostics for Investigation of Mercury Jet Flow in a Magnetic Field

The optical method is considered to investigate MHD processes. Optical methods have considerable advantages over other measurement techniques: they do not introduce any perturbations into the medium being investigated, they possess high sensitivity and accuracy, their response is practically instantaneous, which enables them to be used to investigate turbulent flows and transition states, since they provide the possibility of visually following the phenomenon being investigated, and they enable one to obtain the physical characteristics for the whole space being investigated at the same instant of time. Unlike other probeless methods, optical methods possess high spatial resolution. All these features enable optical methods to be widely employed in MHD experiments and underlie the need to search for new ways of using optical methods which have not yet been employed.

Direct visualization techniques for hydrodynamic examination have often

been employed to investigate the dynamics of MHD flows. In this method, one can measure the time taken for the particles to traverse a given path. Because no quantitative results can be deduced from direct visualization methods and difficulties often arise when investigating things like thin boundary layers in liquids, attention has turned to the use of optical techniques for the investigations of fluid dynamics [20].

3.1 Optical Diagnostics as A Principal Diagnostics for Proton Target Experiment

3.1.1 Working principle of shadowgraph

The major advantage of optical measurements is the absence of an instrument probe that could influence the flow field. The light beam can also be considered as essentially inertialess, so that very rapid transient effects can be studied.

Shadowgraph is often employed in studying shock and flame phenomena, in which very large density gradients are present. It integrates the quantity measured over the length of the light beam. For this reason they are well suited to measurements in two dimensional fields, where there is no index of refraction or density variation in the field along the light beam.

Figure 3.1 shows the displacement of a light for shadowgraph. The index of refraction of a homogeneous transparent medium obtained by Lorentz-Lorenz relation reduces to the Gladstone-Dale equation when $n \simeq 1$:

$$\frac{n-1}{\rho} = C \ , \tag{3.1}$$

where C is the Gladstone-Dale constant and n is the index of refraction of a homogeneous transparent medium. The first or second derivative is given as follows:

$$\frac{\partial \rho}{\partial y} = \frac{1}{C}\frac{\partial n}{\partial y} \quad , \qquad \frac{\partial^2 \rho}{\partial y^2} = \frac{1}{C}\frac{\partial^2 n}{\partial y^2} \ . \tag{3.2}$$

Employing the ideal gas law and assuming that the pressure can be constant, the effect of temperature on the index of refraction and its derivatives can be shown as follows:

$$\frac{\partial n}{\partial y} = -\frac{CP}{RT^2}\frac{\partial T}{\partial y} \tag{3.3}$$

and

$$\frac{\partial^2 n}{\partial y^2} = C[-\frac{\rho}{T}\frac{\partial^2 T}{\partial y^2} + \frac{2\rho}{T^2}(\frac{\partial T}{\partial y})^2] \ . \tag{3.4}$$

If the illumination is uniform entering the test section, it should still be fairly uniform at the exit of the test section because of the short distance the light has traveled. The light, however, is deflected by an angle θ, which is a function of y. The illumination within the region defined by Δy at the position is within the region defined by Δy_{sc} at the screen. The intensity at screen is given as follow:

$$I_o = \frac{\Delta y}{\Delta y_{sc}} I_T \ , \tag{3.5}$$

where I_T is the initial intensity of light. The contrast is given as follow:

$$\frac{\Delta I}{I_T} = \frac{I_o - I_T}{I_T} = \frac{\Delta y}{\Delta y_{sc}} - 1 \simeq -z_{sc} \frac{\partial \theta}{\partial y} \ , \tag{3.6}$$

where z_{sc} is the distance to the screen. Combining Eqn. (3.6) with the angular deflection of ray $\theta = \frac{1}{n_a} \int \frac{\partial n}{\partial y} dz$, the contrast is given as follow:

$$\frac{\Delta I}{I_T} = -\frac{z_{sc}}{n_a} \int \frac{\partial^2 n}{\partial y^2} dz \ , \tag{3.7}$$

where $n_a \simeq 1$ for the ambient air. For gas, Eqn. (3.2) and Eqn. (3.4) can be substituted into Eqn. (3.7):

$$\frac{\Delta I}{I_T} = -\frac{z_{sc}}{n_a} \int C \frac{\partial^2 \rho}{\partial y^2} dz = -\frac{z_{sc}}{n_a} \int C[-\frac{\rho}{T} \frac{\partial^2 T}{\partial y^2} + \frac{2\rho}{T^2} (\frac{\partial T}{\partial y})^2] dz \ . \tag{3.8}$$

Shadowgraph system are rarely used for quantitative density or temperature measurements because the contrast would have to be measured accurately. However, if large gradients of density are present, as in a shock wave, shadowgraph images can be very useful [28]. Thus, shadowgraph is used principally for qualitative descriptions of a density field because it yields information on the first and second derivatives of density. Coupled to a state-of-the art high-speed camera and the long interaction path length of a light beam with a field of view adjustable to arbitrary dimensions, the optical shadow photography

enables one to obtain the physical characteristics for the entire subject being investigated in a short period of time.

3.1.2 Development of optical diagnostic system

An optical diagnostic system is designed and constructed for imaging a free Hg jet interacting with a high intensity proton beam in a pulsed high-field solenoid magnet. The optical imaging system employs a back-illuminated, laser shadow photography technique. Object illumination and image capture are transmitted through radiation-hard multi-mode optical fibers and flexible coherent imaging fibers. A retro-reflected illumination design allows the entire passive imaging system to fit inside the bore of the solenoid magnet. A sequence of synchronized short laser light pulses are used to freeze the transient events and the images are recorded by several high speed charge coupled devices.

3.1.2.1 *optical imaging system and Viewports design*

Laser back-illuminated shadow photography technique is employed in experiment to capture the dynamics of the interaction of the proton beam with a moving free Hg jet. The design of the optical imaging system is based on a few essential criteria which are described below. The entire optical imaging head has to fit inside a small portion of a 1 meter long, 150 mm diameter bore magnet. Figure 3.2 shows the conceptual back illuminated optics design, the installation of 4 Viewports on the primary containment vessel, and the schematic layout of optical components, respectively.

Note that all optics placed inside the interaction beam tunnel are required to be radiation-hard because of high radiation levels in the beam tunnel and the activation of the Hg after proton beam interactions.

A Viewport is located at the beam interaction center and two additional Viewports are located at ± 152.4 mm up/down stream locations. Viewport 4 is positioned at +457.2 mm and is designed to capture the residual dynamics of the proton interaction. Because of limited space inside the magnet bore, object illumination and image capture are transmitted through multi-mode optical fibers and coherent imaging fibers, respectively, all positioned on one side exterior to the primary containment vessel. Figure 3.3 shows the fabricated and assembled optical head containing the integration of ball lens, imaging lens, illumination fiber, and imaging fiber, where a red laser diode is used to illuminate the optical head.

The arrangement resembles a compact endoscope design but with a different illumination scheme. Illumination light pulses are coupled into a 15 meter long multi-mode fiber (ThorLabs BFL22-200). It has a numerical aperture of 0.22, 25° cone angle, with a core diameter of 200 μm that matches that of the fiber-coupled lasers. To provide a $\sim$ 55 mm illumination area at the center of the primary containment vessel over a limited short working distance of $<$ 100 mm, the illumination cone angle has to be opened up to a 43° full cone angle. This is achieved by placing a tiny $\sim$ 0.5 mm diameter sapphire ball lens (Edmund Optics M46-117) at the tip of the illumination fiber and secured by a thin stainless steel plate. At the heart of the illumination arrangement

is a 76 mm diameter Au-coated concave spherical retro-reflector that has a short radius of curvature of 124 mm (Rainbow Research Optics). When the much diverged illumination fiber is placed at the radius of curvature and shined onto the optical axis of the reflector, a retro-reflected beam returns back to the illumination fiber providing the back-illumination scheme. Again, because of the tight environment inside the primary, a Au-coated 90° prism mirror turns the optical path from longitudinal to transverse onto the center of the primary. Two anti-reflection coated sapphire windows (Swiss Jewel Company) are mounted on the primary with airtight seals tested up to 1.4 bar pressure. The diameter and the thickness of the window is 100 mm and 6 mm respectively, sufficiently large enough for the observation of a 1 cm diameter jet and mechanically strong enough to withstand the momentum of a direct impact from Hg jet with a mean velocity of 20 m/s [83].

Based on this optical arrangement, a Hg jet in front of the reflector naturally makes a shadow on the retro-reflected beam. The shadow is collected by a 1 mm diameter AR-coated cylindrical grin objective lens (GrinTech, GT-IFRL-100-inf-50-CC) which has an optical path length of 2.43 mm. The grin lens is coupled onto a coherent image fiber. This flexible coherent imaging fiber is the key optical element of the imaging system. It is a 10 meter long Sumitomo IGN-08/30 fiber with 30,000 picture elements (pixels). Each individual fiber has a core diameter of ~ 4 μm with a total fiber diameter of merely 0.96 mm including coating. It has a bending radius of 40 mm, sufficiently small to allow curving and arching inside the primary containment vessel. All imaging fiber ends

are hand polished in-house to optical finished quality to allow high quality images with maximum light intensity transmission. Figure 3.4 shows the final finished end of an imaging fiber after polishing with 0.3 μm lapping film (ThorLabs, LFG03P). The surface quality and the flatness of the imaging fibers are inspected under a microscope. The imaging fibers are jacketed in-house with reinforced furcation tubing (ThorLab FT030-BK). One end of the imaging fiber is finished with an SMA 905 fiber-optics connector to facilitate coupling to a CCD camera. The other ends of the illumination and imaging fibers are positioned next to each other with $\sim$ 2 mm separation inserted inside a specially fabricated plastic ferrule. The integrated all-in-one ferrule (ball lens, illumination fiber, objective lens, and imaging fiber bundle) is placed at the radius of curvature as well as on the optical axis of the reflector so that it allows both the illumination and the imaging collection to work on one side of the primary. The liquid Hg target is enclosed in a stainless steel primary containment vessel which is placed in the primary beam tunnel (TT2A). A total of four optical imaging heads for each Viewport are mounted on the exterior of the primary, designated as channels 1 to 4. All fibers are routed through a $\sim$ 150 mm diameter, 2 meter long concrete passage to an adjacent beam tunnel (TT2), where radiation is much reduced. All electronics control for the optical diagnostic as well as all other electronics control for the solenoid magnet operation and hydraulic power unit used to generate the Hg jet are also placed in the adjacent tunnel. The exit end of each imaging fiber is coupled to an SMA fiber adaptor (ThorLabs SM1SMA) mounted on an

x-y translator (ThorLab LM1XY). Four 40 × infinitely corrected microscope objective (Newport M-40x) relay the ∼ 0.96 mm image outputs of each imaging fiber onto each corresponding CCD with appropriate lens tubes to fully expand the images onto a typical 10 × 10 mm CCD array. A non-rotating adjustable lens tube zoom housing (ThorLabs SM1ZM) provides fine and accurate adjustment of image focus on CCD.

3.1.2.2 *consideration for alignment of optics*

A retro-reflective mirror captures the output beam of the laser diode and focuses it through the field of view at the target onto the lens of the telescope. The CCD camera views the target through the telescope. Tilting alignment by using fine adjustments on the side of the retro-reflecting mirror can be made and the field of view can be adjusted by moving the imaging lens forwards or backwards. The system is designed to make 6 possible alignments for adjustment. After the retro-reflecting mirror moves forward or backward, the field of view can also be adjusted. The maximum field of view that could be obtained is ∼ 5.0 cm diagonally.

For target to be in focus, one must obey the lens formula:

$$\frac{1}{f} = \frac{1}{c} + \frac{1}{d} \,, \tag{3.9}$$

where c is the distance from the target to the objective lens, d is the distance from the objective lens to the camera, and f is focal length.

3.1.2.3 *high speed cameras and light sources*

Table 3.1 gives the specifications of high speed cameras in terms of some selected attributes. Two FastVision cameras with CCD size of 15.4 × 12.3 mm run with a full 1280 × 1000 pixel resolution at a 0.5 kHz frame rate. One Olympus Encore PCI 8000S camera with 1/3 inch CCD size runs with a 480 × 420 pixel resolution at a 4 kHz recording rate. A high speed "Silica Mountain Devices (SMD)" 64KIM camera with a CCD size of 13.4 × 13.4 mm runs with a reduced single frame size of (960 × 960)/4 pixel resolution at up to 1 MHz frame rate. For the three slower cameras, images collected by each individual imaging fiber overfill the CCD pixels by a factor of ~ 6 and ~ 3, respectively, i.e. one fiber projected onto 6 × 6 and 3 × 3 CCD pixel area, respectively. However, for the SMD camera, each imaging fiber slightly underfills the CCD pixels by a factor of 0.83, i.e. one fiber projected onto nearly a single CCD pixel area. Due to the nature of spatial superposition, an array of imaging fibers imaged by an array of CCD pixels, some images might compose of a honeycomb pattern caused by this pixelation artifact. However, the artifact can be minimized by slightly defocusing the image on the CCD. The FastVision and Olympus CCDs are capable of recording at a frame rate higher than 500 Hz, the architecture for binning at reduced resolution requires a change of the zoom ratio on the image head doom. The SMD camera has a different but fixed binning architecture so that the full field of view is taken at a high speed frame rate with reduced resolution. Except for the SMD camera where images are frozen by the short 150 ns illumination laser pulses, all other

images are arrested by the short adjustable electronic exposure time of 10 $\sim$ 50 μs set on the CCDs.

Synchronized short laser light pulses are used to illuminate the target and freeze the motion of the jet after the impact of the proton beam. For SMD camera, the mask reduces the photosensitive area to 0.03 of the nominal pixel area. The quantum efficiency of the photo-resistive area is 0.18 at 800 nm, and the pixel fill is 200000 electrons. Therefore, a full exposure of a frame of the CCD therefore requires $(960)^2 \times$ 200000/0.03/0.18 $\approx 3.4 \times 10^{13}$ photons or 10 Watts for 800 nm photons. For FastVision camera, the sensor is 1280 $\times$ 1024 pixel (1.03 megapixel) of CCD of total area 15.36 $\times$ 12.29 mm^2 in 8 bits at 500 frames per second (10 bits at 400 frames per second). Maximum frame rate is 500,000 at 1 $\times$ 1280. The mask reduces the photosensitive area to 0.4 of the nominal pixel area. Based on the estimation of required photons, a full exposure of a frame of the CCD therefore requires 1280 $\times$ 1024 $\times$ 200000/0.4/0.18 $\approx 3 \times 10^{12}$ photons or 1 Watts for 800 nm photons.

Optical light pulses are sent through 15 meters of multi-mode illumination fibers. The light sources used in the experiment are all Class 4 lasers, emitting at wavelengths of 808 to 850 nm. Three lasers are capable of emitting a peak optical power of 1 Watt (JDS Uniphase SDL-2300-L2) driven by three independent current drivers (ThorLabs LDC220C). These 1 Watt lasers can be operated from CW to a minimum programmable pulse width of 1 μs limited by the trigger logic pulse. The 4^{th} laser emits at a peak optical power of 25 Watt (Bright Solution BDL20-808-F6) limited by the pulsed current driver (Avtech

AXOZ-A1A-B). It provides a current pulse of 150 ns and is capable of running at the maximum 1 MHz repetition rate, i.e. a frame rate of 1 μs/frame.

The complete transmission of the imaging system is ~ 0.2 per Viewport channel, including 0.85 for the 15 meter long illumination fiber, 0.86 for the sapphire ball lens, 0.86 for each pass of the sapphire Viewport, 0.91 for the retro-reflector, 0.67 for the 10 meter long imaging fiber, and 0.86 for the grin lens and the relay lens. For the SMD camera, the imaging circle filled $\pi/4$ of the CCD array. A measured output energy of 3.5 μJ/pulse is obtained from the Bright Solution (BDL20-808-F6) laser illumination light source for Viewport 2. Therefore the calculated number of photons impinging on the SMD camera reaches 4.2×10^6 photons/pixel. After taking into account the 18% quantum efficiency of the CCD, 7.5×10^5 photoelectrons are generated at the full illumination intensity. Since the SMD camera has full well capacity of $2.2 \times 10^5 e^-$, there is a factor of ~ 3 on the optical power budget reserved for unanticipated optical power loss and for overcoming the possible attenuation due to ionization radiation. Similar calculations for Viewport channels 1 and 3 give a factor of ~ 10 on the optical power budget. This larger factor is mostly due to the long, 10 μs, exposure time set on the FastVision cameras. Overall, the imaging system is designed to have sufficient optical power budget for the illumination of each Viewport throughout the entire experiment.

3.1.2.4 *radiation-hardness*

Because of the high radiation level in the beam tunnel and the activation of the Hg after the proton beam interactions, all optics placed inside the interaction beam tunnel are required to be radiation-hard. One complete set of optics was selected for radiation resistance test done at CERN. This complete set of optics included an Au-coated reflector, sapphire window, illumination fiber, imaging fiber, and Grin objective lens. The experiment has anticipated a total of 200 proton pulses at 14 and 24 GeV with a total of $\sim 3 \times 10^{15}$ protons. The calculated total radiation reaches $\sim$ 1 Mrad equivalent radiation dose. Therefore, all optics except the grin objective lens were irradiated at CERN to a lower energy 1.4 GeV proton beam but up to an equivalent radiation dose of 5×10^{15} protons. Because we missed an opportunity to deliver the grin lens to the CERN irradiation facility, the grin objective lens was instead irradiated at BNL using a Co-60 source up to a total dose of $\sim$ 3 Mrad.

The reflectance of the Au-coated reflector and the transmittance of all other optics are measured at the wavelength of 830 nm before and after irradiation. Table 3.2 shows the effects of irradiation up to an equivalent radiation dose of 1 Mrad on the reflectance and transmittance of the components of the optical diagnostic system. No noticeable change in the reflectance was observed on the Au-coated reflector even though the substrate of the reflector has turned nearly opaque. The sapphire, 5 meter long of illumination fiber, and 0.3 meter long of imaging fiber do not show any additional insertion loss. They are all radiation hard up to a 1 Mrad dose. However, the small grin objective lens

did suffer radiation damage resulting in a 0.73 transmission. This tiny grin objective lens is made of silver-ion exchanged index modification internal to a glass substrate. Therefore it was not anticipated to have a high radiation resistance. However, it is well known that although glass (and silica fibers) lose its transmission in the visible wavelengths, near infrared (NIR) light can still has adequate light throughput for some applications [39]. This is one of the reason we select NIR rather than visible laser light for back-illumination of the Hg jet. Since the back-illuminated NIR light passes the grin objective only once, the 0.27 transmission loss over the entire experiment is tolerable and can be recovered with the present designed laser capability. We should note that the integrity of the imaging properties of the grin lens was unchanged, i.e. no image distortion was observed after the 1 Mrad radiation resistance test.

3.1.2.5 *scintillating fiber channel*

A jacketed 2 meter long 1 mm diameter blue emitting scintillating fiber is attached along with the imaging head to register gamma emission during the proton beam and Hg jet interaction. A 12 meter long 1 mm diameter fiber patch-cord (ThorLabs BFH37-1000) carries the blue scintillated light signal and is fiber-coupled to an Avalanche photodiode (ThorLabs APD210), designated as channel 0. The overall transmission at the center wavelength of 480 nm of the fiber patch-cord is measured to be 0.77. The scintillating signal trace is displayed on an oscilloscope and data can be retrieved remotely from the control room. This scintillating signal serves to confirm the arrival of the

proton beam and has the potential to extract the proton intensity from the scintillating signal pulse level.

3.1.3 Schematic of electronic trigger and high speed camera control

Because we are using several high speed cameras from different vendors, we must use separate camera control software for each camera. The limitation on their exposure time also requires two different set of illumination laser pulse trains. A master trigger pulse, synchronized to the arrival of the proton bunch, is delivered to trigger the Hg loop system, the solenoid magnet system, and the optical diagnostic system together. The Hg jet reaches its steady state for 1 second when the solenoid magnet reaches the highest magnetic induction field of 0 T $\sim$ 15 T. However, there is a significantly long time lag of $\sim$ 10 seconds for the solenoid system to power up to its full capacity. Therefore, the master trigger signal is first sent to a digital delay generator (Stanford Research DG535) to provide a sufficient long delay to synchronize with all other electronic components. These relative and absolute delays are measured by an oscilloscope. By adjusting each independent delay channel, complete synchronization of all cameras with the pulsing of the laser light sources can be achieved by comparing the bright/dark image intensities of each frame for each camera.

Figure 3.5 shows the two sets of pulse sequences used to simultaneously trigger all cameras. The 25W infrared laser consisted of a 17 pulse sequence

with a pulse width of 150 ns. This determines the exposure time of the SMD camera on the Viewport 2. The laser pulse period is set to match the frame rate of the images. The SMD camera collects 16 frames of image. Figure 3.6 shows the traced signals on an oscilloscope when the beam and the beam triggering signal are delivered. After the master trigger from the synchrotron is delivered at time $t = 0$, the proton beam comes in ~ 3 μs. The photodiode response from scintillating fiber has a 20 ns rise time and the level indicates the beam intensity and beam position. The scintillating fiber signal gives the beam arrival time. Therefore, it is possible to set the trigger timing for the cameras and laser driver inputs, which is ~ 2 μs after the master triggering from the proton synchrotron.

Three 1 Watt lasers pulsed to a 0.5 second duration are used to independently illuminate Viewport 1, Viewport 3, and Viewport 4, respectively. Typically the FastVision and Olympus cameras continuously collect 220 frames of images. The exposure times on the cameras are set at $10 \sim 50$ μs respectively to give a sharp image quality. Although the sharpness of images increases with reduced exposure time, much more light is required for illumination. Therefore, a trade off between exposure time and laser intensity is made. On the contrary, the exposure time for SMD camera is determined by the laser pulse width. As the pulse width of the laser decreases, the laser intensity also decreases. In order to utilize the maximum allowable intensity of the 25 W laser, the maximum pulse width of 0.15 μs is used. This pulse width should not seriously jeopardize the image quality even running at its highest frame rate of 1 μs/frame. A

schematic diagram linking all cameras, triggering electronics, and controlling computers are shown in Fig. 3.7. 2 desktops reside in the control room to master the optical diagnostics system. All other electronics and desktops are placed in the TT2 tunnel adjacent to the interaction beam tunnel TT2A. In our setup, all cameras, lasers, and all other associated electronics are placed in an adjacent beam tunnel controlled locally by several desktop computers. Remote control of the entire system is achieved through designated control desktops located in the control room via MS Window XP remote desktop connections from the ethernet network. (see Fig. 3.7).

3.2 Windows Consideration as Viewports

The Hg jet target is observed through four windows. These windows must contain any possible spray of Hg due to intense beam energy deposition, and remain transparent after a radiation dose from the interaction of beam and Hg. Four Viewports are installed within the solenoid bore, which are intended for observation of the Hg jet within primary containment vessel. Viewport 2 is positioned at the center of the solenoid and is the location where the center of the proton beam interacts with the Hg jet.

3.2.1 Fiducial mark on windows

We put fiducial mark on each sapphire window to set the magnitude of the referenced length. The size of fiducial on the back and front windows is varying in image according to the changed field of view. i.e, the back fiducial looks

smaller than the front fiducial. Figure 3.8 shows the artificially marked fiducial on the sapphire window. It gives referencing length scale when we measure the size of jet, velocity, rotation of windows, and the location of magnetic axis on image.

3.2.2 Impact resistance test

We used sapphire windows to obtain enough strength and did surface coating on both sides for anti-reflection at 800 nm wavelength. In order to check the survival from Hg droplet impact, we tested sapphire window using a paint ball gun. A paint ball is a 2.7 gram sphere of radius 8.6 mm containing a colored gel that readily "splats" on impact. The velocity of a paint ball was 95 m/s. The ratio of the force from a paint ball to that due to the dispersal of the entire Hg jet by the proton beam is

$$\frac{F_{paintball}}{F_{mercury}} = \frac{m_{paintball} v_{paintball}^2 r_{mercury}}{m_{mercury} v_{mercury}^2 r_{paintball}} \ . \tag{3.10}$$

The momentum of the paint ball is the same as that of a 7 mm diameter Hg drop at 95 m/s. The sapphire window survived in the test [56].

3.2.3 Pressure leaking test of sapphire windows

The primary containment is mostly welded and the window ports are sealed with rubber gaskets (BUNA-N). Each window is sealed with two sheets of rubber gaskets per port. 21 psi is loaded inside the primary containment to check the sealing of the primary containment. To locate leaks, a Metheson

8850 flammable gas sniffer, which has a 5 ppm sensitivity, and Ar/Methane (90 % / 10 %) was used. All of 8 windows survived the 21 psi pressure for over 17 hours.

3.3 Water Jet Observation for Nozzle Performance Test

Prior to Hg injection in the primary at Oak Ridge National Laboratory(ORNL), extensive optical diagnostics were carried out by pulsing water jets in the system using 4 different types of nozzle configurations. One nozzle showed the most stable shape of jet motion with fairly uniform velocity, $\sim$ 10 mm diameter and 20 m/s respectively.

Due to the spray and wetting of water on the interior of windows, only ambiguous shadow of the water jet was observed. A clear surface motion was required in order to obtain accurate velocity measurement. Therefore, only very qualitative diagnostics was made on the water jet. The traveled distance and diameter of the water jet flow was measured by overlaying a grid of referenced field of view onto the images. The time lapse of each frame was read from the camera frame rates. So, the velocity of jet flow was able to be estimated. These measurements of the water jet tests were done at ORNL. The observations led us to select the design of the final nozzle for the subsequent jet runs.

Table 3.1: Specifications of high speed cameras.

Attributes	SMD 64KIM	FastVision	Olympus Encore PCI 8000S
CCD chip size	13.4 mm × 13.4 mm	15.4 mm × 12.3 mm	1/3 inch
Pixels	960 × 960	1280 × 1024	480 × 420
Pixel size	14 μm	12 μm	13 μm
Single frame	240 × 240	1280 × 1000	480 × 420
Maximum frame rate	1 MHz[1]	0.5 kHz[2]	4 kHz[3]
Full well Capacity	220,000 e^-	$\sim$ 1000 LSB/lux-sec	-
ADC	12 bit	8 bit	8 bit

[1] 16 frames.

[2] at full resolution.

[3] 12.5 μs electronic shutter, with reduced frame size.

Table 3.2: Effects of irradiation up to an equivalent radiation dose of 1 Mrad on the reflectance and transmittance of the components of the optical diagnostic system. Reflectance is inferred on the Au-coated mirror and transmittance is inferred on all other components.

Optical component	Before radiation	After radiation	% difference
Large Au-coated mirror	0.91	0.92	no change
Sapphire window(1 mm)	0.86	0.87	no change
Illumination fiber(5 m)	1	1.02	no change
Imaging fiber (30 cm)	0.67	0.71	no change
Grin lens	0.90	0.66	73 %

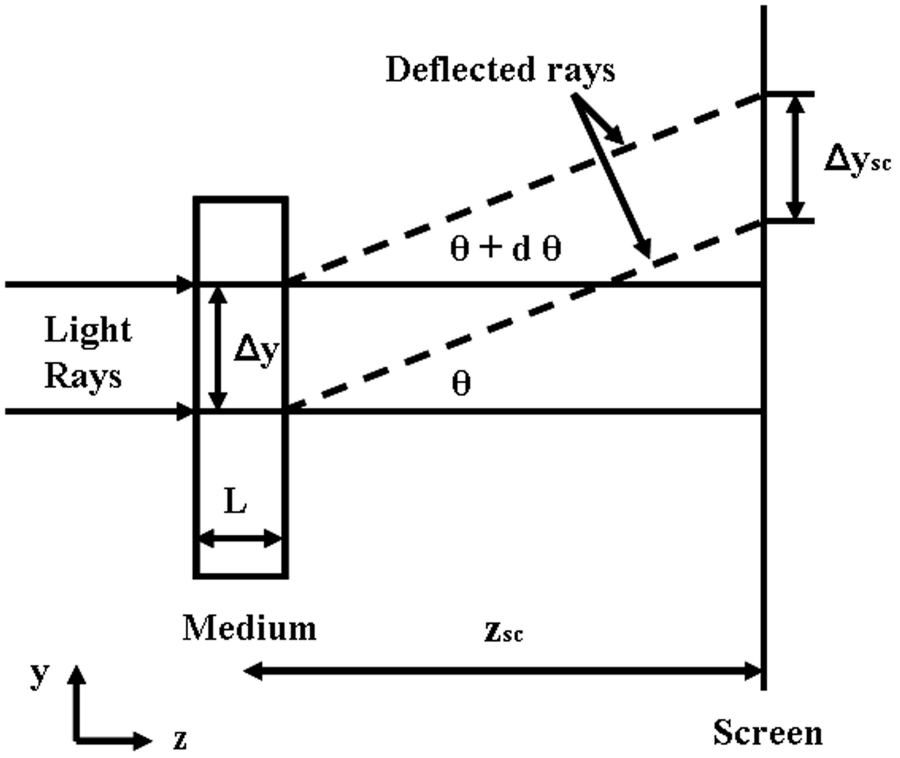

Figure 3.1: Displacement of light beam for shadowgraph.

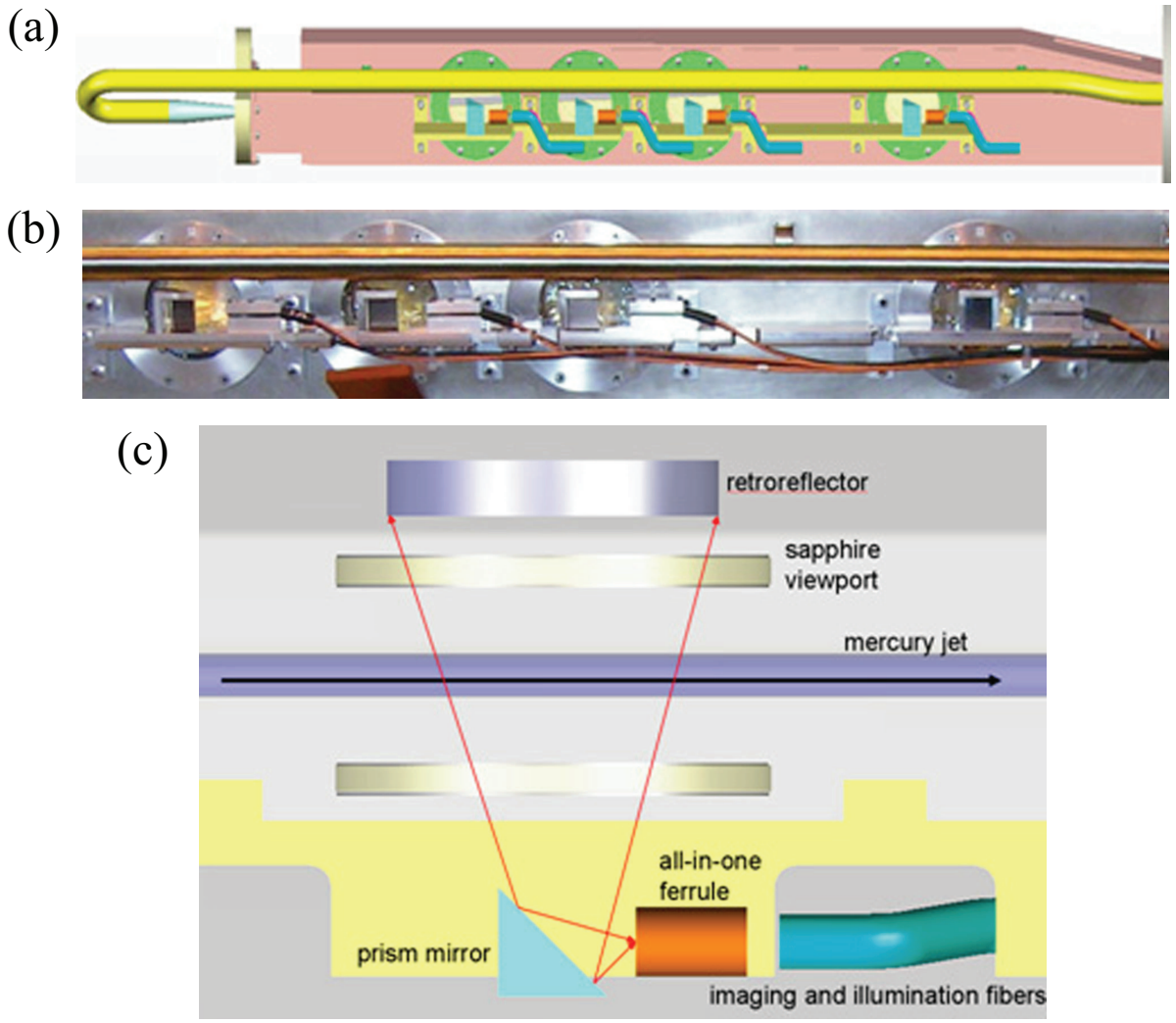

Figure 3.2: Design of optical layout and installation of 4 Viewports of primary containment vessel. a.) Conceptual integration of optics to primary containment vessel. b.) Photograph of installation of optics to primary containment vessel. c.) Schematic layout of optical components.

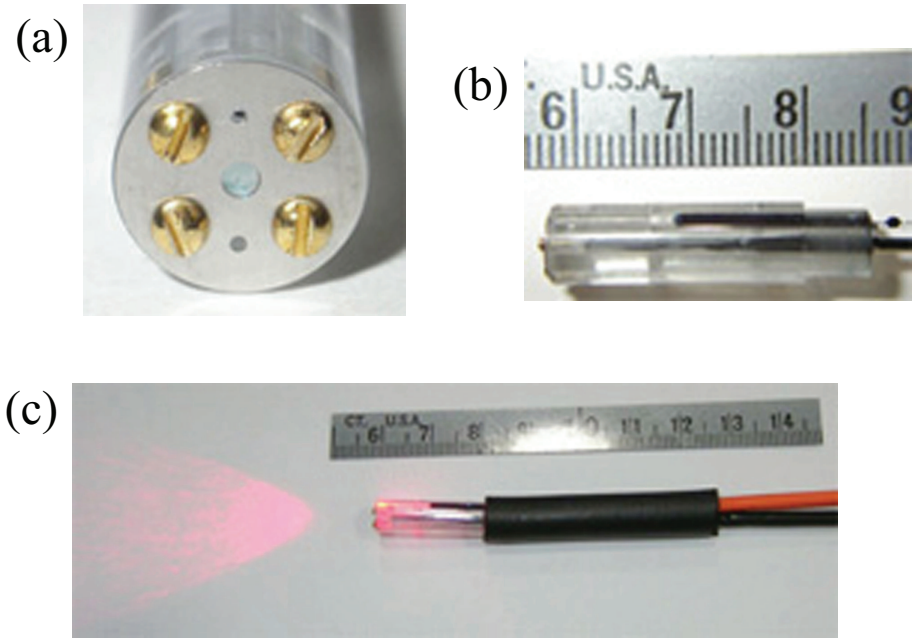

Figure 3.3: Photograph of optical head assembly and its illumination of laser. a.) Front view of optical head assembly. b.) Side view of optical head assembly. c.) Illumination of fiber-optics head assembly.

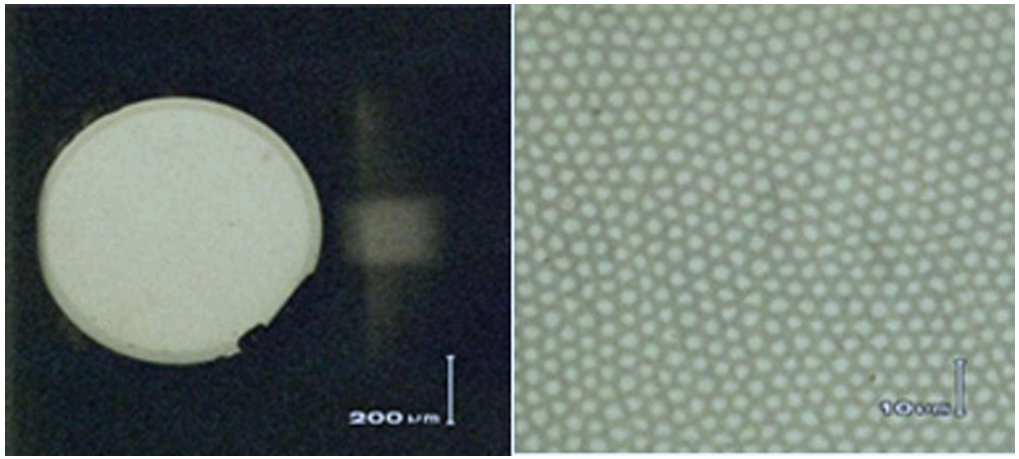

Figure 3.4: Polished fiber end with 50 X and 800 X magnifications, respectively.

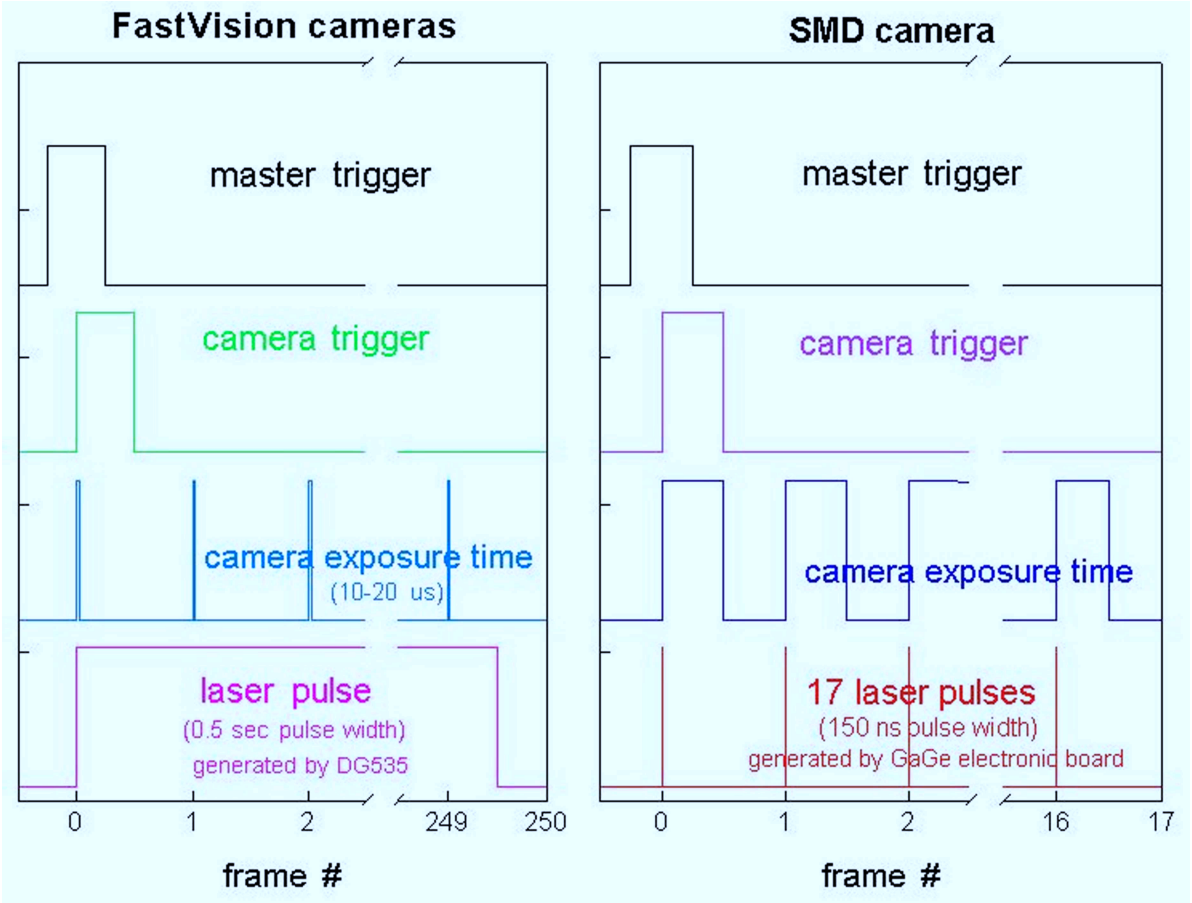

Figure 3.5: Schematic of synchronized signal of high speed camera and laser pulse.

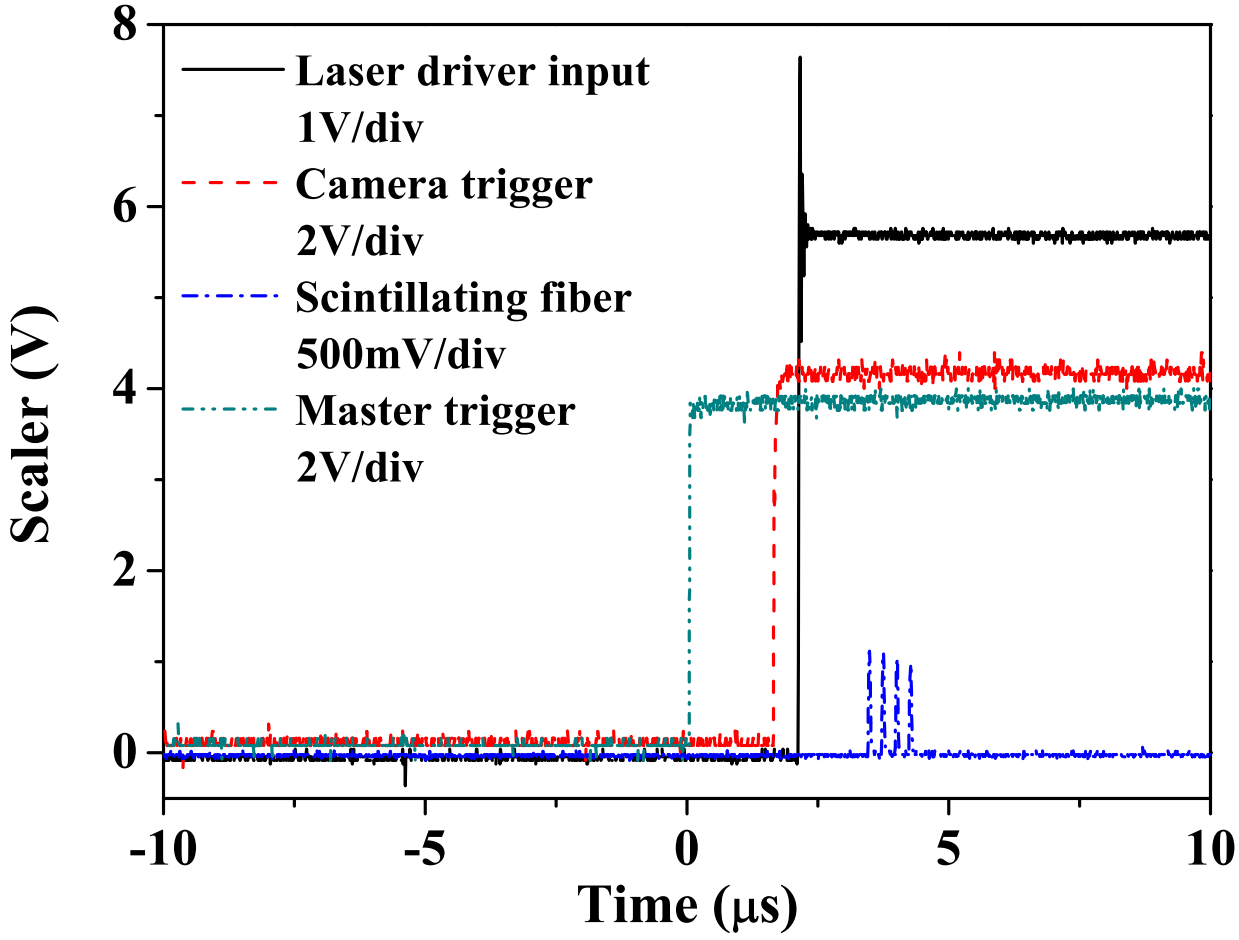

Figure 3.6: The triggering time for high speed camera upon beam arrival.

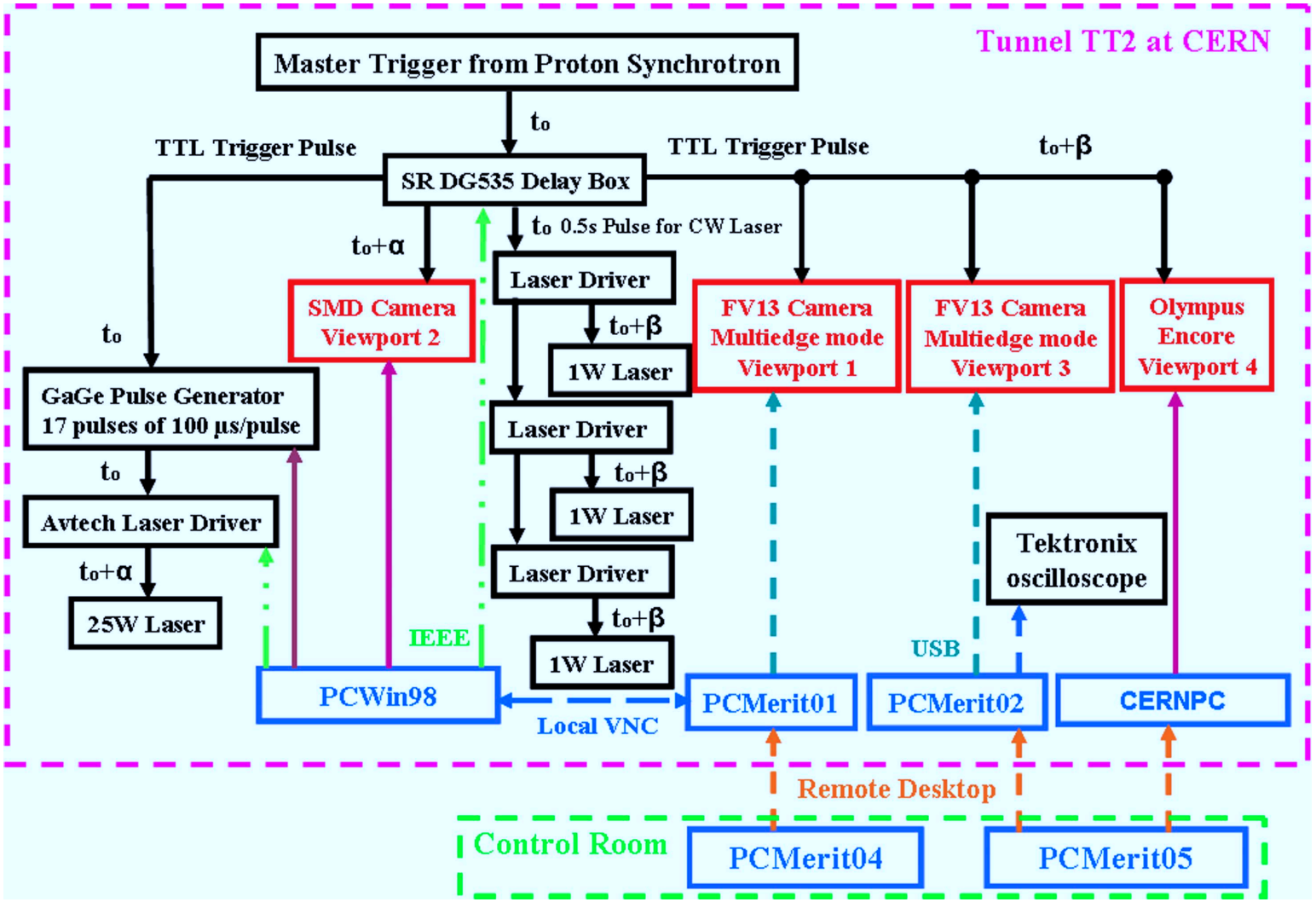

Figure 3.7: Schematic of electrical triggering and high speed camera control in tunnel for experiment.

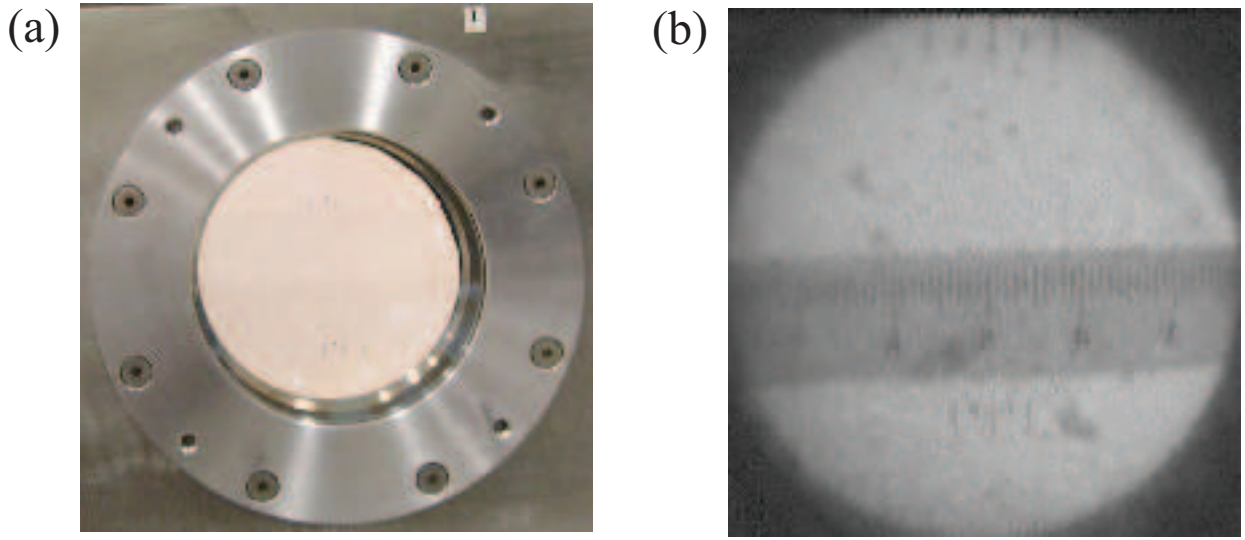

Figure 3.8: Top fiducial on the front window and bottom fiducial on the rear window. a.) Photo of fiducial on the sapphire window assembled in Viewport. b.) Image of fiducial captured by camera.

Chapter 4

Experimental Investigation of Mercury Jet Flow in a Magnetic Field

In this chapter, Hg jet behavior in a magnetic field is investigated. To do this, the collected images are read digitally and the characteristic jet parameters are evaluated based on measurement. Jet deformation such as the free jet surface deformation and surface stabilization are investigated by measuring pixels on the collected images based on 2-D shadow photography. Magnetic field effect on the dynamic behavior of freely moving jet in a magnetic field is discussed. The driving pressure of Hg flow entering inlet pipe is measured to monitor the effect of the magnetic field and assure if the input condition for driving the jet is affected. In order to diagnose the flow rate, the flow velocity in magnetic fields is discussed and the deflection of jet size in various magnetic field is investigated. Based on the observed flow rate of jet, the shape of jet is suggested for the energy deposition calculation by proton beam interaction with Hg jet target.

4.1 Image Analysis for Data Reduction

4.1.1 Image acquisition

$\sim$ 360 complete integrated tests (i.e., with magnet, proton beam, Hg loop system, and optical diagnostic system) were conducted at CERN (European Organization for Nuclear Research) with various values of the proton beam structure (8 harmonic and 16 harmonic), the beam intensity up to 30×10^{12} protons, the beam energy (14 Gev and 24 GeV), and the the magnetic field (0 T, 5 T, 7 T, 10 T, and 15 T) with 15 m/s Hg jet velocity. Figure 4.1 and 4.2 are representative optical diagnostic results collected by the 3 cameras, with and without a magnetic induction field at Plasma Science and Fusion Center in Massachusetts Institute of Technology. Note that only 15 m/s Hg jet shot was run at CERN, and both 15 m/s and 20 m/s shot were run at PSFC in MIT. Also, note that the Olympus Encore PCI 8000S camera for Viewport 4 was integrated in the beam interacting target study done at CERN.

The current in the magnet system generates heat, which is cryogenically removed using liquid nitrogen. As the magnet cools down, all Viewports become foggy up due to condensation. It was found out that $\sim$ 0.5 ℓ of water (from nozzle performance test at Oak Ridge National Laboratory) was not removed from the system prior to loading Hg. Flexible heater strips were installed both on the exterior of the primary containment vessel and on the snout in order to prevent the condensation of the humid air on the Viewports. Although residual Hg droplets in sizes less than 1 mm often adhere to the

sapphire Viewports after every shot, jet motion with adequate image quality could still be collected.

4.1.2 Image processing

To measure the shape of the jet, 8 and 12 bit grey scaled TIF images are converted into digital forms. Background images are subtracted to reject the noise in the image digitization process. The residual data is then transformed into a 2 bit scaled image. Figure 4.3 shows the collected image and its transformed 2 bit scaled image. Only the black and white colored pixels in the 2 bit depth images are used to differentiate the shadow of the jet and the background. Due to the image quality caused by the Hg droplet on window and the quality in fiber optic system, the noise such as black dots exits. A threshold is adjusted according to Otsu's method to highlight the interface between the Hg and background [67]. Otsu's method selects the threshold by minimizing the within-class variance and maximizing the between-class variance of the two groups of pixels separated by the thresholding operator. Otsu's method, which relies on the assumption that all image pixels belong to one of two classes, background or foreground, has been shown to be efficient in image segmentation for bi-level thresholding.

Figure 4.4(a) shows the sensitivity of 2 bit scaled image conversion to the measurement of jet height with respect to the level of 8 bit threshold using Otsu's method. As the threshold level increases, the mean value of the jet height as well as the σ value of the jet height in measurement is approaching

an asymptotic level. The optimally selected threshold value by the Otsu's method in this example is 0.35.

The Hg jet was observed at upstream (Viewport 1), midstream (Viewport 2), and downstream (Viewport 3) locations from the nozzle exit. 220 images are collected at each run for both the upstream and downstream locations, with an image size of 1280 $\times$ 1000 pixels. The most probable transverse jet height within the longitudinal pixel range of 300 to 1000 is shown in the histogram of Fig. 4.4(b). Note that within this range, the transverse jet height probability P could be obtained by counting the number of longitudinal pixel events in the jet image. Let z denotes the transverse direction (in terms of pixels). The number of background events (i.e., outside of the jet) is always larger than that within the jet because the portion of bright background on each image is larger than that of the black jet shadow. The distribution on the left in Fig. 4.4(b) (i.e., $0 < z < 200$) represents the background pixels. Then, the number of pixels corresponding to the jet height is counted within the longitudinal pixel range of 300 to 1000. Each counted pixel numbers are directly averaged to give a jet height measurement and then added up over $\sim$ 200 images for 1 shot of jet run, where the time elapse for the images corresponds to $\sim$ 0.4 s at Viewport 1 and 3. Multiple shots are then used to add up all of the counted vertical jet height. The average of the individually counted vertical pixels is given to indicate the nominal jet height. In a mathematical form, the direct averaging method is described as follow:

$$D_{jet} = \frac{1}{i+j+k} \sum_{1}^{i} \sum_{1}^{j} \sum_{1}^{k} N_{vertical} \ , \tag{4.1}$$

where D_{jet} and $N_{vertical}$ denote the averaged vertical jet height and a individually counted number of vertical pixels respectively. i, j, k represent the number of shots, images in a shot, and vertical lines in a image respectively. On Viewport 2, 16 image files are collected at each run, with an image size of 316 $\times$ 316 pixels. The images are analyzed in the same manner as described above. Viewports 1 and 3 give the same resolution for the images: 1280 $\times$ 1000. Thus, no image re-scaling is needed when comparing the pixel size for these images. However, Viewport 2 gives a resolution of 316 $\times$ 316. Based on the 1 cm scale fiducial mark on the exterior of all Viewports, all images taken on this Viewport are re-scaled to match the resolution of Viewport 1 prior to comparison.

4.1.3 Study on the scaling length and the location of window center

In order to relate the lengths on the collected images at each Viewport, the pixel length on the images is investigated. Since the image size corresponds to the CCD size, any discrepancy in horizontal and vertical pixel size is not considered. Viewports 1 and 3 give the same resolution for the images: 1280 $\times$ 1000. Thus, no image re-scaling is needed when comparing the pixel size for these images but we did the scaling to see any difference on the image length of Viewport 1 and Viewport 3. The fiducial length on the top front window and

the bottom back window is measured and then interpolated to get the length at the mid-span on the primary containment. The interpolated pixel length at the mid-span corresponds to 1 cm at the mi-span of primary containment. Thus, in Viewport 3, a pixel length at the mid-span where the jet is moving is approximated ~ 0.05 mm. Same scaling was done at images in Viewport 3. The ratio of the pixel length in Viewport 3 to Viewport 1 is 1.06.

Viewport 2 gives a resolution of 245×252. Based on the 1 cm scaled fiducial mark on the exterior of all Viewports, all images taken on this Viewport are re-scaled to match the resolution of Viewport 1. A pixel length at the mid-span is approximated ~ 0.21 mm. Viewport 4 gives a different resolution of images depending on the frame rate setting but typically the resolutions of 320×280 was used. A pixel length at the mid-span is approximated $\sim$ 0.21 mm, which is same with Viewport 2.

The distance of the center position between the fiducial and the window is 0.75 inch apart. In order to locate the center of the window at the mid-span, the position where 0.75 inch is apart from the top fiducial and bottom fiducial is found on each image and then the averaged difference in the located position is considered as the center of window.

Based on these scaling study, the measurement is performed in the following investigation. The average and standard deviation of measurement are used to represent results of the following investigation. Based on the standard deviation and the number of events, the error bar, $\sigma/\sqrt{N}$, is calculated to typically give error estimation for each measurement.

4.2 Motion of Mercury Jet and Stability in a Magnetic Field

4.2.1 Jet deflection and surface flattening

Jet motion in a magnetic field is expected to behave differently, depending on the angle between the axis of magnet and the axis of jet, as a result of the differences in the magnitude of components of magnetic field [76]. Figure 4.5(a) and (b) show the axial and radial components of the magnetic field in a solenoid. Figure 4.5(c) and (d) show the transverse and longitudinal components of the magnetic field along the jet axis at different crossing angles. As the crossing angle increases, the transverse component of the magnetic field increases, but with no significant change in the longitudinal component of the magnetic field. An increase of the transverse component of the magnetic field raises the induced axial current on the Hg jet. Therefore, the angle of the Hg jet is launched at 33 milliradian with respect to the axis of solenoid magnet. When the jet is injected without an applied magnetic field, it is difficult to discern the jet surface because of blockage by Hg droplets on the window. Therefore, some errors in the measurement exists (see images in Fig. 4.1(a) through Fig. 4.1(c) and 4.2(a) through 4.2(c)). On the contrary, when a magnetic field is applied, the measurement errors are significantly reduced,leading to significantly less intermittent jet boundaries.

The inertial forces appear to dominate the jet movement when the jet velocity is 15 m/s. The turbulent jet motion is unstable but becomes stabilized

as the magnetic field approaches 5 T. It has been reported that the radial force induced by the transverse component of magnetic field caused by the axially induced current due to the tilted jet angle can significantly increase the jet height [23]. The phenomena of increasing jet thickness with high magnetic induction field is observed for the first time when the magnetic field exceeds 10 T.

Figure 4.6 shows the jet height measurement by direct averaging of vertical jet height from measured pixels on each image. The standard deviation is used to give the error bar. This two plot shows the extreme two conditions of evaluation of the measured jet height, but one can effectively observe the fluctuating amount relative to the nominal jet height according to the various magnetic fields.

At a jet velocity of 15 m/s, the relatively low inertial force reduces the extent of turbulent fluctuation. For this case, the magnetic field does not significantly affect the dynamics of the jet until the magnetic field strength of $\sim$ 5 T reaches. Consequently, the height of the jet decreases only slightly until 5 T since the magnetic field reduces the fluctuating surfaces and the jet is more likely to elongate axially to the jet axis. The results shown in Fig. 4.1 and 4.2 clearly suggest that the magnetic field has constrained (stabilized) the Hg jet flow by smoothing out the edges of the otherwise turbulent flow. At large number of the magnetic field (>10 T), stability is maintained at all Viewports. At 15 T, a larger height (cross sectional distortion) is observed on all Viewports.

The fact that the Hg jet size is relatively reduced from 0 T to 5 T but increases from 10 T to 15 T suggests that the Hg jet might encounter a different type of instability at high magnetic field, namely a quadrupole effect. The quadrupole effect would alter the jet's circular cross-section to become elliptical. From the data obtained with a 15 m/s jet, the jet height at 10 T is smaller than that at 15 T, which is manifested in the vertical elongation of the jet. However, the height at 10 T is smaller than that at 5 T. The issues for such a behavior have to be addressed. There are two possibilities. First, the jet is elongating axially up to 10 T. The equivalence of hydrodynamic pressure with magnetic pressure is more dominantly affecting to the axial elongation of jet than the transverse pressure. However, the transverse magnetic pressure becomes significant once the magnetic field exceeds 10 T. Thus, the jet at 15 T is experiencing the transverse deflection as well as axial deflection, but the the role of transverse deflection plays significantly on the behavior of jet. That can explain why the reduction of jet is appearing up to 10 T and then the expansion of jet is appearing at 15 T.

Second, the optical diagnostics depends only on the side sectional view of jet movement. The reduction of jet size on the minor axis of the elliptical core has to be accompanied by the gain in jet size on the major axis in order to satisfy the continuity condition in flow. In other words, the cross-sectional are in flow should be constant. Although the two dimensional nature of the image data does not distinguish between an elliptical cross section and a circular one, occasional observation of a smaller jet thickness at 15 m/s

with 10 T field as opposed to a 5 T indicates that the jet cross section might vary between the major and minor axis of an elliptical core. It is important to note that within the axial distance of interest, the jet diameter is approximately constant. Therefore, references to "larger jet height" should be interpreted to mean larger distortions of the jet cross section. Since the jet and solenoid field are cylindrically symmetric, it is hard to estimate in what direction the jet is going to be distorted but the ratio of the deflection can be determined experimentally. The ratio also can be compared with the transverse magnetic pressure $B^2/2\mu$ considering the reversed direction of deflection on each plot. Samulyak [77] suggested that the deflection ratio of jet size $\triangle R/R_o$ is proportional to the magnitude $\mathbf{B}_o^2/U$, where the governing MHD equations and free jet boundary condition including Maxwell's equations using low magnetic Reynolds approximation are employed and the Hg jet deflection in magnetic field is calculated by using a hybrid of Eulerian and Lagrangian method, so called Front tracking method. Figure 4.7(a) shows the deflection ratio of Hg jet along the distance from nozzle at 10 T and 15 T magnetic field [78]. The magnetic field stabilizes the Hg jet surface so that the jet surface is getting flattened. In MHD simulation, constant 1 cm diameter of Hg jet is considered. Although the magnetic field causes the jet surface flattening, the nature of turbulence such as growth of jet size is observed in experiment. Therefore, in order to avoid such a turbulent nature between simulation and experiment, the ratio of jet deflection ratio between 10 T and 15 T is evaluated to see the comparison of the magnetic field effect $\mathbf{B}_o^2/U$ between Fig. 4.7(a)

and Fig. 4.6, which is shown in Fig. 4.7(b). It shows somewhat consistency at upstream, but still the ratio diverges as the jet flows to downstream.

As expected, jet motion in a magnetic field behaves differently, depending on the angle between the axis of magnet and the axis of jet, as a result of the differences in the magnitude of components of magnetic field [76]. Figure 4.5(a) and (b) show the axial and radial components of the magnetic field in a solenoid. Figure 4.5(c) and (d) show the transverse and longitudinal components of the magnetic field along the jet axis at different crossing angles. As the crossing angle increases, the transverse component of the magnetic field increases, but with no significant change in the longitudinal component of the magnetic field. An increase of the transverse component of the magnetic field raises the induced axial current on the Hg jet. Therefore, the angle of the Hg jet is launched at 33 milliradian with respect to the axis of solenoid magnet.

The jet surface can readily be extracted from each collected image. The jet axis is approximated by fitting the averaged positions between top surface and bottom surface. This jet axis is moved with an offset until it interferes the top surface bottom surface. The amount of fluctuations of surface is measured by getting the difference between the fluctuation surfaces and the interfering jet axis on a RMS scale. Let $\delta(r,t)$ denotes the probability of turbulence at r, such that δ is defined as 0 in the non-turbulent fluid, where the background is considered here, and is defined as 1 in the turbulent fluid, where the jet is considered here. Time average of δ yields $\zeta(r)$, the intermittency factor at r. The turbulent fluctuations are produced by the intermittency effect

and these fluctuations are significant for scalar quantities. The intermittency characteristics of the turbulence are the appropriate input to be used in defining rough surface for a scattering analysis. When the intermittency phenomenon is present, the conventional turbulent fluctuation is modified by the intermittency function and there is an additional contribution depending on the difference between the mean turbulent quantity and the non-turbulent quantity [96]. However, the probability of the fluctuating jet surface area is introduced to define the intermittency in the following work. The pixel information along the jet axis by changing the translational offset is summed up to represent the intermittency of jet on the top and bottom surface. The intermittency within the jet represents 1 and it is gradually decrease to 0 at the background. The intermittency is between 0 and i at the jet surface depending on the surface fluctuations. Figure 4.8 shows the intermittency as a function of magnetic field and time. Total evaluated time is 160 μs. Without magnetic field, the slope of intermittency at the jet surface is broad and it is oscillating as a function of time. With higher magnetic field, the slope of intermittency at the jet surface is more steep and it keeps same shape with respect to time. This result clearly tells that the magnetic field suppresses the fluctuation of jet surface.

Figure 4.9 shows the measured fluctuations on the jet surface. Surface fluctuations is monotonically decreasing and the surface is flattened approximately up to 5 T. The fluctuations at Viewport 3 (downstream) is larger than that at Viewport 1 (upstream) since the tendency to be turbulent grows. The amount of fluctuations at top surface and bottom surface of jet is almost same, though

the magnetic field is varied. Thus, the symmetry on the jet surface in terms of the surface variations such as fluctuations and wave amplitude is valid. The amount of difference of surface fluctuations at Viewport 1 and Viewport 3 becomes same. It indicates that the jet surface becomes flattened at ~ 5 T in flow velocity 15 m/s. The decreased amount of surface fluctuation at Viewport 1 and Viewport 3 is ~ 0.5 and 1.5 mm RMS respectively. This explains why the jet height is reducing from 0 T to 5 T in Fig. 4.6. The magnetic field makes the wavelength on the jet surface increases. Correspondingly, the wave propagation speed is increasing. Thus, it causes Re_{cr} to increase and the flow becomes laminar due to the stabilization by the magnetic field. The transverse component of magnetic field prevails more over the jet stabilization. Though there is some measurement errors due to the saturation in image brightness, the measurement could show the field effect to the reduction of fluctuation on jet surfaces.

The these observations are supported by previous results. For example, several investigations have suggested that magnetic field suppresses turbulent fluctuations in conducting liquid by stabilizing the flow [80, 27, 44, 6], where stabilization is judged by an increase in the characteristic wavelength of the flow.

4.2.2 Trajectory of mercury jet projectile in a magnetic field

The Hg jet and the beam are launched at 33 and 67 milliradian with respect to the magnetic axis respectively. The trajectory of Hg jet projectile is acted upon by gravity, which is represented as follow:

$$
\begin{aligned}
t &= \frac{x}{v_o \cos\theta} \\
y &= -\frac{g}{2}\, t^2 + v_o \sin\theta\ t + y_{nozzle} \\
|v| &= \sqrt{v_o^2 - 2gx\tan\theta + (\frac{gx}{v_o\cos\theta})^2}\ ,
\end{aligned}
\tag{4.2}
$$

where x is the jet traveling distance, y is the height of jet centroid at x, y_{nozzle} is the vertical position of nozzle, v_o is the launched velocity, and θ is the launched angle of Hg jet. Based on the governing trajectory equation Eqn. (4.2), fit function of the jet flow height can be expressed as

$$
y = a_1 + b_1 x - \frac{g(1+b_1^2)x^2}{2c_1^2}, \tag{4.3}
$$

where $a_1 = y_{nozzle}$, $b_1 = \tan\theta$, and $c_1 = v_o$. The values and error are given in Table 4.3. The distance of jet elevation is determined by measuring the distance from the magnetic axis at center of each window to the jet axis, which is approximated by fitting the averaged positions between top surface and bottom surface. Figure 4.10 shows the trajectory of Hg jet and it's effect by the magnetic field and gravity. The solid line represents the globally fitted value using the trajectory of projectile with different initial launching speed of

jet for the case of 15 m/s and 20 m/s respectively. It shows that the trajectory of Hg flow approximately agrees well with the trajectory of projectile for both 15 m/s and 20 m/s shots. Experiment shows that the trajectory of the Hg jet is parabolic. The magnetic field caused some elevation of Hg jet closer to the center of magnetic field. As the jet moves to downstream, magnetic field effect is more clearly observed since the jet is more likely to elongate to the axial direction. At 15 T, the elevation of jet is observed from Viewport 1 to Viewport 4. It shows that the magnetic force is overcoming the inertia force at 15 T similarly as there is the increase in jet height at 15 T. The overall increase of the jet elevation in upstream, midstream, and downstream at 15 T may have been caused by the asymmetric change of jet height. Possibly the stable equilibrium between magnetic force and gravitational force could be varying according to the variation of magnetic field [25].

The beam trajectory is also given to show the overlap with the Hg jet. It is shown that the overlap length is $\sim$ 30 cm when we consider the height of jet at various position with various magnetic field.

Based on the result of the jet trajectory, the angle of jet axis at Viewport 2 (midstream) is determined by the trigonometric approach using the elevation of jet and the distance along the magnetic axis between Viewport 1 and Viewport 3. Figure 4.11 shows the estimation of jet angle at centner of magnetic axis (Viewport 2), which is approximately 7 $\sim$ 11 milliradian. The jet angle is slightly decreasing with higher magnetic field, which indicates that the jet is more likely to move horizontally following the field line direction.

4.3 Dynamics of Liquid Jet Flow from Nozzle

4.3.1 Jet flow in surrounding medium

Lee [45] investigated the phenomenon of air wake caused by a cylindrical jet emerging from a nozzle and showed the boundary layer of jet by applying continuity of jet mass and matching the loss of jet momentum with air drag on the jet. Figure 4.12 depicts schematically the boundary layer of jet emerging from a nozzle. The conservation of axial momentum and the rate of momentum loss to the skin friction on the jet and the continuity of the liquid jet are expressed as follows:

$$2\pi\rho_a \int_0^{\delta(x)} [a(x)+y]v^2(x,y)dy + \rho_l \pi a^2(x) v_l^2(x) = \rho_l \pi a_o^2 v_{lo}^2, \tag{4.4}$$

$$\frac{d}{dz}[\pi\rho_l a^2(x) v_l^2(x)] = 2\pi a(x)\mu_a \frac{\partial v}{\partial y}|_{y=0}, \tag{4.5}$$

and

$$\pi a^2(x) v_l(x) = \pi a_o^2 v_{lo}, \tag{4.6}$$

where velocity, density, and viscosity are denoted by v, ρ, and μ, respectively, with subscripts a and l for air and liquid, respectively. The subscripts o denotes the initial values at the nozzle. For boundary layer analysis of cylindrical objects, because of the diverging flux characteristics in radial direction, a logarithmic profile is the most appropriate [86, 26]. Thus, the velocity profile of the air induced by the liquid jet is assumed to be as follow:

$$v(x,y) = v_l(x)\{1 - \frac{1}{\beta(x)}\ln[1 + \frac{y}{a(x)}]\} \tag{4.7}$$

and

$$\frac{\delta(x)}{a(x)} = e^{\beta(x)} - 1. \tag{4.8}$$

Substitution of Eqns. (4.7) into Eqns. (4.4) $\sim$ Eqns. (4.6) results in

$$\bar{v}_l(\bar{x}) = \frac{v_l(\bar{x})}{v_{lo}} = \frac{1}{1 - \bar{\rho}[1 + \frac{1}{\beta} - \frac{1}{2\beta^2}(e^{2\beta} - 1)]} \tag{4.9}$$

and

$$\frac{d\beta(\bar{x})}{d\bar{x}} = \frac{\beta^2 - \bar{\rho}[\beta^2 + \beta - \frac{1}{2}(e^{2\beta} - 1)]}{\beta(1 + e^{2\beta}) - (e^{2\beta} - 1)}, \tag{4.10}$$

where $\bar{x} = \frac{4x}{\mathrm{Re}_e a_o}$, $\mathrm{Re}_e = \frac{2a_o\rho_a v_{lo}}{\mu_a}$, and $\bar{\rho} = \frac{\rho_a}{\rho_l}$. For a given value of ρ, the stream velocity $\bar{v}_l(\bar{x})$ and boundary layer thickness $\bar{\delta}(x)$ are obtained. As seen in Fig. 4.13, the Reynolds number plays its role implicitly and this makes the density ratio $\bar{\rho}$ to be varied. Since the cylindrical jet has larger volumes, for the initial momentum of the jet to be maintained, the liquid density must be reduced and the value of the density parameter to be used must be modified to $\bar{\rho} = \rho_a D^2/(\rho_l d_o^2)$, where D and d_o denote diameter of jet and nozzle, respectively.

4.3.2 Pressure loss and magnetic effect on the Hg delivery pipe

Fig. 4.14 (a) and (b) show the pipe inlet pressure for driving jet in various magnetic field strengths. The Hg jet is driven by the piston in syringe and the piston velocity is measured by position sensor. The piston velocity determines the flow rate so that the dynamic pressure head at pipe inlet is determined using the conservation law of flow rate. The pressure sensor installed at the pipe wall measures the static pressure. No significant pressure drop is observed at the pipe inlet in magnetic field strengths. It indicates that the driving pressure in pipe for nozzle is at same conditions regardless of the magnetic field variation.

To obtain the jet velocity, the distance traveled by a fixed point on the jet surface is tracked over a given time period. Figure 4.15 (a) shows the jet velocity measured at Viewport 1, Viewport 2, Viewport 3, and Viewport 4 in various magnetic field strengths. Note that this velocity does not significantly change with the imposition of a magnetic field. Therefore, considering the measurement error in Fig. 4.15 (a), the averaged flow velocity, regardless of magnetic fields, can reasonably indicate the flow velocity given in Fig. 4.15 (b). This explains why the pressure is approximately constant in the pipe, consistent with the report [30].

Another interesting result is that the cross section of Hg jet is more likely to be elliptical since the longitudinal jet flow velocity is constant from upstream to downstream. Regardless of the magnetic field, the Hg jet does not show

jet velocity change. Thus, the jet is changing its shape once it leaves the nozzle from circular to elliptical. Hence, the result in Fig. 4.6 should be again interpreted by the result in Fig. 4.15 in the manner that the jet height at 5 T is elongated on the minor axis followed by the reduction of jet height on the major axis of the elliptical core, and the jet is deflecting further at 10 T. However, the jet height at 15 T is elongated on the major axis, which is manifested by the comparison between the ratio of the reduction of jet height and the increased ratio of the jet height at 15 T. This approach is already mentioned in the above, but it is examined again.

Considering that the driving pressure and the jet velocity are not significantly changed in various magnetic fields, it is concluded that the longitudinal magnetic field does not affect to the pressure loss or velocity degradation while Hg passes inside of the solenoid magnet two times along with the direction of magnetic field line. It is reported that the gradient of longitudinal jet velocity depends on the integration of gradient of longitudinal magnetic field along the magnetic axis plus it's multiplication to longitudinal magnetic field itself [23]. It is expressed as follow:

$$\Delta v(x) = \frac{\kappa}{\rho}\frac{r_o^2}{8}\left(\int_{x_1}^{x_2} \left(\frac{dB_x}{dx}\right)^2 + \frac{d}{dx}\left(B_x \frac{dB_x}{dx}\right)\, dx \right) , \tag{4.11}$$

where r_o is the radius of jet and κ is electrical conductivity. Since the gradient of magnetic field is increasing (plus) at entrance and decreasing (minus) at exit, it seems that there is an increasing velocity gradient (acceleration) at upstream and decreasing velocity gradient (deceleration) at downstream

but it is $\leq$ 0.5 m/s due to the relatively high density comparing with the electrical conductivity only if we consider the effect by the magnetic field. The experimental result shows slight effect of magnetic field.

4.3.2.1 *pressure loss in pipe flow*

Hg delivery pipe is connected from syringe pump to nozzle and it is passing parallel with solenoid magnetic field line next to the primary containment. A loss coefficient is defined as follows:

$$\begin{aligned} (h_{loss}) &= K_1\frac{v_1^2}{2g} + K_2\frac{v_2^2}{2g} + \ldots + K_N\frac{v_N^2}{2g} \ , \\ A_1v_1 &= A_2v_2 = \ldots = A_Nv_N = A_Rv_R \ , \end{aligned} \tag{4.12}$$

where the subscript R signifies a reference location and K represents the loss coefficient. The general thermodynamic loss, so called the head loss h_{loss}, is defined as follow:

$$\int_1^2 \delta F = (h_{loss})_{1,2} = \frac{p_1 - p_2}{\rho g} + \frac{v_1^2 - v_2^2}{2g} + (z_1 - z_2) \ . \tag{4.13}$$

Darcy-Weisbach equation is given to express the head loss of wherever the density is constant as follow:

$$\frac{\Delta p}{\rho g} = f\frac{L}{d}\frac{U^2}{2g} \ , \tag{4.14}$$

where f, L, d are friction factor, the pipe length, and the diameter of pipe respectively. Considering that the Re = 1800000 and e/d = 0.002 for commercial steel in terms of Nikuradse's sand grain scale, turbulent friction

factor f via Moody plot or by Colebrook Eqn. (4.15) is approximated to 0.024. Colebrook simply combined the expressions for the friction factor for smooth and rough pipes into a single transition equation of the equivalent form as follow:

$$\frac{1}{\sqrt{f}} = 1.74 - 2\ log\ (\ 2\frac{e}{d} + \frac{18.7}{\mathrm{Re}\sqrt{f}}\ )\ . \tag{4.15}$$

Note that Colebrook's expressions for the friction factor in the transition region reduces to Prandtl's smooth pipe equations when the relative roughness approaches zero, and reduce to von Karman's fully rough pipe equation at very high pipe Reynolds number [4].

The loss coefficients for elbows are presented as follows, where a and R represent the inside radius of the elbow and the radius of curvature of the centerline of the elbow respectively. For $\mathrm{Re}(a/R)^2 > 91$, the loss coefficient is expressed as follow [36]:

$$K_{elbow} = 0.00241\ \alpha\ \theta\ (\ \frac{R}{a}\ )^{0.84}\mathrm{Re}^{-0.17}\ , \tag{4.16}$$

where θ is the bend angle in degrees and α is an empirical factor given as:

$$\alpha_{\theta=90^\circ} = 0.95 + 17.2\ (\ \frac{R}{a}\ )^{-1.96}\ . \tag{4.17}$$

Inputting R=1.942 and a=0.442, $\alpha = 1.9$ and $K_{elbow} = 0.1232$. A correction term is applied to the 90° elbow to determine the loss coefficient for arbitrary angle of elbow [74].

$$K_\theta = (\ C_\theta\ )_{elbow}\ K_{90^\circ}\ , \tag{4.18}$$

where C_{elbow} is given in the referenced manual [74]. The C_θ is 0.28 at $\theta = 23^\circ$ and $K_\theta = 0.0345$.

The loss coefficient for the reducer or well-rounded inlet loss is $K_{reducer} = 0.05$ based on the flow area of the smaller piping section [4].

Finally, the loss coefficient for the abrupt contraction is given based on the velocity at exit as follow [4]:

$$\begin{aligned} K_{contraction} &= (\frac{1}{C_D^2} - 1)(1 - \beta^4)\ , \\ C_D &= \frac{Q_{acutal}}{Q_{ideal}}\ , \end{aligned} \tag{4.19}$$

where the discharge coefficient C_D is given in reference [4]. The mean discharge coefficient is given as 0.815 based on the water tests in short pipes. According to Eqn. (4.19), this yields a maximum loss coefficient at $\beta = 0$ of 0.506. Assuming $\beta = A_2/A_1 = 0.9$, $K_{contraction}$ yields 0.1738.

The head losses and the contribution of each geometry are given in Table 4.2. Total length of pipe is 87.1 inch. The diameter of inside pipe is 0.884 inch. The diameter of inside nozzle is 0.4 inch. Total pressure head loss is 2.3358 m., which corresponds to $\sim$ 16 % of input pressure head. The main loss is caused by large length with friction by surface roughness inside pipe, which is over $\sim$ 50 %. The loss from pipe bend is somewhat low comparing with others.

Based on the calculated head loss, the jet velocity at nozzle is determined

assuming the pressure right after nozzle exit is atmospheric. The pipe inlet pressure is given in Fig. 4.14(a) and (b). The elevation of the pipe inlet and the nozzle is $\sim$ 2.9 inch. The calculated jet velocity from nozzle including the pressure loss in pipe is 15 $\pm$ 1 m/s, which is $\sim$ 10 % larger than the measured result in Fig. 4.15, where the jet velocity is $\sim$ 13.5 m/s. Jet velocity in nozzle position was reported in Fig. 4.14(c) with $\sim$ 15.8 m/s by using incompressible constant flow rate between pipe inlet and nozzle exit, where piston size is 10 inch, nozzle inside size is 0.4 inch, and moving position of piston for injection of Hg jet was measured with respect to 10 Hz of data acquisition rate via NI hardware [31]. The magnetic field increases the fluid pressure by an amount of $B^2/2\mu$, in directions perpendicular to the magnetic field, and decreases the fluid pressure by the same amount, in the parallel direction of the magnetic field. The fluid pressure including the magnetic pressure has to balance with the atmospheric pressure and surface tension of jet, and it should satisfy the continuity condition. The fluid pressure will find equilibrium point since the fluid pressure perpendicular to the magnetic field line is mutually symmetric. Therefore, the jet is changing to be elliptical. Hence, the pressure drop is not occurred significantly and correspondingly the longitudinal jet velocity is not changed with magnetic fields in Fig. 4.15.

4.3.2.2 *measurement of wall tap pressure*

Wall tap is used in order to measure static pressure, wherein small pressure tap is located at a point on pipe surface so that it does not disturb the fluid.

Tap size error arises because of a local disturbances of the boundary layer. At tap Re greater than 385, the error in static pressure caused by the tap size is given as follow:

$$\frac{e_{tap}}{\tau} = 0.269 \ (\mathrm{Re}_d^*)^{0.353} \ , \tag{4.20}$$

where $\frac{e_{tap}}{\tau} = 12.74$ and

$$\mathrm{Re}_d^* = \frac{v^* d_{tap}}{\nu}$$
$$\mathrm{Re}_d^* = \sqrt{\frac{f}{8}} \ (\frac{d_{tap}}{d}) \ \mathrm{Re} \ , \tag{4.21}$$

where d_{tap} is the tap diameter, Re_d^* is the tap Re number, and v^* is the friction velocity. The friction factor is 0.024. The inside diameter of tap and inside diameter of pipe are 0.5, 0.884 inch respectively, which yields $\mathrm{Re}_d^* = 55764$. Combining the Darcy friction factor with the wall shear stress yields

$$f = 4 \ (\frac{\tau}{\rho v^2/2g}) \ . \tag{4.22}$$

Therefore, the error in a static pressure can be expressed in a non-dimensionalized form by the dynamic pressure $p_{dynamic}$ as follow:

$$\frac{e_{tap}}{p_{dynamic}} = (\frac{e_{tap}}{\tau})\frac{f}{4} \ , \tag{4.23}$$

where $\frac{e_{tap}}{p_{dynamic}} = 0.0764$. The error of static pressure in Fig. 4.14 (a) is estimated to give 7.64 % uncertainty of the dynamic pressure in Fig. 4.14 (b).

Table 4.1: Error estimation of fiducial length at each Viewport.

Viewport number	Fiducial length (cm)	Scaling factor
1	1.0 ± 0.095	1.0 (reference)
2	1.0 ± 0.091	4.3 ± 0.81
3	1.0 ± 0.062	1.0 ± 0.16
4	1.0 ± 0.067	4.3 ± 0.70

Table 4.2: Estimation of pressure head losses by geometry of pipe in Hg loop.

Geometry in pipe for Hg loop	Calculated pressure head loss	Percentage in total pressure head loss (%)
Friction by surface roughness	1.4176	60.7
Elbows in pipe bend ($3 \times 90°$, $2 \times 23°$)	0.2629	11.3
Reducer, Contraction in nozzle	0.6553	28

Table 4.3: Parameterized coefficients, its error, and statistics summary of fit function in figures.

Figure	**1**	**2**	**3**	**4**	**5**	**6**	**7**	**8**	**9**	**10**
4.10(B=0 T,V=15 m/s)	-0.01448	9.97E-04	0.03375	0.00379	-	-	-	-	13.6445	0.85213
4.10(B=5 T,V=15 m/s)	-0.01448	9.97E-04	0.03375	0.00379	-	-	-	-	13.85258	0.89937
4.10(B=10 T,V=15 m/s)	-0.01448	9.97E-04	0.03375	0.00379	-	-	-	-	14.13407	0.96089
4.10(B=15 T,V=15 m/s)	-0.01448	9.97E-04	0.03375	0.00379	-	-	-	-	14.48514	0.99102
4.10(B=15 T,V=20 m/s)	-0.01448	9.97E-04	0.03375	0.00379	-	-	-	-	18.85852	2.2851
Figure	**11**	**12**	**13**	**14**	**15**	**16**	**17**	**18**	**19**	
4.10(B=0 T,V=15 m/s)	-	-	-	-	20	13	25.15504	0.92629	0	
4.10(B=5 T,V=15 m/s)	-	-	-	-	20	13	25.15504	0.92629	0	
4.10(B=10 T,V=15 m/s)	-	-	-	-	20	13	25.15504	0.92629	0	
4.10(B=15 T,V=15 m/s)	-	-	-	-	20	13	25.15504	0.92629	0	
4.10(B=15 T,V=20 m/s)	-	-	-	-	20	13	25.15504	0.92629	0	

1 : a_1 value, **2** : a_1 standard deviation,

3 : b_1 value, **4** : b_1 standard deviation, **5** : b_2 value, **6** : b_2 standard deviation,

7 : b_3 value, **8** : b_3 standard deviation , **9** : c_1 value, **10** : c_1 standard deviation,

11 : c_2 value, **12** : c_2 standard deviation, **13** : c_3 value, **14** : c_3 standard deviation,

15 : Number of points, **16** : Degrees of freedom, **17** : Reduced χ^2, **18** : Adjusted $\mathbf{R}^2$, **19** : χ^2 probability.

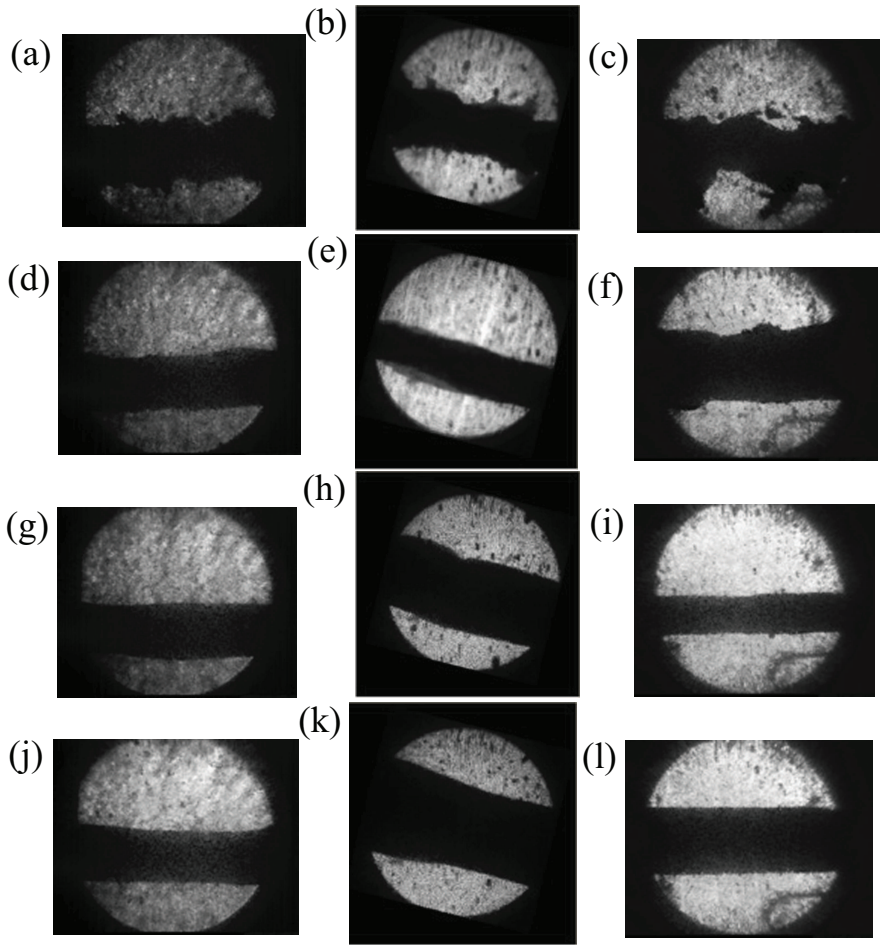

Figure 4.1: Hg jet flows as observed from each of 3 Viewports. The jet flows from left to right on each image. The first, second, and third columns represent Viewport 1, 2, and 3, respectively. The individual caption shows the applied magnetic field. The jet velocity is 15 m/s. Images on Viewport 2 has a 14° clockwise rotation due to the SMD software. a.) B=0 T. b.) B=0 T. c.) B=0 T. d.) B=5 T. e.) B=5 T. f.) B=5 T. g.) B=10 T. h.) B=10 T. i.) B=10 T. j.) B=15 T. k.) B=15 T. l.) B=15 T.

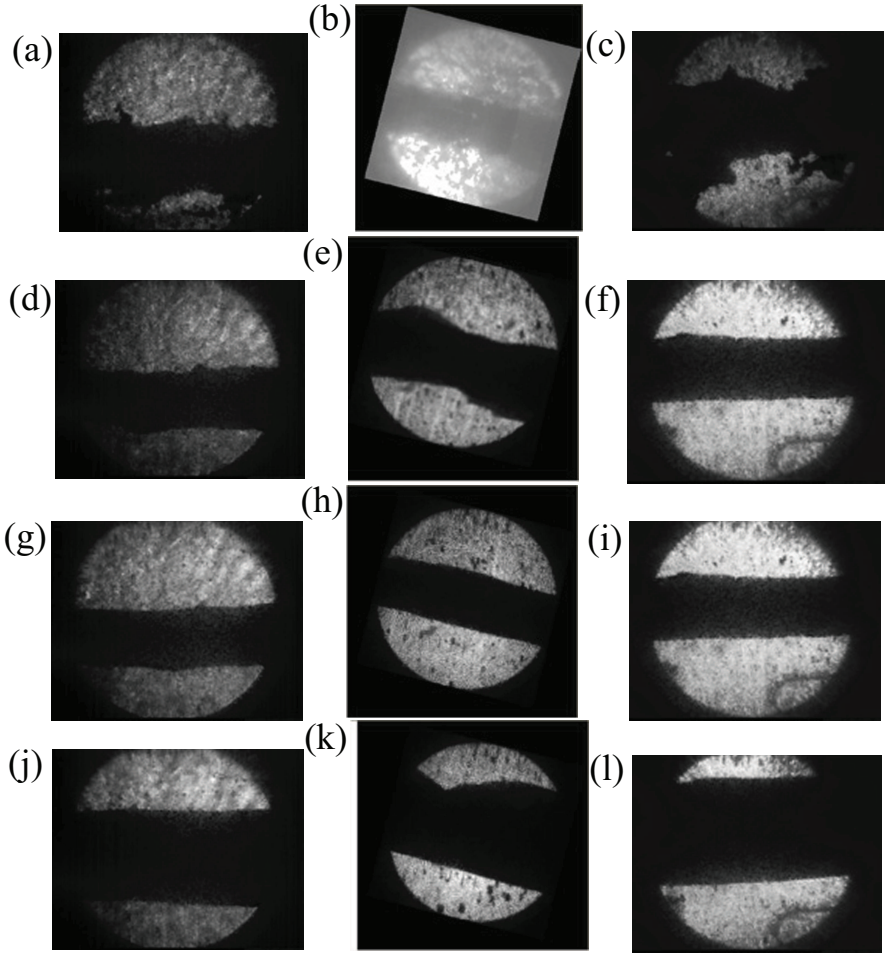

Figure 4.2: Same as Fig. 4.1 but with a jet velocity of 20 m/s. a.) B=0 T. b.) B=0 T. c.) B=0 T. d.) B=5 T. e.) B=5 T. f.) B=5 T. g.) B=10 T. h.) B=10 T. i.) B=10 T. j.) B=15 T. k.) B=15 T. l.) B=15 T.

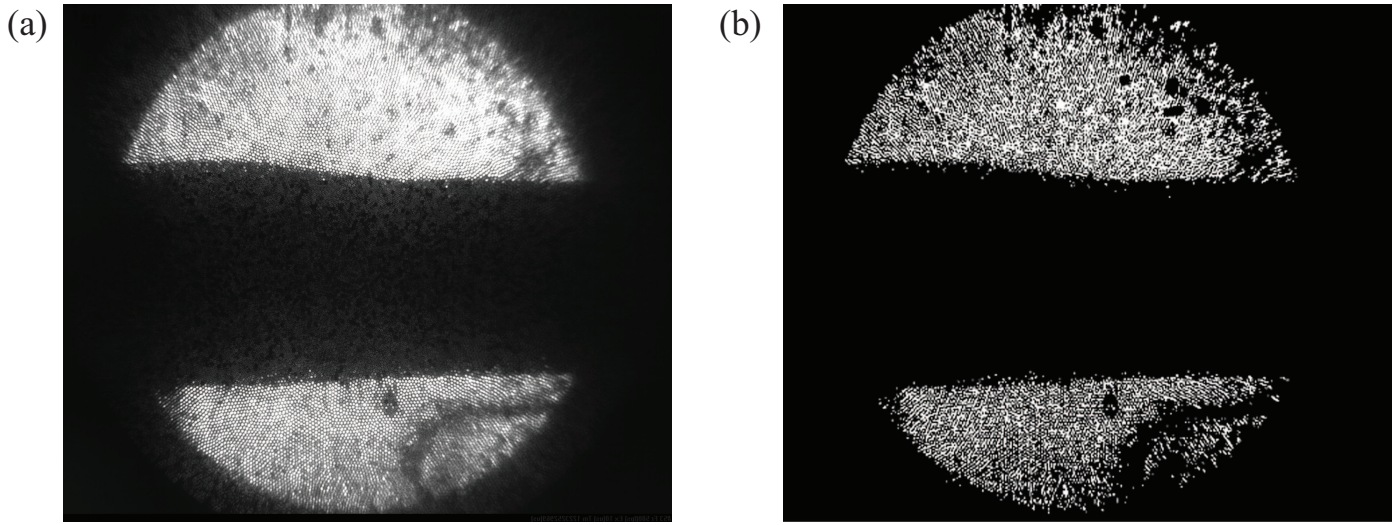

Figure 4.3: Image data conversion for image analysis. a.) Collected image data. b.) 2 bit scaled image data.

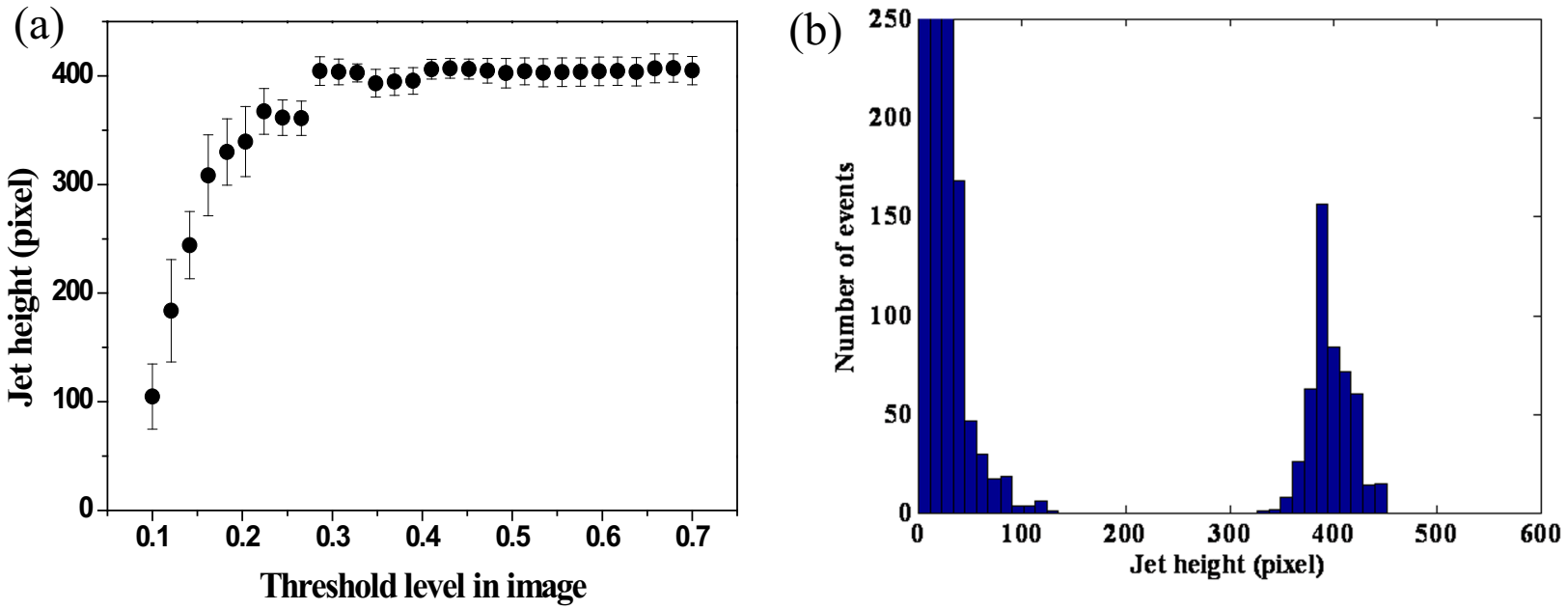

Figure 4.4: Jet height determination from image analysis. a.) Sensitivity of threshold in a 2 bit scaled image conversion. b.) Histogram of number of events in the jet height measurement.

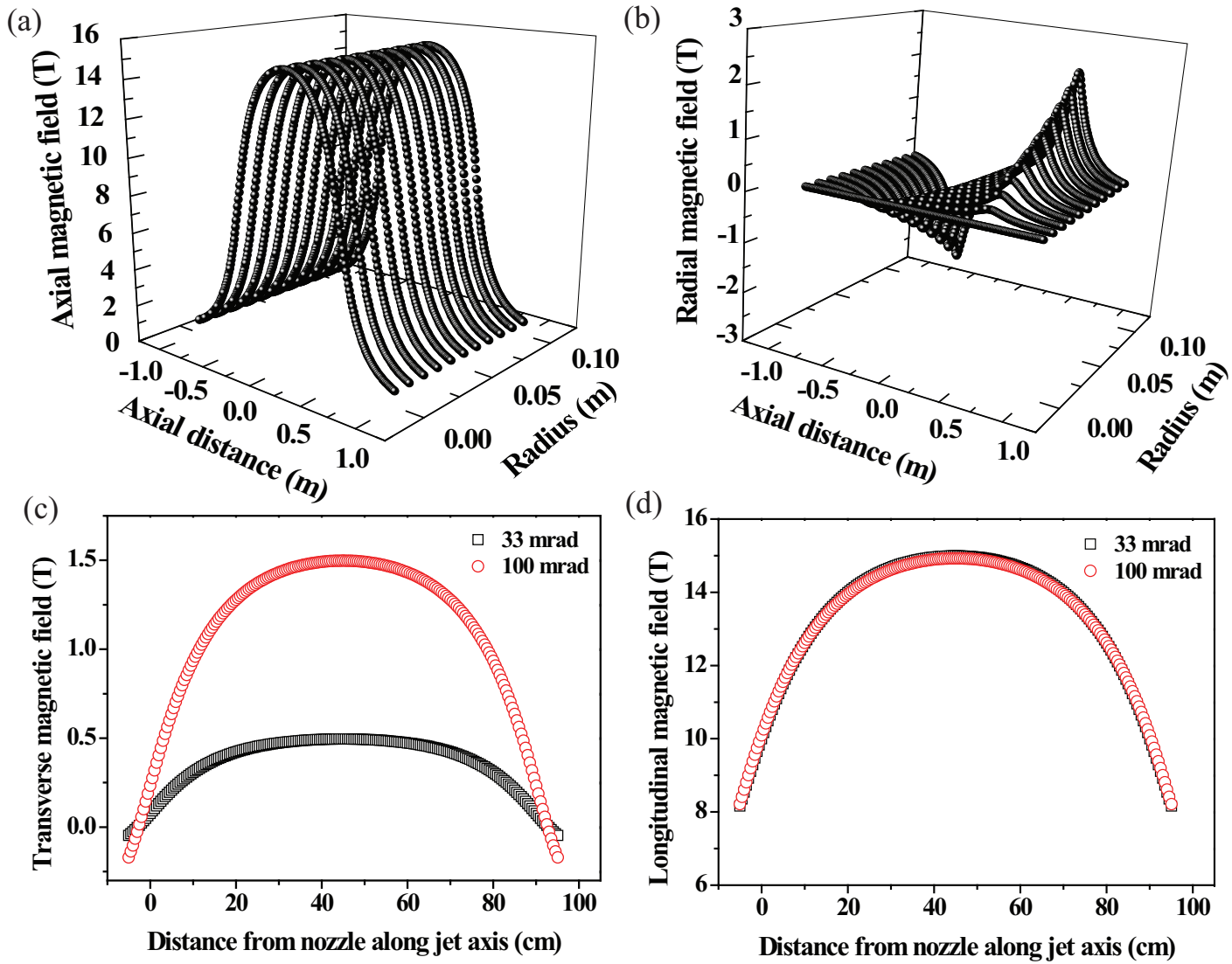

Figure 4.5: Calculated solenoid magnetic field map. a.) Radial field map. b.) Axial field map. c.) Transverse component of magnetic field along jet axis. d.) Longitudinal component of magnetic field along jet axis.

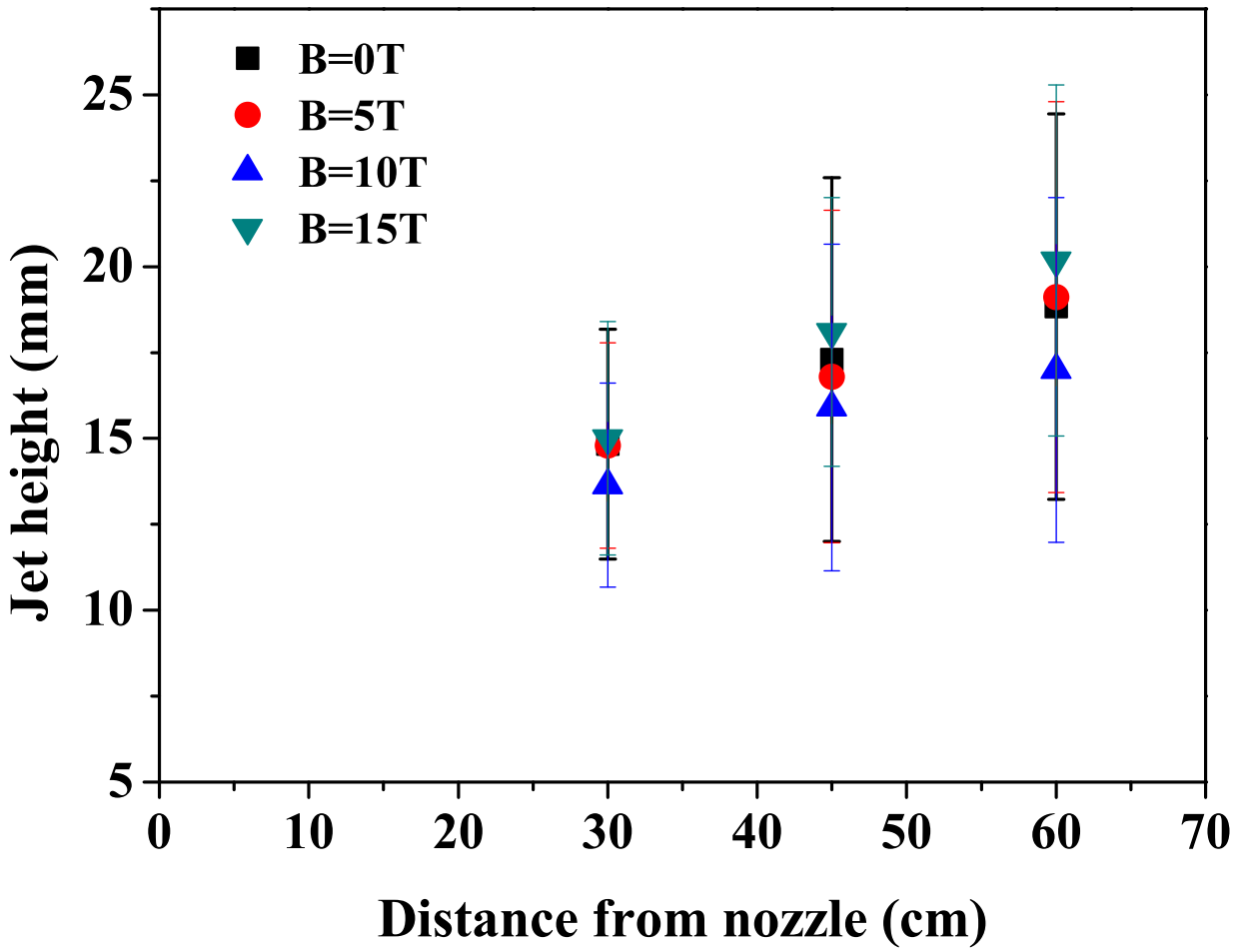

Figure 4.6: Hg jet height measurement from direct averaging of vertical height in magnetic fields on each image.

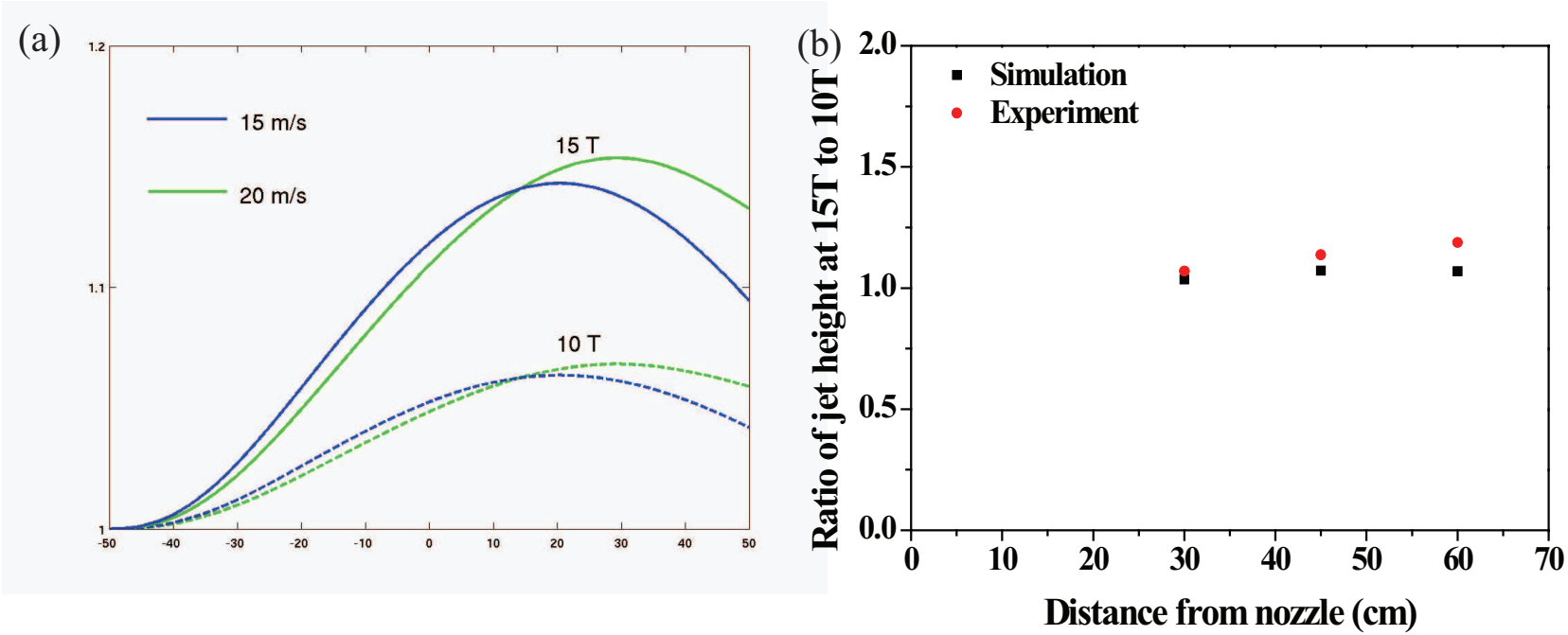

Figure 4.7: Comparison of Hg jet deflection ratio at 15 T to that at 10 T. a.) Numerical calculation of deflection ratio [78]. b.) Comparison of jet deflection ratio.

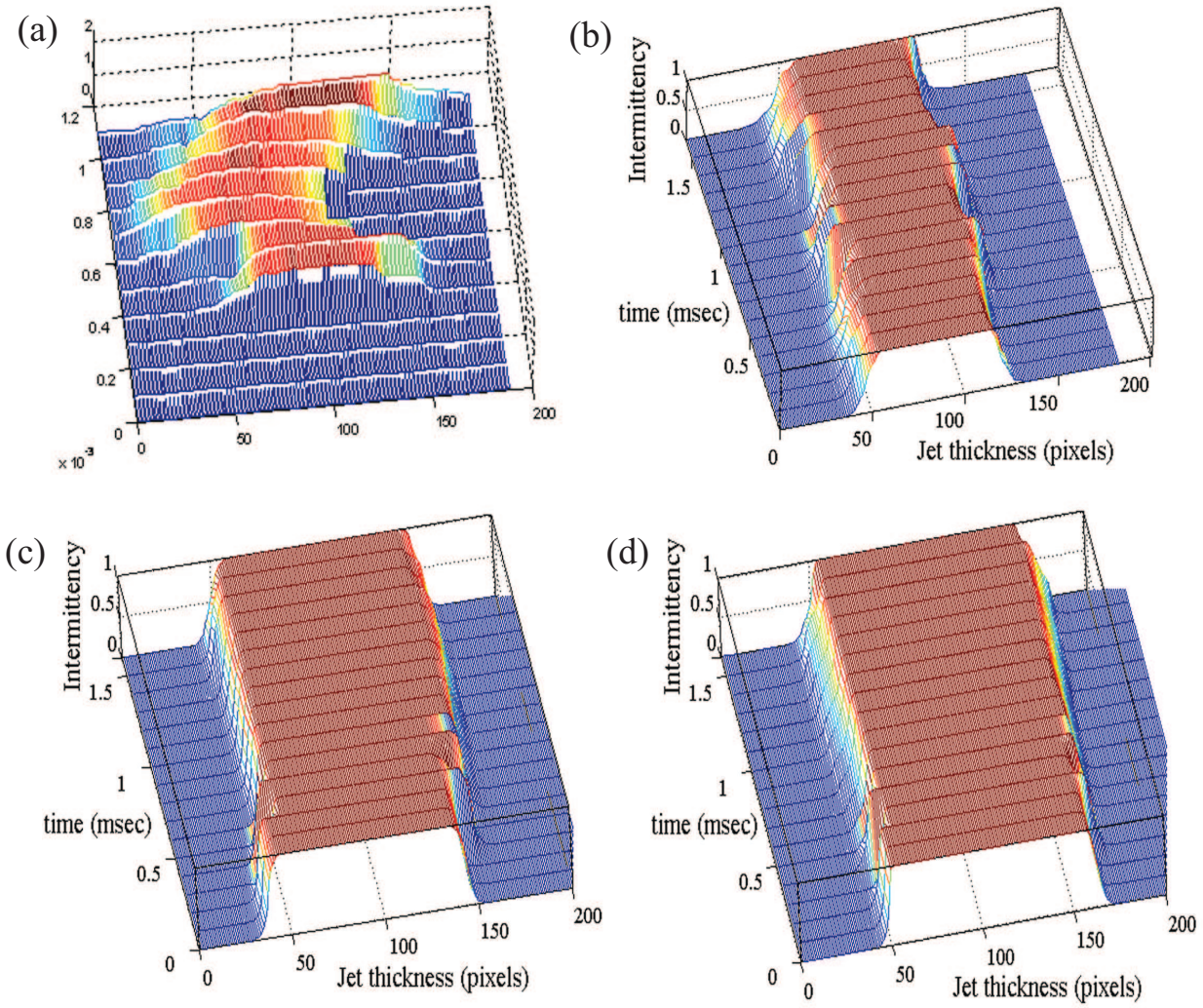

Figure 4.8: Intermittency of Hg jet at Viewport 2. The jet velocity is 15 m/s. a.) B=0 T. b.) B=5 T. c.) B=10 T. d.) B=15 T (continued).

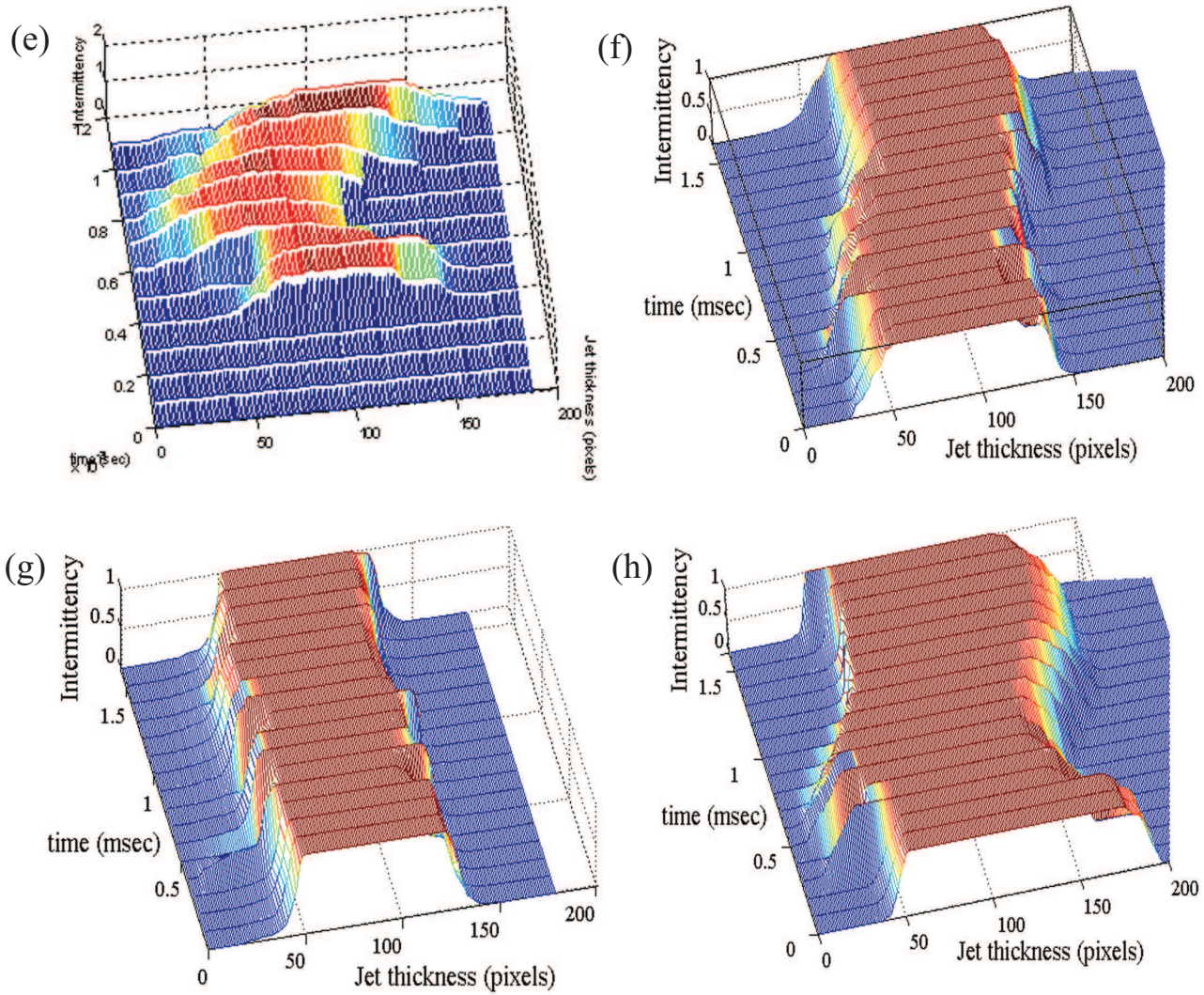

Figure 4.8: Intermittency of Hg jet at Viewport 2. The jet velocity is 20 m/s. e.) B=0 T. f.) B=5 T. g.) B=10 T. h.) B=15 T.

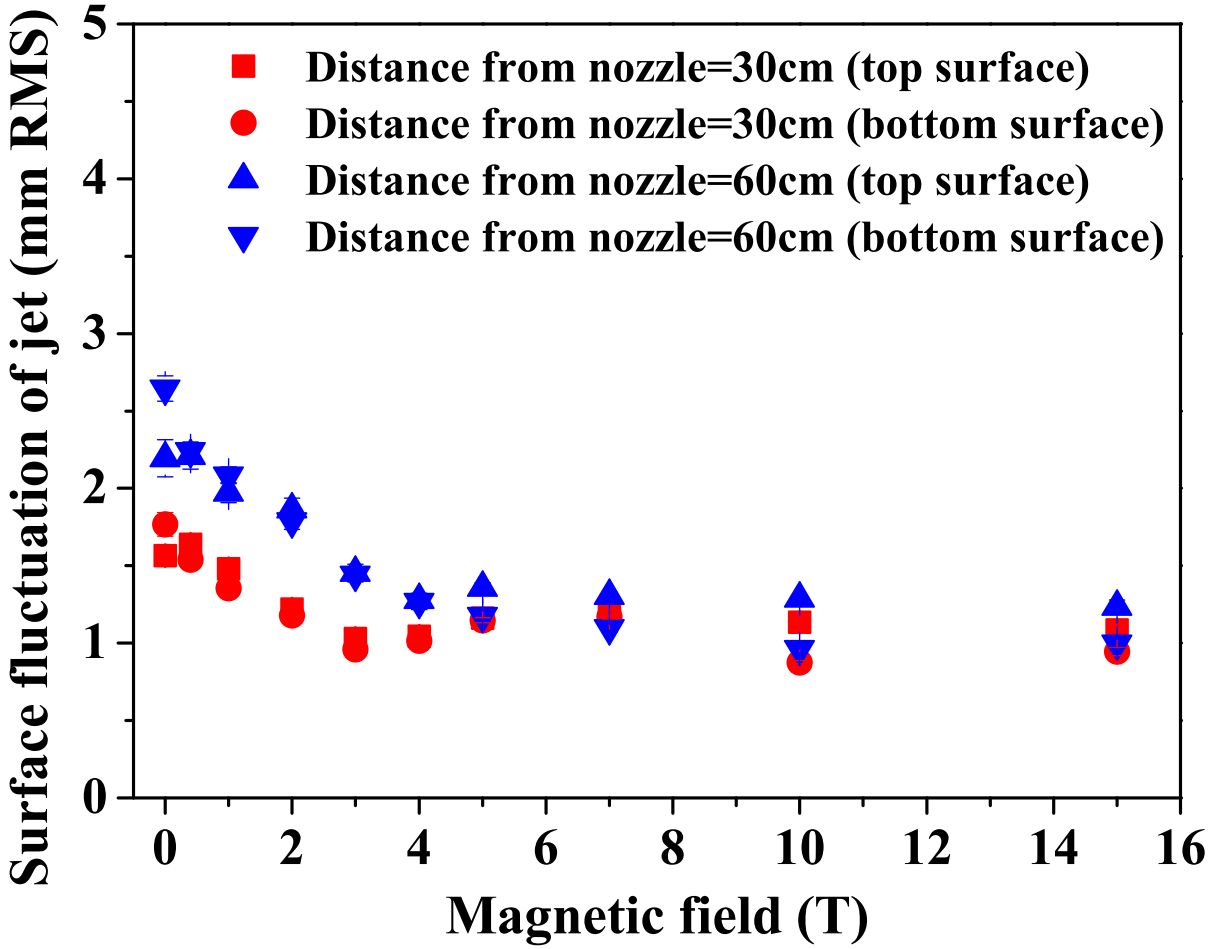

Figure 4.9: Measurements of surface fluctuations of Hg jet at upstream and downstream in magnetic fields.

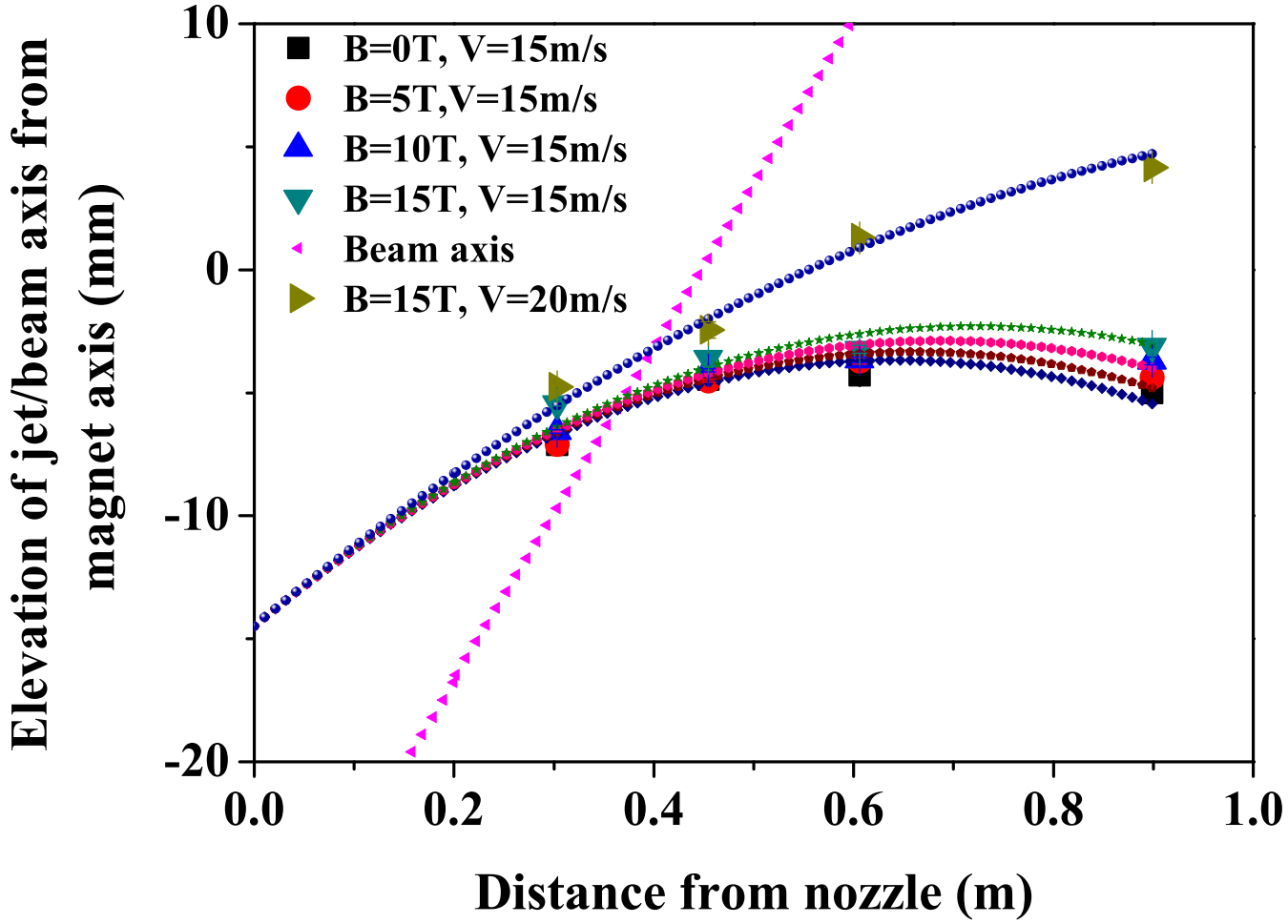

Figure 4.10: Trajectory of beam axis and Hg jet axis with respect to magnetic axis in magnetic fields. Solid line represents the globally fitted values using the formula of trajectory of projectile with different launching velocity.

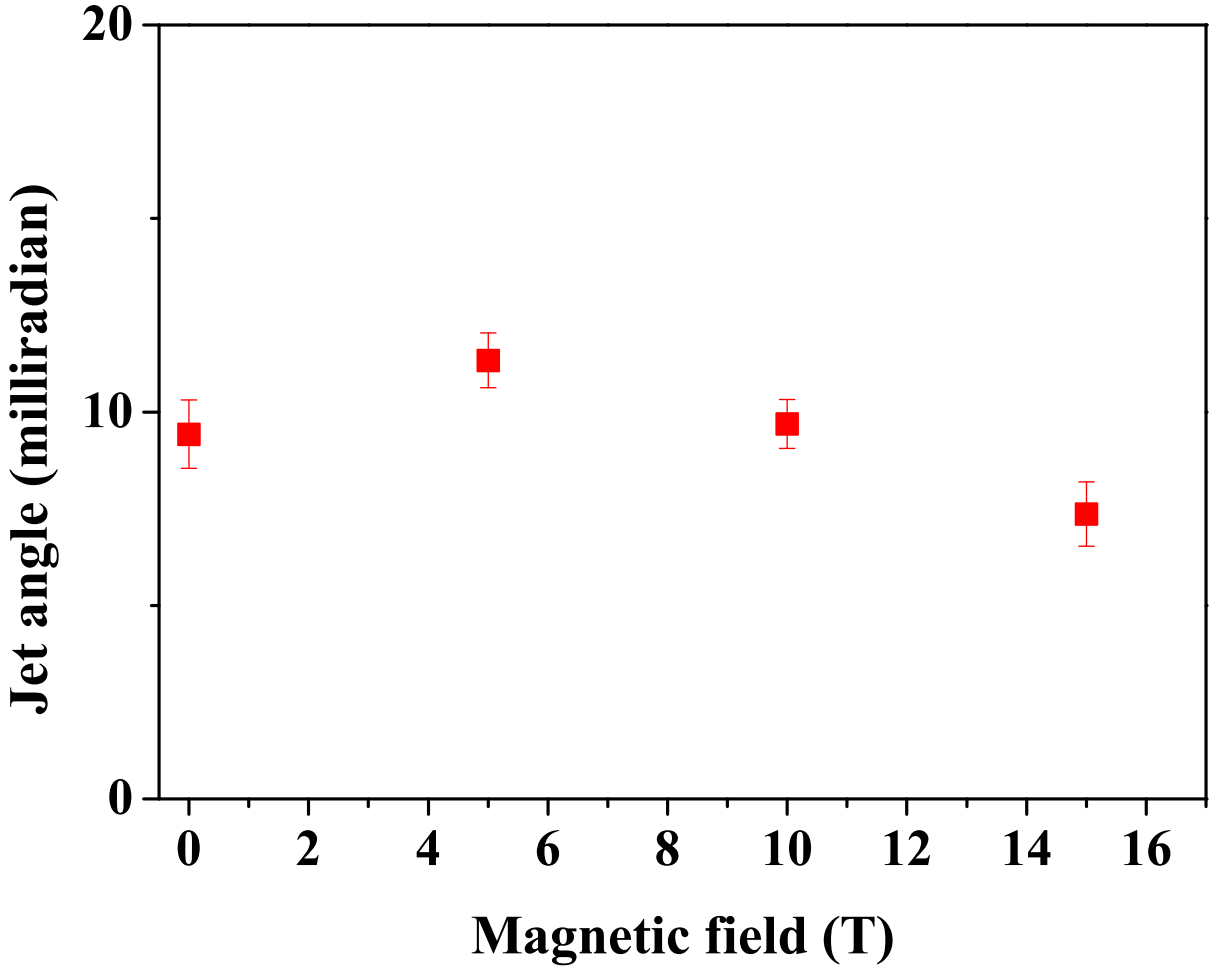

Figure 4.11: The estimation of angle of Hg jet axis at the center of Viewport 2 as a function of magnetic field.

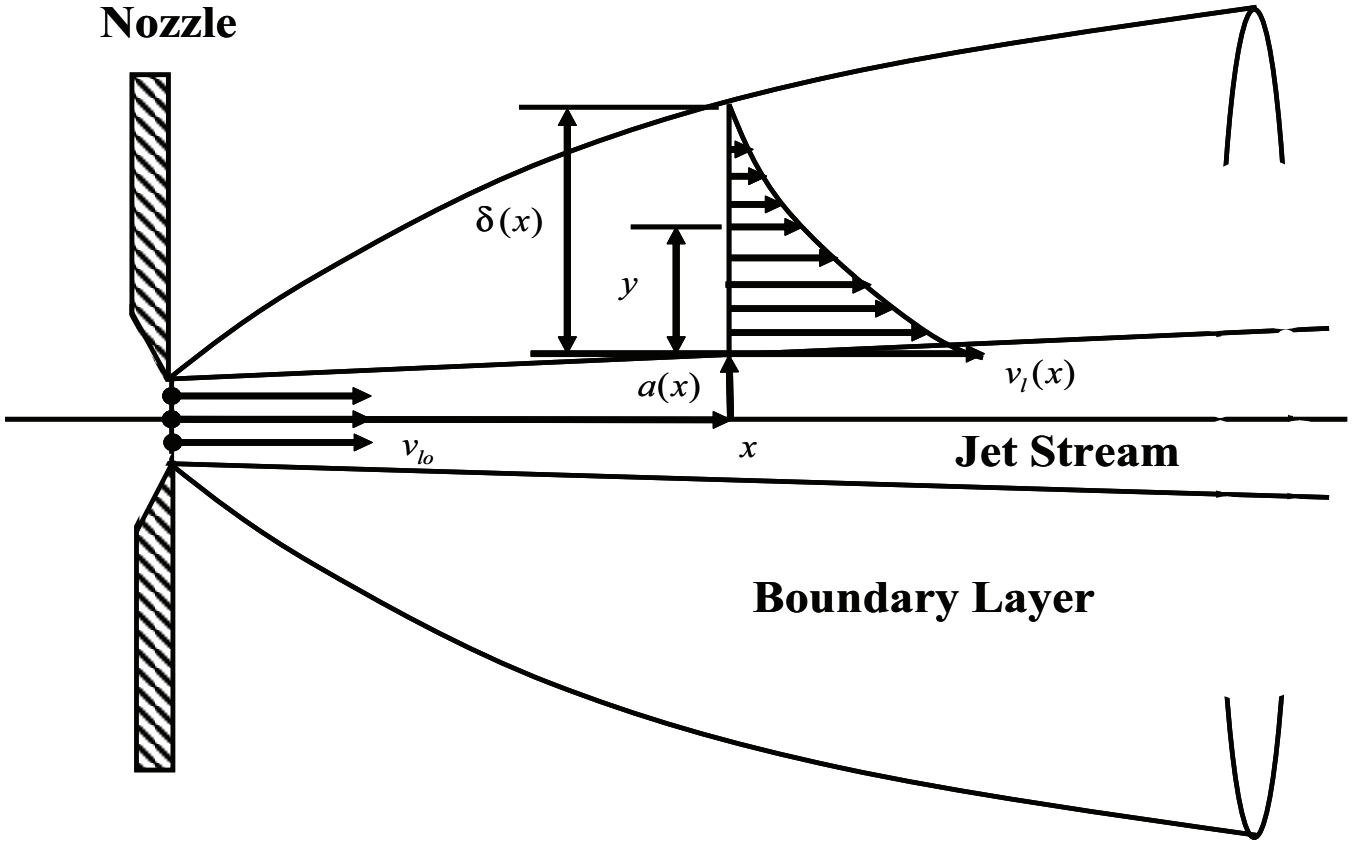

Figure 4.12: Boundary layer induced by a jet emerging from a nozzle.

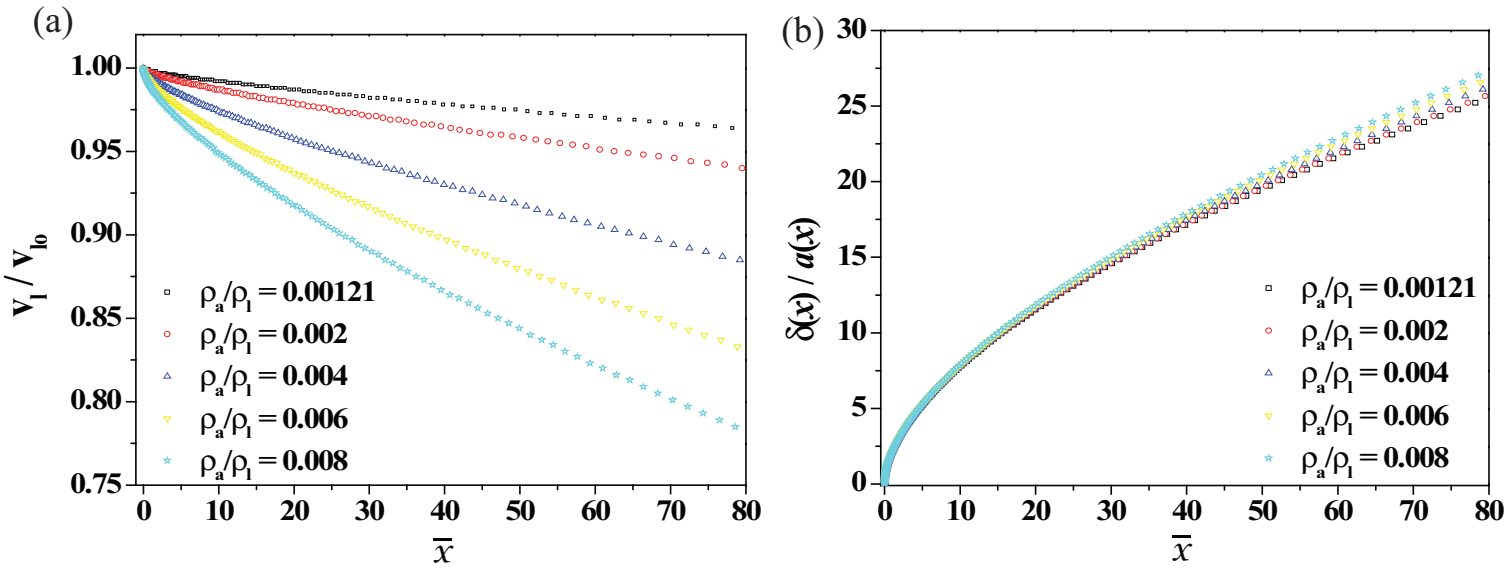

Figure 4.13: Stream velocity and boundary layer thickness for various values of density ratio.

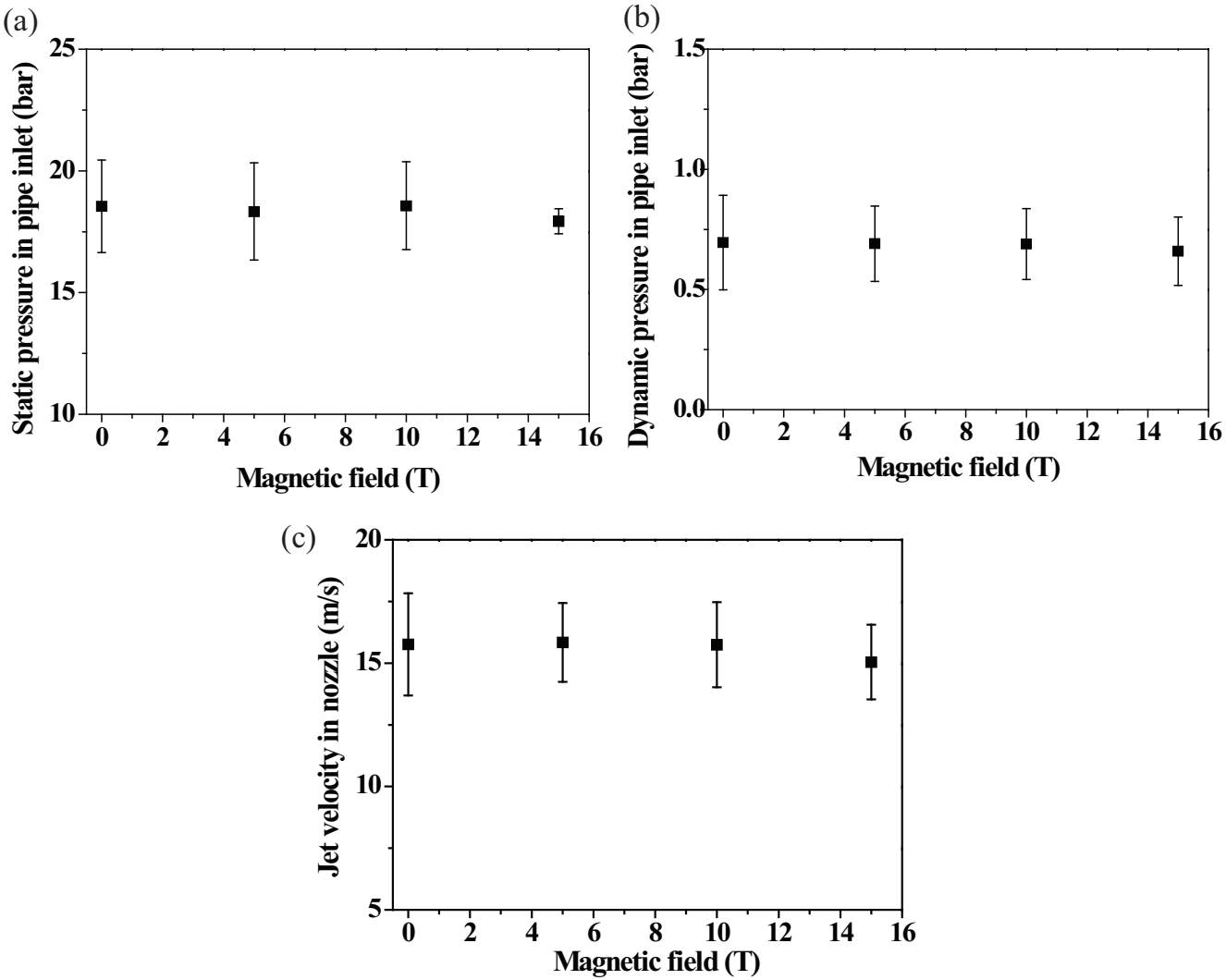

Figure 4.14: Pipe inlet pressure for driving Hg jet. a.) Static pressure. b.) Dynamic pressure. c.) Jet velocity in nozzle [30].

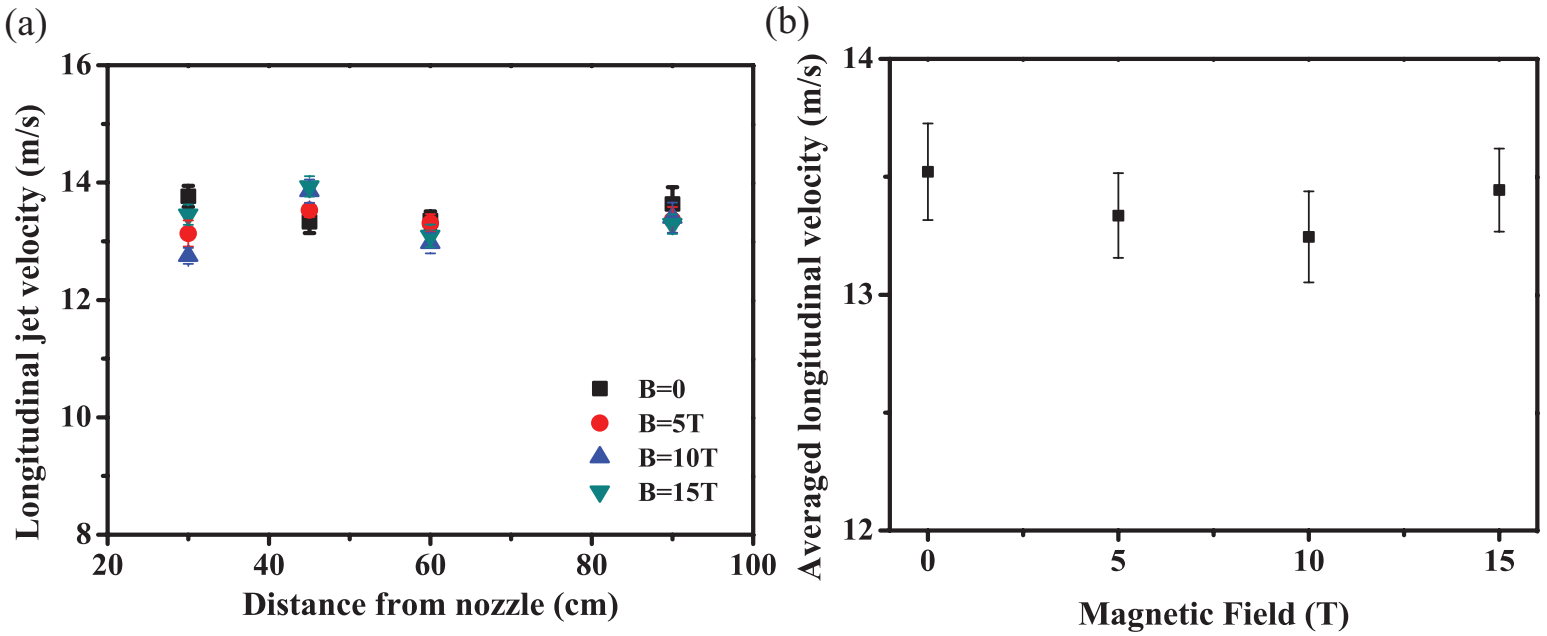

Figure 4.15: Longitudinal Hg jet velocity in magnetic fields. a.) Velocity at each Viewport dependent of magnetic fields. b.) Averaged velocity at each Viewport independent of magnetic fields.

Chapter 5

Interaction of an Intense Proton Beam with Hg Jet in a Magnetic Field

In this chapter, the jet's interacting characteristics in magnetic fields are investigated. The disruption of the jet interacting with various beam intensities and beam energy is observed and the magnetic suppression to it is discussed. The captured images show the mechanism of the beam-jet interaction, and the qualitative consistency with the distribution of calculated energy deposition is discussed. The energy deposition induced by the proton beam generates filaments on the Hg jet surface due to thermal stress.

5.1 High Energy Proton Beam Structure

5.1.1 Proton synchrotron machine

Neutrino factories requires a large number of muons, which are obtained from the decay of pions. Efficient production of pions can be achieved by colliding an intense proton beam with a high-Z target. An important consideration

is the problem of removing the power deposited by the proton beam without interfering with the process of extracting the end-product, which is the muon beam. Experiments on the interaction of a 14 GeV and 24 GeV proton beam with pulse structures of 4 to 16 bunches per pulse and the spot sizes in the order of 2 to 10 mm^2 RMS up to 30 tera-protons(Tp) per pulse in magnetic fields up to 15 T have been carried out at CERN. Figure 5.1 (a) shows the infrastructures for experiment at CERN. All equipments for experiment are installed at tunnel TT2/TT2A and these are controlled remotely from control room. The proton beam is delivered from proton synchrotron ring and the beam setup is schematically shown in Fig. 5.1 (b). The PS machine is set up in harmonic 16 bunches and the extracted protons fill the machine in bunch pairs. A bunch in harmonic 8 mode is consisted of a bunch pair. Therefore, a bunch period in harmonic 8 mode is two times of a bunch period in harmonic 16 mode. Each bunch can fill protons up to 2 2.5×10^{12}. Therefore, the maximum beam intensity can be achieved up to 32×10^{12} protons. Figure 5.2 shows the layout of tunnel at CERN, where equipments for experiment are installed. Electronic equipments for optical diagnostics, hydraulic power unit, and cryogenic system are positioned at tunnel TT2. Hg loop system, solenoid magnet, and beam diagnostic system are positioned at tunnel TT2A. The fibers for optical diagnostics of Hg target in solenoid magnet and cables for controlling the Hg loop system and solenoid magnet are connected between TT2 and TT2A passing through an artificially drilled hole.

5.1.2 Proton beam pulse length

In order to produce the design number of 10^{21} muons/year in muon storage ring, 4 MW of proton beam power is desired. For our experiment, the CERN PS ran typically in a harmonic 16 mode. Hence, it is possible to fill with 2×10^{12} protons/bunch and therefore up to 32×10^{12} protons/spill. One beam pulse consists of several beam bunches. The bunch lengths for harmonic 16 mode are 50 ns and 30 ns at full width at half maximum (FMWH) respectively. The bunch lengths for harmonic 8 mode are 70 ns and 40 ns at full width at half maximum (FMWH) respectively. The bunch-to-bunch differences for harmonic 16 mode and harmonic 8 mode are multiples of 131 ns and 262 ns respectively. The proton beam pulse structure of harmonic 8 and harmonic 16 in 14 GeV, 6 Tp is shown in Fig. 5.3. The spot size of beam at the experiment is in the order of 2 to 10 mm^2 RMS. This allows to place up to 32×10^{12} protons on the Hg target, generating a peak energy deposition of $\sim$ 150 J/g.

5.1.3 Proton beam envelope by optics and camera screen

The proton beam with 14 GeV and 24 GeV beam energy is employed in the experiment. As the number of protons in a beam pulse increases, it is reported [17] that the beam spot size increases. The beam spot size is calculated by CERN using the measured beam emittance, dispersion, and the momentum spread of the beam particle. The emittance is measured by measuring the beam profile in a position of known beam parameters based on optics. The

geometrical emittance ε is defined by

$$\varepsilon = \frac{(2\sigma)^2}{\beta}. \tag{5.1}$$

The normalized emittance ε^* is defined by

$$\varepsilon^* = (\beta\gamma)\varepsilon \quad , \quad \beta\gamma = \frac{P}{M} \ , \tag{5.2}$$

where β and γ are the relativistic functions at the measurement point, and P and M are momentum and mass of a proton respectively. Considering dispersion and emittance of beam, the spot size is estimated as follow:

$$\sigma = \frac{1}{2}\sqrt{\varepsilon \cdot \beta + (D_p \frac{\delta p}{p})^2} \ , \tag{5.3}$$

where D_p is the dispersion function at the measurement point and $\frac{\delta p}{p}$ is the momentum spread of the particle beam. The measured $\frac{\delta p}{p}$ for 14 GeV beam is 1.66 (2 σ, 0.1 %) and 1.1 for 24 GeV beam [17]. The normalized emittance is directly measured as a function of beam intensity from accelerator machine as follow:

$$\varepsilon^*_{2\sigma} = f(width_{4\sigma}, \quad \frac{\delta p}{p}_{2\sigma}) = \frac{(\frac{width_{4\sigma}}{2})^2 - (|D_p|\frac{\delta p}{p}_{2\sigma})^2}{\beta}. \tag{5.4}$$

The beta function and dispersion function from optics are calculated using parameters of quadrupole strengths and locations, which are the values at the position of Hg target [17]. The estimated 1 σ beam spot at Hg target position is given in Table 5.1. Figure 5.4 shows the estimated 1 σ beam spot size at the

center of target based on optics [17]. Figure 5.5 shows the measured 1 σ beam spot size at the phosphor camera screen monitor installed $\sim$ 4.2 m away from the center of magnet before entering the magnet [85]. It is also reported [85] that the beam spot size increases as the number of protons increase. Due to the saturation of image, the measured beam spot size is shown as $\sim$ 2 times larger than the estimated beam spot size from optics. Figure 5.6 (c) shows the beam sizes distribution measured by phosphor screen monitor as a function of recorded time interval between each beam shot, where the histogram for events of beam size in horizontal plane is shown in Fig. 5.6 (a) and the histogram for events of beam size in vertical plane is shown in Fig. 5.6 (b). This plots show that the possible residual saturation of image by phosphor screen monitor is not related with recorded time interval between each beam shot. The distribution of beam spot size is uniform regardless of the possible residual saturation by the screen monitor.

5.2 MARS Simulation for Energy Deposition to Mercury Jet by Proton Beam

5.2.1 Physics model

MARS is a Monte Carlo code for inclusive and exclusive simulation of 3D hadronic and electromagnetic cascades, muon and heavy ion transport in accelerator, detector, and shielding components in the energy range from a fraction of an eV up to 100 TeV [62]. In MARS code, hadron production, neutrino interactions, electromagnetic interactions of heavy particles, and electromagnetic

showers are considered. For hadron production, information on the nuclides generated in nuclear collisions is scored, or reported in the results of the simulation, which covers a hadron kinetic energy range up to 100 TeV. For neutrino interactions, the model permits the selection of the energy and angle of each particle (ν, e, μ)emanating from a simulated interaction. These particles, and the showers initiated by them, are then further processed in the code. Four types of neutrino interactions are distinguished ($\nu_\mu, \bar{\nu_\mu}, \nu_e, \bar{\nu_e}$) and the model identifies all possible types of neutrino interactions with nuclei. The corresponding formulas for these processes as well as results of Monte Carlo simulations are considered. For electromagnetic interactions of heavy particles, electromagnetic interactions of muons and charged hadrons in arbitrary materials are simulated. Radiative processes and atomic excitation and ionization with energy transfer are considered. The electromagnetic showers are based on the physics of electromagnetic interactions and it gives electron and photon interactions in composite solid, liquid, and gaseous materials [62].

5.2.2 Mercury jet modeling in MARS code

Using MARS code, calculation of energy deposition is performed at Fermi National Accelerator Laboratory [89]. For the modeling of jet in MARS, the experimentally measured Hg jet size and trajectory in magnetic field with assumption of sectionally elliptic jet shape and circular jet shape with equivalently reduced mass density to the initial flow rate from nozzle are employed. The proton beam is passing through the center of magnetic axis.

For simplicity, the z coordinate of modeling in MARS defines as 0 at the center of magnetic axis along the direction of magnetic field. Accordingly, the x coordinate of modeling in MARS defines as the vertical direction perpendicular to the direction of magnetic field. The measurement of vertical distance between magnetic axis and the center of jet is given in Table 5.2, where the measured jet size as well as approximated mass density for case simulation of assumed circular jet shape are also given. The vertical distance in cm in MARS code between center of jet and magnetic axis is employed as follow:

$$x_{vert} = -1.4522 - 3.65 \times 10^{-2} \times zz - 3.1672 \times 10^{-4} \times zz^2 + 5.4206 \times 10^{-9} \times zz^4, \tag{5.5}$$

where $zz = z - 46$ in cm. Figure 5.7 (a) and (b) show the sectional view of elliptic and circular jet, and Fig. 5.7 (c) shows the sectional side view of jet interacting with proton beam in a magnetic field, where the magnetic field direction and strength are indicated as arrows. Number of meshes and sizes are given in Table 5.2. Using MARS code, calculation of energy deposition in $GeV/g/proton$ with various magnetic field strengths and beam intensities is performed at Fermi National Accelerator Laboratory [88]. Note that 1 eV = 1.6022^{-19} J is used for conversion of energy unit between eV and J.

5.2.3 Energy deposition to mercury jet

5.2.3.1 *effect of magnetic field on energy deposition*

Figure 5.8 shows the averaged energy deposition in J/g along the jet axis for the case of 2 Tp according to the variation of magnetic field. Calculated energy deposition of each meshed volume is averaged along the jet axis with respect to azimuthal angle and radial distance using Eqn. (5.6):

$$E_{p,\ average}(z) = \frac{\sum_r \sum_{\theta=0}^{2\pi} \rho\ V_\theta^r(r,\theta,z) E_{p,\theta}^r(r,\theta,z)}{\sum_r \sum_{\theta=0}^{2\pi} \rho\ V_\theta^r(r,\theta,z)}\ , \tag{5.6}$$

where V_θ^r and $E_{p,\theta}^r$ represent the volume of each mesh along azimuthal angle at each radial distance and its energy deposition respectively. As the magnetic field increases, the distribution of energy deposition over the jet increases dependent of jet size. This indicates interaction of charged particles with magnetic field, so that more atomic excitation and ionization with energy transfer occurs in higher magnetic field. Also, the electromagnetic shower produced by a particle that interacts via the electromagnetic force gives electron and photon interactions in Hg. From the equation of particle motion and Lorentz force in Eqn. (5.7), the momentum of charged particle has an influence of the intensity of magnetic field followed by Maxwell's equations:

$$\frac{d\mathbf{p}}{dt} = e[\mathbf{E} + \mathbf{v} \times \mathbf{B}], \tag{5.7}$$

where e is the charge on the particle and $\mathbf{v}$ is the particle velocity. Figure 5.9 (a) and Figure 5.10 (a) show the azimuthal averaged energy deposition over

the orientation in sectional jet area along the jet axis for the case of 2 Tp with 24 GeV and 14 GeV in 10 T. Calculated energy deposition of each meshed volume is averaged along the jet axis and azimuthal angle with respect to radial distance using Eqn. (5.8):

$$E_{p,\ average}(\theta, z) = \frac{\sum_r \rho\ V_\theta^r(r, \theta, z) E_{p,\theta}^r(r, \theta, z)}{\sum_r \rho\ V_\theta^r(r, \theta, z)}\ . \tag{5.8}$$

Larger distribution of energy deposition occurs at bottom ($\sim$ 270 °)of jet where the beam enters. Gradually the larger distribution moves to the top ($\sim$ 90 °) of jet where the beam leaves. Figure 5.9 (b) and Figure 5.10 (b) show the azimuthal averaged energy deposition according to the variation of magnetic field along the orientation in sectional jet area for the case of 2 Tp with 24 GeV and 14 GeV in 10 T. Calculated energy deposition of each meshed volume is averaged along the azimuthal angle with respect to jet axis and radial distance using Eqn. (5.9):

$$E_{p,\ average}(\theta) = \frac{\sum_z \sum_r \rho\ V_z^r(r, \theta, z) E_{p,z}^r(r, \theta, z)}{\sum_z \sum_r \rho\ V_z^r(r, \theta, z)}\ , \tag{5.9}$$

where V_z^r and $E_{p,z}^r$ represent the volume of each mesh along axial jet axis at each radial distance and its energy deposition respectively. Larger axially averaged energy deposition is at bottom ($\sim$ 270 °) of jet and the distribution of energy deposition increases as the magnetic field increases. The geometrical distribution of energy deposition depending on the applied magnetic field does not changes but keeps uniform profile of distribution, which indicates that the profile of distribution is most likely dependent on jet shape.

5.2.3.2 *effect of proton beam spot size on energy deposition*

Figure 5.11 shows the averaged energy deposition per proton along the jet axis using Eqn. (5.6) according to the variation of incident number of protons in 5 T. As shown in Fig. 5.4, the beam spot size increases as the incident number of protons increase, where beam spot area is defined as $\sigma_x \sigma_y$. We speculate on peak energy deposition and total energy deposition in Hg jet. Peak energy deposition is the largest energy found in entire meshes on the jet model and total energy deposition is the summed energy in entire meshes on the jet model. Figure 5.12 shows the variation of peak energy deposition per proton and total energy deposition per proton to Hg jet with respect to the incident number of protons and proton beam spot size from Fig. 5.4 at both 14 GeV and 24 GeV beam energy in magnetic fields. The total energy deposition amounts to $\sim 6 \sim 8$ % of the incident beam energy and the total energy deposition is slightly decreasing depending on the variation of beam spot size. However, the total energy deposition increases as the magnetic field increases. As discussed in Fig. 5.8, it again indicates interaction of charged particles with magnetic field, so that more atomic excitation and ionization with energy transfer occurs in higher magnetic field. However, the peak energy deposition is independent of magnetic field strength for given protons but influenced by beam parameters. The lines in Fig. 5.12 represent the global fit of calculated peak energy deposition per proton and calculated total energy deposition per proton using Eqn. (5.10) and Eqn. (5.11) respectively, shown as

$$E_p = (a_1 + b_1 N_p^{b_2}) E_b^{c_1} \ , \quad E_p = (a_1 + b_1 A_b^{b_2}) E_b^{c_1} \tag{5.10}$$

and

$$E_p = a_1 (B - b_1)^{b_2} E_b^{c_1} + N_p b_3 E_b^{c_2} \ , \quad E_p = a_1 (B - b_1)^{b_2} E_b^{c_1} + A_b b_3 E_b^{c_2} \ , \tag{5.11}$$

where N_p, A_b, B, E_p, and E_b denote number of protons, beam spot area, magnetic field, energy deposition, and beam energy respectively. Note that the parameterized values of coefficients and errors of the fit functions are given in Table 5.3. The peak energy deposition as a function of incident number of protons decreases with square rooted power of number of protons, and it increases with ~ 1.5 power of beam energy between 14 GeV and 24 GeV. The ratio of beam energy between 14 GeV and 24 GeV is ~ 1.7. The total energy deposition decreases slightly linearly with number of protons and increases with 0.06 power of magnetic field strength. Thus, the total energy deposition as a function of incident number of protons has an increase with ~ 1.4 power of beam energy as an offset between 14 GeV and 24 GeV, and ~ 0.9 power of beam energy as an slope in fit function , which indicates possibly that the absolute ratio of power ~ 1.5 due to the beam energy difference is separated into two coefficient terms ratio of c_1 to c_2 in fit function.

Based on the result in Fig. 5.12, the incident number of protons are multiplied to the peak energy deposition per proton, which yields results in Fig. 5.13 on a logarithmic scale. The peak energy deposition with respect to the number of

protons increases parabolically due to the increase of parabolically approximated beam cross sectional area, which directly influences to the peak energy deposition to Hg jet. Also, the higher magnetic field again results in larger total energy deposition to Hg jet.

The solid line in Fig. 5.13 (a) and (b) represent the fit of calculated peak energy deposition using Eqn. (5.12) and Eqn. (5.13) respectively, shown as

$$E_p = a_1 N_p^{b_1} E_b^{c_1} \tag{5.12}$$

and

$$E_p = a_1 N_p^{b_1 + b_2 B^{b_3}} E_b^{c_1}. \tag{5.13}$$

The fit result from Eqn. (5.12) shows that the peak energy increases with ~ 0.8 power of beam intensity on a linear scale, which can be a linear relation on a logarithmic scale with ~ 0.8 between beam intensity and peak energy deposition, and ~ 1.6 between beam energy and number of protons. The fit result from Eqn. (5.13) shows that the total energy deposition increases with ~ 0.9 power of beam intensity, but it slightly increases with ~ 0.4 power of magnetic field. On a logarithmic scale, total energy deposition increases linearly with ~ 1.4 times of beam energy. This study is useful since it allows one to extrapolate the trend for estimation of profile of energy deposition, so that one can approximate the profile of energy deposition over all of the region of Hg jet based on the characteristic relations in energy deposition to magnetic field, beam intensity, and Hg jet shape.

5.3 Observation of Proton Beam Interaction and Hg Jet Response by Energy Deposition

5.3.1 Hg jet pressurization by energy deposition of proton beam

The energy deposition E_p due to ionization losses of the protons is ~ 33 J/g and additional ionization due to secondary particles from interactions of the protons in the target raises this to a peak of $\sim$ 100 J/g at 10 cm into the target [55]. The energy deposition, E_p, leads to peak pressure P_p that can be estimated as follow:

$$P_p \approx K\alpha_v \Delta T = \frac{\alpha_v K E_p}{c_p} \ , \tag{5.14}$$

where α_v is the thermal volumetric expansion coefficient, which corresponds to 3 times of thermal linear expansion coefficient, K is the bulk modulus, E_p is the energy deposition, and c_p is the specific heat capacity. For Hg, $\alpha_v = 180 \times 10^{-6}$/K , $K = 25$ GPa, $c_p = 138$ J/(K kg). A peak value of E_p=100 J/g corresponds to a peak stress of $\sim$ 3000 MPa. The Hg target is disrupted by the proton beam, leading to a breakup into droplets. The strain energy is built up in the jet due to compression [84].

5.3.2 Observation of proton beam interaction and jet breakup

Figure 5.14 is the photographs of the typical Hg jet interacting mechanism with a 16 Tp, 14 GeV proton beam at 5 T captured at Viewport 3 at a 500 μs frame rate, which shows clearly how the Hg jet is responding from the sudden energy deposition by the proton beam. The beam hits the Hg jet at the bottom surface, passing through the center of jet at Viewport 2, leaving the Hg jet on the top surface. The captured photos show the response of the Hg jet at upstream, midstream, and downstream with the interaction of the proton beam. There are filaments on the top surface of jet at downstream, where the beam is leaving, and on the bottom surface of the jet at upstream, where the proton beam is entering. The jet break up voids at midstream, where the beam is passing through and possibly caused by the cavitations from energy deposition.

5.3.2.1 *energy deposition calculation with low intensity of proton beam and its observation*

Figure 5.15 (a) shows the distribution of energy deposition by 24 GeV, 3 Tp intensity of proton beam in 5 T. Calculated energy deposition of each meshed volume is averaged along jet axis and vertical radius of jet with respect to azimuthal angle using Eqn. (5.15):

$$E_{p,\ average}(r,z) = \frac{\sum_{\theta=0}^{2\pi} \rho\ V_{\theta}^{r}(r,\theta,z) E_{p,\theta}^{r}(r,\theta,z)}{\sum_{\theta=0}^{2\pi} \rho\ V_{\theta}^{r}(r,\theta,z)}\ . \tag{5.15}$$

The energy density distribution is plotted according to the radial position of Hg jet from jet center. Therefore, the peak of energy deposition density exists respectively depending on the radial position. It shows that the maximum energy deposition density is obtained at the bottom surface of jet at $\sim$ 13 cm from the center of magnet, where Viewport 1 is actually positioned, and the peak energy density moves to the center of Hg jet followed by the larger energy density located at the top surface of the Hg jet. The peak energy deposition density is moving corresponding to the beam interacting trajectory in Hg jet. The most dense energy deposition is distributed at the center of Hg jet between upstream and midstream, where Hg jet breaks up. The collected photos in Fig. 5.15 (b) clearly supports these simulation results, where the frame rate is 2 ms and measured disruption length at Viewport 3 is 11 cm.

5.3.2.2 *energy deposition calculation with high intensity of proton beam and its observation*

Figure 5.16 (a) shows the distribution of energy deposition by 24 GeV, 10 Tp intensity proton beam in 5 T. Averaged energy deposition is also calculated using Eqn. (5.15). The distribution profile of energy deposition throughout Hg jet is similar with low intensity of beam. The collected photos in Fig. 5.16 (b) clearly supports these simulation results again, where the frame rate is 2 ms and measured disruption length at Viewport 3 is 17 cm. However, the jet breakup voids the midstream where the beam is passing through, which is different comparing with the observation of the case of low intensity beam. These voids are not observed at 3 Tp intensity of beam,

possibly indicates threshold of the existence of cavitation or breakup induced by energy deposition.

5.3.3 Hg jet disruption and magnetic suppression of the disruption

The disruption length is determined by counting the number of frames at Viewport 3, where the complete disruption of the jet is observed. The time delay between Viewport 2 and Viewport 3 is $\sim$ 10 ms. Thus, the disruption generated at Viewport 2 by the beam could be observed at Viewport 3 after 10 ms, where the jet is moving with typically a velocity of 15 m/s. Each image is separated into 10 segments vertically in order to locate the position of disruption. Thus, the accuracy of the measurement to define the location of starting(ending) disruption in measurement could be increased. The disruption length is given by multiplying the frame rate by the counted number of images and investigated according to the beam energy, beam intensity, and magnetic field. 230 events out of 360 beam shots are evaluated for the disruption length. About 130 events out of 360 beam shots are evaluated for the detection of particles without Hg jet. Thus, the images for these events are not collected. Figure 5.17 shows the standard deviation of the evaluated disruption lengths with respect to the disruption length. The solid line represents the curve fitted approximation of the reduced data distribution, where the line asymptote logarithmic. This curve fitted line is used for estimation of the standard deviation of the measured disruption length for the case that

only one shot is available for disruption length measurement. Correspondingly, the error bar is determined by dividing the the estimated standard deviation by the root square of the number of samples N for each data point.

5.3.3.1 *characteristics of beam structure in disruption length, harmonic 8 and 16*

The proton beam pulse structure of harmonic 8 and harmonic 16 in 14 GeV, 6 Tp is shown in Fig. 5.3. A pulse carries same number of protons with doubled bunch structures. Figure 5.18 shows the dependence of the disruption length of the Hg jet on the proton beam pulse structure with a 14 GeV beam in 5 T. The solid line in Fig. 5.3 (a) and (b) show the global fit and independent fit of disruption length with both harmonic 8 and harmonic 16 bunches as a function of total energy deposition respectively. A liner fit function is used as follow:

$$L^{disruption} = a_1(E_p - b_1), \tag{5.16}$$

where E_p and $L^{disruption}$ denote the total energy deposition and disruption length respectively. The χ^2 probability of global fit in Fig. 5.3 (a) is 0.056. The χ^2 probability of each independent fit in Fig. 5.3 (b) by using the sum of χ^2 and degrees of freedom of each independent fit yields 0.051. From this point of view, there is no statistical difference between the two ways of fitting, so that one could conclude that the disruption length does not depend on harmonic number. The disruption of Hg jet is affected by the number of protons, resulted from energy deposition by the interacting number of protons. The short time

difference in each bunch structure is negligible. The disruption on the Hg jet surface disappears when the beam intensity is less than $\sim$ 4 Tp according to Fig. 5.19. The threshold of beam intensity is $\sim$ 4 Tp for 14 GeV in 5 T.

5.3.3.2 *disruption length with 14 GeV proton beam*

Figure 5.19 shows the disruption length with beam intensities up to 30 Tp for a 14 GeV beam. The peak and total energy deposition to Hg with 14 GeV beam energy at 30 Tp in 15 T is $\sim$ 52 J/g and 3700 J by approximating it from Fig. 5.13, where the disruption length corresponds to $\sim$ 23 cm $\pm$ 5 cm for 10 T to $\sim$ 18 cm $\pm$ 5 cm for 15 T respectively. At high intensities of beam, the disruption length appears to be approaching an asymptotic level. The magnetic field suppresses weak disruption such as onset of generation of the filaments on the jet surface. The threshold of the disruption for beam intensity is around 4 Tp in 5 T and the magnetic field can increase it, though the effect is not clear in Fig. 5.19 due to the difficulty in quantifying and judging to measure the small amount of the disruption length.

5.3.3.3 *disruption length with 24 GeV proton beam*

Figure 5.20 shows the disruption length with the beam intensities up to 30 Tp for a 24 GeV proton beam. The estimation of disruption length is performed by estimating the extent of energy in Hg jet along jet axis larger than the energy deposition threshold experimentally determined by threshold intensity of beam as follow :

$$L_{E_p}^{disruption}(z) = z_2 - z_1,\ E_p(z) \geq E_{p,\ threshold}^{peak}(z), \quad L_{E_{p,\ threshold}^{peak}}^{disruption}(z) = 0, \quad (5.17)$$

where $L^{disruption}$ and $E_{p,\ threshold}^{peak}$ represent the length of disruption and peak energy of threshold intensity of beam experimentally determined for jet disruption. For example, Fig. 5.16 (a) shows the profile of energy deposition along jet axis. Therefore, energy in Hg jet is known. By using Eqn. (5.12), one can estimate peak energy deposition at 3.7 Tp , which is the experimentally determined threshold intensity of beam. Now, in Fig. 5.15 (a), find the extent of length along jet axis where the energy in Hg jet is larger than the peak energy at threshold intensity of beam. The length along jet axis determined here is judged as disruption length of jet for estimation purpose and it is plotted in Fig. 5.20.

According to Fig. 5.13, the peak and total energy deposition to Hg with 24 GeV beam energy at 30 Tp in 10 T is $\sim$ 125 J/g and 8200 J, where the disruption length corresponds to $\sim$ 22 cm $\pm$ 5 cm for 10 T to $\sim$ 17 cm $\pm$ 5 cm for 15 T respectively. The results again show that the magnetic field suppresses the disruption length. The disruption length appears to be approaching an asymptotic level. If there is no magnetic field, the disruptions are always generated by proton beam regardless of the beam intensities, though weak disruptions on the Hg jet surface are observed with low beam intensities. The threshold of the disruption for beam intensity is $\sim$ 1 Tp at 5 T but the higher magnetic field increases it. The estimation of disruption length in 10 T based on the calculation of energy deposition using the beam spot size from optics

is somewhat qualitatively agreed with the experimental measurement, but the estimation in 0 T based on the beam spot size from optics underestimates the experimental results. Possibly, the difference in MARS model may cause the difference of energy deposition calculation and the beam spot size is more likely to be larger at 0 T. Therefore, possibly the estimation by energy deposition from larger beam spot size is more likely to be fit to the experimental measurement for the case of 0 T. For theses estimations, the independent threshold of beam intensity is chosen individually from the experimental results depending on the conditions of individual cases for estimation. Therefore, the energy for threshold is differently used for each case of estimation using the beam size from optics. For the case of estimation of 0 T, 5 T, and 10 T, 0.8 Tp, 1.5 Tp, and 3.7 Tp of threshold beam intensities are chosen respectively.

5.3.3.4 *comparison of measurement at Viewport 3 and Viewport 4*

In order to check measurement of the disruption length at Viewport 3, measurement of disruption length at Viewport 4 is also performed. Fig. 5.21 (a) shows the disruption length at Viewport 3 for 23 events with a harmonic 16 beam structure, 16 Tp, 14 GeV beam energy in 5 T. Figure 5.21 (b) shows the disruption length at Viewport 4 for the same events. Figure 5.21 (c) shows the difference of disruption length between Viewport 3 and Viewport 4 from Fig. 5.21 (a) and (b). The solid line represents the average and distribution of the disruption length difference based on gaussian distribution approximation. The difference of measured disruption length at Viewport 3 and Viewport 4

is 1.3 ± 3.5 cm. It seems that the reason for the difference of the disruption length measurement between Viewport 3 and Viewport 4 is mainly caused by the fluctuation of the proton beam and the Hg jet in a magnetic field. Thus, slightly larger measurement of disruption length is observed at Viewport 4. The disrupted surface shape seems to be constrained in magnetic fields. Therefore, the same disrupted shape on jet surface at Viewport 3 is observed at Viewport 4 (30 cm apart from Viewport 3) without variation of the disruption length.

5.3.3.5 *measurement of disruption length in pump-probe condition as a check*

Figure 5.22 shows the measured disruption length of multiple events with pump-probe condition as a check. The conditions of each group in pump-probe events are given in Table A.4. There are 4 groups at 14 GeV and each group has different number of bunches and time delay between pump and probe. Figure 5.22 (a) shows the histogram of disruption length and Fig. 5.22 (b) shows statistics summary such as average, minimum, maximum, and median value. In group 2, qualitatively meaningful distribution of measurements is given, which is 19.8 ± 6.1 cm. In sub-category of group 2, various time delay between 6 bunches and 2 bunches does not show significant difference in disruption length. This check is agreed with the result provided in both Fig. 5.19 and Fig. 5.23.

5.4 Hg Jet Disruption by Energy Deposition

Figure 5.23 shows the disruption of Hg jet in magnetic fields as a function of total energy deposition and fit of model using Eqn. (5.10) up to 25 T. Figure 5.24 shows the disruption of Hg jet in magnetic fields as a function of fluence and fit of model using Eqn. (5.10) up to 25 T, where the fluence is defined as the normalized beam intensity by beam spot area $Tp/(\sigma_x \sigma y)$. Figure 5.25 shows the disruption of Hg jet in magnetic fields as a function of peak energy deposition and fit of model using Eqn. (5.10) up to 25 T. χ^2 values indicate comparison of goodness of fit for Fig. 5.23, Fig. 5.24, and Fig. 5.25, where the fit of model as a function of total energy deposition yields the lowest χ^2 value. The extent of disruption of jet is dominated by the distribution of energy deposition over the entire jet interacting with proton beam. Therefore, the total energy deposition is more likely to play a role in determining of the extent of disruption of Hg jet. The total energy deposition in magnetic fields is investigated. The total energy deposition depending on interacting number of protons at both 14 GeV and 24 GeV beam energy is calculated from Fig. 5.13 (b). Thus, Fig. 5.19 and Fig. 5.20 are combined as a function of total energy deposition, which shows the results of experiment in disruption length at a glance. As a final important result for experiment, Fig. 5.23 shows the disruption of Hg jet in magnetic fields as a function of total energy deposition and its extrapolation up to 25 T. The global fit with multi-variables for disruption length using the measured disruption length is:

$$L^{disruption} = a_1(E_p - (b_1 + b_2 B^{b_3}))^{\frac{1}{c_1 + c_2 B + c_3 B^2}}, \tag{5.18}$$

where E_p and B are energy deposition and magnetic field respectively. The parameterized values of coefficients and errors of the fit functions are given in Table 5.3. The threshold of disruption increases in 0.8 power of magnetic field, and it is 338 J of total energy deposition with no magnetic field. Also, the threshold of disruption is $\sim$ 10 J of peak energy deposition with no magnetic field, and it increases in 1.2 power of magnetic field. The disruption length approximately increases in square root power of total energy deposition with no magnetic field, but it is suppressed in $\sim \ 1/(2 + 0.04B)$ power of total energy deposition with magnetic field. Power consumption is dominated by the repetition rate. Thus, the capability to replace the disrupted jet determines the beam power. The optimal interaction length for the 24 GeV beam energy is in the region of 30 cm which corresponds to approximately 2 interaction length for Hg [41]. In Fig. 5.23, the disruption length in 15 T is less than 20 cm and the total energy deposition is $\sim$ 8000 J. According to Fig. 5.13 (b), approximately $6 \sim 8$ % of beam energy is deposited into Hg target. Therefore, $100 \sim 133$ kJ of beam energy can be recycled with a 70 Hz repetition rate for 20 m/s jet. The disruption length at 30×10^{12} protons with 24 GeV beam energy in a magnetic field of 15 T is less than 20 cm at 24 GeV beam energy in Fig. 5.20, thus preserving the 70 Hz beam repetition rate option. This result validates that a target system capable of supporting proton beams with powers of up to 8 MW, which is a key result for this experiment [41].

Table 5.1: Estimated 1 σ beam spot size at the target [17]. The beam spot size is plotted in Fig. 5.4.

1 (GeV/c)	**2** (Tp)	**3** -	**4** (mm.mrad)	**5** (mm)	**6** (mm)	**7** (mm.mrad)	**8** (mm)	**9** (mm)
14	1	14.925	0.0456	1.508193	1.5951	0.1047	0.1708	0.7178
14	5	14.925	0.1208	1.508193	1.7290	0.1453	0.1708	0.8391
14	10	14.925	0.2149	1.508193	1.8830	0.1961	0.1708	0.9695
14	15	14.925	0.3090	1.508193	2.0253	0.2469	0.1708	1.0844
14	20	14.925	0.4030	1.508193	2.1583	0.2977	0.1708	1.1883
14	25	14.925	0.4971	1.508193	2.2836	0.3485	0.1708	1.2837
14	30	14.925	0.5911	1.508193	2.4023	0.3993	0.1708	1.3726
24	1	25.586	0.0266	0.999405	1.0753	0.0610	0.1132	0.5444
24	5	25.586	0.0705	0.999405	1.1899	0.0848	0.1132	0.6376
24	10	25.586	0.1254	0.999405	1.3192	0.1144	0.1132	0.7377
24	15	25.586	0.1802	0.999405	1.4369	0.1440	0.1132	0.8257
24	20	25.586	0.2351	0.999405	1.5457	0.1737	0.1132	0.9052
24	25	25.586	0.2899	0.999405	1.6474	0.2033	0.1132	0.9783
24	30	25.586	0.3448	0.999405	1.7431	0.2329	0.1132	1.0463

1 : Beam momentum
2 : Beam intensity
3 : $\beta\gamma$
4 : Emittance, horizontal plane (1σ)
5 : $D_p\frac{\delta p}{p}$ (1σ), horizontal plane
6 : Beam size, horizontal plane (1σ)
7 : Emittance, vertical plane (1σ)
8 : $D_p\frac{\delta p}{p}$ (1σ), vertical plane
9 : Beam size, vertical plane (1σ)

Table 5.2: Measurement of vertical distance of jet centroid from magnetic axis and jet size for modeling in MARS code for the cases of sectionally elliptic and circular jet shape.

1 (T)	**2** (mm)	**3** (mm)	**4** (mm)	**5** (mm)	**6** (mm)	**7** (mm)	**8** (g/cm^3)	**9** (degree)	**10** -	**11** (cm)	**12** -
Elliptic jet shape											
0	7.11	4.46	4.28	5.01	8.65	2.9	13.55	62,80,90,100,118,179,242,260,270,280,298,360	12	2	50
5	7.1	4.52	3.7	4.38	8.4	3.0	13.55	62,80,90,100,118,179,242,260,270,280,298,360	12	2	50
10	6.57	4.08	3.66	3.71	7.95	3.15	13.55	62,80,90,100,118,179,242,260,270,280,298,360	12	2	50
15	5.45	3.6	3.24	3.11	9.05	2.76	13.55	62,80,90,100,118,179,242,260,270,280,298,360	12	2	50
Circular jet shape											
0	7.11	4.46	4.28	5.01	8.65	8.65	4.50	30,60,90,120,150,180,210,240,270,300,330,360	12	2	50
5	7.1	4.52	3.7	4.38	8.4	8.4	4.77	30,60,90,120,150,180,210,240,270,300,330,360	12	2	50
10	6.57	4.08	3.66	3.71	7.95	7.95	5.32	30,60,90,120,150,180,210,240,270,300,330,360	12	2	50
15	5.45	3.6	3.24	3.11	9.05	9.05	4.11	30,60,90,120,150,180,210,240,270,300,330,360	12	2	50

1 : Magnetic field
2 : Vertical distance at Viewport1
3 : Vertical distance at Viewport2
4 : Vertical distance at Viewport3
5 : Vertical distance at Viewport4
6 : Vertical radius of jet
7 : Horizontal radius of jet
8 : Hg density
9 : Azimuthal meshed angle
10 : Number of azimuthal mesh
11 : Axial meshed size
12 : Number of axial mesh

Table 5.3: Parameterized coefficients, its error, and statistics summary of fit function in figures.

Figure	**1**	**2**	**3**	**4**	**5**	**6**	**7**	**8**	**9**	**10**
5.12(a)	0.74078	0.03855	-0.06864	0.01598	0.50641	0.05307	-	-	1.48078	0.0158
5.12(b)	0.02228	8.60E-04	-1.09835	0.36388	0.0613	0.00759	-5.49E-04	1.62E-04	1.36185	0.01097
5.12(c)	0	0	4.10076	0.37658	-0.56357	0.01667	-	-	0.821	0.03034
5.12(d)	0.02814	0.00155	-1.11612	0.38081	0.05682	0.00729	-4.71E-04	1.41E-04	1.31199	0.01724
5.13(a)	0.06023	0.0073	0.80386	0.0105	-	-	-	-	1.5568	0.04025
5.13(b)	3.52931	0.3187	0.88872	0.01003	0.02553	0.01138	0.3758	0.16582	1.4208	0.02953
5.18(a)	1.43E-04	1.86E-05	647.56071	89.38814	-	-	-	-	-	-
5.18(b)(H8)	1.70E-04	3.77E-05	638.26526	126.57444	-	-	-	-	-	-
5.18(b)(H16)	1.39E-04	2.18E-05	680.28969	113.41709	-	-	-	-	-	-
5.23	0.00649	0.00348	338.24297	15.76037	115.38009	47.56862	0.82899	0.22938	1.92463	0.29005
5.24	0.09242	0.01457	1.56733	0.12275	0.66907	0.18602	0.71351	0.14258	1.59393	0.26343
5.25	0.04119	0.01018	9.93998	0.48595	0.98744	0.0975	1.21081	0.07709	1.74961	0.25844

Figure	**11**	**12**	**13**	**14**	**15**	**16**	**17**	**18**	**19**	
5.12(a)	-	-	-	-	32	28	14.67464	0.99691	0	
5.12(b)	0.91711	0.10273	-	-	32	26	256.24604	0.99909	0	
5.12(c)	-	-	-	-	32	29	29.85134	0.99371	0	
5.12(d)	1.96014	0.10329	-	-	32	26	271.9889	0.99904	0	
5.13(a)	-	-	-	-	32	29	95.44974	0.99168	0	
5.13(b)	-	-	-	-	32	27	3972.28821	0.99628	0	
5.18(a)	-	-	-	-	11	9	1.84	0.85406	0.056	
5.18(b)(H8)	-	-	-	-	5	3	1.97369	0.82927	0.1155	
5.18(b)(H16)	-	-	-	-	6	4	1.77779	0.88853	0.1301	
5.23	0.03939	0.01079	0	0	36	30	1.82037	0.88724	0.0039	
5.24	0.06785	0.03317	0	0	36	30	2.18746	0.86451	0.0001	
5.25	0.05655	0.02131	0	0	36	30	2.86591	0.82248	2.6019e-7	

1 : a1 value, **2** : a1 standard deviation, **3** : b1 value, **4** : b1 standard deviation, **5** : b2 value,

6 : b2 standard deviation, **7** : b3 value, **8** : b3 standard deviation , **9** : c1 value, **10** : c1 standard deviation,

11 : c2 value, **12** : c2 standard deviation, **13** : c3 value, **14** : c3 standard deviation, **15** : Number of points,

16 : Degrees of freedom, **17** : Reduced χ^2, **18** : Adjusted $\mathbf{R}^2$, **19** : χ^2 probability.

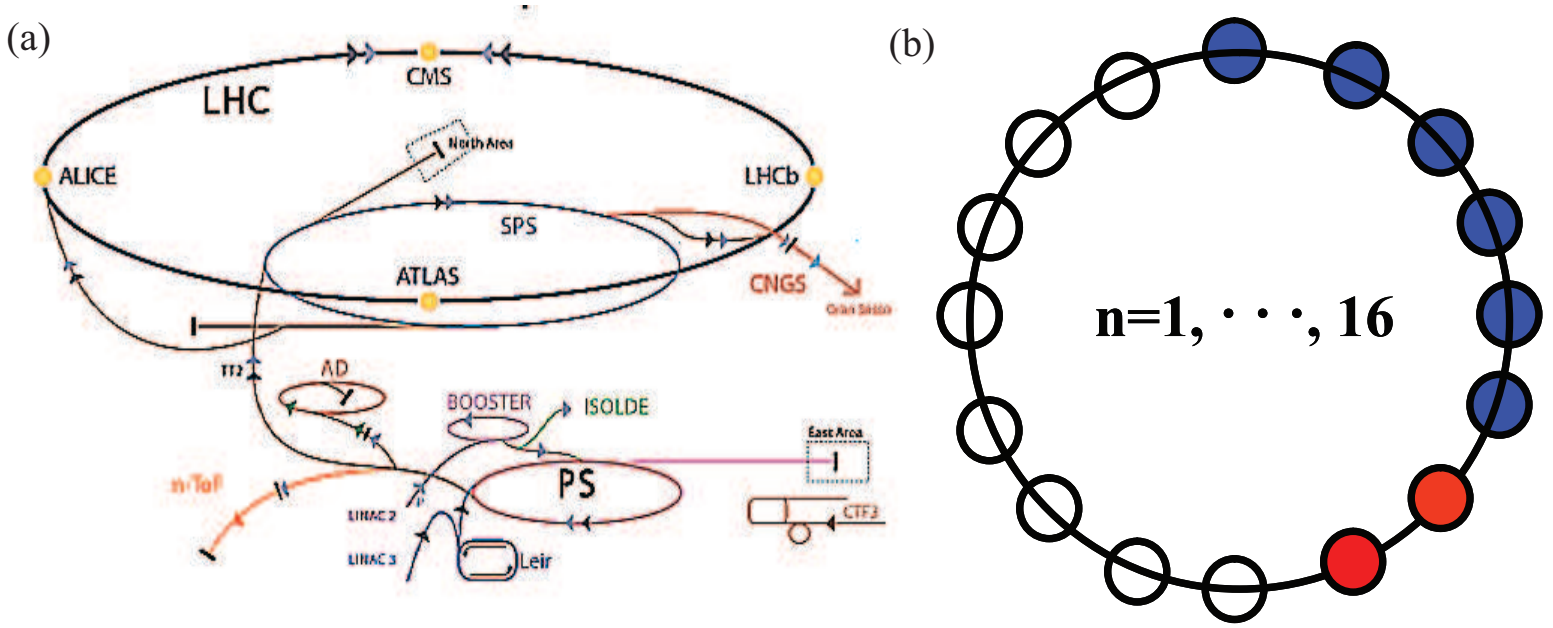

Figure 5.1: Infrastructures for experiment at CERN. a.) CERN accelerator complex and TT2 tunnel for experiment. b.) 16 harmonics of beam extraction in proton synchrotron.

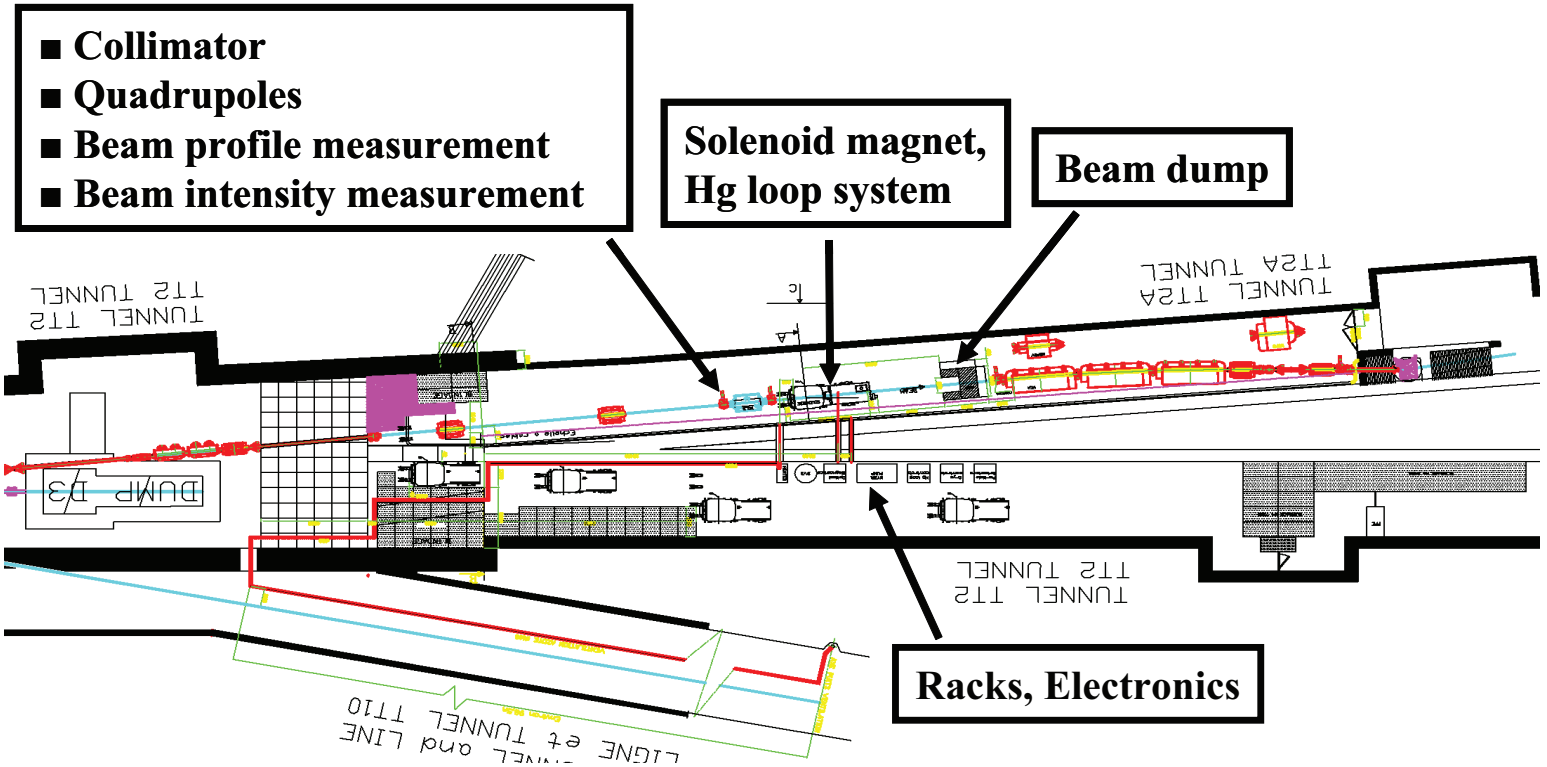

Figure 5.2: Installation of integrated experimental components in tunnel TT2/TT2A for Hg target experiment. Extracted proton beam comes from left to right in tunnel TT2A.

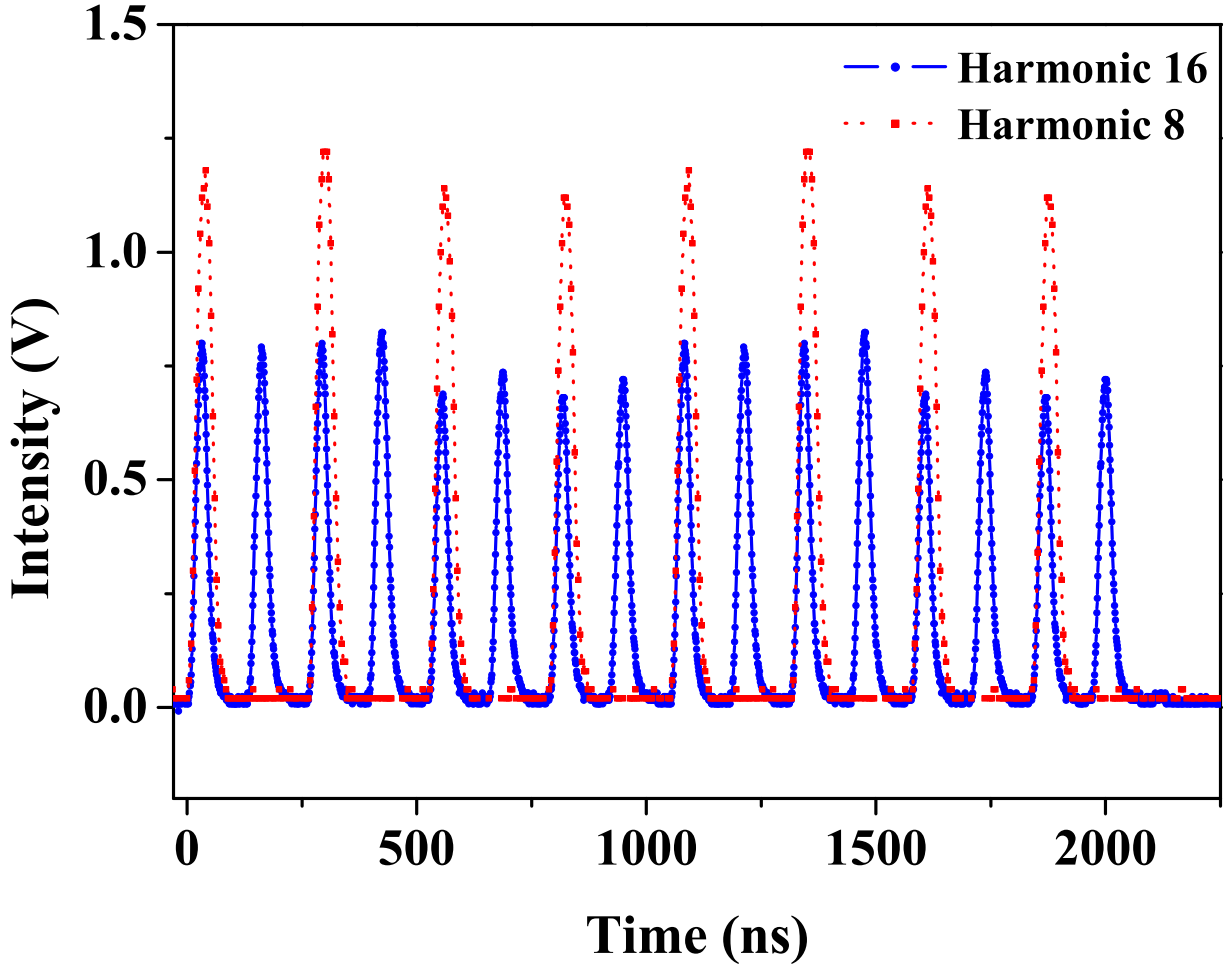

Figure 5.3: Proton beam pulse structure of harmonic 8 and harmonic 16 in 6 Tp with 14 GeV. Tp=10^{12} protons.

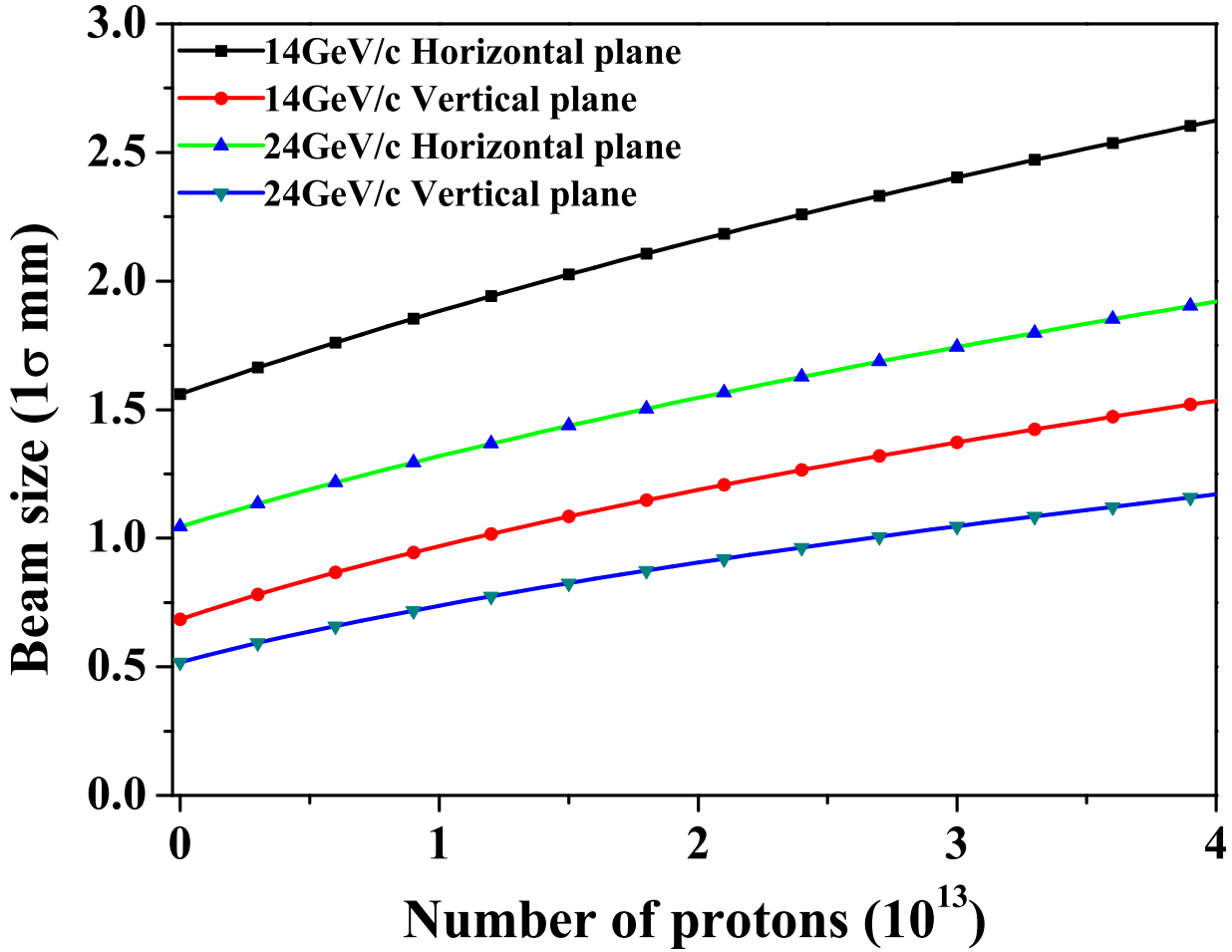

Figure 5.4: 1 σ proton beam size at the center of magnet by optics [17]. The beam spot size is given in Table 5.1.

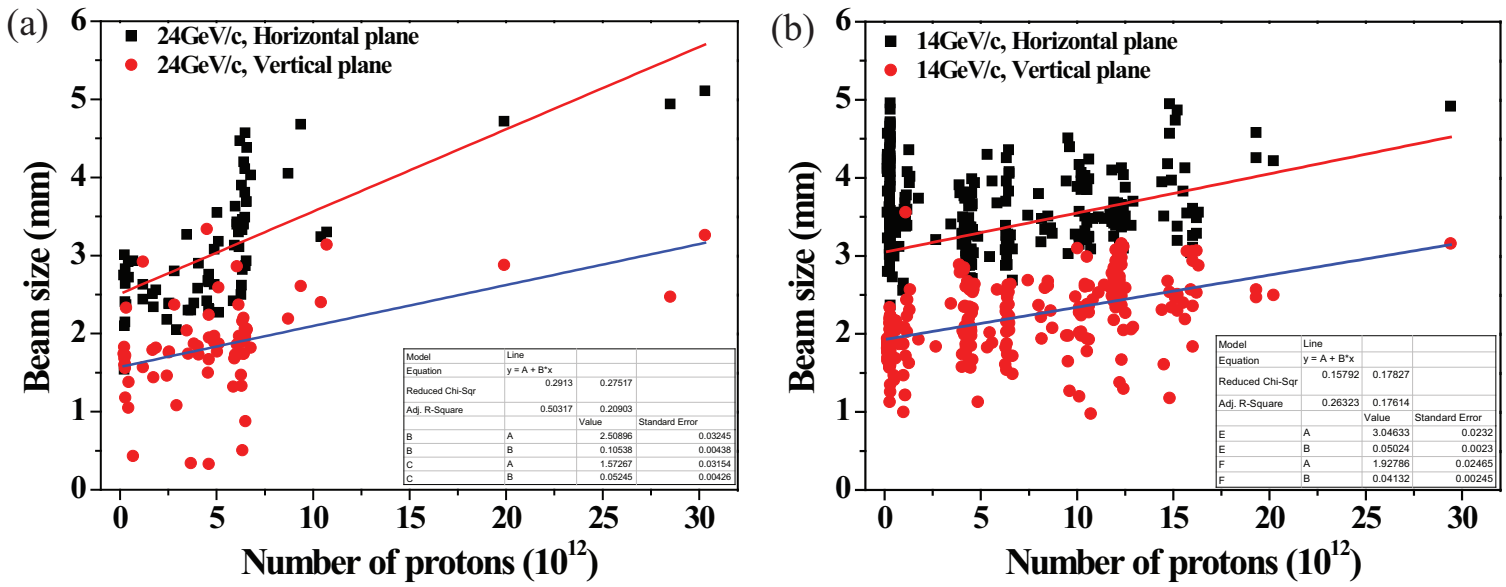

Figure 5.5: 1 σ proton beam size by camera screen monitor [85]. a.) 14 GeV beam. b.) 24 GeV beam.

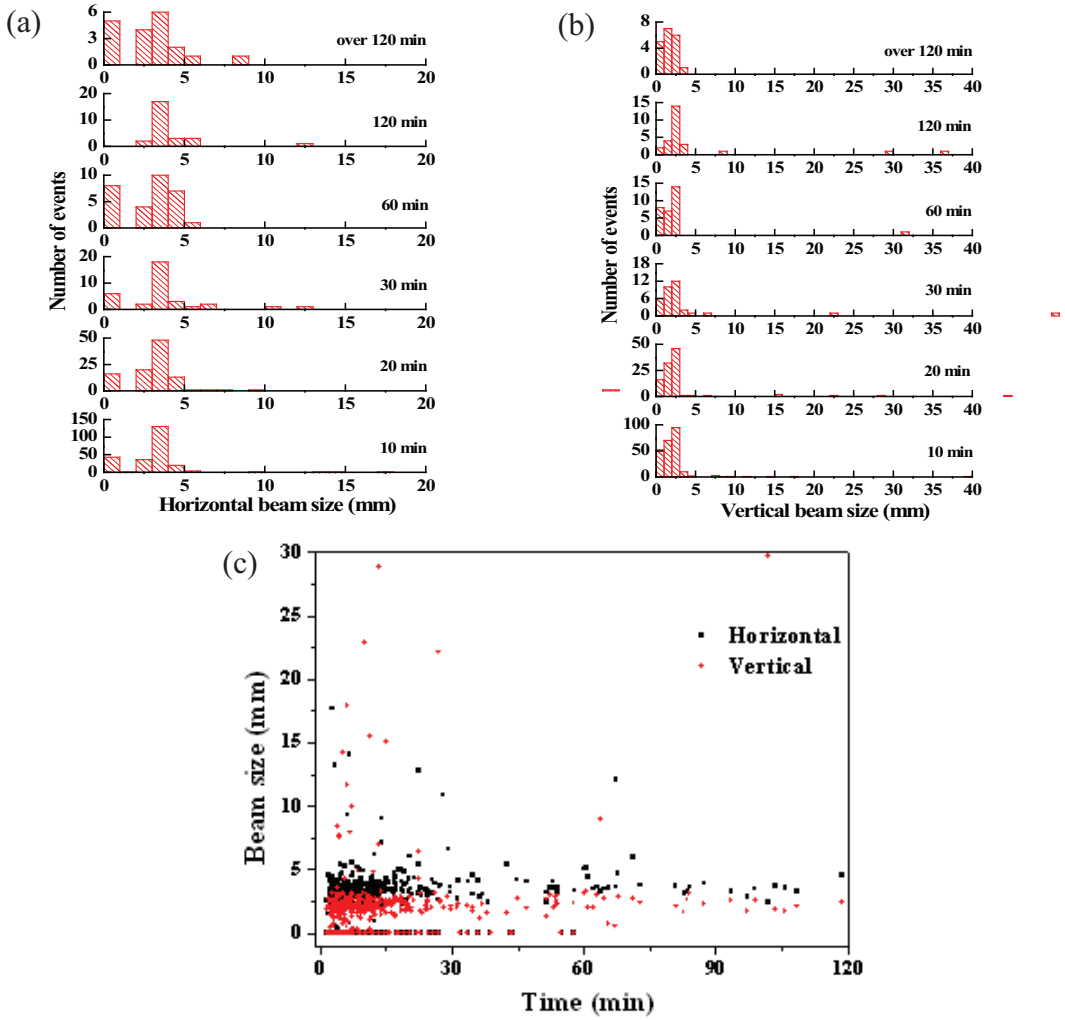

Figure 5.6: Beam size measured by phosphor screen monitor as a function of recorded time interval between each beam shot. a.) Histogram of beam size in horizontal plane. b.) Histogram of beam size in vertical plane. c.) Beam size distribution.

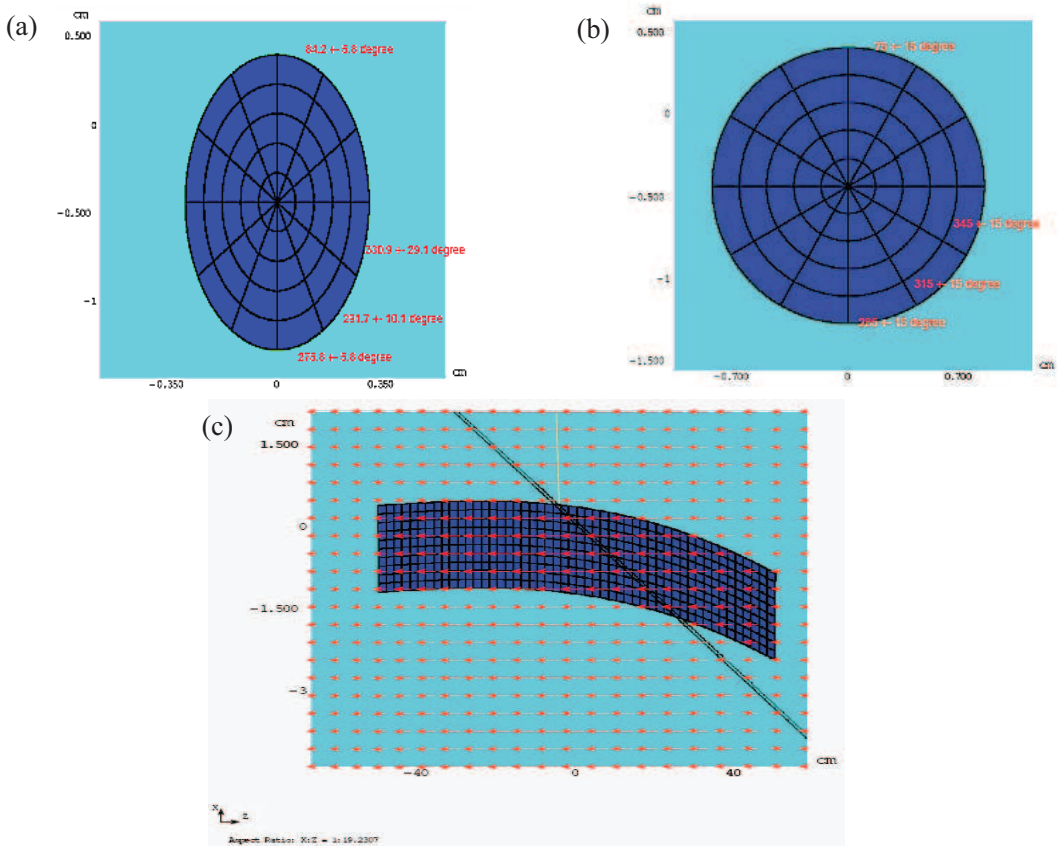

http://www.hep.princeton.edu/~mcdonald/mumu/target/Striganov/edep-grav.pdf

Figure 5.7: Modeling in MARS code for energy deposition calculation [89]. a.) Sectional view of elliptic jet. b.) Sectional view of circular jet. c.) Side view of Hg jet interacting with proton beam. Arrow indicates the direction and strength of magnetic field.

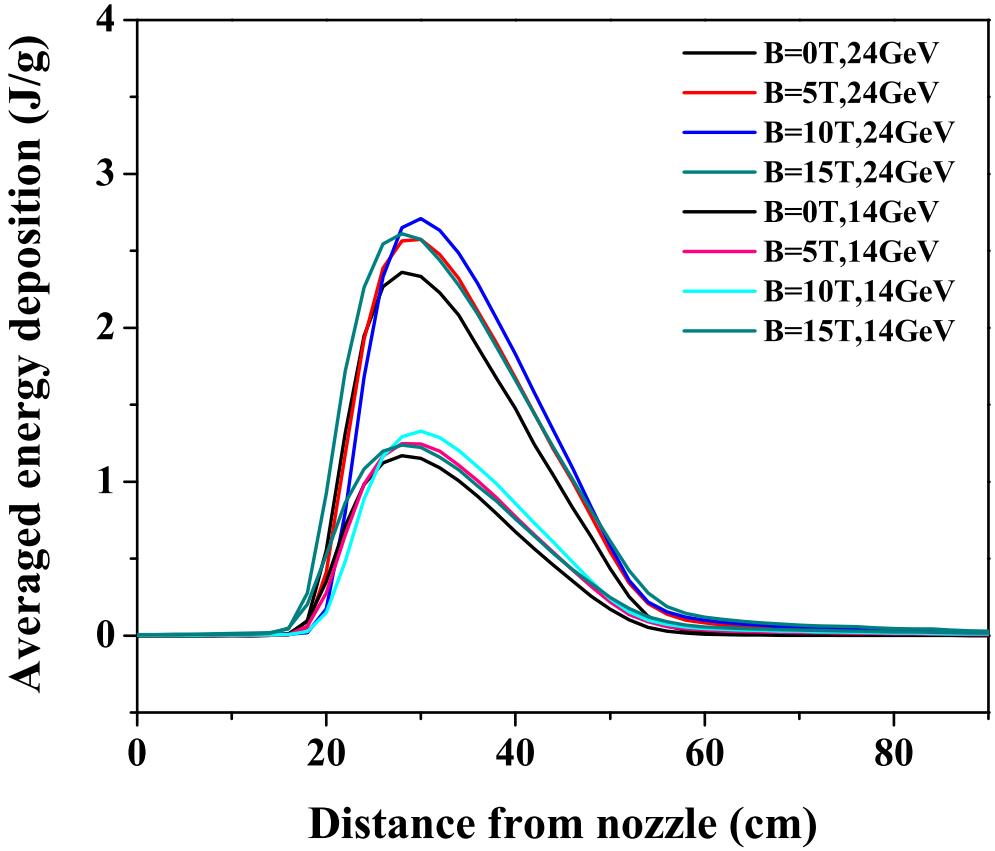

http://www-ap.fnal.gov/~strigano/merit/edep_in_target/gravity/24gev-beam-updated/ellipse/new/
http://www-ap.fnal.gov/~strigano/merit/edep_in_target/gravity/24gev-beam-updated/ellipse/

Figure 5.8: Influence of magnetic field on the energy deposition distribution to Hg jet. Beam intensity is 2 Tp and energy deposition in J/g is averaged using Eqn. (5.6).

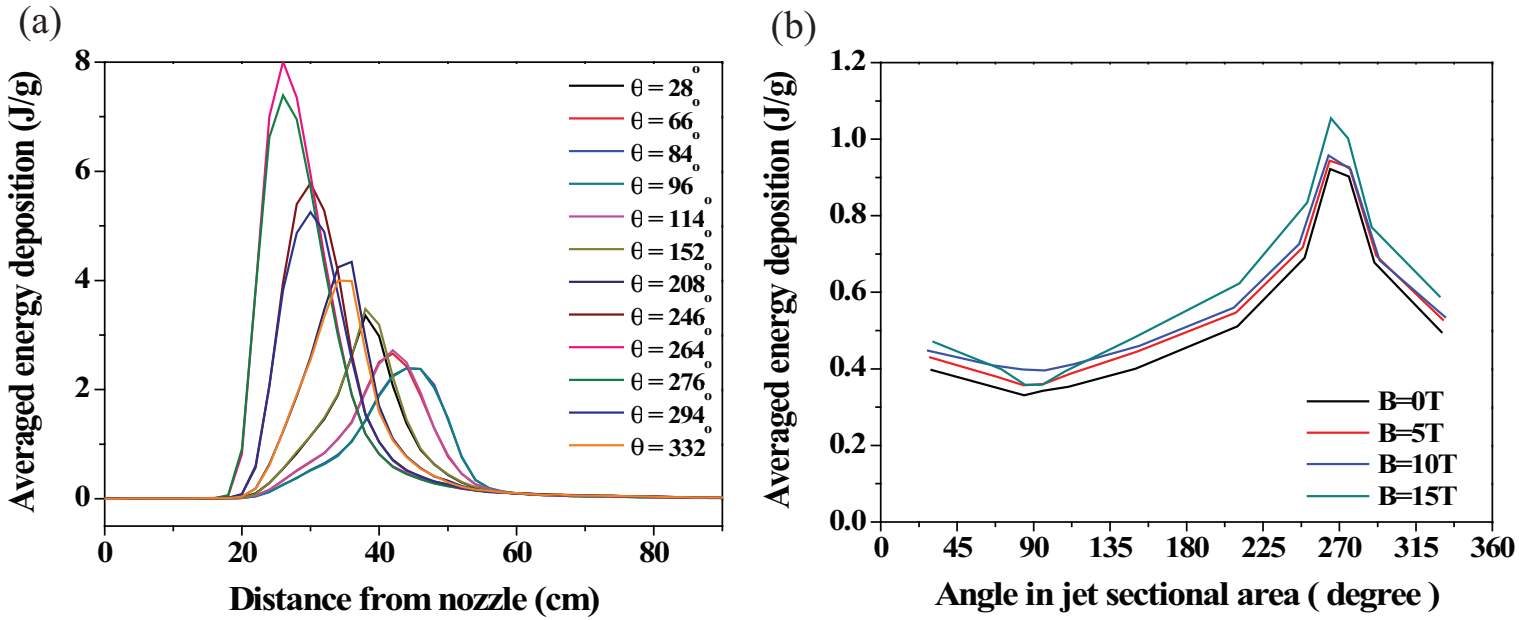

http://www-ap.fnal.gov/~strigano/merit/edep_in_target/gravity/24gev-beam-updated/ellipse/new/
http://www-ap.fnal.gov/~strigano/merit/edep_in_target/gravity/24gev-beam-updated/ellipse/

Figure 5.9: Azimuthal energy deposition distribution along jet axis interacting with 24 GeV proton beam. Beam intensity is 2 Tp and magnetic field is 10 T. a.) Along jet axis. Energy deposition in J/g is averaged using Eqn. (5.8). b.) Along azimuthal angle in jet cross section. Energy deposition in J/g is averaged using Eqn. (5.9).

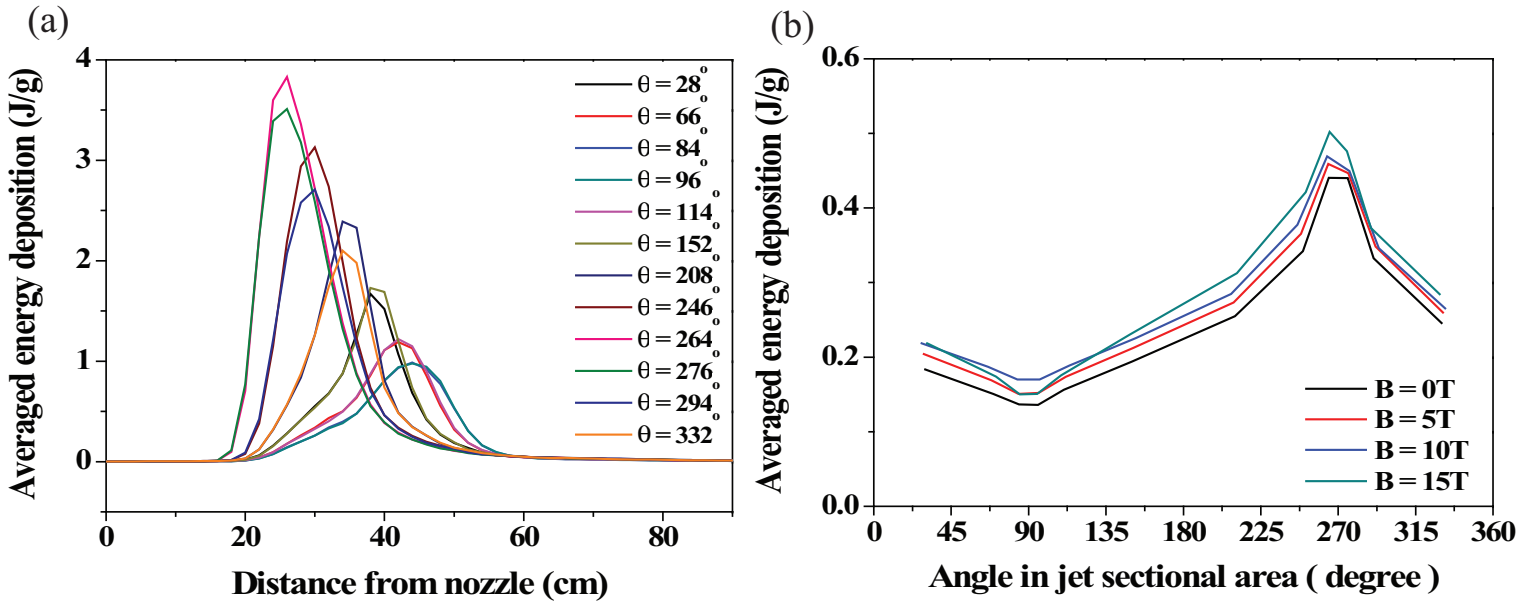

http://www-ap.fnal.gov/~strigano/merit/edep_in_target/gravity/24gev-beam-updated/ellipse/new/
http://www-ap.fnal.gov/~strigano/merit/edep_in_target/gravity/24gev-beam-updated/ellipse/

Figure 5.10: Azimuthal energy deposition distribution along jet axis interacting with 14 GeV proton beam. Beam intensity is 2 Tp and magnetic field is 10 T. a.) Along jet axis. Energy deposition in J/g is averaged using Eqn. (5.8). b.) Along azimuthal angle in jet cross section. Energy deposition in J/g is averaged using Eqn. (5.9).

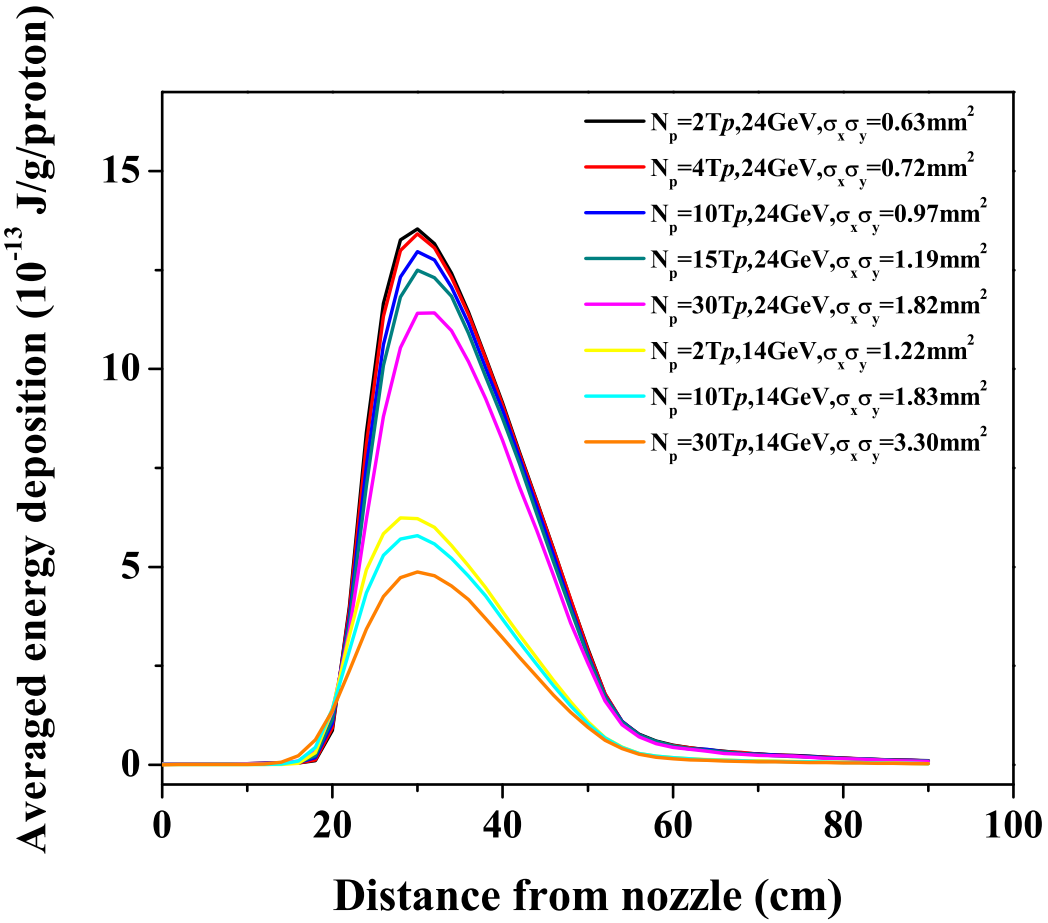

http://www-ap.fnal.gov/~strigano/merit/edep_in_target/gravity/24gev-beam-updated/ellipse/new/
http://www-ap.fnal.gov/~strigano/merit/edep_in_target/gravity/24gev-beam-updated/ellipse/

Figure 5.11: Energy deposition distribution per proton according to the variation of beam spot size along jet axis. Magnetic field is 5 T and energy deposition in J/g is averaged using Eqn. (5.6). $\sigma_x\sigma_y$ is calculated from Fig. 5.4.

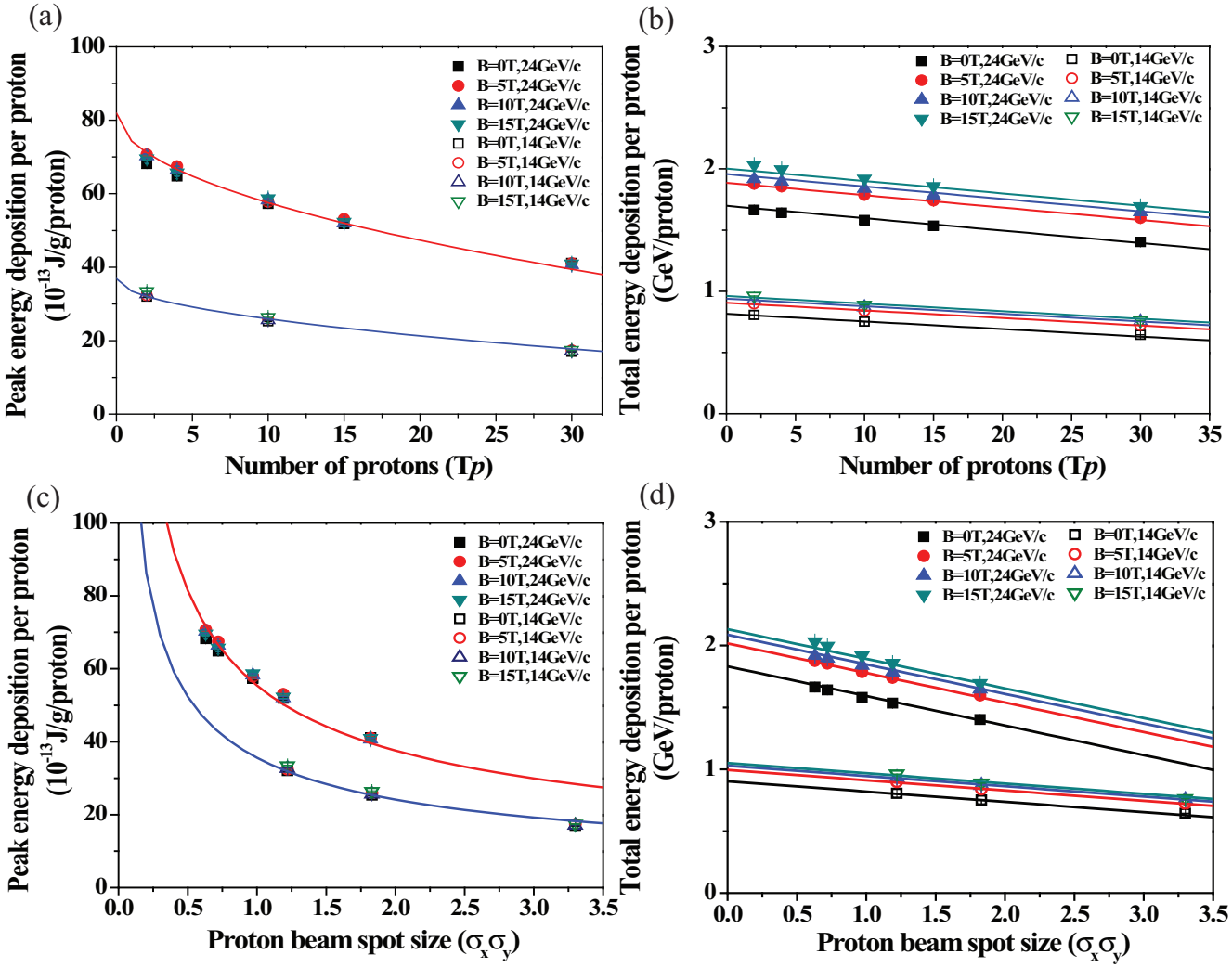

Figure 5.12: Simulation of peak energy deposition per proton and total energy deposition per proton according to the beam spot size and beam intensity. Fits of model fit to Striganov's calculation results. Eqn. (5.10) and Eqn. (5.11) are used for fit of model of peak energy deposition and total energy deposition, respectively. a.) Peak energy in J/g per proton by beam intensity. b.) Total energy in J/g per proton by beam intensity. c.) Peak energy in J/g per proton by beam spot size. d.) Total energy in J/g per proton by beam spot size.

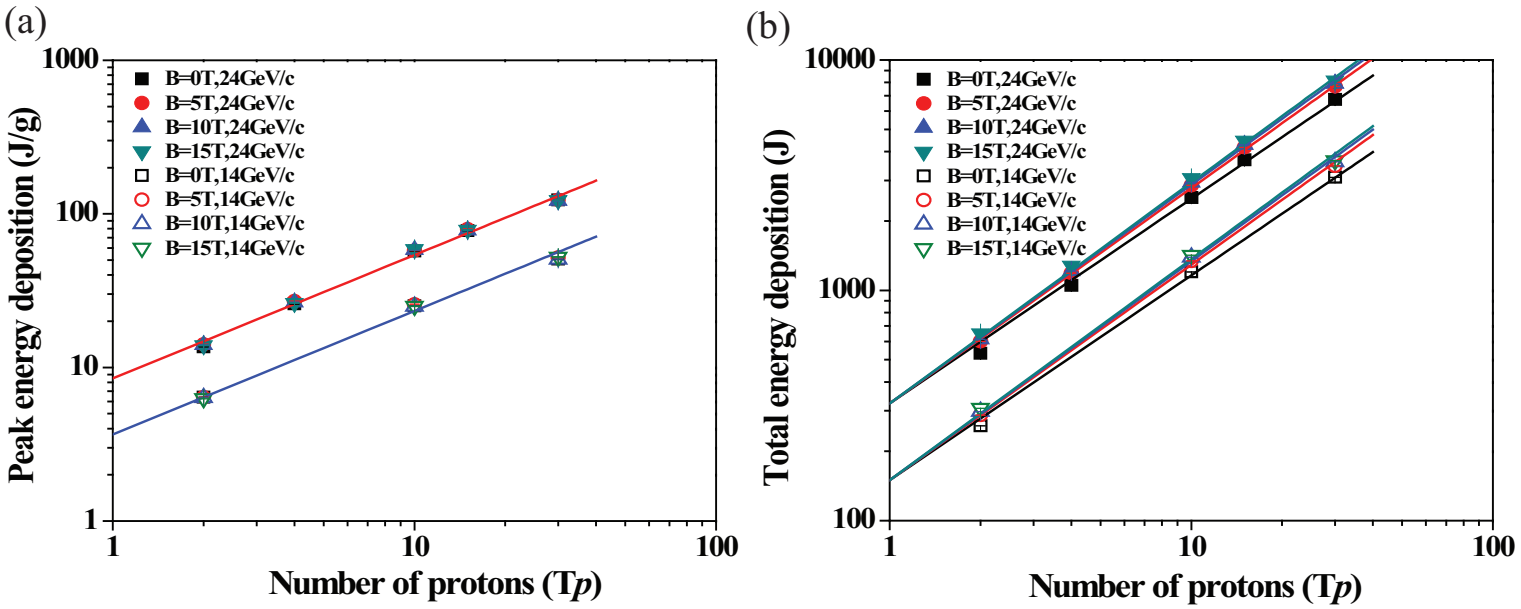

Figure 5.13: Simulation of peak energy deposition and total energy deposition in total number of protons. Fits of model fit to Striganov's calculation results. a.) Peak energy deposition in J/g and fit of model using Eqn. (5.12). b.) Total energy deposition in J and fit of model using Eqn. (5.13).

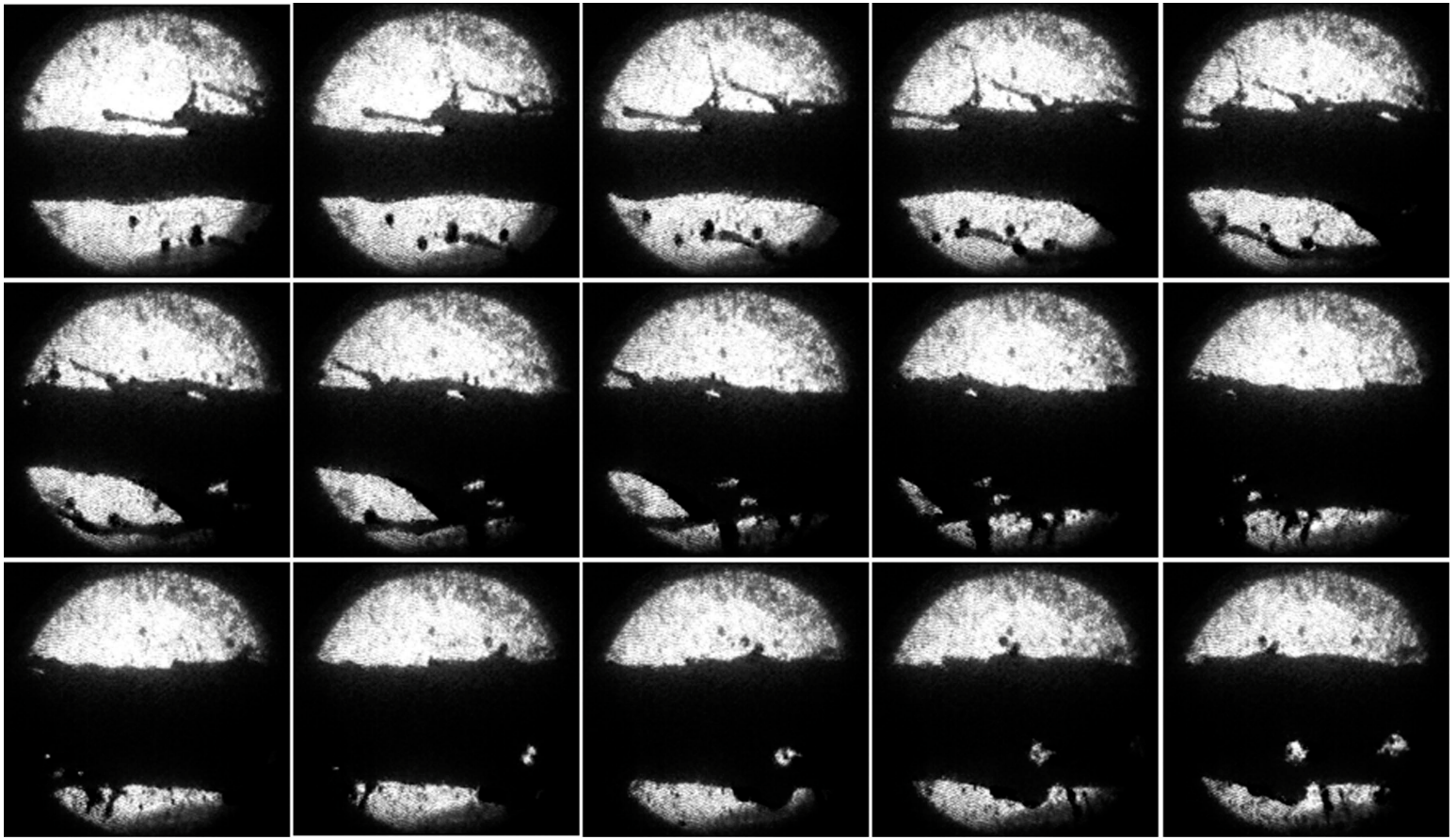

Figure 5.14: Photographs of the Hg jet interaction with 16 Tp, 14 GeV proton beam in 5 T. Captured at Viewport 3 at 500 μs frame rate (continued).

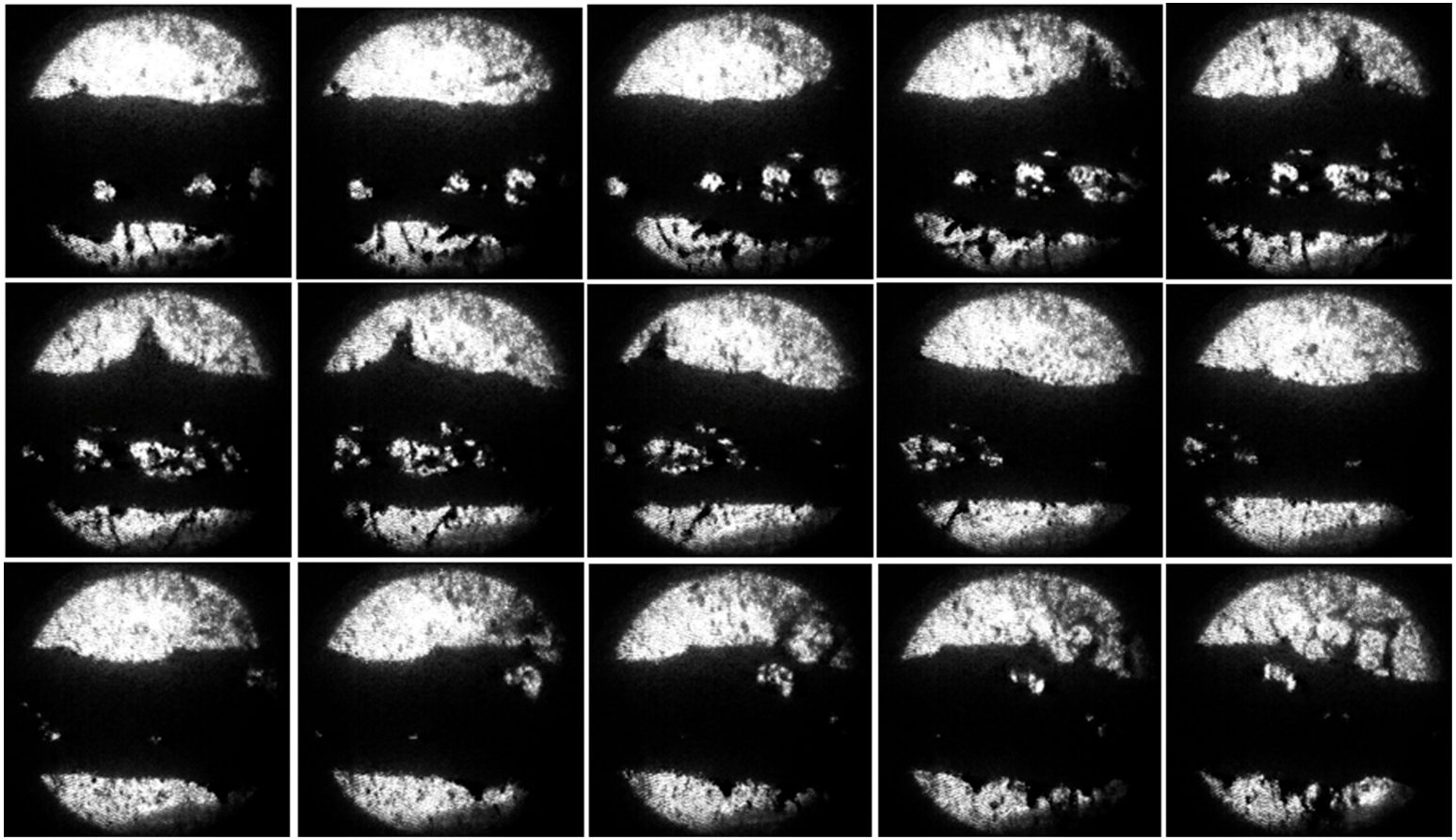

Figure 5.14: Photographs of the Hg jet interaction with 16 Tp, 14 GeV proton beam in 5 T. Captured at Viewport 3 at 500 μs frame rate (continued).

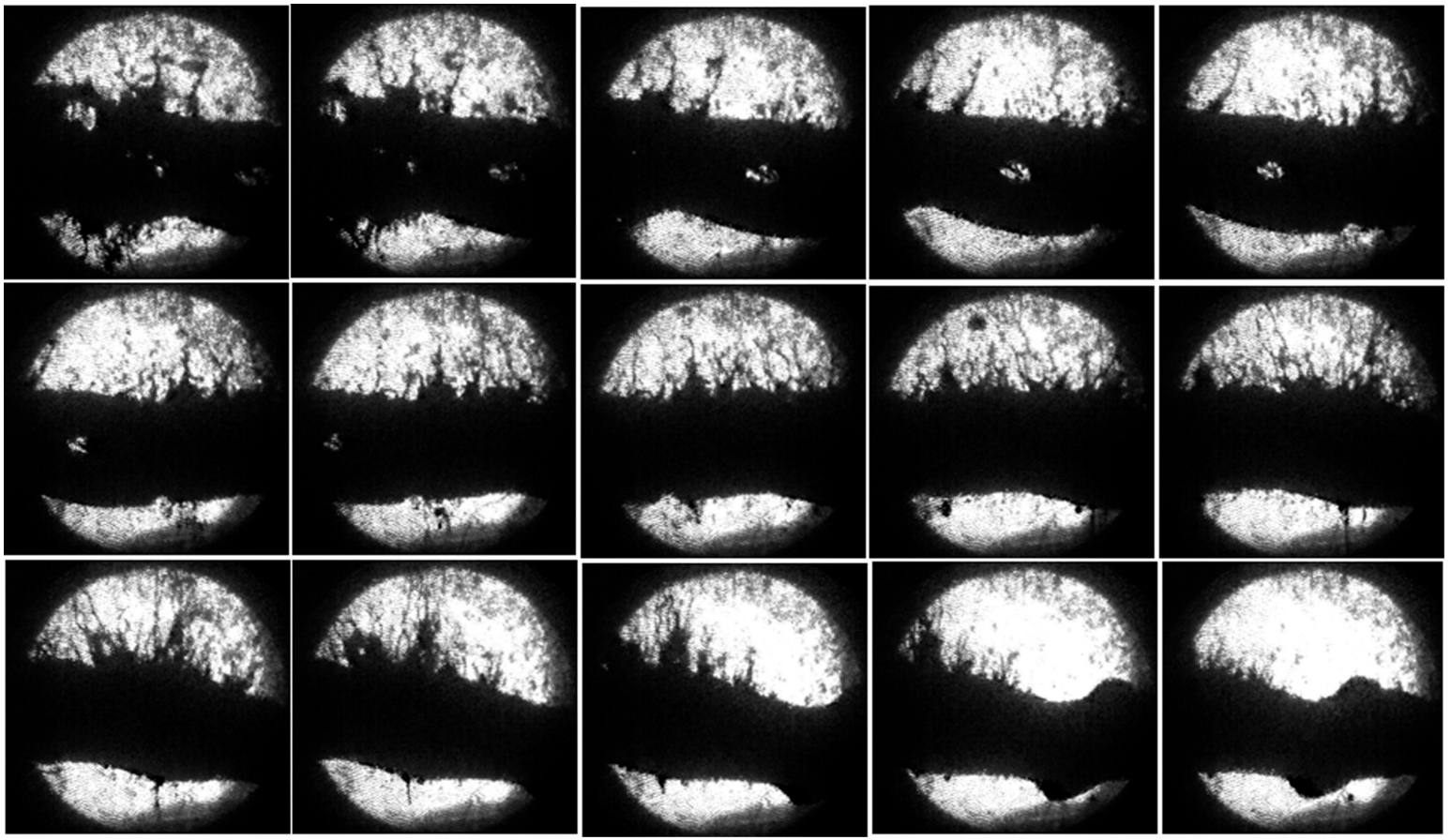

Figure 5.14: Photographs of the Hg jet interaction with 16 Tp, 14 GeV proton beam in 5 T. Captured at Viewport 3 at 500 μs frame rate.

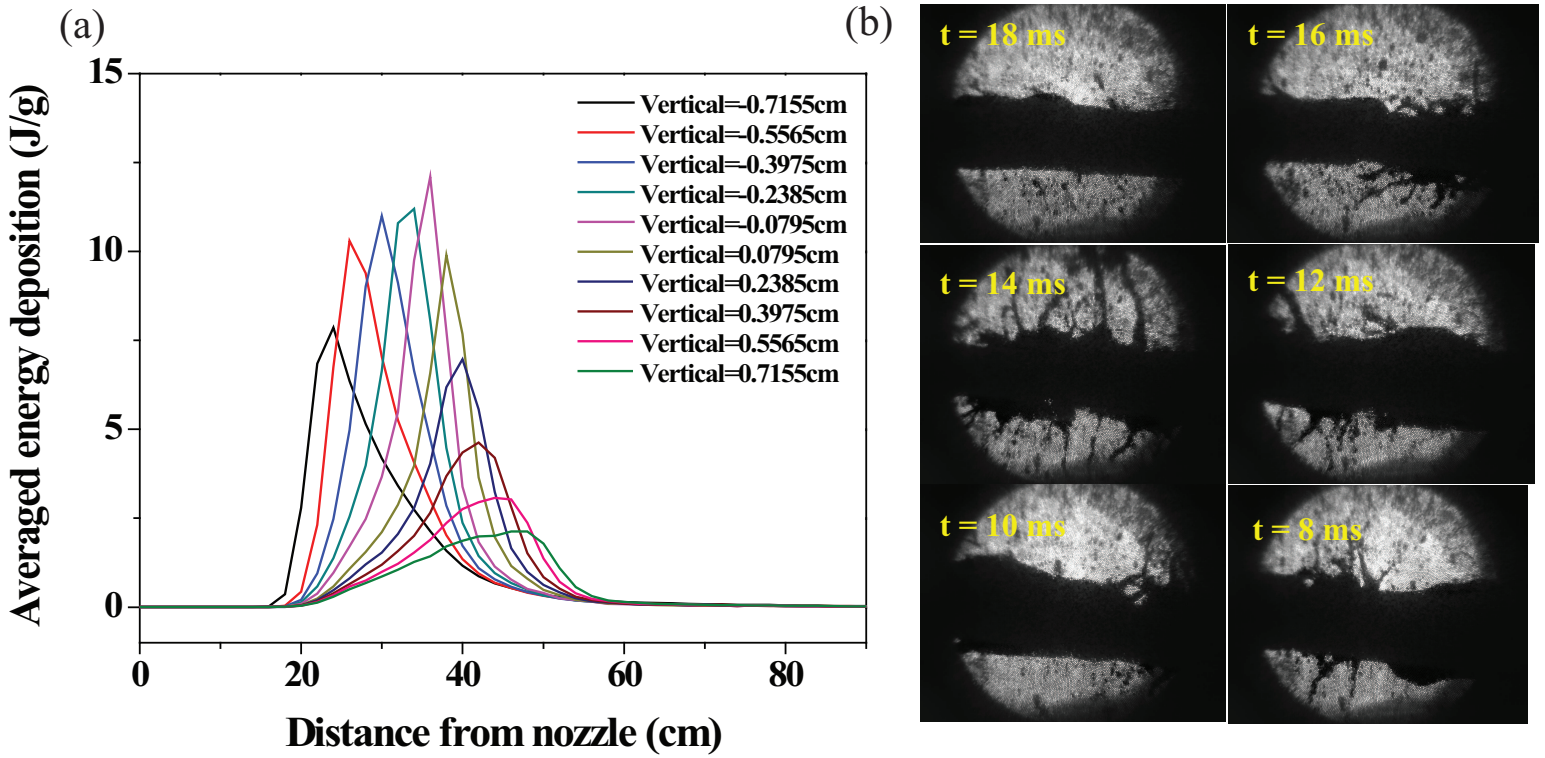

Figure 5.15: Qualitative comparison of the jet response by interaction of low intensity (3 Tp) of 24 GeV beam in 5 T. a.) Calculated averaged energy deposition using Eqn. (5.15) according to the vertical distance from jet center. b.) Observation of jet response by captured image.

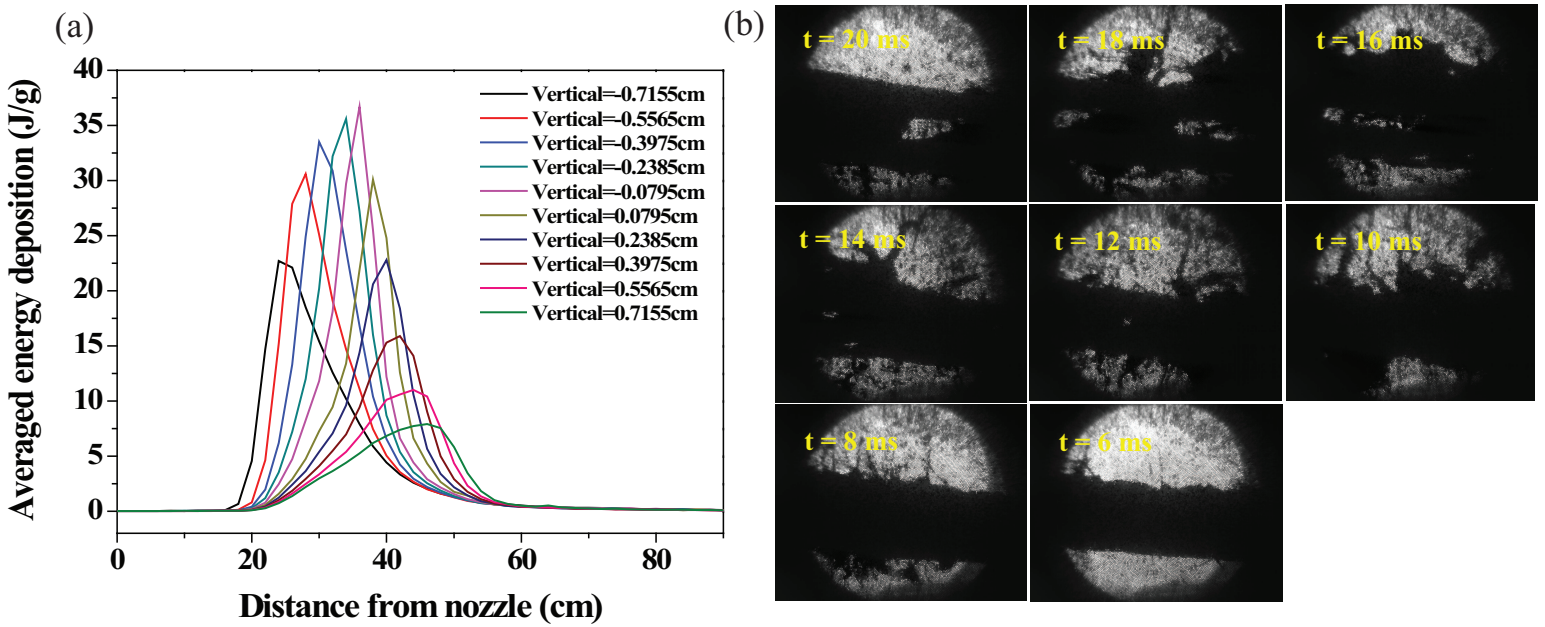

Figure 5.16: Qualitative comparison of the jet response by interaction of high intensity (10 Tp) of 24 GeV beam in 10 T. a.) Calculated averaged energy deposition using Eqn. (5.15) according to the vertical distance from jet center. b.) Observation of jet response by captured image.

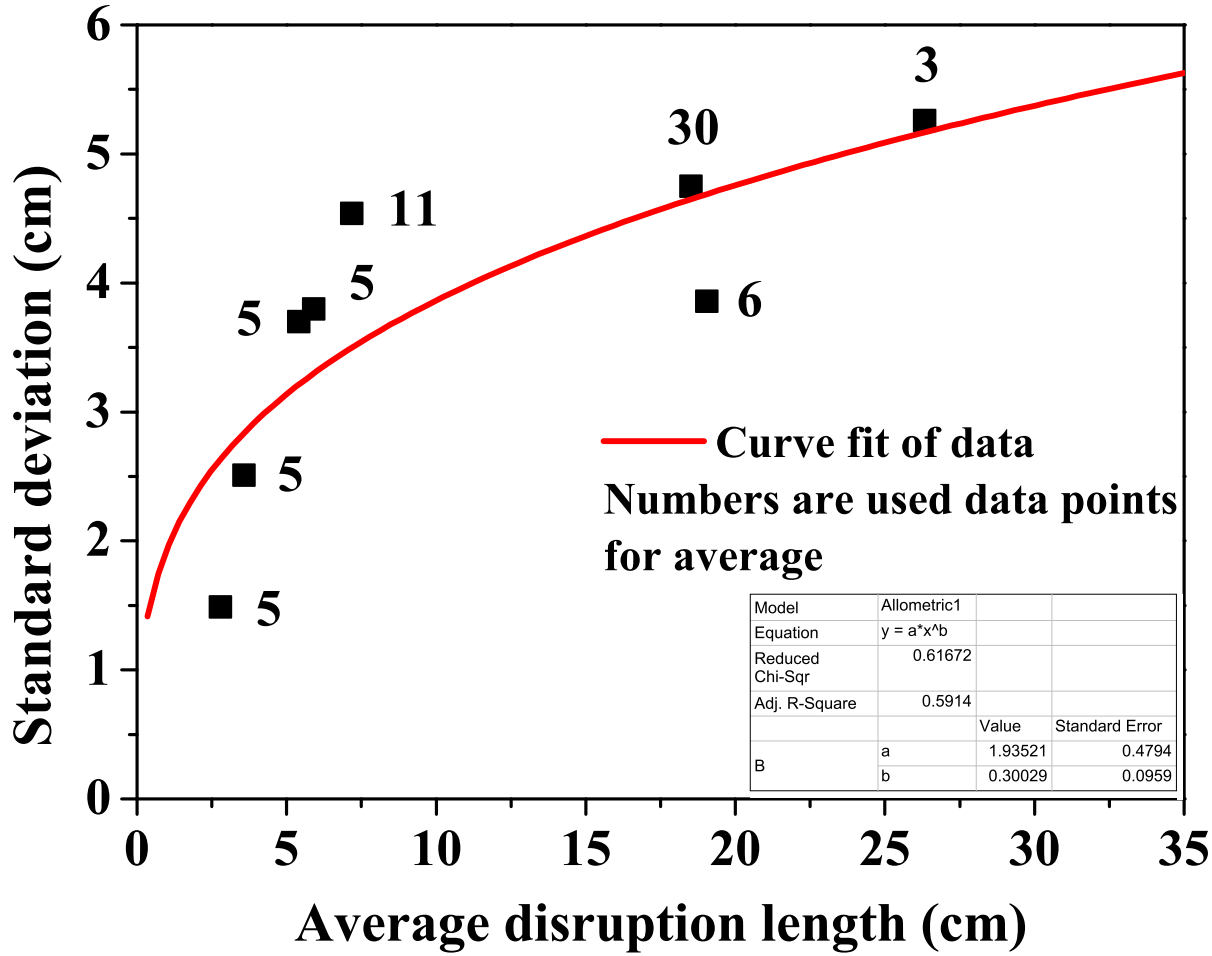

Figure 5.17: Standard deviation of disruption length as a function of disruption length and fit of model. The fitted curve is $\sigma_{disruption} = 1.9352\ \mathrm{L}_{disruption}^{0.3}$.

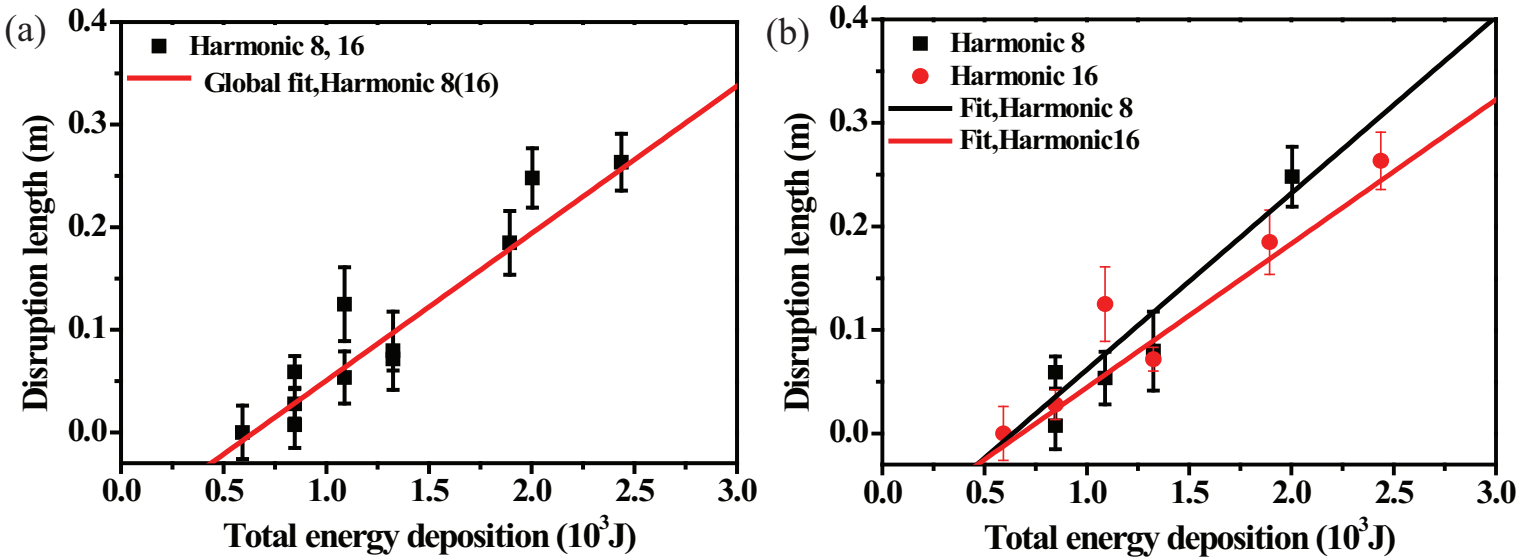

Figure 5.18: Disruption length of Hg jet depending on the beam pulse structure as a function of 14 GeV beam intensity in 5 T. a) Global fit of harmonic 8 and 16 using Eqn. (5.16). b.) Independent fit of harmonic 8 and 16 using Eqn. (5.16).

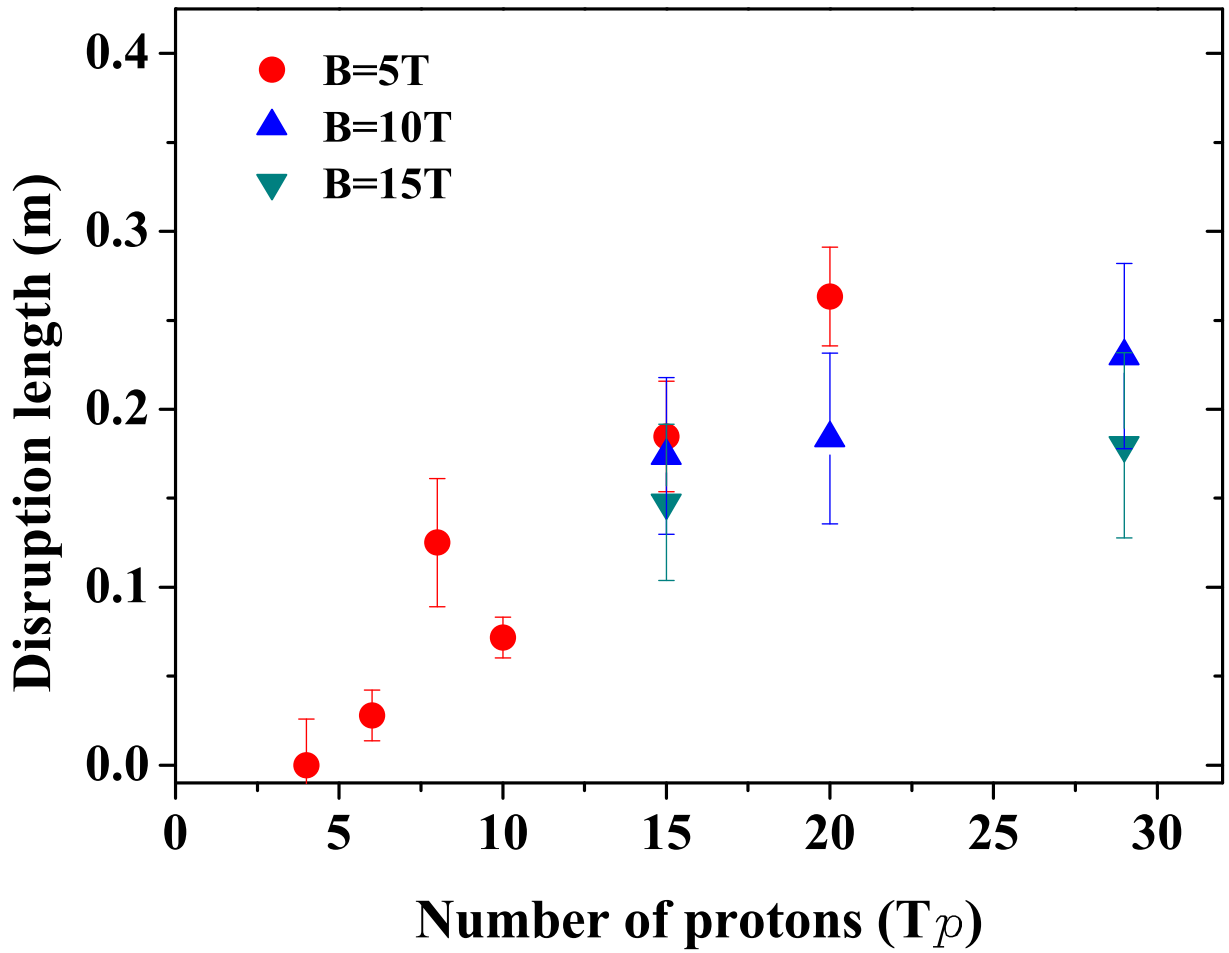

Figure 5.19: Disruption length of Hg jet as a function of 14 GeV beam intensity and magnetic field. Harmonic 16 with 16 bunches is used.

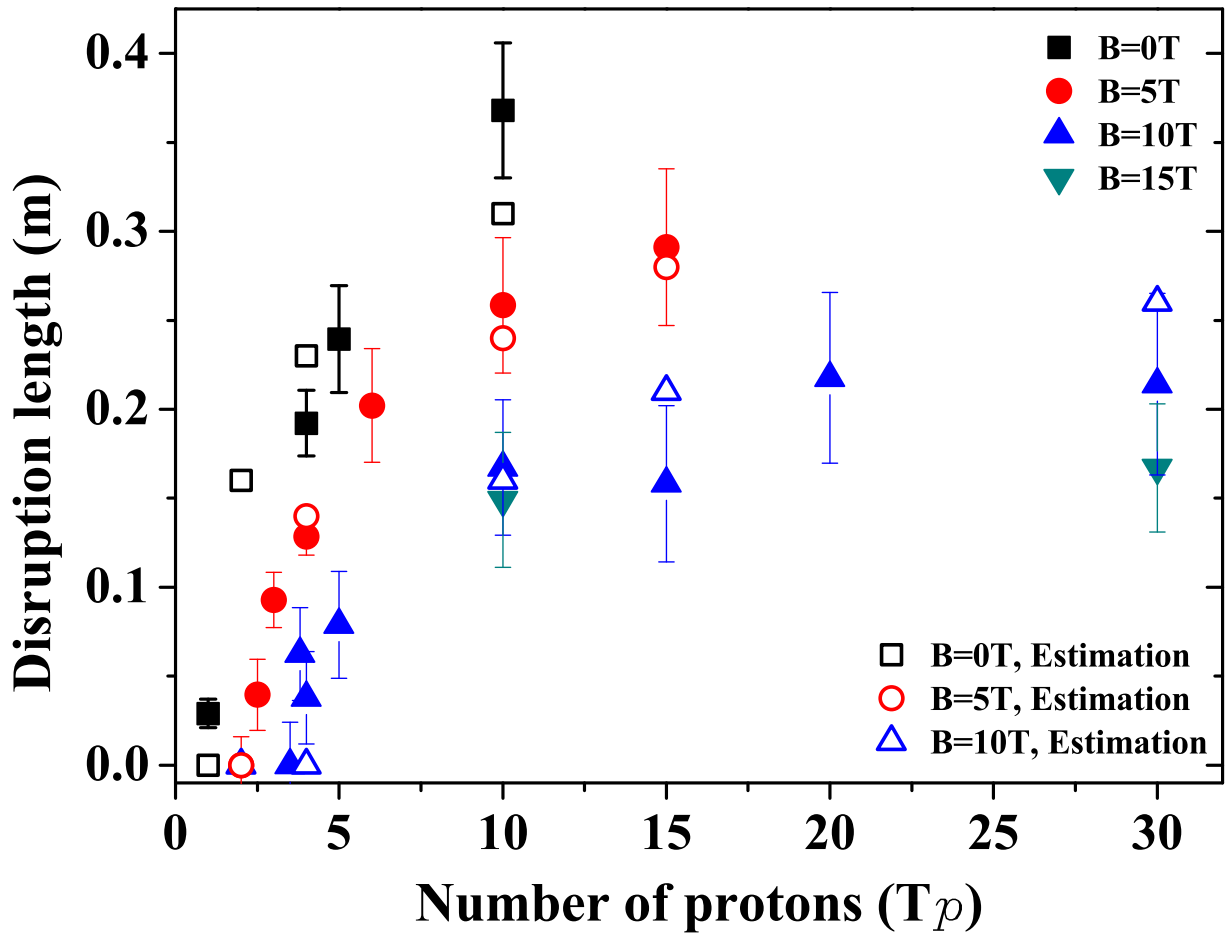

Figure 5.20: Disruption length of Hg jet and its estimation as a function of 24 GeV beam intensity and magnetic field. The estimation of disruption length by energy deposition calculation is compared by using disruption model of Eqn. (5.17).

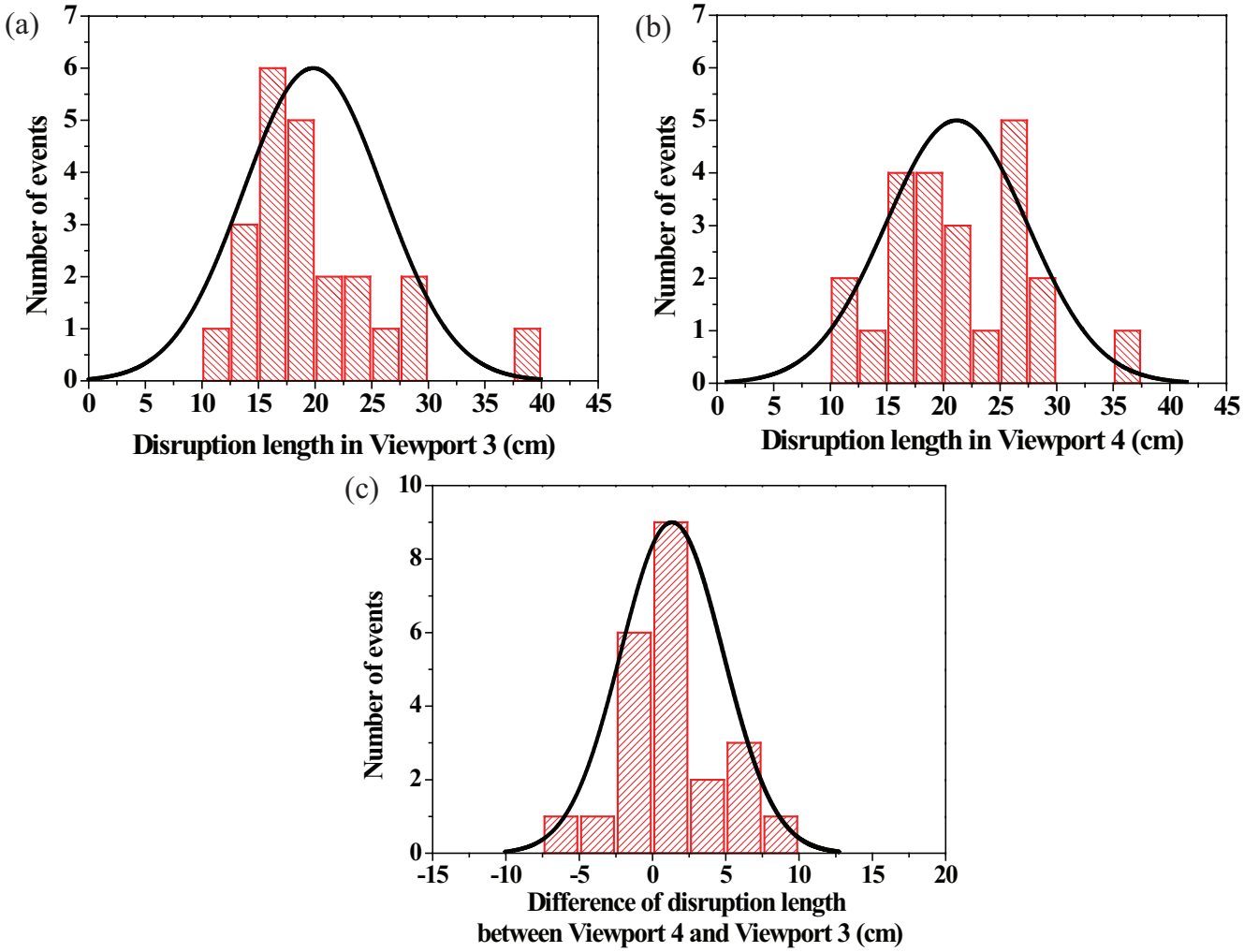

Figure 5.21: Comparison of disruption length measurement at Viewport 3 and Viewport 4. a) Disruption length at Viewport 3. b.) Disruption length at Viewport 4. c.) Difference of the disruption length at Viewport 3 and Viewport 4.

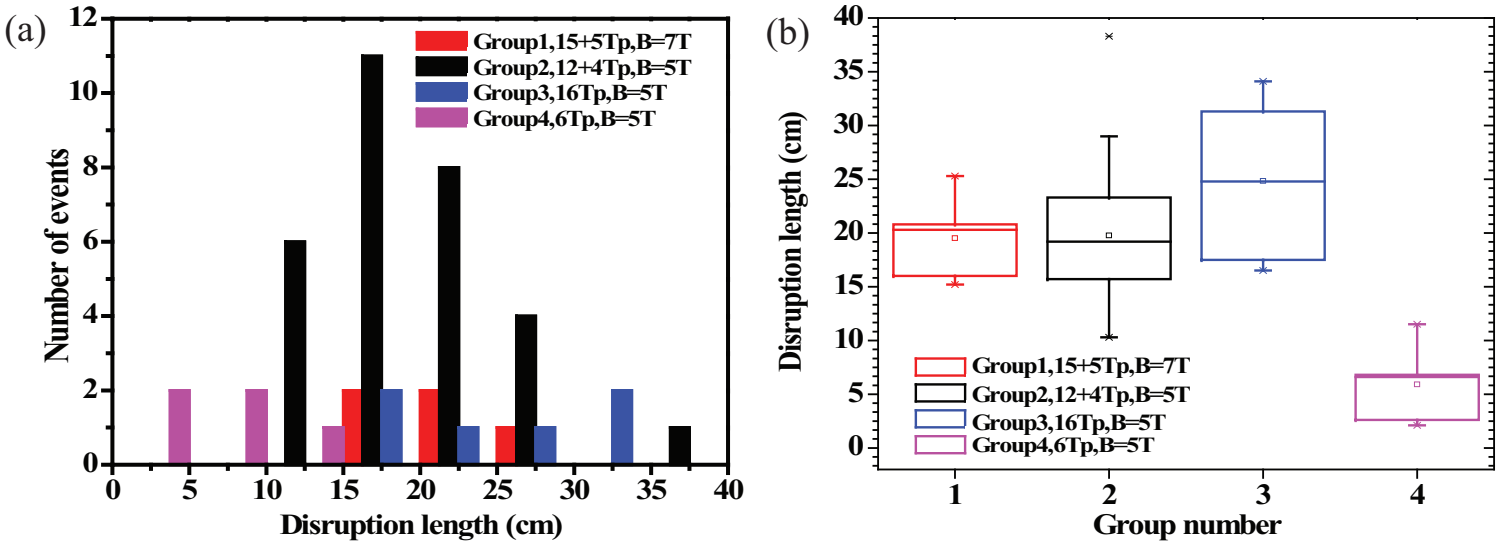

Figure 5.22: Multiple disruption length measurements in same condition. Pump-probe conditions with harmonic 8 and 16 bunches are used. The conditions of each group in pump-probe events are given in Table A.4. a.) Histogram of disruption length in each group. b.) Disruption length of each group.

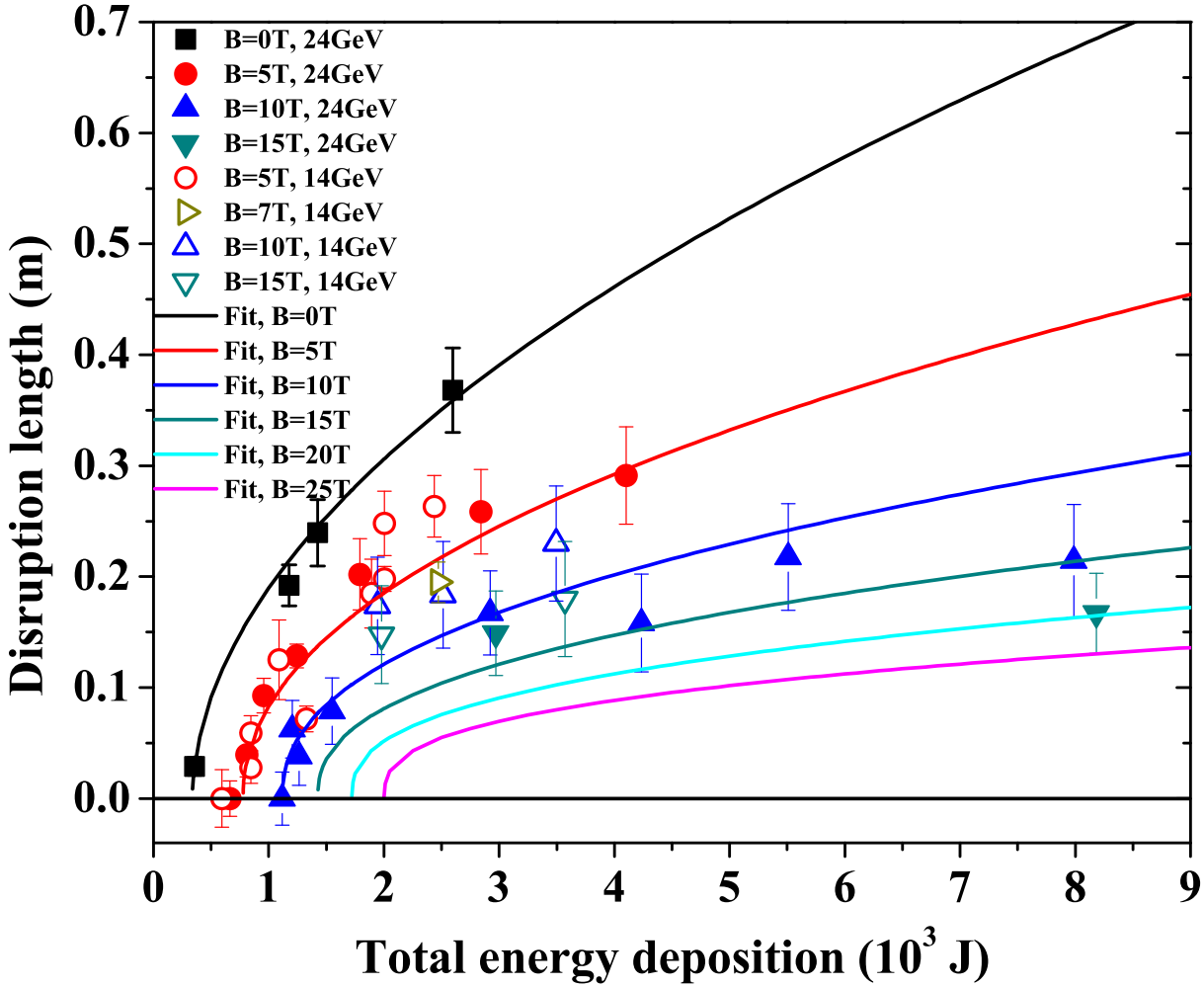

Figure 5.23: Disruption of Hg jet in various magnetic fields as a function of total energy deposition and fit of model using Eqn. (5.18).

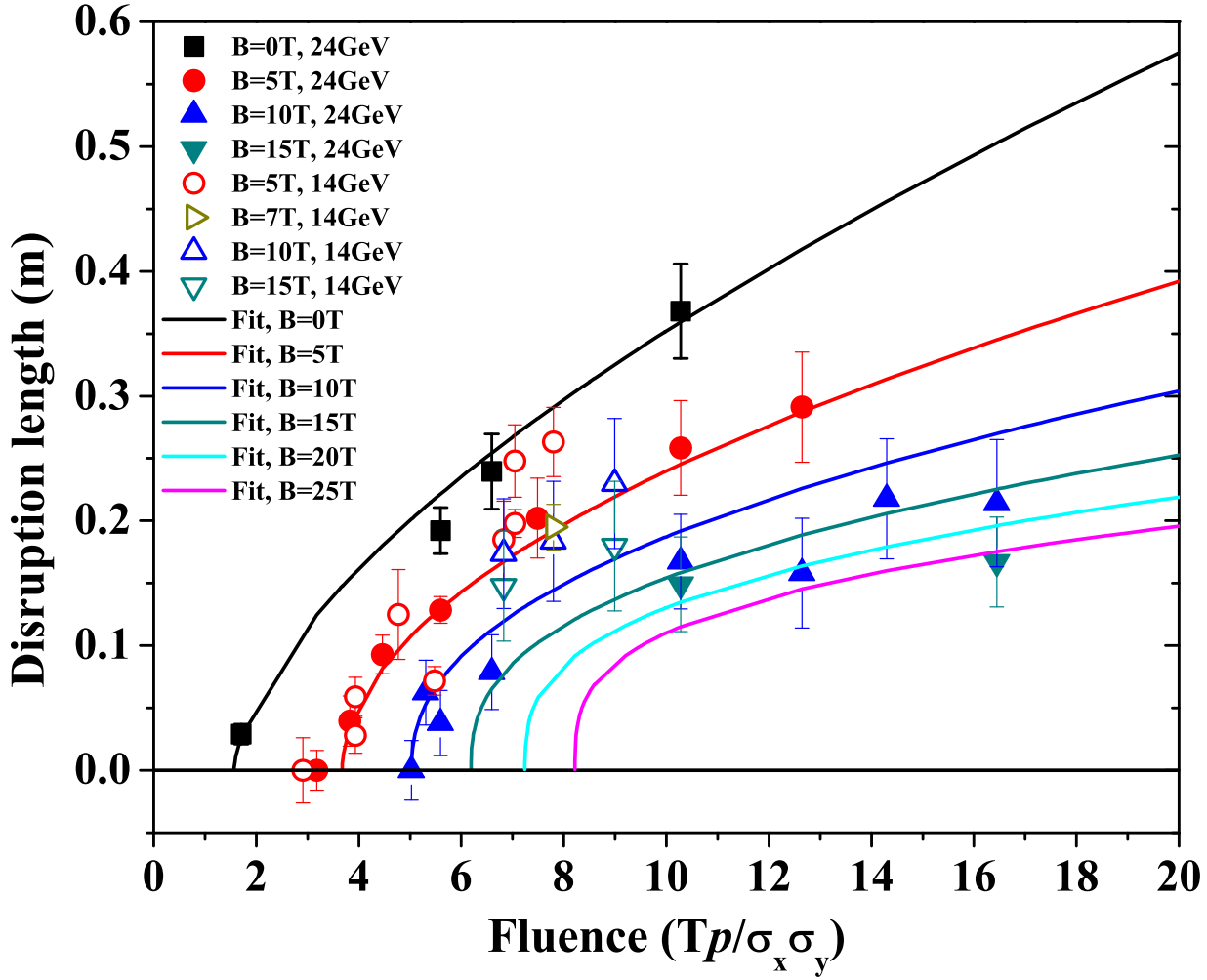

Figure 5.24: Disruption of Hg jet in various magnetic fields as a function of fluence and fit of model using Eqn. (5.18).

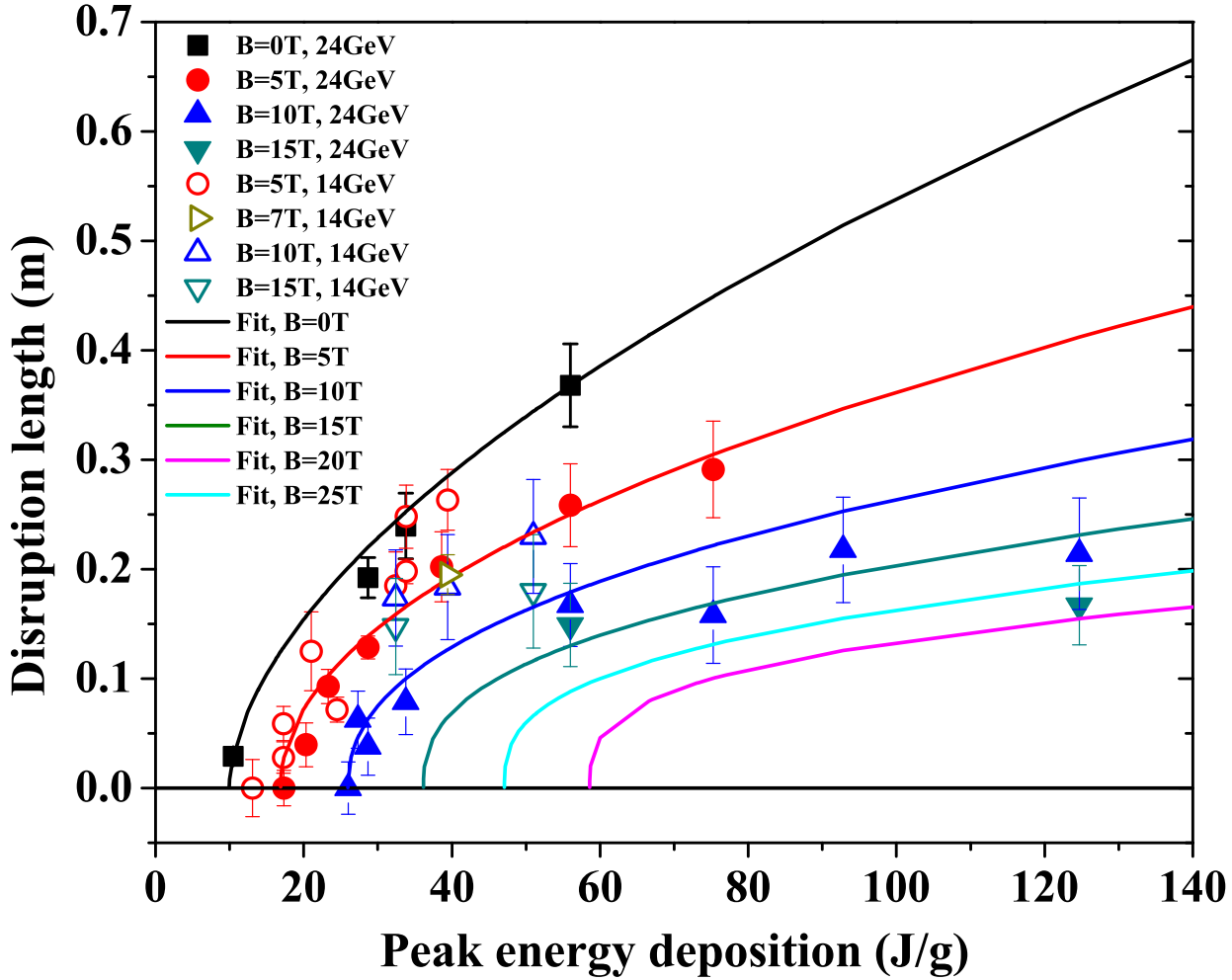

Figure 5.25: Disruption of Hg jet in various magnetic fields as a function of peak energy deposition and fit of model using Eqn. (5.18).

Chapter 6

Mercury Jet Surface Development in a Magnetic Field

In this chapter, the velocity of filament emanating from jet surface caused by disruption in a magnetic field is investigated. The energy deposition induced by proton beam generates filaments on the Hg jet surface due to thermal stress. The filament velocity leaving from the jet surface and the effect of magnetic field on it are discussed. It explains that the joule damping dissipates the kinetic energy on a time scale of joule damping term.

6.1 Filament Model on Jet Surface

6.1.1 Geometry of viewing mercury filament

It is investigated [58] that the observed motion of filament by 2D image has geometric relations with the viewing angle by focal length in optics. The filaments ejected from Hg jet by the proton beam interaction are viewed via shadow photography from a focal length $f = 9.15$ cm from the center of the jet.

The jet is supposed to have elliptical cross section. The schematic geometry of viewing Hg filament is depicted at Fig. 6.1. The measurement describes the projection $y_m(t)$ onto the y axis of a ray from the observer to the surface. McDonald [58] assumes that the filaments leave perpendicularly as shown in Fig. 6.1. The elliptic expression is given as Eqn. (6.1):

$$\frac{x^2}{a^2} + \frac{y^2}{b^2} = 1 \ . \tag{6.1}$$

Suppose a filament leaves the surface with velocity v_o at time t_o from point (x_o, y_o), at time $t > t_o$, the travel distance d is then $v_o(t - t_o)$ assuming that the velocity is constant. The position of the filament is $x_d = x_o + d\sin(\theta)$ and $y_d = y_o + d\cos(\theta)$. Using the trigonometric notation of slope at point (x_o, y_o), the position of the filament, y_m, as projected onto the y axis is

$$\begin{aligned} y_m &= y_d \frac{f}{f - x_d} \approx y_d(1 + \frac{x_d}{f}) \\ &= b\cos\theta + v_o(t - t_o)\cos\theta + \frac{[a + v_o(t - t_o)][b + v_o(t - t_o)]}{2f}\sin 2\theta \ . \end{aligned} \tag{6.2}$$

Thus, the apparent velocity of the filament along y axis is

$$v_m = \frac{dy_m}{dt} \approx v_o[\cos\theta + \frac{a + b + 2v_o(t - t_o)}{2f}\sin 2\theta] \ . \tag{6.3}$$

The earliest time t_{om} that a filament can be seen via projected shadow photography when $y_m = b$ is given as follows:

$$t_{om} \approx t_o + \frac{b(1 - \frac{v_m}{v_o})}{v_m} \tag{6.4}$$

and

$$v_m \approx \frac{v_o}{1 + v_o \frac{(t_{om} - t_o)}{b}} \ . \tag{6.5}$$

6.1.2 Distribution of filaments on jet surface

McDonald [58] suggested three cases of possible distribution of filaments on jet surface, which can indicate the probable existence of filaments in observation. First, in case that the filaments are distributed uniformly in angle θ, the probability of the existence of the filaments is

$$P(\theta)d\theta = \frac{d\theta}{2\pi} \ . \tag{6.6}$$

Second, in case that the filaments are distributed uniformly in angle θ, the probability of the existence of the filaments is

$$P(\theta)d\theta = \frac{d\phi}{2\pi} = \frac{ab}{a^2 \sin^2\theta + b^2 \cos^2\theta} \frac{d\theta}{2\pi} \ . \tag{6.7}$$

Third, in case that the filaments are distributed uniformly in position s around the circumference C of the ellipse, the probability of the existence of the filaments is

$$P(\theta)d\theta = \frac{ds}{C} \approx \frac{2\sqrt{a^2 \cos^2\theta + b^2 \sin^2\theta}}{3(a+b) - \sqrt{(3a+b)(a+3b)}} \frac{d\theta}{2\pi} \ . \tag{6.8}$$

6.1.3 Estimation of filament velocity

Sievers and Pugnat [84] reported the response of solid and liquid target to rapid heating by the incident proton beam. The parabolic radial energy deposition density E_{beam} is considered, dropping to 0 at the outer radius $a =$ 1 cm as follow:

$$E_p = E_o[1 - (r/a)^2] \ . \tag{6.9}$$

The increase in temperature causes pressure rise. It is assumed that the rise time for the temperature is of the same order of magnitude with the beam energy deposition, 10^{-9} s, and thermal expansion is initially prevented by the mass inertial of the material. From the definition of bulk modulus K, the resulting instantaneous thermal pressure for Hg is

$$\Delta p(r) = K\alpha_v \Delta T(r) \ . \tag{6.10}$$

If the thermal heating occurs very slowly comparable to the material's dynamic frequency, it would correspond to quasi-static thermal expansion. It is believed that the energy stored in the material due to the initial thermal expansion may be converted into kinetic energy bombarding the liquid flow away. Corresponding to the thermal expansion caused by the pressure rise, strain energy is stored in the liquid flow due to the compression, which can be expressed as

$$\frac{E_{strain}}{V} = \frac{K(\alpha_v \Delta T(r))^2}{2} \ , \tag{6.11}$$

where E_{strain} represents the converted beam energy. Hence, it indicates that the thermal volumetric expansion is proportional to the jet expansion velocity with the coefficient of compressibility of jet material. The order of the velocity with which the boundary of the liquid material is given by the thermal expansion at the boundary divided by the time over which the sound travels across the radius of the jet, which is in units of $c\alpha_v T_o$ [84]. The pressure and the velocity at the boundary are reduced by extending the time of heating, which depends on the compressibility like

$$p \sim \frac{1}{\kappa} \quad , \quad v \sim \frac{1}{\sqrt{\kappa}} \ , \tag{6.12}$$

where κ is the compressibility of material.

6.2 Observation of Filament Development on Mercury Jet Surface

6.2.1 Image calibration

6.2.1.1 *image calibration with proton beam arrival signal*

In order to investigate the time response of filament, we need to establish the accuracy and calibration of the measurement based on the optical diagnostics setup. Figure 3.6 shows the traced signals on an oscilloscope when the beam and the beam triggering signal are delivered. The scintillating fiber signal gives

the beam arrival time. Therefore, it is possible to set up the trigger timing for the cameras and laser drivers, which is ~ 2 μs after the master electronic triggering signal from the proton synchrotron. Therefore, the first image of the SMD camera shows the condition of jet at the time before the beam arrives since the exposure time of SMD camera is 150 ns. All of electronic delays including the cable delays are less than 1 μs. The maximum frame rate of SMD camera is up to 1 MHz. The accuracy of camera frame rate is checked by using laser pulses. Laser pulses with certain periods are generated and then monitored at oscilloscope through photodiode. The frame rate of camera is set at the same values of laser pulse period. The frame rate is checked by monitoring the variation of intensity of image captured from camera, which is judged as negligibly uniform. Otherwise, the contrasts of consecutively captured images was varied under a slight time difference by frame rate and/or pulse period because of short laser pulse time 150 ns.

6.2.1.2 *time delay structure of the triggered image to the beam arrival signal*

Figure 6.2 (b) shows the time structures between freezing image after laser enabling and proton beam arrival. Figure 6.2 (a) shows the specifications of 25 W laser, where the response time to reach the peak laser, wavelength of laser, and optical power for various pulse rates are investigated [92]. Laser emits ~ 250 ns after receiving the 16 pulse trigger from the pulse generator. The time of flight of light to the primary vessel is ~ 60 ns. Once the light source arrives at the primary vessel, the freezing image of Hg jet flow is

instantaneously generated and it is then transmitted through the optical fiber corresponding to the light speed $\sim$ 4 ns/m, where $\sim$ 60 ns is taken for the used imaging fiber length. From the traced signals in Fig. 3.6, the proton beam arrival time is measured. Considering the time of flight from primary vessel through scintillating fiber, $\sim$ 60 ns delay is estimated, so that the time delay between the 1^{st} acquired image and the actual proton beam arrival is given as $T_3 - T_2$ in Fig. 6.2 (b), which is considered for the velocity analysis of filaments.

6.2.2 Parameter optimization with uncertainty

6.2.2.1 *nonlinear curve fit for estimation of model*

Selecting a model of the right form to fit a set of data requires the use of empirical evidence in the data, knowledge of the process, and some trial-and-error experimentation. Much of the need to iterate stems from the difficulty in initially selecting a function that describes the data well. Some scientific theory describing the mechanics of a physical system provide a functional form for the process, which type of function makes an ideal starting point for model development. So, a practical approach is to choose the simplest possible functions that have properties ascribed to the process. Fitting models that are more complex than necessary means that random noise in the data will be modeled as deterministic structure. This will unnecessarily reduce the amount of data available for estimation of the residual standard deviation, potentially increasing the uncertainties of the results obtained when the model is used.

Numerical methods for model validation, such as R^2 statistic, are useful, which is focused on a particular aspect of the relationship between the model and the data and try to compress that information into a single descriptive number. The residuals from a fitted model represent the differences between the responses observed and the corresponding prediction of the response computed using the regression function.

The nonlinear regression model is

$$\mathbf{Y} = f(\mathbf{X}, \Theta) + \epsilon \ , \tag{6.13}$$

where $\mathbf{X} = (x_1, x_2, \ldots, x_m)$ are independent variables, $\Theta = (\Theta_1, \Theta_2, \ldots, \Theta_k)$ are parameters, and ϵ is the random error assuming the mean is equal to 0 with normal distribution, where k is the degree. A measure of the quality of nonlinear fitting parameters is the chi-square value:

$$\chi^2 = \sum_{i=1}^{n} w_i (y_i - \hat{y}_i)^2 \ , \tag{6.14}$$

where w_i is the weighting coefficient, y_i are the experimental data points, and $\hat{y}_i$ are the predicted points. To fit the model, the residual is defined as

$$r_i = y_i - \hat{y}_i \ . \tag{6.15}$$

It conforms to a normal distribution with the mean equal to 0 and the variance equal to σ_i^2. Then the maximum likelihood estimates of the parameters Θ_i can be obtained by minimizing the chi-square value, defined as

$$\chi^2 = \sum_{i=1}^{n} \frac{(y_i - \hat{y}_i)^2}{\sigma_i^2} \ . \tag{6.16}$$

If the error is treated as weight, $w_i = \frac{1}{\sigma_i^2}$ can be defined in the chi-square minimizing equation, where σ_i are the measurement errors. The quality of regression can be measured by the coefficient of determination, R^2, which is defined as

$$R^2 = 1 - \frac{\sum_{i=1}^{n} w_i (y_i - \hat{y}_i)^2}{\sum_{i=1}^{n} (y_i - \bar{y})^2} \ . \tag{6.17}$$

In order to express the relationship between independent variables and dependent variables and a degree of confidence in regression model, the adjusted R^2 for validation of goodness of fit measurement is defined as

$$\bar{R}^2 = 1 - \frac{\frac{\sum_{i=1}^{n} w_i (y_i - \hat{y}_i)^2}{n^* - k}}{\frac{\sum_{i=1}^{n} (y_i - \bar{y})^2}{n^*}} \ . \tag{6.18}$$

Note that if intercept is included in the model, the degree of freedom is $n^* = n - 1$. Otherwise, $n^* = n$ [65]. The adjusted R^2 avoids the effect of the degrees of freedom by adding variables in the model, which results in rising of R^2. Therefore, the adjusted R^2 overcomes the rise in R^2 when fitting a small sample size by multiple predictor model.

The covariance value indicates the correlation between two variables, and the matrices of covariance in regression show the inter-correlations among all parameters. The correlation matrix rescales the covariance values. Parameter errors are equal to the square root of diagonal terms in covariance matrix and

the covariance matrix of the regression and correlation between parameters are defined as

$$Cov\ (\Theta_i, \Theta_j) = \sigma^2 (X'\ X)^{-1} \tag{6.19}$$

and

$$Cor\ (\Theta_i, \Theta_j) = \frac{Cov\ (\Theta_i, \Theta_j)}{\sqrt{Cov\ (\Theta_i, \Theta_i)}\sqrt{Cov\ (\Theta_j, \Theta_j)}}\ . \tag{6.20}$$

6.2.2.2 *Levenberg-Marquardt minimization*

To estimate the $\hat{\Theta}$ value with the least square method, we need to solve the normal equations which are set to be zero for the partial derivatives of χ^2 with respect to each $\hat{\Theta}_p$:

$$\frac{\partial \chi^2}{\partial \hat{\Theta}_p} = 0\ . \tag{6.21}$$

Employing an iterative strategy to estimate the parameter values, it starts with some initial values Θ_o. With each iteration, χ^2 value is computed and then the parameter values are adjusted to reduce the χ^2. When χ^2 values computed in two successive iterations are small enough compared with the tolerance, the fitting is converged. The Levenberg-Marquardt algorithm is employed for an iterative technique that locates a local minimum of a multivariate function that is expressed as the sum of squares of nonlinear function. Levenberg-Marquardt is considered as a combination of steepest descent and the Gauss-Newton

method [71]. When the solution is far from a local minimum, the algorithm behaves like a steepest descent method. When the solution is close to a local minimum, it becomes a Gauss-Newton method and exhibits fast convergence [71].

Given the residuals r_i $(i = 1,\ \ldots,\ n)$ of parameters $\Theta = (\Theta_1, \Theta_2, \ldots, \Theta_p)$, with $n \geq k$, the Gauss-Newton algorithm finds the minimum of χ^2 given in Eqn. (6.16). Starting with an initial guess Θ_o for the minimum, the method proceeds by the iteration $\Theta^{s+1} = \Theta^s + \delta\Theta$ with an increment $\delta\Theta$ satisfying the equation given as Eqn. (6.22) using Eqn. (6.21):

$$(\mathbf{J}_r^T \mathbf{J}_r)\delta\Theta = -\mathbf{J}_r^T \mathbf{r} \ , \tag{6.22}$$

where $\mathbf{r}$ is the vector of r_i and $\mathbf{J}_r$ is the Jacobian of $\mathbf{r}$ with respect to Θ. The residuals r_i are defined as $r_i(\Theta) = y_i - f(x_i,\ \Theta)$. In order to find the parameters Θ that a given model function $y = f(x, \Theta)$ fits best data points, the increment $\delta\Theta$ can be expressed in terms of Jacobian of the function as follow:

$$(\mathbf{J}_f^T \mathbf{J}_f)\delta\Theta = \mathbf{J}_f^T \mathbf{r} \ . \tag{6.23}$$

The Levenberg-Marquardt iteration is a variation on the Newton iteration. The equation $\mathbf{N}\delta\Theta = \mathbf{J}_f^T \mathbf{r}$ are augmented to $\mathbf{N}'\delta\Theta = \mathbf{J}_f^T \mathbf{r}$ where $N'_{ij} = (1\ + \delta_{ij}\ \lambda)\ N_{ij}$ with δ_{ij} the Kronecker delta. The λ is initialized to a small value, e.g. 10^{-3}. If the value obtained for $\delta\Theta$ reduce the residuals, the increment is accepted and λ is divided by 10 before the next iteration. If the residuals

increase then λ is multiplied by 10 and the augmented equations are solved again until an increment is obtained that reduces the residuals. For large λ, the iteration approaches a steepest descent [65].

6.2.2.3 *chi-square probability*

The chi square statistic for an experiment with n possible outcomes, performed m times, in which $Y_1, Y_2, \cdots, Y_n$ are the number of experiments which resulted in each possible outcome, with probabilities of each outcome $p_1, p_2, \cdots, p_n$ is:

$$\chi^2 = \sum_{1 \leq i \leq n} \frac{(Y_i - mp_i)^2}{mp_i} \ . \tag{6.24}$$

Note that $y_1, \cdots, y_n$ are independently normally distributed with mean μ and variance σ^2, then $\bar{y}$ will be precisely normally distributed with mean mean μ and variance σ^2/n. By substitution of $d\ S^2/\sigma^2 = t$ into sampling distribution, the probability density function P that a χ^2 value calculated for an experiment with d degrees of freedom is due to chance is:

$$P_{\chi^2,\ d} = [2^{d/2}\ \Gamma(\frac{d}{2})]^{-1} \int_{\chi^2}^{\infty} (t)^{\frac{d}{2}-1} e^{-\frac{t}{2}} dt \ , \tag{6.25}$$

where Γ is the generalization of the factorial function to real and complex arguments:

$$\Gamma_x = \int_0^{\infty} (t)^{x-1} e^{-t} dt \ . \tag{6.26}$$

Tables for the chi-square distribution with d degrees of freedom are given in percentiles [18]. The P percentile is given as

$$Pr(\chi^2(d) \leq \chi_p^2(d)) = 1 - P \ . \tag{6.27}$$

Noth that the probability calculation from χ^2 is an approximation which is valid for large values of n, and is only meaningful when calculated from a large number of independent experiments.

6.2.3 Filament distribution and uncertainty of measurement

6.2.3.1 *observation of filaments on jet surface*

Figure 6.3 shows photographs of filament evolution on the Hg jet surface at 25 μs frame rate, where the beam is 10 Tp, 24 GeV and the magnetic field is 10 T. The first collected image among 15 images is brighter than the rest of 14 images. It indicates that the radiation generated by the interaction of Hg with proton beam affects the transmittance and/or reflectance of optical components, resulting in the production of darker images as one sees the rest of collected 14 images.

6.2.3.2 *measurement of traveled distance of filament*

To obtain the vertical filament velocity, the distance traveled by a fixed point on the jet surface is tracked over a given time period. The jet volume, where the maximal energy is deposited, results in the initial generation of the filaments. The higher jet velocity occurs when the filaments is initially protruded out of the jet surface and then the jet velocity decreases due to the magnetic damping and viscous dissipation. So, the velocity at steady state is

obtained in order to evaluate its effect on the beam intensity and magnetic field.

The quality of optical images varies from shot to shot since the radiation or jet dispersion may make image quality varies. The most difficulty in measurement is to discern the edge of filaments as it moves somewhat far away from surface because the initial jet filament edge is dense(clearly black) but it looks like dissipating, dilute, and disappearing (grey or similar with background) as it moves further. Because measurement is done in several points, there may be some error in measurement after some steady velocity(constant peak velocity) for weak filament velocity measurement.

The image size at Viewport 2 is 240 by 240. Using graphic software, pixels on image is picked to locate the edge of filament. Therefore, the uncertainty, while locate the position y_m, is reported to be $\pm$ 2 pixels, which corresponds to the difference of $\sim \pm$ 17 m/s filament velocity. This uncertainty can occur randomly. The peak strong filament which gives constant velocity within $\pm$ 2 pixels until the end of 15 frames is assumed to be considered as there is constant uncertainty, $\pm$ 2 pixels. The weak filament which gives constant velocity within $\pm$ 2 pixels until the filament reaches some frames, for example, 3 $\sim$ 7 frames, is also assumed to be considered as there is a constant uncertainty, $\pm$ 2 pixels, where the black edge of filament is clearly observed. However, after the some frames, for example, 3 $\sim$ 7 frames, because the original edge of filament dilute or dissipates or disappear, the uncertainty in measurement may not be constant. In this case, measurement is stopped at that frame.

6.2.4 Linear regression with the first order polynomial

6.2.4.1 *curve fit function*

The heaviside step function is defined as the integral of the Dirac delta function as follow:

$$H(t) = \int_{-\infty}^{t} \delta(\xi) d\xi \ . \tag{6.28}$$

The ramp function is the antiderivative of the Heaviside step function:

$$R(t) = \int_{-\infty}^{t} H(\xi) d\xi = tH(t) \ . \tag{6.29}$$

In a discrete form, it is defined as an alternative form for our linear regression model as follow:

$$R(t) = \begin{cases} y_m = b, & t \leq t_{om} \\ y_m = b + v_m(t - t_{om}), & t > t_{om} \end{cases} \ , \tag{6.30}$$

where y_m, b, v_m, and t_{om} denote the measured position of the filament as projected onto the y axis in image, the measured position of jet surface before the filament are developed, the apparent velocity of the filament along the y axis, and measured the earliest time that a filament can be seen via shadow photography respectively.

6.2.4.2 *parameter estimation using multiple position of filaments*

Shot 11019 is chosen for illustration. Using Eqn. (6.30) for linear regression model with measured data points y_m and t, minimizing R^2 yields b, v_m, and

t_{om}. Figure 6.4 (a) shows the illustration of multiple data points where the intercept of x axis and slope estimate the onset time of filament via shadow photography and apparent velocity projected on y axis in image, which are t_{om} = 43.6 ± 4.5 μs and v_m = 55.5 ± 0.8 m/s respectively. The reduced R^2 value and adjusted $\bar{R}^2$ values are 1.749 and 0.998 respectively. Based on Eqn. (6.30), the fit function to data points is as follow:

$$y_m = c_1(t - b_1) + a_1 \ , \tag{6.31}$$

where t and y_m denote the measured time and position of filament respectively and the units for a_1, b_1, and c_1 are pixels, μs, and pixel/μs respectively. The parameterized values of coefficients and error values to fit function are given in Table 6.1.

In case of larger velocity of filaments, maximally measurable data points are limited to $\sim 2 \sim 3$ points due to the limited field of view in optical diagnostic image. Figure 6.4 (b) shows the illustration for the case of 3 data points. The onset time from regression model yields underestimated value such as negative time delay because the data points are equal or smaller than the number of parameters in fit function. Thus, assumption is that the real onset time for such a large velocity should be between typical onset time 50 μs and 0 μs, which corresponds to the onset time of 25 ± 25 μs. Therefore, the slope of fit curve is determined by fixing the assumed onset time accordingly, which yields the filament velocity of 148 ± 24.5 m/s. The error is determined directly by dividing approximated filament velocity of the cases of t_{om} = 0 and t_{om} =

50 μs by 2. The shot 10008 is chosen for the case of illustration of parameter estimation of 3 data points. The fit function to data points for the case of negative onset time (black solid line) in Fig. 6.4 (b) is as follow:

$$y_m = c_1 t + a_1 \ . \tag{6.32}$$

And Eqn. (6.31) is employed for the case of having fixed $b_1 = 0$ μs and $b_1 = 50$ μs onset time (blue and red solid line) in in Fig. 6.4 (b). As one expects, this approach for a special case yields large uncertainty.

6.2.4.3 *filament velocity distribution on jet surface*

Figure 6.5 (b) shows the velocity distribution of filaments over the jet surface shown in Fig. 6.3 according to the location of filaments from Fig. 6.5 (a), whose filaments are used for Fig. 6.6 and Fig. 6.7. Figure 6.6 (a) and (b) show calculated estimation and measured estimation of filament velocity as a function of observed onset time of filaments respectively. v_o=60 μs and t_o=40 μs for upwards filaments are used with Eqn. (6.5) for calculated estimation. t_o=70 μs for downwards filaments are used. As the estimated apparent velocity of filaments projected on y axis in image increases, the estimated onset time of filaments decreases. This shows the evidence of the geometric effects of viewing filaments. Assuming the filaments are generated perpendicular to the jet surface, as the filaments leaves farther from the jet surface, it takes more time to make an initial observation in images. Thus,it is possible to consider the low velocity of filaments with large onset time leaves

from more close to the center of jet normal to the side view shown in images. Note that the velocity of each filament is approximated with uncertainty by doing linear regression using the fit function in order to give one representative velocity according to each filament. Low velocity of filaments close to 0 showed larger error of approximation of onset time due to the uncertainty of the very small observed traveling distance of filaments.

According to the notation in Fig. 6.5 (a), Fig. 6.7 (a) shows the velocity of filaments on the upward free surface of jet as a function of time and Fig. 6.7 (b) shows the velocity of filaments on the downward free surface of jet as a function of time. Note that the instantaneous velocity as defined in Eqn. (6.33) is used for velocity measurement in Fig. 6.7. The onset time of filament increases as the peak velocity of filament decreases, which indicates the possible evidence of the geometric effect of viewing filaments.

6.3 Filament Velocity on Mercury Jet Surface

6.3.1 Magnetic dissipation of energy

As a conducting liquid moves through a static magnetic field, electric currents are generated. This, in turn, leads to ohmic heating such as Joule dissipation. As the thermal energy of the fluid rises, there is a corresponding decrease in its kinetic energy, and thus the fluid decelerates. This results in a suppression of the motion of filament. According to Davidson's approximation [14], the Eqn. (2.42) shows the energy decay with respect to time depending on the magnetic damping time constant, where $\tau = \rho/\sigma B^2$. The implication

is that the filaments decelerates on a time scale of τ. Figure 2.2 (a) shows the decay of the normalized energy of flow in magnetic fields with respect to time due to the magnetic damping. Figure 2.2 (b) shows the integral calculation of Fig. 2.2 (a) with respect to time.

6.3.2 Time response of filaments in a magnetic field

Since the camera is triggered before beam arrives at the Hg jet and the laser pulse width is 150 ns, the first collected image shows the condition of Hg jet before beam interacts. Thus, the velocity of filament can always be judged as 0 m/s in the following Fig. 6.8. Since the joule damping dissipates the energy with an exponential factor, the energy dissipation arises rapidly in the beginning depending on the magnetic field term B^2. Thus, higher magnetic field will have higher damping effect so that it takes more rising time to peak velocity. The magnitude of steady peak velocity is reduced by increased applied magnetic field strength, which is possible indication of the magnetic damping role induced by the joule damping dissipation.

Figure 6.8 shows the time response of instantaneous filament velocity as a function of magnetic field with 14 GeV, 20 Tp beam and 24 GeV, 10 Tp beam respectively. The expression for the calculation of instantaneous velocity assuming Δt_n is small enough is

$$v_n = \frac{y_m(t_n) - y_m(t_{n-1})}{\Delta t_n} \ . \tag{6.33}$$

6.3.3 Proton beam induced filament velocity in a magnetic field

6.3.3.1 *filament velocity with 14 GeV beam in a magnetic field*

Figure 6.9 (a) shows the filament velocity as a function of 14 GeV beam intensity and magnetic field corresponding to the observed onset time of filaments shown in Fig. 6.9 (b). Note that the data points without having onset time data is reported by crude measurements of 2 positions of filament from 500 μs frame rate shot images since the estimation of onset time by fitting is inadequate. The filament velocity increases with the beam intensity. However, the magnetic field suppresses the filament velocity. At low intensity of proton beam, the charged beam may be fluctuating depending on the initial conditions at experiment. Thus, the observed onset time of filaments is large at low intensity of beam and it decreases as the intensity of proton beam increases, see Fig. 6.9 (b). Therefore, there are scattering distributions of filament velocity at lower intensity of beam over the resulting data points. The slope of the data points in velocity at higher magnetic fields decreases comparing with that associated with lower magnetic field. All velocities are less than 50 m/s regardless of magnetic fields. The filament velocity for the case of 14 GeV beam with 30 Tp in 10 T is $\sim$ 30 m/s.

6.3.3.2 *filament velocity with 24 GeV beam in a magnetic field*

Figure 6.10 (a) shows the filament velocity as a function of 24 GeV beam intensity and magnetic field corresponding to the observed onset time of filaments

shown in Fig. 6.10 (b). Again, at low intensity of proton beam, the charged beam may be fluctuating depending on the initial conditions at experiment. Thus, the observed onset time of filaments is large at low intensity of beam and it decreases as the intensity of proton beam increases, see Fig. 6.10 (b). The filament velocity increases with the beam intensity. The slope of the increase in velocity is $\sim 4 \times$ larger that that for the 14 GeV beam case, where the ratio of peak energy deposition between 14 GeV and 24 GeV beam energy is ~ 2.3 based on the calculation given in Fig. 5.13 (a), which implies the relationship of peak energy deposition to maximum filament velocity. However, the magnetic field suppresses the filament velocity. At relatively low intensity of beam as in the 14 GeV beam case, the charged beam is unstably fluctuating depending on the event conditions at experiment. Thus, the observed onset time of filaments is large at low intensity of beam and it decreases as the intensity of proton beam increases, see Fig. 6.10 (b). All velocities are less than 180 m/s regardless of magnetic fields, and the filament velocity for the case of 24 GeV beam with 30 Tp in 15 T is ~ 60 m/s.

6.3.3.3 *measurement of filament velocity in pump-probe condition as a check*

Figure 6.11 shows the measured filament velocity of multiple events with pump-probe conditions as a check. The conditions of each group in pump-probe events are given in Table A.4. There are 2 groups at 14 GeV and each group has different number of bunches and time delay between pump and probe. Figure 6.11 (a) shows the histogram of filament velocity and Fig. 6.11 (b) shows

statistics summary such as average, minimum, maximum, and median value. In group 2, qualitatively meaningful distribution of measurements are shown, which is 10.2 ± 3.6 m/s. The pump condition is meaningful due to the delay of beam delay, though there is no significant difference in sub-category of group 2. However, This check shows low velocity comparing with the results shown in Fig. 6.9 (a). One thing to evaluate is that there is another error that should be considered in filament velocity analysis, so called uncertainty distribution of filament velocity under repetition with same condition of experiment. This is judged by ~ 40 % of the measured velocity, which is integrated in the following key result shown in Fig. 6.12.

6.4 Filament Velocity on Jet Surface by Energy Deposition

The energy deposition according to the interacting number of protons at both 14 GeV and 24 GeV beam energy is calculated by Fig. 5.13. Thus, Fig. 6.9 and Fig. 6.10 could be combined as a function of energy deposition, which shows the combined result of experiment in maximum filament velocity together. Figure 6.12 shows the filament velocity in magnetic fields as a function of peak energy deposition and fit is according to Eqn. (6.34). Figure 6.13 shows the filament velocity in magnetic fields as a function of total energy deposition and fit is according to Eqn. (6.34). The same threshold values of peak energy and total energy deposition with those in Fig. 5.23 and Figure 5.25 in various magnetic fields are used in order to connect mutual interplay between

results. In other words, the threshold peak energy deposition for filament velocity uses the same value with that for disruption length in order to keep consistency between the onset of disruption and filament. χ^2 values between Fig. 6.12 and Fig. 6.13 are not significantly different, although Fig. 5.23 has lower χ^2 value possibly due to effects of the forcefully adopted threshold values from Fig. 5.23 and Fig. 5.25.

As discussed, the filament velocity on jet surface is dominated by the distribution of energy deposition interacting with proton beam. Hence,the peak energy deposition plays a role in determining the maximum filament velocity in viewpoint that the velocity distribution on jet surface can be normalized using the peak energy deposition. The employed global fit with multi-variables for filament velocity using the measured filament velocity is:

$$v_m = a_1(E_p - (b_1 + b_2 B^{b_3}))^{c_1 + c_2 B + c_3 B^2} \ , \tag{6.34}$$

where E_p and B are energy deposition and magnetic field respectively. The parameterized values of coefficients and errors of the fit functions are provided in Table 6.1. Note the error of each measured maximum filament is adjusted by $\sim$ 40 % of the measured velocity in order to expect somewhat improved fit result with reduced χ^2, as discussed previously in multiple events analysis with pump-probe condition. According to Fig. 6.12, the threshold of filament velocity increases in 1.2 power of magnetic field, and it is $\sim$ 10 J/g of peak energy energy deposition with no magnetic field. The filament velocity increases in linear ($\sim$ 1.24) power of peak energy deposition with no magnetic

field, but it is reduced in $\sim\ 1.24 - 0.015B$ power of peak energy deposition with magnetic field.

For muon collider in the future, higher beam intensity equivalent with 80 Tp in 20 T of 24 GeV proton beam energy is required. The peak energy deposition at 80 Tp with 24 GeV beam is $\sim$ 255 J. The total energy deposition for the case of 80 Tp with 24 GeV beam is $\sim$ 20.7 kJ. The maximum filament velocity at 255 J of peak energy in 20 T is expected to be $\sim$ 119 m/s. The maximum filament velocity at 20.7 kJ of total energy in 20 T is expected to be $\sim$ 129 m/s.

6.5 Comparison of Filament Velocity with Numerical Calculation As a Check

This chapter provides explicitly an comparison of filament velocity measurement based on the results of numerical calculation as a check purpose. Considering that the major and minor axes of the elliptic jet shape are 0.8 cm and 0.3 cm respectively, numerical calculation of filament velocity is performed with 14 GeV beam with 10 Tp in 0 T using Frontier MHD code based on front tracking method. The calculated energy deposition into the Hg jet from MARS code is used for calculation of filament velocity, and the velocity of 20 filaments in different positions are evaluated [7]. It is reported that the filament velocity along minor axis is much larger than that along the major axis and the filaments grow in the normal direction to the surface [8].

Figure 6.14 (a) shows the initial pressure contour in Hg jet from energy

deposition caused by proton beam interaction, where the peak pressure reached at $\sim$ 14000 bar [8]. 3 positions for filament velocity measurement in simulation are picked, which is schematically depicted in Fig. 6.14 (b) [7]. The filament velocity resulted in depending on the distance from position of peak energy deposition. Thus, different results of filament velocity are calculated in simulation considering the location of picked filaments, which is shown in Fig. 6.14 (c) [7]. The filament velocity v_o for position 1,2 and 3 at $\sim$ 80 μs are estimated to be 18, 33, and 28 m/s respectively from Fig. 6.14 (c). Approximating that the angles ϕ for point 2 and point 3 are 10 $^\circ$ and 20 $^\circ$ followed by the notation given in Fig. 6.1, the apparent filament velocity along the y axis and the earliest visible time delay on images via shadow photography are estimated using Eqn. (6.3) and Eqn. (6.4) respectively, which is shown in Fig. 6.14 (d) with measured maximum filament velocity and correspondingly estimated time delay from measurement. Note that 60 $^\circ$ and v_o=28 m/s from calculated result are used for the case of velocity at $\sim$ 800 μs with experimental measurement, and 40 % of the measured filament velocity is used for giving the velocity measurement error for consideration of uncertainty from multiple measurement under same condition. Since the apparent filament velocity varies depending on the estimated angle ϕ, appropriate angle is chosen based on the estimated value of the earliest visible time delay of filament. Simulation with no magnetic field estimates somewhat larger velocity than experimental measurement under 5 T of magnetic field due to magnetic field and estimated angle ϕ.

Table 6.1: Parameterized coefficients, its error, and statistics summary of fit function in figures.

Figure	**1**	**2**	**3**	**4**	**5**	**6**	**7**	**8**	**9**	**10**
6.4(a)	128	0.93517	43.57	4.44411	-	-	-	-	-0.26374	0.00392
6.4(b)(black)	112.1	-	-	-	-	-	-	-	-0.52	-
6.4(b)(blue)	122	0	0	0	-	-	-	-	-0.5865	0.01587
6.4(b)(red)	122	0	50	0	-	-	-	-	-0.81911	0.10777
6.12	0.76998	0.65104	9.93998	0	0.98744	0	1.21081	0	1.23776	0.398
6.13	0.02454	0.0425	338.243	0	115.38	0	0.82899	0	1.00378	0.29245

Figure	**11**	**12**	**13**	**14**	**15**	**16**	**17**	**18**	**19**	
6.4(a)	-	-	-	-	15	12	1.74908	0.99773	0.0505	
6.4(b)(black)	-	-	-	-	2	0	0	0	0	
6.4(b)(blue)	-	-	-	-	3	2	12.31396	0.99622	0	
6.4(b)(red)	-	-	-	-	3	2	281.74259	0.91351	0	
6.12	-0.01468	0.01776	0	0	25	22	2.19995	0.08635	0.0009	
6.13	-0.00671	0.0079	0	0	25	22	1.85595	0.22959	0.0082	

1 : a1 value, **2** : a1 standard deviation,

3 : b1 value, **4** : b1 standard deviation, **5** : b2 value, **6** : b2 standard deviation,

7 : b3 value, **8** : b3 standard deviation , **9** : c1 value, **10** : c1 standard deviation,
11 : c2 value, **12** : c2 standard deviation, **13** : c3 value, **14** : c3 standard deviation,

15 : Number of points, **16** : Degrees of freedom, **17** : Reduced χ^2, **18** : Adjusted $\mathbf{R}^2$, **19** : χ^2 probability.

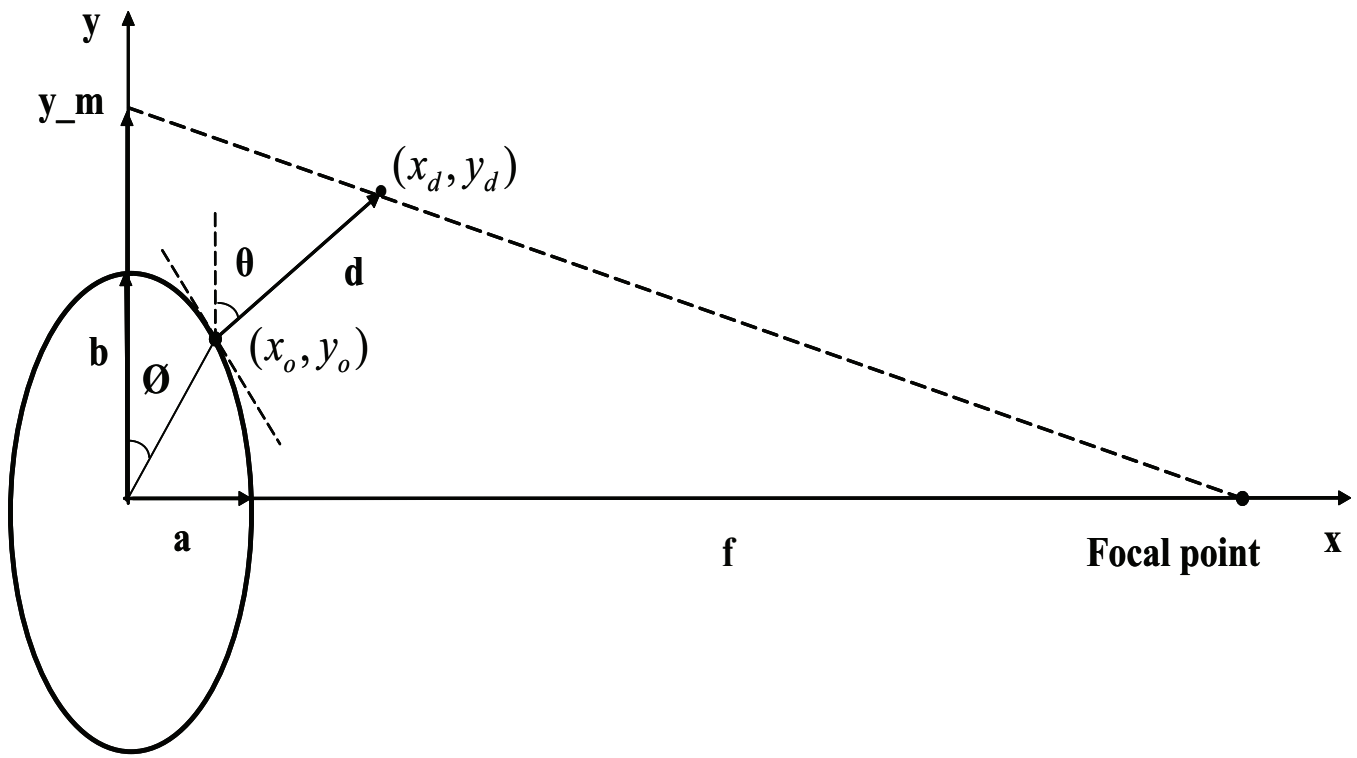

Figure 6.1: Schematic geometry of viewing filament on the Hg jet [58].

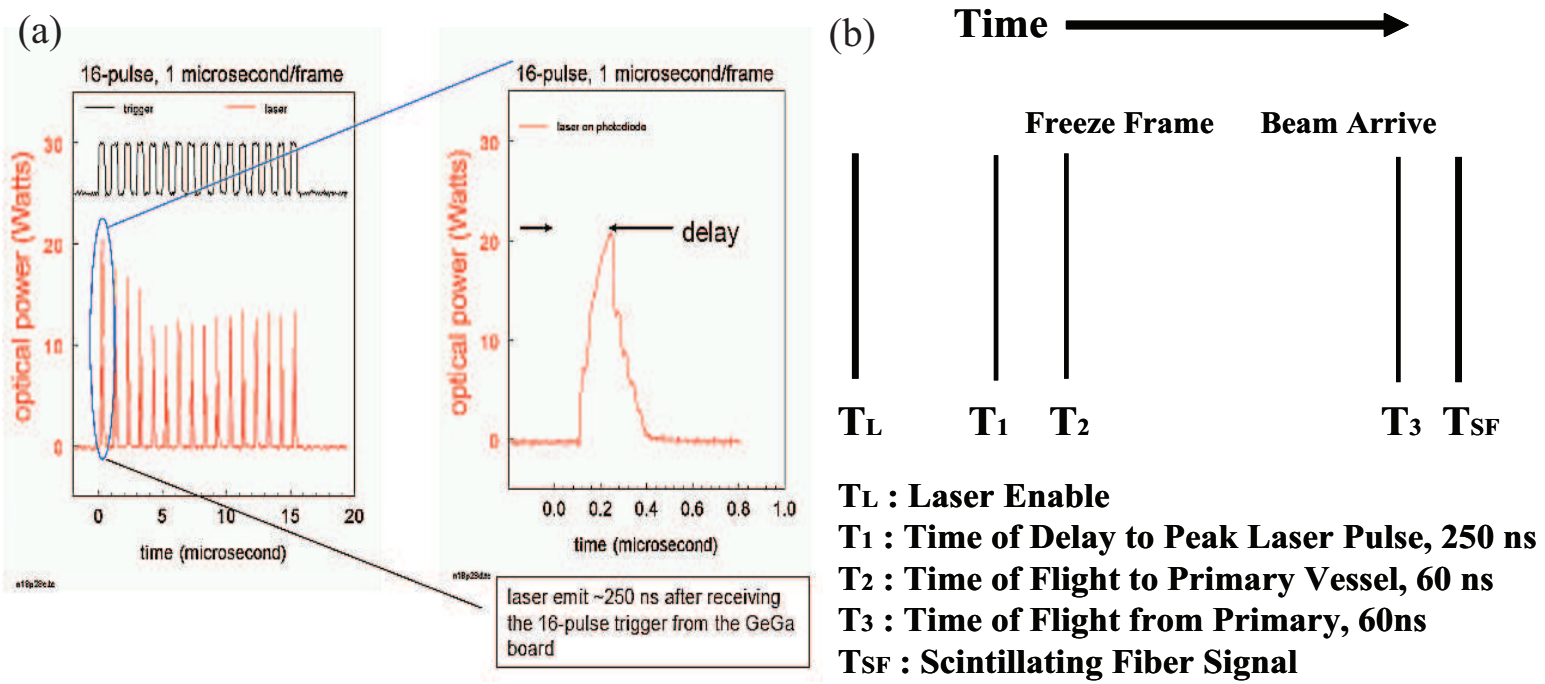

Figure 6.2: Time delay estimation of devices for triggered image calibration. a.) Measurement of characteristic response of 25 W laser used for high speed camera at Viewport 2 [92]. b.) Time structures between light source enabling and proton beam arrival.

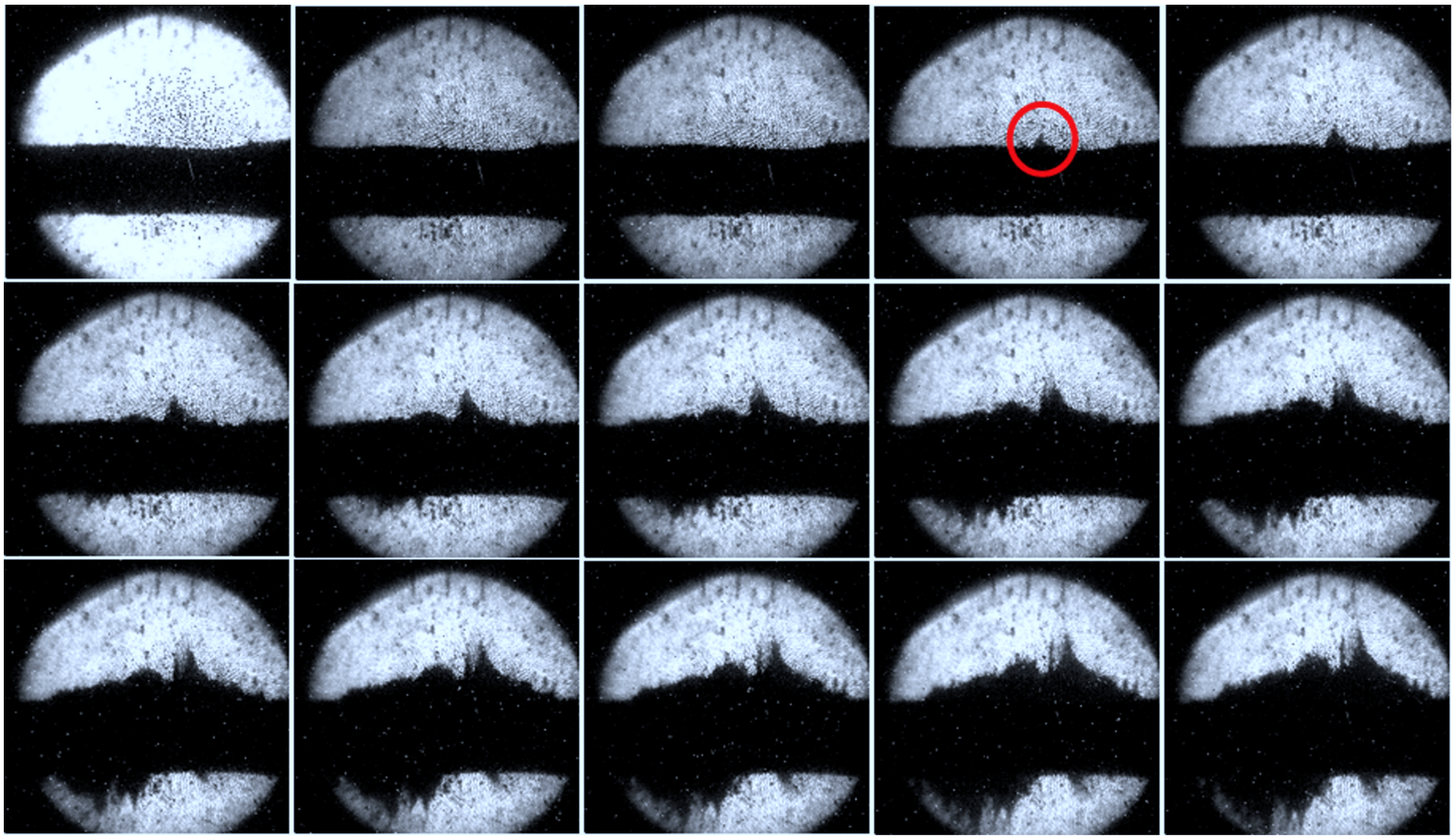

Figure 6.3: Photographs of filament evolution on the Hg jet surface as a function of time at 25 μs frame rate. The beam is 10 Tp with 24 GeV. The magnetic field is 10 T. The red circle on the 4^{th} image of the top row points the filament that is used for velocity measurement in Fig. 6.8 (b).

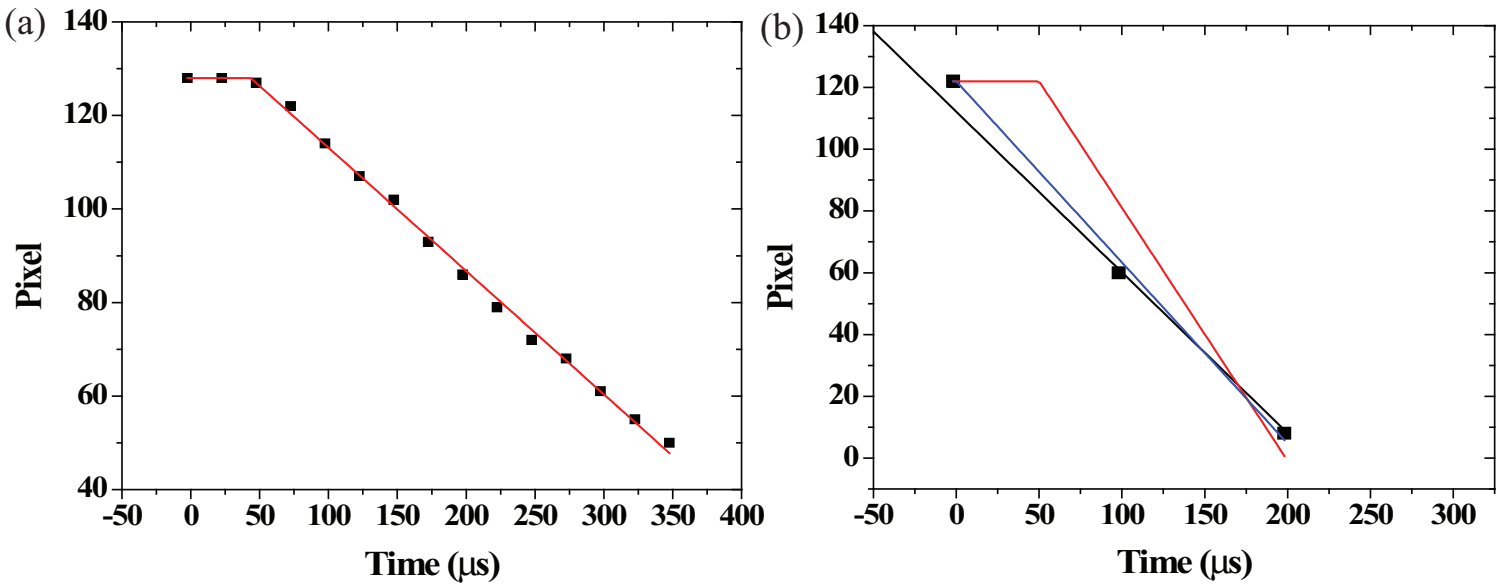

Figure 6.4: Illustration of bilinear fit for parameters estimation. a.) Multiple data points. b.) 3 data points.

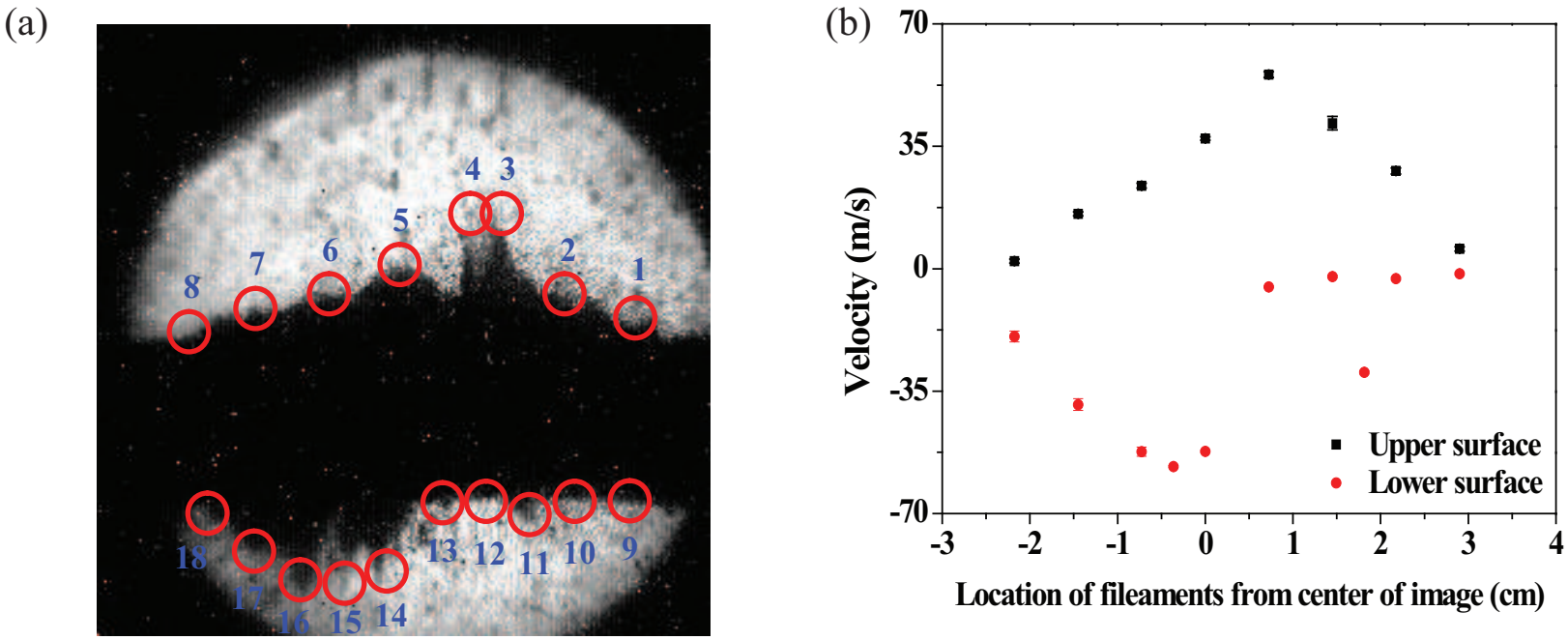

Figure 6.5: Location of 18 points of filament on the Hg jet surface for velocity measurement and its velocity. The shot condition is same with Fig. 6.3. The numbers above red circles point the filament that is used for velocity estimation in Fig. 6.6 and Fig. 6.7. a.) Location of filaments for measurement. b.) Filament velocity at each location.

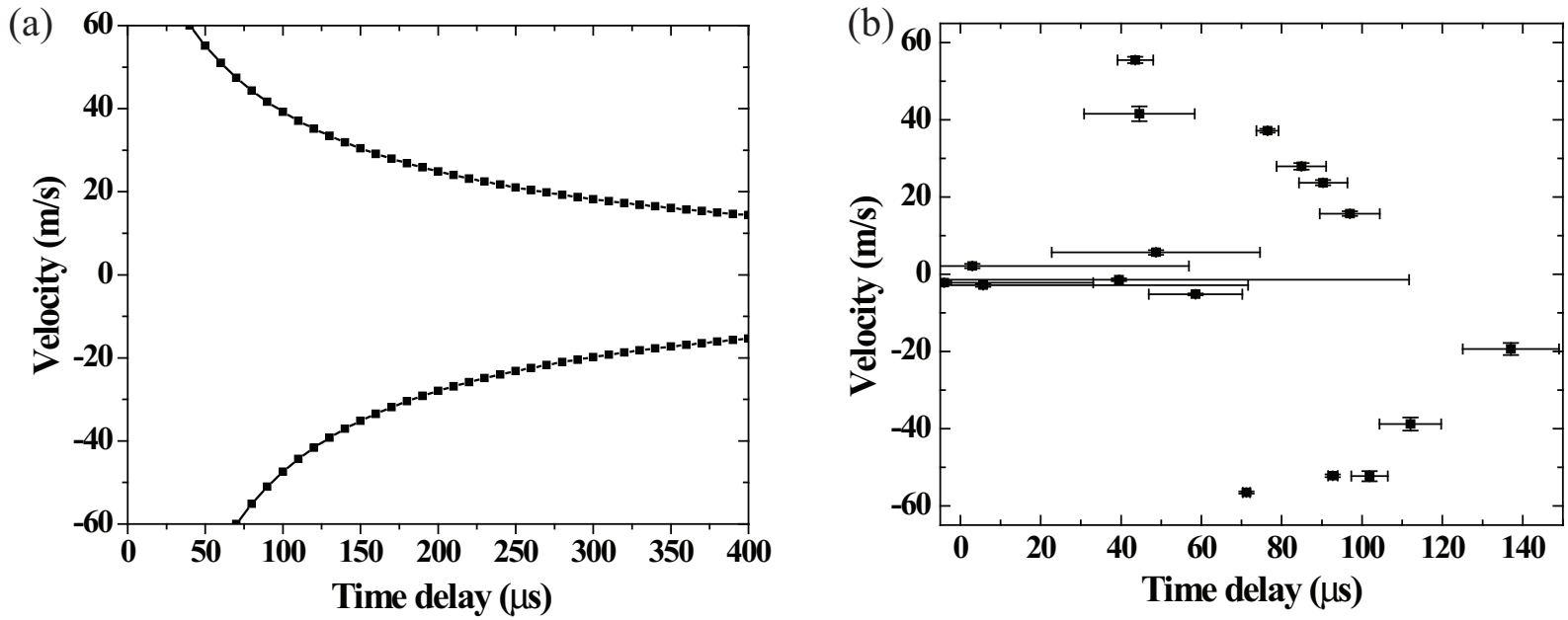

Figure 6.6: Estimation of velocity and onset time of filaments shown in Fig. 6.3. The beam is 10 Tp with 24 GeV and magnetic field is 10 T. a.) Calculated estimation of filament velocity as a function of onset time of filaments. v_o=60 μs and t_o=40 μs for upwards filaments are used with Eqn. (6.5). t_o=70 μs for downwards filaments are used. b.) Measured estimation of filament velocity and onset time of filaments.

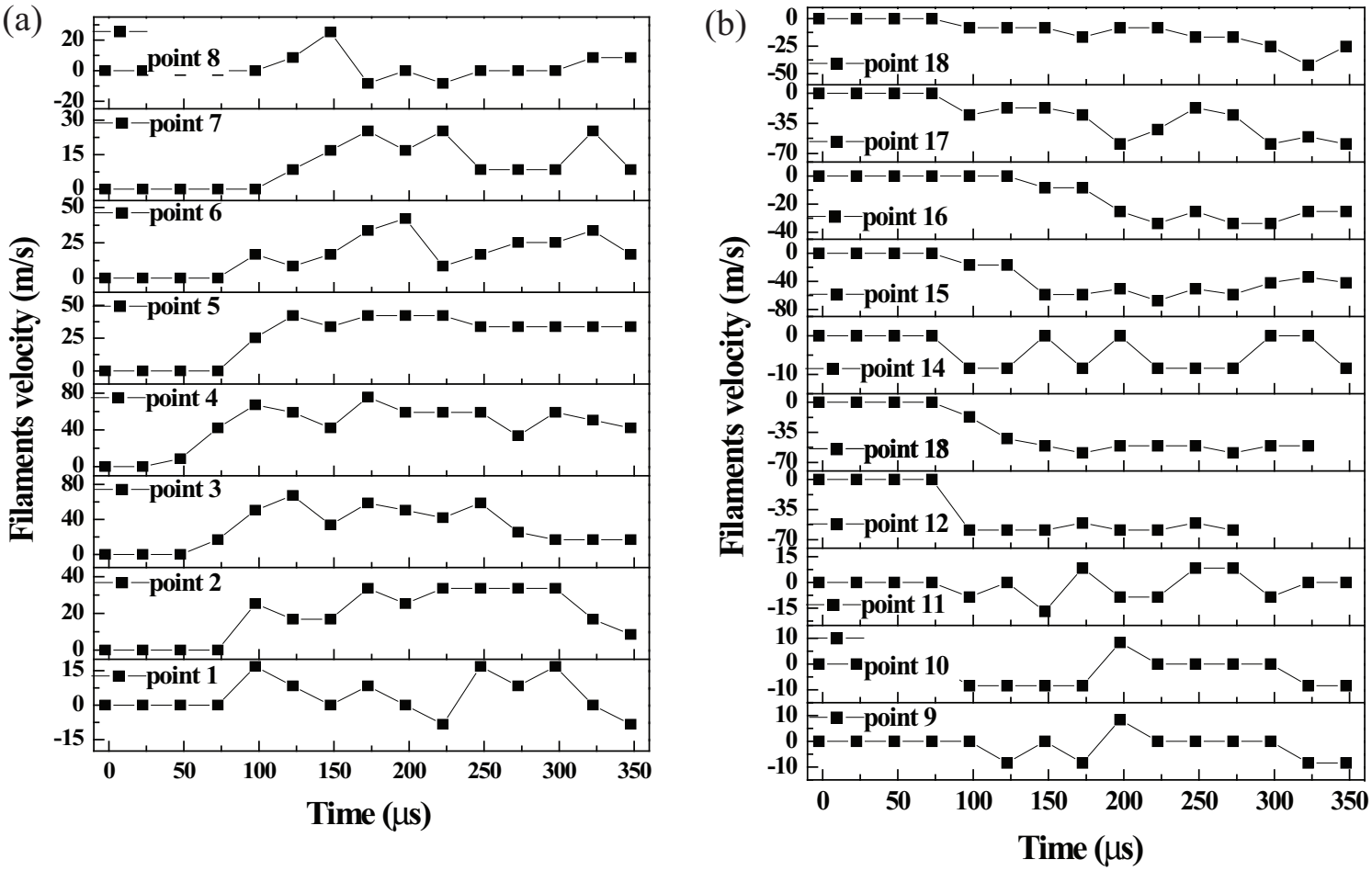

Figure 6.7: Time response of instantaneous filament velocity on jet surface for various filaments shown in Fig. 6.5. The beam is 10 Tp with 24 GeV. The magnetic field is 10 T. a.) Upper surface. b.) Lower surface.

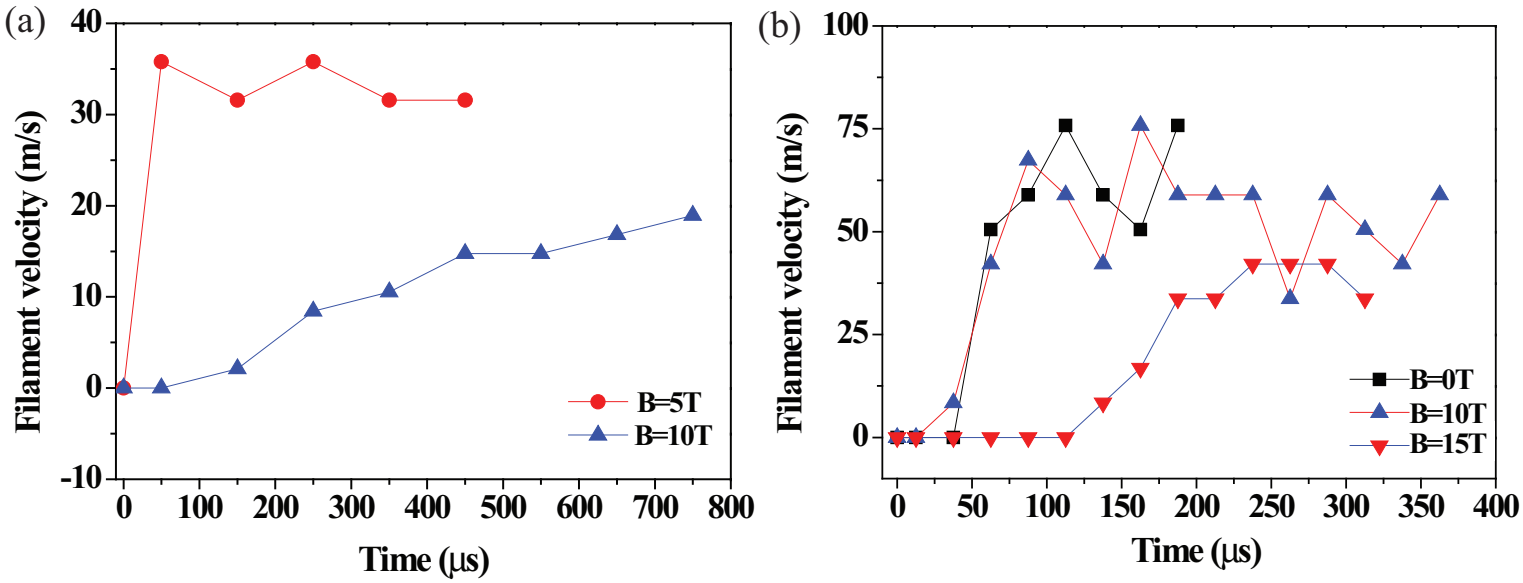

Figure 6.8: Time response of instantaneous filament velocity as a function of magnetic field. Equation (6.33) is used for measuring instantaneous filament velocity. The half of elapsed time between each frame is used to indicate the time at each filament velocity. a.) 14 GeV, 20 Tp beam. b.) 24 GeV, 10 Tp beam.

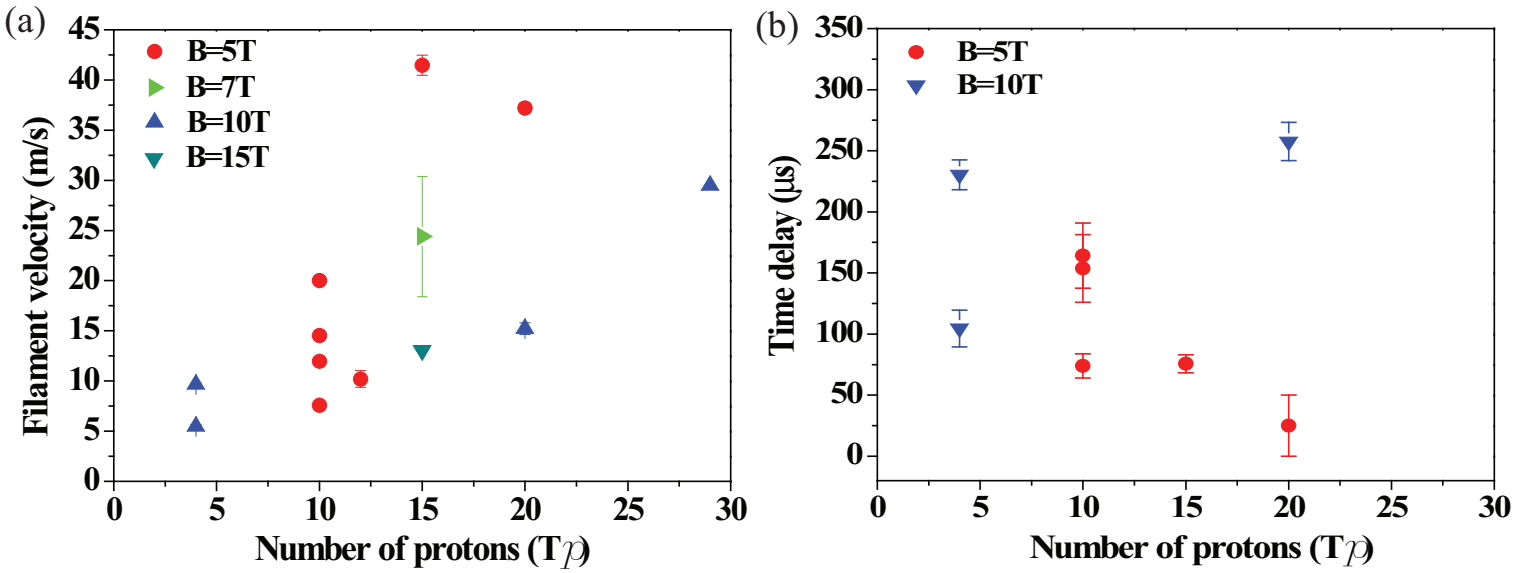

Figure 6.9: Maximum observed filament velocity as a function of 14 GeV beam intensity in magnetic fields. a.) Maximum observed filament velocity. b.) Onset time of that filament.

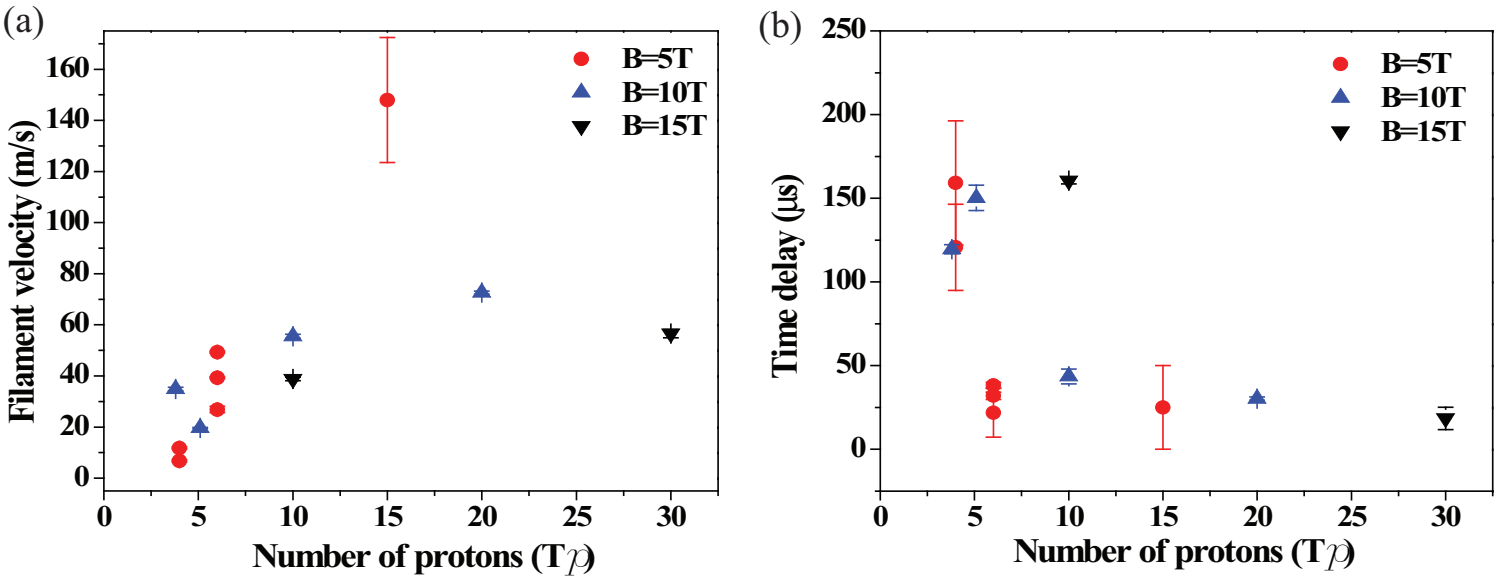

Figure 6.10: Maximum observed filament velocity as a function of 24 GeV beam intensity in magnetic fields. a.) Maximum observed filament velocity. b.) Onset time of that filament.

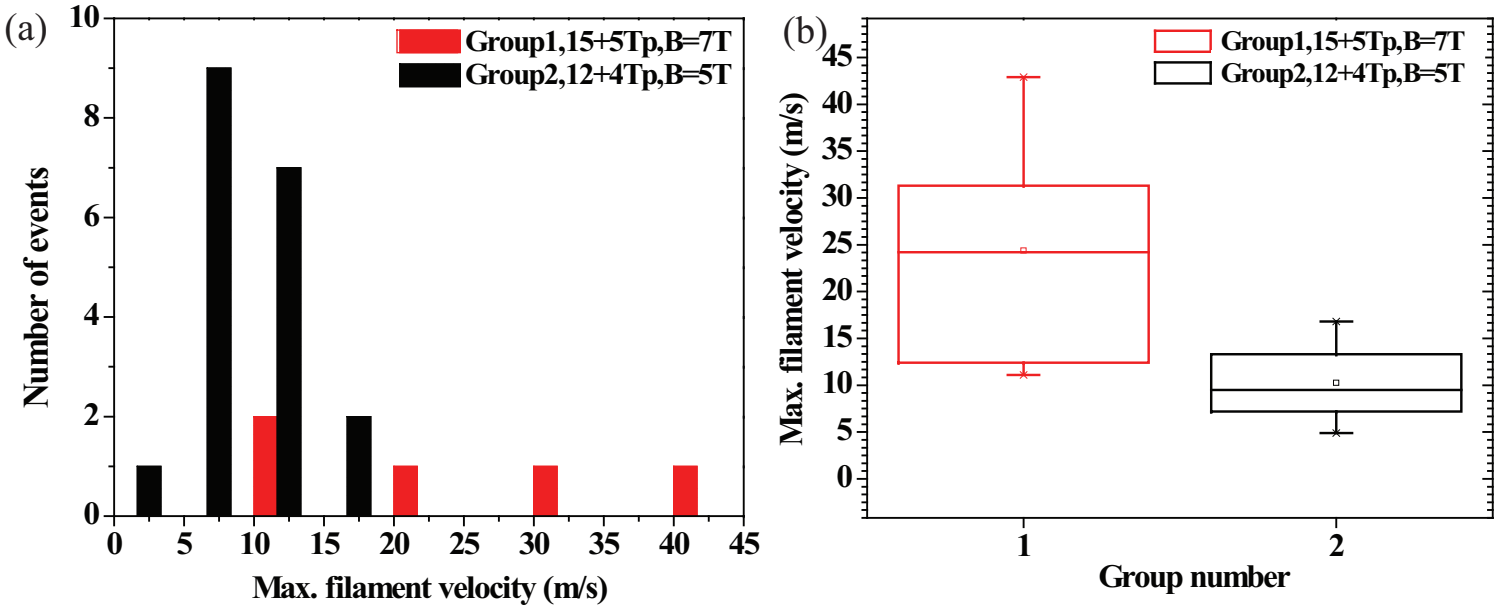

Figure 6.11: Filament velocity measurement in same conditions. Pump-probe conditions with harmonic 8 and 16 bunches are used. The conditions of each group in pump-probe events are given in Table A.4. a.) Histogram of maximum observed filament velocity in each group. b.) Maximum observed filament velocity of each group.

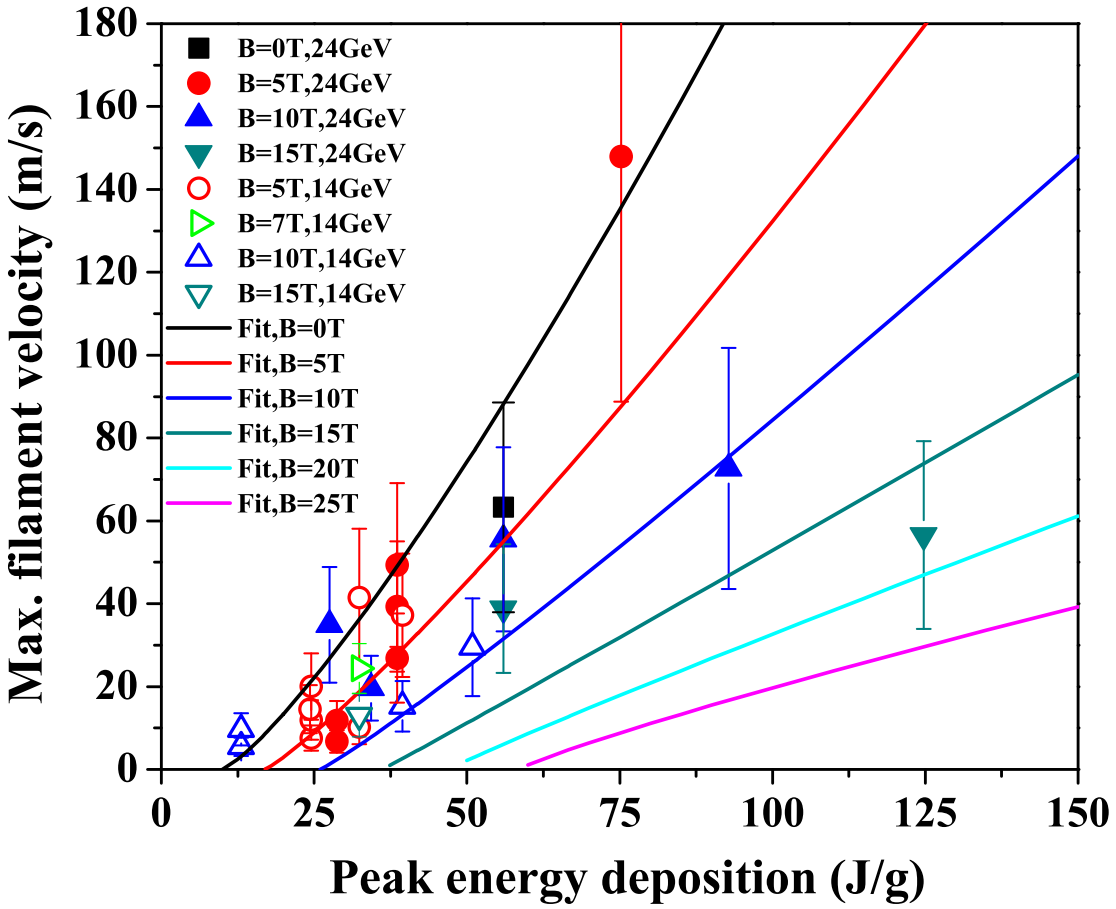

Figure 6.12: Maximum observed filament velocity as a function of peak energy deposition in various magnetic fields and fit is according to Eqn. (6.34).

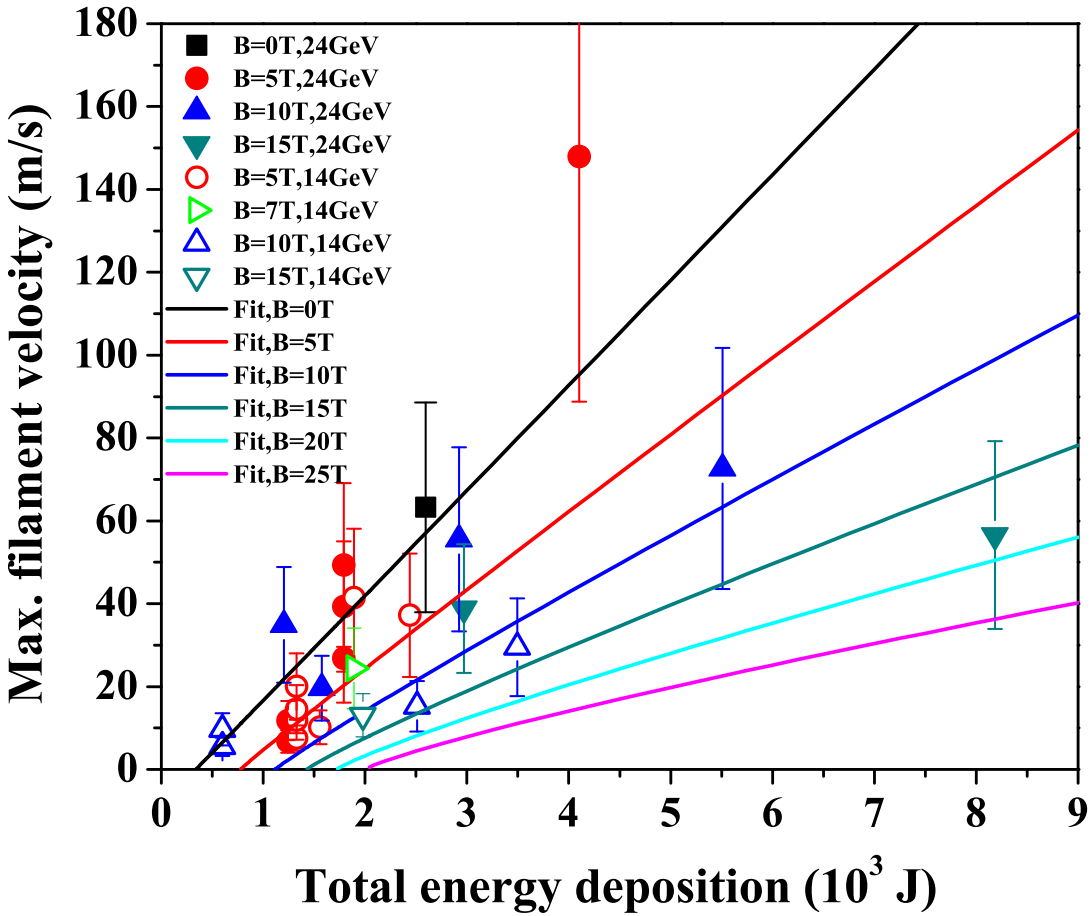

Figure 6.13: Maximum observed filament velocity as a function of total energy deposition in various magnetic fields and fit is according to Eqn. (6.34).

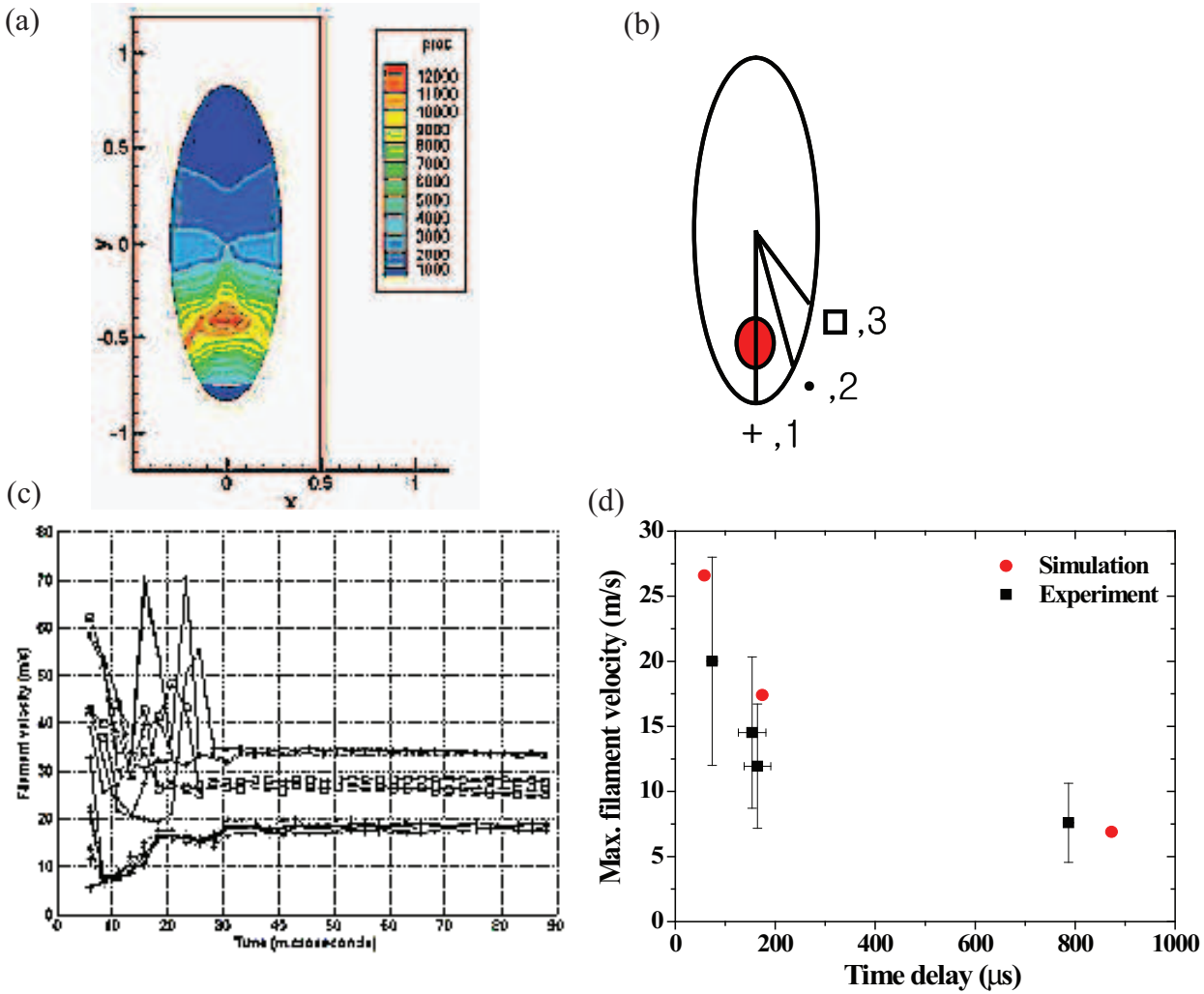

Figure 6.14: Comparison of calculated filament velocity with measurement. 10 Tp with 14 GeV in 0 T is considered in simulation, but 5 T in measurement. a.) Initial pressure contour in Hg jet by energy deposition [8]. b.) Schematic location of picked filament for velocity calculation [7]. c.) Calculated filament velocity on the position 1, 2, and 3 [7]. d.) Apparent filament velocity in simulation and measurement. The apparent filament velocity and the earliest visible time delay in simulation are estimated using Eqn. (6.3) and Eqn. (6.4)

Chapter 7

Conclusions

7.1 Mercury Intense Target Experiment

This experiment is a proof-of-principle test for a high-Z target system capable of accepting a high intensity 4 MW proton beam. The system allows for the production of copious pions which subsequently decay into muons. An experiment at the CERN proton synchrotron that combines a free Hg jet target with a 15 T solenoid magnet with 14 GeV and 24 GeV proton beam was performed. It validates the liquid type of target concept for production of an intense secondary source of muons. When interacted with a beam pulse of 30×10^{12} protons on the Hg target, this generates a peak energy deposition of $\sim$ 125 J/g, which leads to the disruption of Hg target. For this experiment, a 15 T pulsed solenoid was designed. The Hg jet loop system generates a Hg jet from 1 cm diameter nozzle with velocity 15 m/s. An optical diagnostic system based on back-illuminated laser shadow photography is employed to investigate the Hg jet flow. Synchronized short laser light pulses are used to illuminate and freeze the motion of the jet. A total of four optical imaging heads for

each Viewport are mounted on the exterior of the primary containment vessel. Four high speed cameras are used to simultaneously collect images on four Viewports. Integrated all-in-one compact optical heads, consisting of ball lens, illumination fiber, objective lens, and imaging fiber bundle, are placed at the radius of curvature of a retro-reflector allowing for the illumination and imaging collection on one side of the Hg primary containment vessel. Due to the short time of frame rate, the time delay between illumination of the light source and captured image at camera CCD is adjusted, which is judged by the uniformity of consecutive collected image brightness as well as the triggering signal pulse on the oscilloscope for each component of device, so that timing of transient motion of jet interacting with proton beam could be validated. In experiment, the fiber optics coupled diagnostic system played an principal diagnostic role in providing Hg jet target behavior interacting intense proton beam in a high magnetic field. The optical diagnostic system in design requirement had space limited restriction and ultimate environment such as high magnetic field and high radiation area since it was placed in the center of high magnetic field of solenoid right next to the beam-jet interaction. However, no significant image distortion and no change in the functions of instruments including remote control were observed under such a restricted environment during experiment.

7.2 Mercury Jet in a Magnetic Field

In order to understand a conducting flow in a magnetic field, MHD equations considering Lorentz force effect based on the Navier-Stokes equations and Maxwell equations are reviewed. The suppression of vorticity by the perpendicular magnetic field is reported based on the role of Stuart number. As a result, the rotational motion of jet on the surface becomes more two dimensional motion of flow and thus the jet surface is more stabilized, which is observed qualitatively. The energy deposition mechanism by a sudden interaction of proton beam are reviewed by employing energy of state, where the formation of cavities is believed to take place and the cavitation bubbles influence the wave dynamics in Hg. Two phase equation of state is reported to consider the pressure change by energy deposition of proton beam, leading to the breakup of jet and generation of filaments on Hg jet surface. The role of magnetic damping and global energy equations are reviewed, where the global kinetic energy declines exponentially on a time scale of magnetic damping constant if the flow velocity is perpendicular to the applied magnetic field. The phenomenology of magnetic damping explains the decrease of filament velocity as a function of time in a magnetic field.

The motion of Hg jet at Viewport $1 \sim 4$ enabled us to understand Hg jet condition at upstream, midstream, and downstream. Image processing provides the Hg jet size in various magnetic fields. Optical diagnostic observation showed the effects of the magnetic field on the distortion of Hg jet induced by axial current along jet axis interacting with transverse magnetic field generated

by the angle of jet axis with respect to the magnetic field axis, generating Lorentz force, which is possibly the onset of a quadrupole effect at larger than 10 T. The jet size becomes larger at larger magnetic field than 10 T. The comparison of measurement with numerical calculation using Frontier MHD code showed somewhat consistency between 10 T and 15 T, but the experiment observed the nature of diverging turbulent jet. Nevertheless, the stabilizing effect of the magnetic field on turbulent Hg jet is observed. The wave length on the jet surface increases as magnetic field increases. Thus, the jet surface is getting flattened. Therefore, the jet is getting more stabilized. The experimental results clearly show that the magnetic field stabilizes the Hg jet by reducing the amount of fluctuations on jet surface and smoothing out the edges of the otherwise turbulent Hg flow, as previously reported in the literatures [6, 27, 44, 80] and predicted in Frontier MHD simulation. Gravity affected the Hg jet trajectory, so that the Hg jet bended down at downstream. But this deflection of the Hg jet by gravity is reduced at higher magnetic field. The jet axis becomes more straight toward the direction of magnetic field line. The global fit of measured position of jet centroid approximated the Hg jet flow trajectory in a magnetic field, which enabled us to check the position of nozzle and launching velocity of Hg jet at nozzle.

It is reported that the transverse magnetic field drops pressure of flow, resulting decrease the flow velocity and change of velocity profile, so called Hartmann flow. However, it was observed that the longitudinal jet velocity was not changed in ~ 15 T of longitudinal magnetic field. This can be deduced

from Lorentz force equation, where the flow velocity and magnetic field are cross product. This result reinforces the assumption of the Hg jet shape in a magnetic field to be elliptic. The pressure at pipe inlet driven by the syringe piston is measured. The Hg driving pressure was same independent of the magnetic field. Therefore, the Hg flow was not influenced by the longitudinal magnetic field. However, pressure head losses by pipe geometry are investigated. Friction of inside pipe was contributed mainly among several head losses. According to the velocity measurement at upstream, mid-stream, and downstream, it was not significantly changing, but same comparable to that at 0 T. Therefore, the magnetic field effect at the pipe bend is expected to be somewhat negligible, but possibly some discharging loss from nozzle may contribute to reduction of flow velocity.

The comprehensive optical diagnostics allowed us to have a better understanding of the behavior of a conducting jet moving in a high magnetic field environment up to 15 T with jet velocity 15 m/s.

7.3 Disruption of Hg Jet and Filament on Jet Surface in a Magnetic Field

Proton beam spot size by optics is estimated by measuring dispersion and emittance of beam. Also, measurement of beam spot size by camera screen monitor is performed, which showed 2 times larger than that by optics. The beam spot size scales with beam intensity.

Numerical Monte Carlo simulation was performed at FNAL by collaborator

for calculation of energy deposition into Hg jet, where the jet size, trajectory, and proton beam spot size from measurement and magnetic field, beam intensity, and beam energy were input. The jet shape was assumed to be elliptic based on observation and measurement of jet size and flow velocity. The peak energy deposition as well as total energy deposition into Hg jet were calculated. Multi-variable fit provides the relation of peak energy deposition and total energy deposition with beam intensity, beam energy, and magnetic field. Also, the mass weighted averaged energy deposition shows the distribution of energy along jet axis as well as the influence of beam intensity and magnetic field. Since the beam spot size increases with beam intensity, the peak energy deposition decreases with beam intensity, appearing to be parabolically decreasing. However, the total energy deposition into Hg jet was not significantly changed with beam intensity, which approximated to be $\sim 6 \sim 8$ % of the incident beam energy.

The observation of interaction of proton beam up to 30 Tp at both 14 GeV and 24 GeV beam with 15 m/s jet was performed, which provided key results to validate the performance of high power target. The disruption as manifested by the jet break up is caused by energy deposition of proton beam. The disruption typically starts at the bottom surface of Hg jet where the proton beam enters. The disruption typically ends at the top surface of Hg jet where the proton beam leaves. The jet breakup is observed typically at center of jet flow where the maximum energy is deposited. This phenomenon is consistent with the beam trajectory across the jet and the result of energy deposition

distribution calculated by MARS code, as well. Based on the threshold of beam intensity causing the disruption of Hg jet in various magnetic fields, the extent of length of disruption over the entire jet is estimated using the calculated distribution of energy deposition, which gives somewhat agreement with experimentally measured disruption length. A proton beam pulse is composed of 8 and 16 bunches with a doubled bunch period. The effect of pulse structure on disruption length is negligible, which means that the instantaneous time incident to Hg jet by beam does not affect to difference of energy deposition into Hg jet. From the parameterized fit to total energy deposition, peak energy deposition, and fluence, the energy deposition into Hg jet according to beam intensity, beam energy, and magnetic field is estimated, which provides an extrapolated estimation up to 25 T. The threshold of disruption increases in ~ 0.8 power of magnetic field, and it is ~ 338 J of total energy deposition with no magnetic field. Also, the threshold of disruption is ~ 10 J of peak energy deposition with no magnetic field, and it increases in 1.2 power of magnetic field. The disruption length increases in square root power of total energy deposition with no magnetic field, but it is suppressed in $\sim\ 1/(2 + 0.04B)$ power of total energy deposition with magnetic field.

The time scale of magnetic damping indicates the rate of decay of global kinetic energy due to the magnetic field. Therefore, the rising time to peak velocity increases as the magnetic field increases, which corresponds to the transient response time as an indication of magnetic damping. At low intensity of proton beam, the charged beam may be fluctuating depending on the initial

conditions at experiment. Thus, the observed onset time of filament was scattered much at low intensity of beam and it decreases as the intensity of proton beam increases. Therefore, the distribution of filament velocity at lower intensity of beam is more scattered. The effect of geometry of viewing filament is observed. The onset time of filament decreases as the uniformly distributed filament velocity on jet surface increases. The maximum observed filament velocity scales with beam intensity due to the increased energy deposition, but the magnetic field slows the maximum observed filament velocity.

From the parameterized fit to peak energy deposition and total energy deposition, the energy deposition into Hg jet according to beam intensity, beam energy, and magnetic field is estimated, which provides an extrapolated estimation up to 25 T. Measurement from multiple events with repetition under same condition using pump-probe shot showed somewhat good agreement with disruption length results and provided possible error value for deviation occurred by repeating experiment under same condition. The threshold of filament velocity increases in 1.2 power of magnetic field. The filament velocity increases in linear (~ 1.24) power of peak energy deposition with no magnetic field, but it is slowed in $\sim\ 1.24 - 0.015B$ power of peak energy deposition with magnetic field. Comparison of filament velocity with numerical simulation was performed as a check. The effect of geometry of viewing filaments were considered and the measurement showed somewhat lower than that in simulation due to the magnetic field effect and uncertainty of estimated location of filament for consideration of geometry of viewing filament.

Based on the measured data from observation of image and energy deposition estimated by elliptic jet model in MARS code, various global fit provided estimation of the key results and statistic approach such as χ^2 probability provided quality of the goodness of fit. Thus, the various investigations from the analysis of Hg jet motion in a magnetic field and the analysis of disruption length and filament velocity were able to be integrated for providing the basis of forming the conclusion of the experiment.

7.4 Feasibility of High-Z Target for Future Particle Acceleration

The performance and feasibility of utilizing liquid metal jet as a high power target was investigated. The liquid jet target concept is based on the target being recycled after each pulse. Therefore, the power of the target is evaluated in terms of the replacing capability. The optimal interaction length for the 24 GeV beam energy is in the region of 30 cm which corresponds to approximately 2 interaction length for Hg. For a 20 m/s jet velocity, replacing two interaction lengths will be taken in 14 ms thus allowing for operations with a repetition rate of up to 70 Hz. The disruption length at 15 T is less than 20 cm and the total energy deposition is $\sim$ 8000 J. Therefore, 100 $\sim$ 133 kJ of beam energy can be recycled with a 70 Hz repetition rate for 20 m/s jet. This result validates that a target system capable of supporting proton beams with powers of up to 8 MW, which concludes the experiment for investigation of feasibility of Hg jet as a high power target.

Bibliography

[1] M. M. Alsharoa *et al.*, 2003, "Recent progress in neutrino factory and muon collider research within the muon collaboration," *Phys. Rev. ST Accel. Beams*, **6**, 081001. [1]

[2] C. M. Ankenbrandt *et al.*, 1999, "Status of muon collider research and development and future plans," *Phys. Rev. ST Accel. Beams*, **2**, 081001.

[3] J. R. J. Bennett *et al.*, 2004, "Studies of a target system for a 4 MW, 24 GeV proton beam," proposal to the CERN INTC Committee, INTC-P-186, *CERN-INTC-2003-033, INTC-I-049*. [2]

[4] Robert P. Benedict, 1980, *Fundamentals of pipe flow*, John Wiley & Sons, Inc.

[5] A. Bernadon *et al.*, 1998, "A proposal for an R&D program for targetry and capture at a muon collider source," *BNL E951 Proposal*. [3]

[6] V. A. Bernshtam, S. V. Kozyrev, A. I. Él'kin, 1982, "Stability of flow of films of a conducting viscous liquid in longitudunal magnetic field," *Magnetohydrodynamics*, **18**, p. 132.

[7] W. Bo, 2009, "3D Target simulations with front tracking/ghost fluid method," *MERIT Review*. [4]

[8] W. Bo, 2009, "Mercury jet target simulations," *MUTAC Review*. [5]

[1] http://www.cap.bnl.gov/mumu/pubs/prstab-030422/prstab.pdf
[2] http://www.hep.princeton.edu/~mcdonald/mumu/target/cern_proposal.pdf
[3] http://www.hep.princeton.edu/~mcdonald/mumu/target/targetprop.pdf
[4] http://www.hep.princeton.edu/~mcdonald/mumu/target/Bo/hgjet_bo.pdf
[5] http://www.hep.princeton.edu/~mcdonald/mumu/target/samulyak/samulyak_040609.pdf

[9] Herman Branover, 1978, *Magnetohydrodynamic flow in ducts*, John Wiley & Sons, Inc.

[10] Michael P. Brenner, 2002, "Single bubble sonoluminescence," *Rev. Mod. Phys.*, **74**, pp. 425-440.

[11] G. A. Carlson, 1975, "Dynamic tensile strength of mercury," *J. Appl. Phys.*, **46**, pp. 4069-4070.

[12] Donald Chang, Thomas Lundgren, 1961, "Duct flow in magnetohydrodynamics," *Z. Angrew. Math. Phys.*, **12**, pp. 100-114.

[13] I. G. Currie, 1993, *Fundamental Mechanics of Fluids*, Marcel Dekker, Inc.

[14] P. A. Davidson, 1999, "Magnetohydrodynamics in materials processing," *Annu. Rev. Fluid Mech.*, **31**, pp. 273-300.

[15] G. F. D. Duff, D. Naylor, 1966, *Differential equations of applied mathematics*, John Wiley & Sons, Inc.

[16] I. Efthymiopoulos, A. Fabich, J. Lettry, 2005, "CERN installation," *MERIT Review.* [6]

[17] I. Efthymiopoulos, 2008, "The MERIT experiment (nToF11)," *MUTAC Review.* [7]

[18] David H. Evans, 1992, *Probability and its applications for engineers*, Marcel Dekker, Inc.

[19] A. Fabich, 2002, "High power proton beam shocks and magnetohydrodynamics in a mercury jet target for a neutrino factory," *CERN-THESIS-2002-038.* [8]

[20] A. G. Fedin, 1973, "Use of optical methods in investigating MHD processes," *Magnetohydrodynamics*, **9**, pp. 301-308.

[21] T. A. Gabriel, J. R. Haines, T. J. McManamy, P. Spampinato, and B. W. Riemer, 2001, "Targets for high intensity particle production," *Proc. Part. Accel. Conf.*, Chicago, pp. 737-741.

[6] http://www.hep.princeton.edu/~mcdonald/mumu/target/fabich/Fabich_121205.pdf
[7] http://www.hep.princeton.edu/~mcdonald/mumu/target/Ilias/ie_080408.pdf
[8] http://www.hep.princeton.edu/~mcdonald/mumu/target/thesis-2002-038.pdf

[22] J. Gallardo *et al.*, 2001, "Calculation for a mercury jet target in a solenoid magnet capture system," *Proc. Part. Accel. Conf.*, Chicago, pp. 627-629.

[23] J. Gallardo *et al.*, 2002, "First order perturbative calculations for a conducting liquid jet in a solenoid," *MUC-NOTE-TARGET-242, MU-047.* [9]

[24] D. Gao, N. B. Morley, 2002, "Equilibrium and initial linear stability analysis of liquid metal falling film flows in a varying spanwise magnetic field," *Magnetohydrodynamics*, **38**, No. 4, pp. 359-375.

[25] A. K. Geim, M. D. Simon, M. I. Boamfa, M. J. Lighthill, 1999, "Magnetic levitation at your finger tips," *Nature*, **400**, p. 323.

[26] M. B. Glanert, M. J. Lighthill, 1955, "The axissymmetric boundary layer on a long thin cylinder," *Proc. Roy. Soc. Ser.*, **A230**, p. 188.

[27] Richard R. Gold, 1962, "Magnetohydrodynamic pipe flow: Part 1," *J. Fluid Mech.*, **13**, pp.505-512.

[28] R. J. Goldstein, 1991, *Fluid mechanics measurements*, Hemisphere Publishing Co.

[29] Andrew Gray and G. B. Mathews, 1966, *A treatise on Bessel functions and their applications to physics*, Dover, Inc.

[30] V. Graves, 2007, "MIT testing results," *MUTAC Review.* [10]

[31] V. Graves, 2007, "Hg system operation review," *MERIT Review.* [11]

[32] J. Hartmann, 1937, "Hg dynamics I," *Kgl. Danske Videnskab Selskabs Math. Fys.*, **15**, No. 6.

[33] A. Hassanein, I. Konkashbaev, 2001, "Dynamics of liquid metal jets penetrating a strong magnetic field in high power colliders," *Proc. Part. Accel. Conf.*, Chicago, pp. 624-626.

[9] http://www-mucool.fnal.gov/mcnotes/public/pdf/muc0242/muc0242.pdf

[10] http://www.hep.princeton.edu/~mcdonald/mumu/target/graves/VGraves-070418.pdf

[11] http://www.hep.princeton.edu/~mcdonald/mumu/target/graves/Hg_System_Operation_Review.ppt

[34] A. Hassanein, 2000, "Liquid metal targets for high power applications: Pulsed heating and shock hydrodynamics," *Laser and Particle Beams*, **18**, pp. 611-622.

[35] F. Haug, 2009, "Cooling system for the MERIT high power target experiment," *NFMCC Review*. [12]

[36] H. Ito, 1960, "Pressure losses in smooth pipe bends," *Trans. ASME.: J. Basic Eng.*, **82**, p. 131.

[37] Uhlenbusch J., Fishcer E., 1961, "Hydromagnetische strömung im kreiszylindrischen rohr," *Z. Phys.*, **165**, pp. 190-198.

[38] Colin Johnson, 2002, "A self focusing mercury jet target," *CERN-NUFACT-113*. [13]

[39] T. Kakuta, T. Shikama, M. Marui, 1999, "Optical fibers and their applications for radiation measurement," *Seventh Int. Conf. Nucl. Eng.*, Tokyo, Japan, p. 19.

[40] H. G. Kirk *et al.*, 2001, "Target studies with BNL E951 at the AGS," *Proc. Part. Accel. Conf.*, Chicago, pp. 1531-1537.

[41] H. G. Kirk *et al.*, 2008, "The MERIT high power target experiments at the CERN PS," *Proc. European Part. Accel. Conf.*, Genoa, Italy, *WEPP169*.

[42] H. G. Kirk *et al.*, 2008, "A 15 T pulsed solenoid for a high power target experiment," *Proc. European Part. Accel. Conf.*, Genoa, Italy, *WEPP170*.

[43] B. A. Kolovandin, 1965, "Stability of flow of conducting liquid with free surface in the presence of magnetic and electric fields," *Prikl. Mekh.*, **1**, No. 11, p. 95.

[44] S. V. Kozyrev, A. I. Él'kin, 1981, "Stability of flow of thin films of electrically conducting liquid in crossed magnetic and electric fields," *Magnetohydrodynamics*, **17**, No. 4, p. 353.

[12] http://www.hep.princeton.edu/~mcdonald/mumu/target/Pereira/MERIT_PRESENTATION.pdf

[13] http://slap.web.cern.ch/slap/NuFact/NuFact/nf113.pdf

[45] H. C. Lee, 1977, "Boundary layer around a liquid jet," *IBM J. Res. Develop.*, p. 48.

[46] J. Lettry *et al.*, 2003, "Thermal shocks and magnetohydrodynamics in high power mercury targets," *J. Phys. G: Nucl. Part. Phys.*, **29**, p. 1621.

[47] Junwoo Lim *et al.*, 1998, "Control of streamwise vortices with uniform magnetic fluxes," *Phys. Fluids*, **10**, No. 8, p. 1997.

[48] S. P. Lin, D. J. Kang, 1987, "Atomization of a liquid jet," *Phys. Fluids*, **30**, pp. 2000-2006.

[49] C. A. Martins, 2005, "Power converter for the TT2 mercury target project," *MERIT Review.* [14]

[50] K. T. McDonald *et al.*, 2001, "The primary target facility for a neutrino factory based on muon beams," *Proc. Part. Accel. Conf.*, Chicago, p. 1583.

[51] K. T. McDonald, 2000, "Cooling of a target by helium gas," *Princeton /μμ/00-25.* [15]

[52] K. T. McDonald, 2000, "Damping of radial pinch effects," *Princeton /μμ/00-26.* [16]

[53] K. T. McDonald, 2000, "Magnetohydrodynamics of a continuous mercury jet coaxially entering a solenoid," *Princeton /μμ/00-29.* [17]

[54] K. T. McDonald, 2000, "Magnetohydrodynamics of a pulsed mercury jet entering a solenoid at an angle," *Princeton /μμ/00-30.* [18]

[55] K. T. McDonald, 2000, "Optics for E951 target tests in the A3 beamline," *Princeton /μμ/00-28.* [19]

[14] http://www.hep.princeton.edu/~mcdonald/mumu/target/CERN/martins_160305.pdf
[15] http://www.hep.princeton.edu/~mcdonald/mumu/target/thermal.pdf
[16] http://www.hep.princeton.edu/~mcdonald/mumu/target/radialpinch.pdf
[17] http://www.hep.princeton.edu/~mcdonald/mumu/target/continuousjet.pdf
[18] http://www.hep.princeton.edu/~mcdonald/mumu/target/pulsedjet.pdf
[19] http://www.hep.princeton.edu/~mcdonald/mumu/target/a3optics.pdf

[56] K. T. McDonald, H. Park, 2006, "Animation of the paintball test of a 6 mm thick sapphire window," *MERIT Review.* [20]

[57] K. T. McDonald, 2008, *Private Communication.*

[58] K. T. McDonald, 2008, "Geometry of viewing mercury drops," *Princeton /μμ/00-28.* [21]

[59] P. Michael, 2005, "PSFC west cell power convertors," *MERIT Review.* [22]

[60] R. Menikoff, B. Plohr, 1989, "The Riemann problem for fliud flow of real materials," *Rev. Mod. Phys.*, **61**, pp. 75-130.

[61] N. V. Mokhov, 2001, "Paricle production for a muon storage ring: I. Targetry and π/μ yield," *Nucl. Inst. Methods Phy. Res.*, **A472**, pp. 546-551.

[62] N. V. Mokhov, O. E. Krivosheev, 2000, "MARS code status," *FERMILAB-Conf-00/181.* [23]

[63] Neil B. Morley *et al.*, 2000, "Liquid megnetohydrodynamics: recent progress and future directions for fusion," *Fusion Eng. and Des.*, **51**, pp. 701-713.

[64] Neil B. Morley, Sergey Smolentsev, Donghong Gao, 2002, "Modeling infinite/axisymmetric liquid metal magnetohydrodynamic free surface flows," *Fusion Eng. and Des.*, **63**, pp. 343-351.

[65] 2007, *Origin 8 User Guide*, OriginLab Corporation.

[66] S. Ozaki, R. Palmer, M. Zisman, J. Gallardo, 2001, "Neutrino factory feasibility study 2," *BNL-52623.* [24]

[67] N. Otsu, 1979, "A threshold selection method from gray-level histograms," *IEEE Trans. Sys. Man. Cyber.*, **9**, pp. 62-66.

[20] http://www.hep.princeton.edu/~mcdonald/mumu/target/paintball/paintball_sapphire.gif
[21] http://www.hep.princeton.edu/~mcdonald/mumu/target/droplet.pdf
[22] http://www.hep.princeton.edu/~mcdonald/mumu/target/MIT/West_Cell_Power_Convertors.pdf
[23] http://lss.fnal.gov/archive/2000/conf/Conf-00-181.pdf
[24] http://www.cap.bnl.gov/mumu/studii/FS2-report.html

[68] Shuzo Oshima *et al.*, 1987, "The shape of a liquid metal jet under a non-uniform magnetic field," *JSME Int. J.*, **30**, No. 261, pp. 437-448.

[69] R. B. Palmer, 1998, "Muon collider design," *BNL-65242*, CAP-200-MUON-98C. [25]

[70] Mark A. Pinsky, 1991, *Partial differential equations and boundary value problems with applications*, McGraw-Hill, Inc.

[71] Jose Pujol, 2007, "The solution of nonlinear inverse problems and the Levenberg-Marquardt method," *Geophys.*, **72**, pp. W1-W16.

[72] R. D. Reitz, F. V. Bracco, 1982, "Mechanism of atomization of a liquid jet," *Phys. Fluids*, **25**, pp. 1730-1742.

[73] Uflyand Y. S., 1960, "Hartmann problem for a circular tube," *Soviet Phys.*, **5**, pp. 1194-1196.

[74] SAE, 1960, "Aero-space thermodynamics manual," pp. A18-A20.

[75] R. Samulyak, Y.Prykarpatskyy, 2004, "Richtmyer-Meshkov instability in liquid metal flows: influence of cavitation and magnetic fields," *Math. Comp. in Simulations*, **65**, pp. 431-446.

[76] R. Samulyak, 2006, "Target simulations," *MUTAC Review.* [26]

[77] R. Samulyak, J. Du, J. Glimm, Z. Xu, 2007, "A numerical algorithm for MHD of free surface flows at low magnetic Reynolds numbers," *J. Comp. Phys.*, **226**, pp. 1532-1549.

[78] R. Samulyak, 2007, "Mercury target simulations," *Oxford-Princeton High Power Target Review.* [27]

[79] J. A. Shercliff, 1953, "Steady motion of conducting fluids in pipes under transverse magnetic fileds," *Proc. Camb. Phil. Soc.*, **49**, pp. 136-144.

[80] J. A. Shercliff, 1956, "The flow of conducting flows in circular pipes under transverse magnetic fields," *J. Fluid Mech.*, **13**, pp. 644-666.

[25] http://www.osti.gov/bridge/servlets/purl/658363-S5MT4Z/webviewable/658363.pdf

[26] http://www.hep.princeton.edu/~mcdonald/mumu/target/samulyak/mutac06_samulyak_targetsimulations.pdf

[27] http://www.hep.princeton.edu/~mcdonald/mumu/target/samulyak/samulyak_110708.pdf

[81] J. A. Shercliff, 1962, "Magnetohydrodynamic pipe flow: Part 2 High Hartmann number," *J. Fluid Mech.*, **13**, pp. 513-518.

[82] J. A. Shercliff, 1965, *A textbook of magnetohydrodynamics*, Pergamon Press.

[83] N. Simos, 2005, "MERIT experiment window study," *BNL Review.* [28]

[84] P. Sievers, P. Pugnat, 2000, "Response of solid and liquid targets to high power proton beams for neutrino factories," *CERN LHC/2000-4, CERN-NuFACT Note 035.* [29]

[85] G. Skoro, 2008, "MERIT beam spot size : saturations and projections," *MERIT Review.* [30]

[86] K. Stewartson, 1955, "The asymtotic boundary layer on a circular cylinder in axial incompressible flow," *Q. Appl. Math.*, **13**, p. 113.

[87] P. T. Spampinato *et al.*, 2005, "A free jet mercury system for use in a high power target experiment," *Proc. Part. Accel. Conf.*, Knoxville, p. 1637.

[88] S. Striganov, 2009, Private Communication. [31] [32] [33]

[89] S. Striganov, 2009, "Energy deposition of 24 GeV/c protons in gravity affected mercury jet," *MERIT Review.* [34]

[90] P. Thieberger, H. G. Kirk, R. J. Weggel, K. T. MacDonald, 2003, "Moving solid metallic targets for pion production in the muon collider/neutrino factory project," *Proc. Part. Accel. Conf.*, Portland, p. 1634.

[91] P. H. Titus, 2007, "Design report: MERIT BNL E951 15 T pulsed magnet for mercury target development," *MERIT Review.* [35]

[92] T. Tsang, 2006, Private Communication.

[28] http://www.hep.princeton.edu/~mcdonald/mumu/target/simos/Simos_121205.pdf
[29] http://cdsweb.cern.ch/record/468537/files/lhc-2000-004.pdf
[30] http://www.hep.princeton.edu/~mcdonald/mumu/target/Skoro/Saturation_profiles.pdf
[31] http://www-ap.fnal.gov/~strigano/merit/edep_in_target/gravity/24gev-beam-updated/
[32] http://www-ap.fnal.gov/~strigano/merit/edep_in_target/gravity/24gev-beam-updated/ellipse/
[33] http://www-ap.fnal.gov/~strigano/merit/edep_in_target/gravity/24gev-beam-updated/ellipse/new/
[34] http://www.hep.princeton.edu/~mcdonald/mumu/target/Striganov/edep-grav.pdf
[35] http://www.hep.princeton.edu/~mcdonald/mumu/target/MIT/design/magnet_design_0307.pdf

[93] N. Tsoupas *et al.*, 2003, "Injection acceleration and extraction of high intensity proton beam for the neutrino facility project at BNL," *Proc. Part. Accel. Conf.*, Portland, p. 1637.

[94] C. D. West, 2000, "Cavitation in a mercury target," *ORNL/TM2000/263.* [36]

[95] H. Q. Yang, 1992, "Asymmetric instability of a liquid jet," *Phys. Fluids*, **30**, pp. 681-689.

[96] K. T. Yen, 1967, "Role of intermittency in free turbulent flows," *AIAA*, **5**, No. 12, pp. 2187-2192.

[97] W. M. Yao *et al.*, 2006, "Accelerator physics of colliders," *J. Phys.*, **33**, No. 1, pp. 35-62.

[36] http://www.hep.princeton.edu/~mcdonald/mumu/target/hg_cavitation.pdf

Appendix A

Tabular Data for Chapter 3, 4, 5, and 6

A.1 Specifications of Optics

Table A.1: Specifications of optical components in optical diagnostics.

Item	Value
Right angle prism mirror	Gold coated, 25 × 25 × 35.4, Surface flatness $\lambda/10$
Gradient index lens	
Size	d=1.0 mm, L=2.48 mm
Numerical aperture	0.5
Working distance	Infinity
Coating	AR coated at 800 ∼ 960 nm
Sapphire ball lens	D=0.5 mm, Al_2 O_3, Index of refraction=1.77
Retro-reflecting Parabolic mirror	
Diameter	76.2 mm
Thickness	12.7 mm
Focal length	444 mm
Coating	Gold
Microscope objective	
Magnification	40 ×
Numerical aperture	0.65

Continued on next page

Table A.1: *Continued from previous page*

Item	**Value**
Working distance	0.6 mm
Clear aperture	5.0 mm
Power	160 mm (tube length) / f
Optical fiber	
Number of picture elements	30000
Jacketing diameter	800 μm
Picture elements area diameter	720 μm
Coating diameter	960 μm
Core material	GeO_2 containing Silica
Coating material	Silicone
Numerical aperture	0.35
Allowable bending radius	40 mm
Core diameter	200 μm

A.2 Mercury Properties

Table A.2: Properties of mercury.

Property	**Value**	**Unit**
Atomic number	80	-
Atomic mass	200.59	-
Number of neutrons	121	-
Classification	Transition metal	-
Melting point	-38.87	°C
Boiling point	356.58	°C
Density	13.456 at 25 °C	g/cm^3
Isotopes	Hg-194 Hg-206	-
Group in periodic table	12	-
Period in periodic table	6	-
Electrical conductivity	1.06×10^6 at 25 °C	Ω^{-1} m^{-1}
Thermal conductivity	8.34	W m^{-1} K^{-1} at 27 °C
Specific heat	0.139	J g^{-1} K^{-1}
Heat of vaporization	59.229	kJ/mol
Heat of fusion	2.295	kJ/mol
Electrical resistivity	961 at 25 °C	n Ω· m
Speed of sound	1451.4 at 20 °C	m/s
Coeff. thermal expansion	60×10^{-6} at 20 °C	K^{-1}
Bulk modulus	25	GPa
Dynamic viscosity	1.552×10^{-3}	kg m^{-1} s^{-1}
Kinematic viscosity	1.145×10^{-7}	m^2 s^{-1}
Dielectric constant	1.00074	-
Surface tension	485.5 (Hg-Air) at 25 °C	mN/m °C
Magnetic susceptibility	- 2.9×10^{-5}	-

A.3 Specifications of Hg Pressure Sensor

Table A.3: Features of pressure transducer (Swagelok PTI-S-AG400-15AW).

Item	**Value**
Accuracy	0.5 % LPC of span
Hysteresis	0.1 % of span
Response time	1 milliseconds
Process connection	G1/2B EN, Internal diaphragm type
Max. working pressure	400 bar
Min. working pressure	0 bar
Sensor type	Metal thin film
Over pressure rating	800 bar
Temperature rating(media)	-30 to 100 °C

A.4 Measurement of Events with Pump-Probe Condition

Table A.4: Measurement of disruption length and filament velocity in pump-probe condition with 8 and 16 harmonic bunches.

Condition		N[1], DL[2]	A[3], DL	S[4], DL	N, V[5]	A, V	S, V
Group 1	12+4 bunches 15+5 Tp 7 T	5	19.5	4.1	5	24.4	13.4
Group 2	6+2 bunches 12+4 Tp 5 T	30	19.8	6.1	19	10.2	3.6
Group 2, Spec. 1	700 μs delay	12	19	5	6	12.4	3.7
Group 2, Spec. 2	350 μs delay	11	22.2	7.2	7	8.4	1.9
Group 2, Spec. 3	40 μs delay	7	17.3	5	6	10.2	4.1
Group 3	8 bunches 16 Tp 5 T	6	24.8	7.1	-	-	-
Group 4	8 bunches 6 Tp 5 T	6	5.9	3.8	-	-	-

[1] N represents number of events for measurement.

[2] DL (cm) represents disruption length of jet.

[3] A represents average of measurement.

[4] S represents standard deviation of measurement.

[5] V (m/s) represents filament velocity on jet surface.

A.5 Beam Program List and Disruption Length Measurement

Table A.5: Measured disruption length and beam shot program. Item 1 is shot number. The first digit represents experiment run day and last 2 $\sim$ 3 digits represent shot numbers of the day. For example, in shot 2003, 2 represents experiment day 2 and 3 represents shot number 3 of experiment day 2. Item 2 is number of bunches. Item 3 is number of protons (Tp). Item 4 is magnetic field (T). Item 5 is designated velocity of jet shot (m/s). Item 6 is $L_{disruption}$ (m). Item 7 is $\sigma_{disruption}$ ($\pm$ m).

1	**2**	**3**	**4**	**5**	**6**	**7**
2002	1	0.25	0	0	-	-
2003	1	0.25	0	0	-	-
2004	1	0.25	0	0	-	-
2005	1	0.25	0	0	-	-
2006	1	0.25	0	0	-	-
2007	1	0.25	0	0	-	-
2008	1	0.25	0	0	-	-
2009	1	0.25	0	0	-	-
2011	1	0.25	0	0	-	-
2012	1	0.25	0	0	-	-
2013	1	0.25	0	0	-	-
2014	1	0.25	0	0	-	-
2015	1	0.25	0	0	-	-
2016	1	0.25	0	0	-	-
2017	1	0.25	0	0	-	-
2018	1	0.25	0	0	-	-
2019	1	0.25	0	0	-	-
2020	1	0.25	0	0	-	-
2021	1	0.25	0	0	-	-

Continued on Next Page...

Table A.5 – Continued

1	2	3	4	5	6	7
2022	1	0.25	0	0	-	-
2023	1	0.25	0	0	-	-
2026	1+1	0.5	0	15	0.085	4.000
3003	1+1	0.5	0	0	-	-
3005	1+1	0.5	0	0	-	-
3006	12+4	4	0	0	-	-
3007	12+4	4	0	0	-	-
3008	12+4	4	0	0	-	-
3011	12+4	4	0	0	-	-
3012	12+4	4	0	0	-	-
3014	1	0.25	0	0	-	-
3015	1	0.25	0	0	-	-
3016	1	0.25	0	15	No image	-
3017	1	0.25	0	15	0	0.000
3018	1	0.25	0	15	0	0.000
3019	1	0.25	0	15	0.013	0.021
3020	1	0.25	0	15	0	0.000
3021	1	0.25	0	15	0.005	0.016
3022	1	0.25	0	15	0.029	0.027
3023	1	0.25	0	15	0	0.000
3024	1	0.25	0	15	No image	-
3025	1	0.25	5	15	0	0.000
4001	1	0.25	0	15	0.018	0.023
4002	1	0.25	5	15	0	0.000
4003	1	0.25	5	15	0	0.000
4004	1	0.25	5	15	0	0.000
4005	1	0.25	5	15	0.054	0.032
4006	1	0.25	5	15	0.019	0.023
4007	1	0.25	5	15	0	0.000
4008	1	0.25	5	15	0	0.000
4009	1	0.25	5	15	No image	-
4010	1	0	5	0	-	-
4011	1	0.3	0	0	-	-
4012	1	0.3	5	0	-	-
4013	1	0.3	0	0	-	-
4014	1	0.3	5	15	0.007	0.017

Continued on Next Page...

Table A.5 – Continued

1	2	3	4	5	6	7
4015	16	10	5	15	0.031	0.027
4016	16	10	5	0	-	-
4017	16	10	0	15	0.038	0.029
4019	16	10	0	15	0.062	0.033
4020	2	0.5	0	0	-	-
4021	2	0.5	0	0	-	-
4023	2	0.5	0	0	-	-
4024	2	0.5	0	0	-	-
4025	2	0.5	0	0	-	-
4026	2	0.5	0	0	-	-
4028	16	10	0	0	-	-
4030	16	10	0	15	0.143	0.043
4031	16	10	5	15	0.08	0.036
5003	4	1	5	15	0	0.000
5004	16	10	5	15	0.111	0.040
5005	16	10	5	15	No image	-
5006	16	10	5	15	No image	-
5007	16	10	5	15	0.024	0.025
5008	16	10	5	15	0.031	0.027
5009	8	5	5	15	0.033	0.028
5010	8	5	5	15	0.022	0.025
5011	8	5	0	15	0.084	0.037
5012	16	10	5	15	No image	-
5014	16	15	0	15	No image	-
5015	16	15	5	15	0.189	0.047
5016	16	15	5	15	0.18	0.046
5017	16	20	5	15	0.303	0.054
5018	16	20	5	15	0.283	0.053
5019	16	20	5	15	0.204	0.048
5020	16	20	10	15	0.184	0.046
6001	16	4	0	15	0	0.000
6002	16	4	0	15	0.027	0.026
6003	16	10	5	15	0.105	0.039
6004	16	10	5	15	0.105	0.039
6005	16	10	5	15	0.035	0.028
6006	16	10	5	15	0.173	0.046

Continued on Next Page...

Table A.5 – Continued

1	2	3	4	5	6	7
6007	16	10	5	15	0.028	0.026
6008	16	10	5	15	0.052	0.032
6009	16	10	5	15	0.079	0.036
6010	16	10	5	15	0.074	0.035
6011	16	10	5	0	-	-
6012	1	0.25	0	0	-	-
6013	1	0.25	0	0	-	-
6014	1	0.25	0	0	-	-
6015	1	0.25	0	0	-	-
6016	1	0.3	0	0	-	-
6017	1	0.3	0	0	-	-
6018	1	0.3	0	0	-	-
6019	1	0.3	0	0	-	-
6020	1	0.3	0	0	-	-
6021	1	0.3	0	0	-	-
6022	1	0.3	0	0	-	-
6023	1	0.3	0	0	-	-
6024	16	4	0	0	-	-
6025	16	4	0	0	0.092	0.038
6026	16	4	0	15	0.101	0.039
6027	16	4	0	15	0.095	0.038
6028	16	4	5	15	0.005	0.016
6029	16	4	5	15	0.038	0.029
6030	16	4	10	15	0.044	0.030
6031	16	4	10	15	0.058	0.033
7001	16	4	0	0	-	-
7002	16	4	5	0	-	-
7003	16	4	10	0	-	-
7004	16	4	0	15	0.019	0.023
7005	16	4	0	15	0.036	0.028
7006	16	4	10	15	0.014	0.021
7008	16	4	0	0	-	-
7009	16	4	0	0	-	-
7010	16	4	0	0	-	-
7011	16	4	0	0	-	-
7012	16	4	0	0	-	-

Continued on Next Page...

Table A.5 – Continued

1	2	3	4	5	6	7
7013	16	4	0	0	-	-
7014	16	4	0	0	-	-
7015	16	4	0	0	-	-
7016	16	4	10	15	0	0.000
7017	16	4	10	0	-	-
7021	16	4	0	0	-	-
7022	16	4	0	0	-	-
7023	16	4	10	15	0.082	0.036
7024	16	4	10	0	-	-
7025	16	4	10	0	-	-
8001	16	4	0	0	-	-
8002	16	4	0	15	0.016	0.022
8003	16	4	0	15	0.024	0.025
8004	16	4	0	0	-	-
8005	16	4	0	15	0.051	0.032
8006	16	4	0	0	-	-
8007	16	4	0	15	0.147	0.043
8008	16	4	0	0	-	-
8009	16	4	0	15	0.132	0.042
8010	16	4	0	15	0.419	0.059
8011	16	4	0	0	-	-
8012	16	4	0	15	0.041	0.030
8013	16	4	0	0	-	-
8014	16	4	0	15	0.107	0.039
8015	16	4	0	0	-	-
8016	16	4	5	15	0	0.000
8017	16	4	5	0	-	-
8018	16	4	5	15	0.027	0.026
8019	16	4	5	0	-	-
8020	-	0	5	15	0	0.000
8021	16	4	5	15	0	0.000
8022	16	4	5	0	-	-
8029	16	4	7	15	No image	
8030	16	4	7	15	0	0.000
8031	16	4	7	0	-	-
8032	16	4	7	15	0	0.000

Continued on Next Page...

Table A.5 – Continued

1	2	3	4	5	6	7
8033	16	4	7	0	-	-
8034	12+4	15+5	7	15	0.208	0.048
8035	12+4	15+5	7	15	0.152	0.044
8036	12+4	15+5	0	0	-	-
8037	12+4	15+5	7	15	0.16	0.044
8038	0	0	7	0	-	-
8039	-	-	0	0	-	-
8040	-	-	0	0	-	-
8041	12+4	15+5	7	15	0.203	0.048
8042	12+4	15+5	7	0	-	-
8043	12+4	15+5	7	0	-	-
8044	12+4	15+5	7	15	0.253	0.051
8045	12+4	15+5	7	15	0.165	0.045
8046	12+4	15+5	0	0	-	-
8047	12+4	15+5	7	0	-	-
9003	1	0.25	5	15	0	0.000
9004	16	4	5	15	0.064	0.034
9005	16	4	5	15	0.082	0.036
9006	16	4	5	15	0.215	0.049
9008	16	4	5	15	0.08	0.036
9009	12	3	5	15	0.108	0.040
9010	8	2	5	15	0	0.000
9011	-	-	-	-	0.068	0.034
9012	10	2.5	5	15	0.04	0.029
9013	-	-	-	-	0.04	0.029
9014	12	3	5	15	0.078	0.036
9015	16	6	7	15	0.162	0.045
9016	16	4	7	15	0.109	0.040
9017	12	3.32	7	15	0.005	0.016
9018	12	3.64	7	15	0	0.000
9019	12	3.78	7	15	0.04	0.029
9020	12	5.1	10	15	0.079	0.036
10001	16	4	0	0	No image	-
10002	16	4	0	0	No image	-
10003	16	4	0	15	0.188	0.047
10004	16	4	5	15	0.202	0.048

Continued on Next Page...

Table A.5 – Continued

1	2	3	4	5	6	7
10005	16	4	5	15	0.128	0.042
10006	18	4	10	15	0.038	0.029
10007	16	10	5	15	0.258	0.051
10008	16	15	5	15	0.291	0.053
10009	4	6	5	15	0.154	0.044
10010	2+2	6	5	15	0.184	0.046
10011	2+2	6	5	15	0.294	0.053
10012	4	6	5	15	0.228	0.049
10013	4	6	5	15	0.182	0.046
10014	4	6	5	0	-	-
10015	2+2	6	5	15	No image	-
10016	8	6	5	15	0.155	0.044
10017	8	6	5	0	-	-
10018	4+4	6	5	15	0.25	0.051
10019	4+4	6	5	0	-	-
11001	4	1	0	15	0.029	0.027
11002	16	6	5	15	0.202	0.048
11004	4	6	5	15	0.26	0.051
11005	4	6	5	15	0.246	0.051
11006	4	6	5	15	0.239	0.050
11007	4	6	5	15	0.174	0.046
11008	4	6	5	15	0.122	0.041
11010	4	6	5	15	0.194	0.047
11019	16	10	10	15	0.167	0.045
11020	16	3.5	10	15	0	0.000
11021	16	3.8	10	15	0.062	0.033
11022	16	15	10	15	0.158	0.044
11032	16	20	10	15	0.218	0.049
11033	16	30	10	15	0.214	0.049
11034	16	30	15	15	0.164	0.045
12001	4	5	0	15	0.201	0.048
12003	4	5	0	15	0.238	0.050
12004	4	5	0	15	0.273	0.052
12005	4	5	0	15	0.245	0.051
12007	-	-	0	15	0.039	0.029
12006	4	4	0	15	0.149	0.044

Continued on Next Page...

Table A.5 – Continued

1	2	3	4	5	6	7
12008	4	4	0	15	0.252	0.051
12009	4	4	5	0	-	-
12010	4	4	5	15	0.103	0.039
12011	4	4	5	15	0.079	0.036
12012	4	4	5	15	0	0.000
12013	4	4	5	0	-	-
12014	4	4	0	0	-	-
12015	4	4	5	15	0.105	0.039
12016	4	4	5	0	-	-
12029	8	15	15	15	0.046	0.031
12031	8	10	0	15	0.368	0.057
12032	8	10	15	15	0.149	0.044
12033	16	30	15	20	0.17	0.045
13001	2	2.5	0	15	0.042	0.030
13002	4	5	0	15	0.129	0.042
13003	4	5	0	15	0.138	0.043
13004	4	8	0	15	0.156	0.044
13007	6+2	16	5	15	0.157	0.044
13008	6+2	16	5	15	0.202	0.048
13009	6+2	16	5	15	0.196	0.047
13010	6+2	16	5	15	0.157	0.044
13011	6+2	16	5	15	0.17	0.045
13012	6+2	16	5	0	-	-
13013	6+2	16	5	15	0.221	0.049
13014	6+2	16	5	0	-	-
13015	6+2	16	5	15	0.167	0.045
13016	6+2	16	5	0	-	-
14008	6	6	5	15	0.061	0.033
14009	6	6	5	15	0.103	0.039
14010	6	6	5	15	0	0.000
14011	6	10	5	15	0.174	0.046
14012	6	10	5	0	-	-
14013	6	10	5	0	-	-
14014	6	10	5	15	0.151	0.044
14015	6	10	5	15	0.261	0.052
14017	6+2	16	5	15	0.29	0.053

Continued on Next Page...

Table A.5 – Continued

1	2	3	4	5	6	7
14018	6+2	16	5	15	0.239	0.050
14019	6+2	0	5	15	0.127	0.042
14020	6+2	16	5	0	-	-
14021	6+2	16	5	0	-	-
14022	6+2	16	5	15	0.233	0.050
14023	6+2	16	5	0	-	-
14024	6+2	16	5	15	0.119	0.041
14025	6+2	16	5	0	-	-
14026	6+2	16	5	15	0.215	0.049
14027	6+2	16	0	0	-	-
14028	6+2	16	5	15	0.186	0.047
14029	6+2	16	5	15	0.283	0.053
14030	6+2	16	5	0	-	-
14031	6+2	16	5	15	0.138	0.043
14032	6+2	16	5	0	-	-
14033	6+2	16	5	15	0.189	0.047
14034	6+2	16	5	15	0.383	0.058
14035	6+2	16	5	0	-	-
14036	6+2	4	5	15	0.032	0.027
14037	8	4	5	15	0	0.000
15001	8	4	5	15	0.014	0.021
15002	6+2	16	5	15	0.228	0.049
15003	6+2	16	5	15	0.117	0.041
15004	6+2	16	5	15	0.259	0.051
15005	6+2	16	5	0	-	-
15006	6+2	16	5	15	0.245	0.051
15007	6+2	16	5	0	-	-
15008	6+2	16	5	15	0.2	0.048
15009	6+2	16	5	0	-	-
15010	6+2	16	5	15	0.103	0.039
15011	6+2	16	5	15	0.188	0.047
15012	6+2	16	5	15	0.26	0.051
15013	6+2	16	5	0	-	-
15014	6+2	16	5	15	0.195	0.047
15015	6+2	16	5	0	-	-
15016	6+2	16	5	15	0.173	0.046

Continued on Next Page...

Table A.5 – Continued

1	2	3	4	5	6	7
15017	6+2	16	5	0	-	-
15018	6+2	16	5	15	0.157	0.044
15019	6+2	16	5	15	0.132	0.042
15020	8	16	5	15	0.341	0.056
15021	8	16	5	15	0.165	0.045
15022	8	16	5	15	0.236	0.050
15023	8	16	5	15	0.26	0.051
15024	8	16	5	0	-	-
15025	8	16	5	15	0.175	0.046
15026	8	16	5	0	-	-
15027	8	16	5	15	0.313	0.054
15028	8	16	5	15	-	-
15029	8	6	5	15	0.066	0.034
15030	8	6	5	0	-	-
15031	8	6	5	15	0.068	0.034
15032	8	6	5	0	-	-
15033	8	6	5	15	0.026	0.026
15034	8	6	5	0	-	-
15035	8	6	5	15	0.021	0.024
15036	8	6	5	0	-	-
15037	8	6	5	15	0.115	0.040
15038	8	10	5	15	0.08	0.036
15039	8	8	5	15	0.053	0.032
15040	8	8	5	15	0.054	0.032
15041	8	6	5	15	0.008	0.018
15042	8	6	5	15	0.007	0.017
15043	16	6	5	15	0.027	0.026
15044	4	12	5	15	0.043	0.030
15045	4	12	5	15	0.027	0.026
16001	4	2	0	15	0.082	0.036
16002	4	10	4.1	15	0.068	0.034
16003	4	12	4.1	15	0.205	0.048
16004	4	14	6	15	0.222	0.049
16005	8	12	5	15	0.136	0.042
16006	8	12	5	15	0.208	0.048
16007	8	12	5	15	0.189	0.047

Continued on Next Page...

Table A.5 – Continued

1	2	3	4	5	6	7
16008	4+4	6+6	5	15	0.212	0.048
16009	4+4	6+6	5	15	0.071	0.035
16010	4+4	6+6	5	15	0.164	0.045
16011	4+4	6+6	5	15	0.215	0.049
16012	4	14	5	15	0.229	0.050
16013	4	14	10	15	0.188	0.047
16014	4	12	10	15	0.172	0.045
16015	4	12	15	15	0.144	0.043
16016	4	10	5	15	0.131	0.042
17001	16	6	5	15	0.015	0.022
17002	16	8	5	15	0.125	0.041
17003	16	6	5	15	0.037	0.029
17004	16	6.3	5	15	0.048	0.031
17005	16	6	5	15	0.013	0.021
17006	16	6	7	15	0.093	0.038
17007	16	4.2	7	15	0	0.000
17008	16	8	7	15	0.101	0.039
17009	8+8	8	7	15	0.074	0.035
17010	8+8	8	7	15	0.062	0.033
17011	8+8	8	7	15	0.155	0.044
17012	8+8	8	7	15	-	-
17013	8+8	8	7	15	0.047	0.031
17014	8+8	8	7	15	0	0.000
17015	8+8	7.5	7	15	0.016	0.022
17016	8+8	7.4	7	15	0.086	0.037
17017	8+8	8.4	7	15	0.111	0.040
17018	8+8	6	7	15	0.057	0.033
17019	8+0	4	7	15	0.007	0.017
17020	8+0	6	7	15	0.059	0.033
17021	16	15	10	15	0.174	0.046
17022	16	15	15	15	0.148	0.043
17023	16	29	15	15	0.18	0.046
17024	16	29	10	20	0.23	0.050

Appendix B

Image Data for Chapter 6

B.1 Images for Filament Velocity Measurement at Viewport 2

Table B.1: Properties of shots used for filament velocity analysis. Item 1 is shot number. Item 2 is camera frame rate (μs). Item 3 is beam energy (GeV). Item 4 is number of bunches. Item 5 is number of protons (Tp). Item 6 is magnetic field (T). Item 7 is designated velocity of jet shot (m/s). Item 8 is lag time between peak laser emission and proton beam arrival (μs).

1	2	3	4	5	6	7	8
11004	25	24	4	6	5	15	-4.03
11007	25	24	4	6	5	15	-3.97
11010	25	24	4	6	5	15	-3.99
11019	25	24	16	10	10	15	-2.43
11021	25	24	16	3.8	10	15	-2.43
11032	25	24	16	20	10	15	-2.03
12031	25	24	8	10	0	15	-1.93
12032	25	24	8	10	15	15	-1.83
12033	25	24	16	30	15	20	-1.85

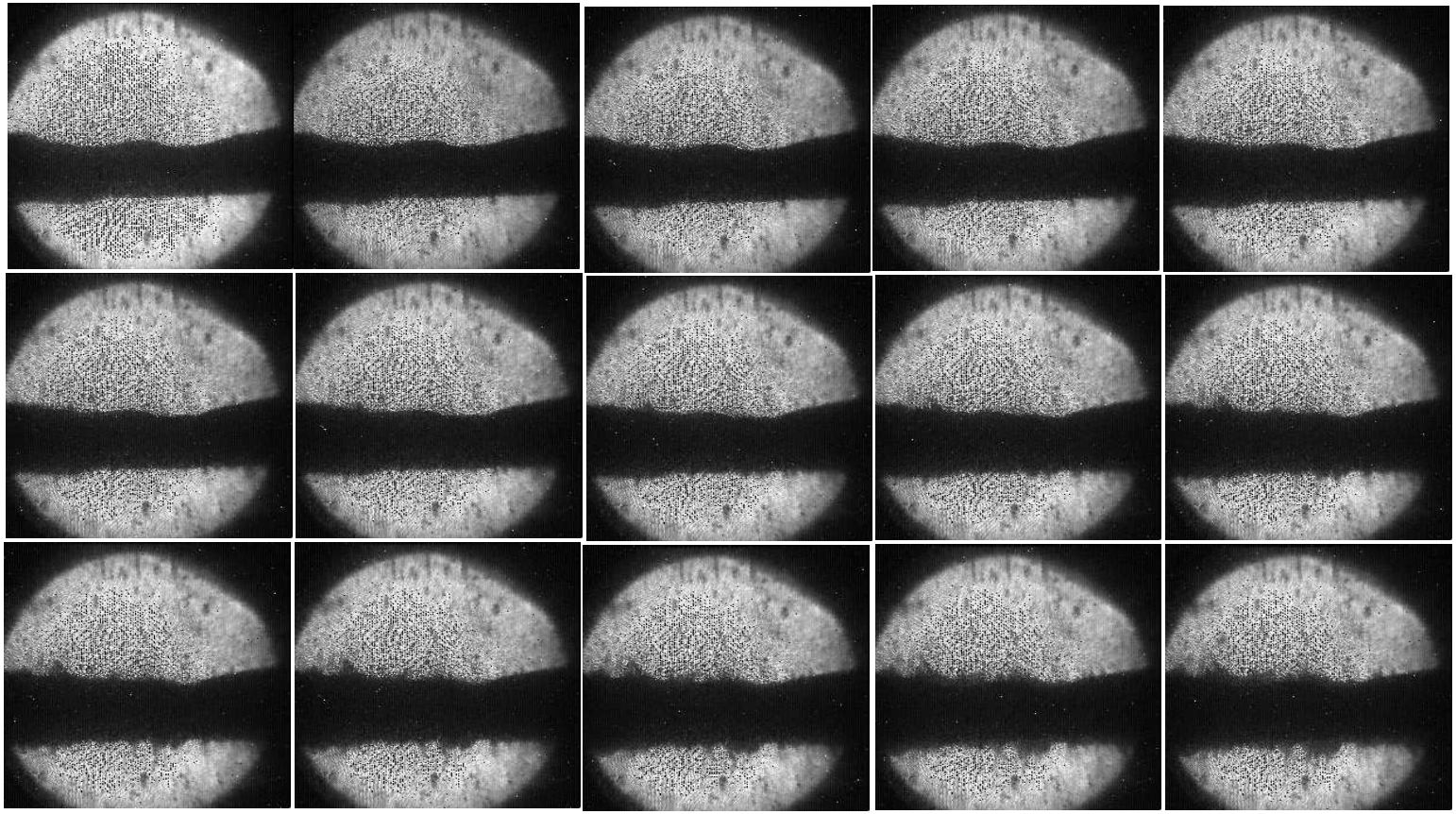

Figure B.1: Shot number is 11004. Photo of sequence of 15 frames of captured image, where the timing for the 1^{st} image is given in column 8 in Table B.1.

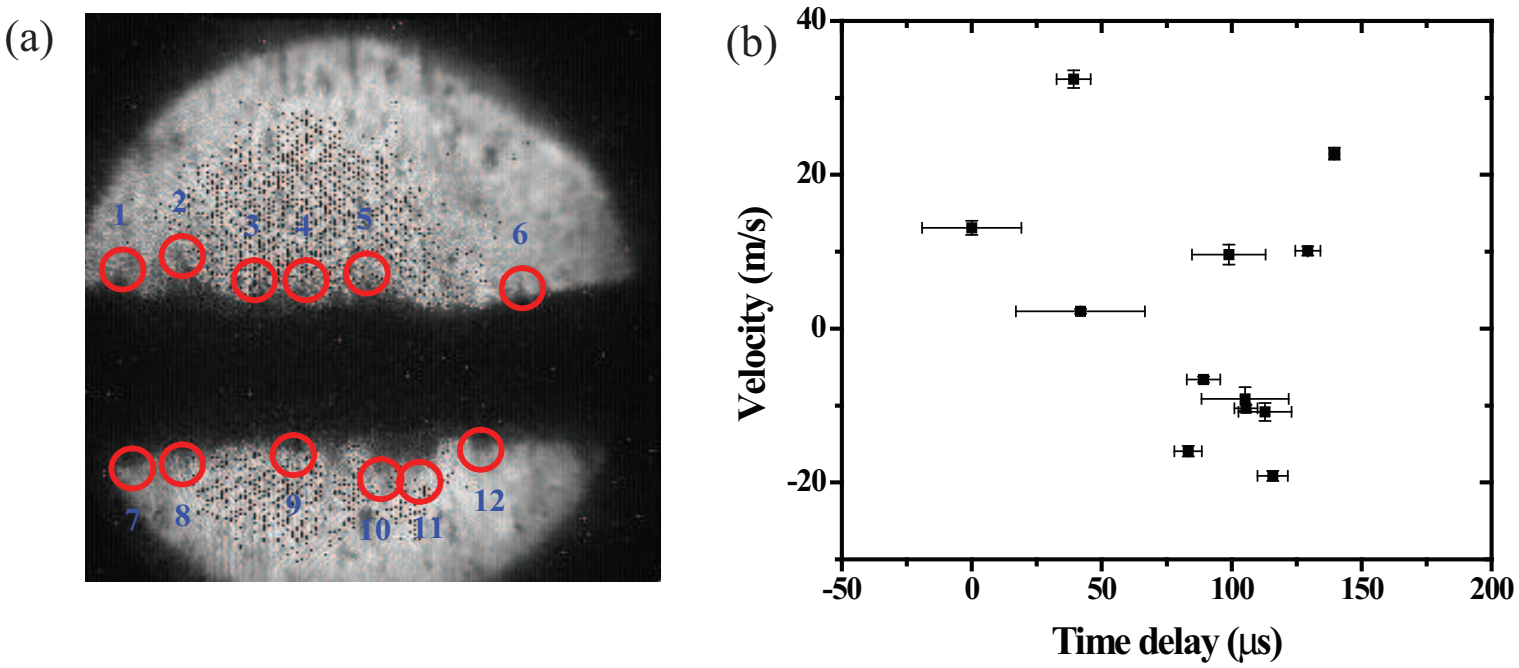

Figure B.2: Location on the Hg jet surface for filament velocity measurement. Red circles indicate the location of filaments analysis. Shot number is 11004. a.) Illustration of measured filaments. b.) Onset time of measured filament velocity.

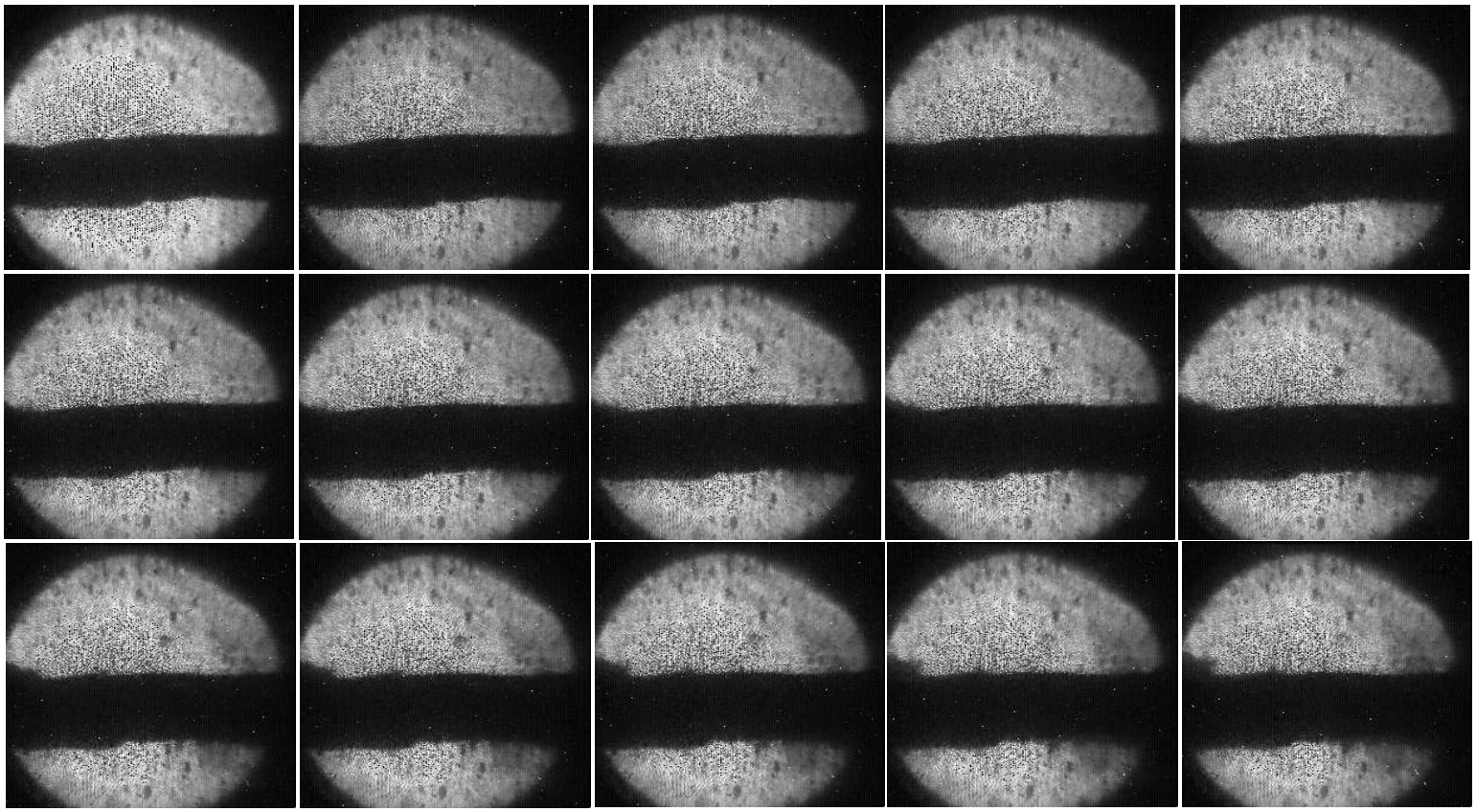

Figure B.3: Shot number is 11007.

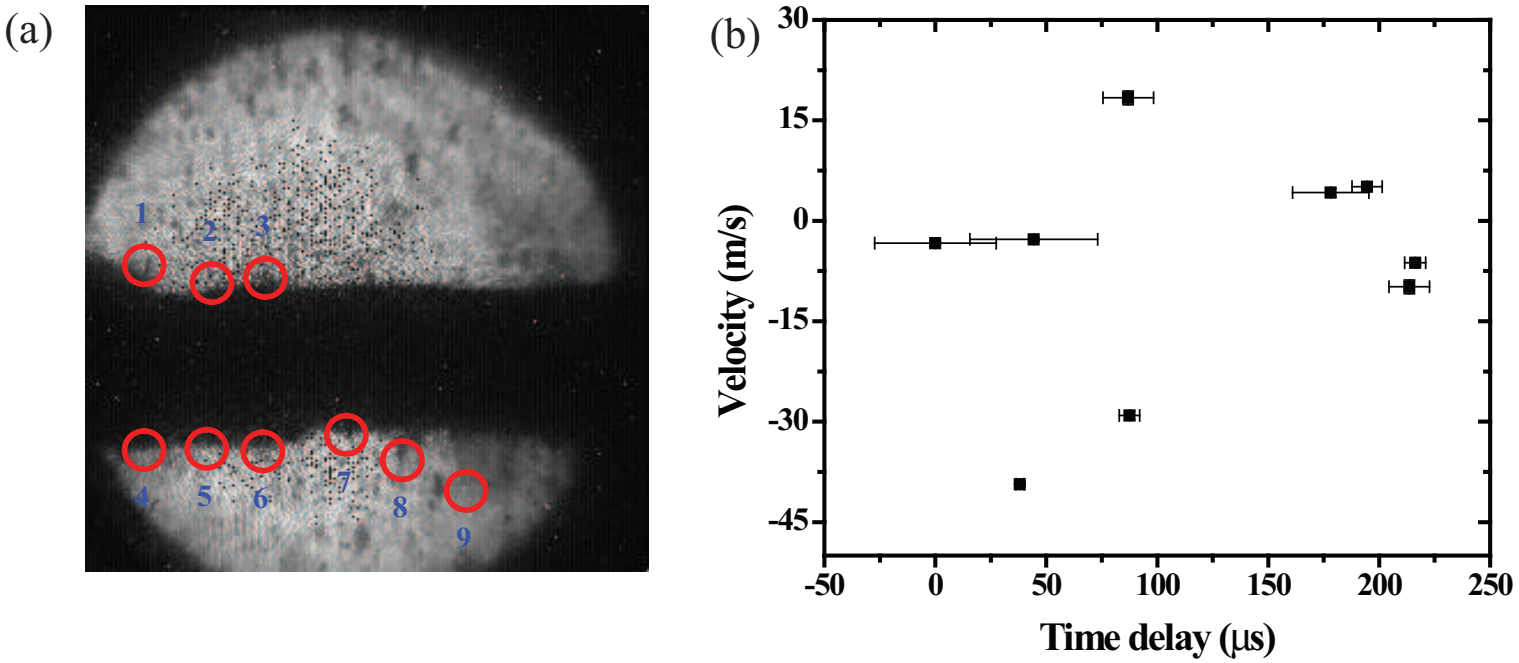

Figure B.4: Shot number is 11007. a.) Illustration of measured filaments. b.) Onset time of measured filament velocity.

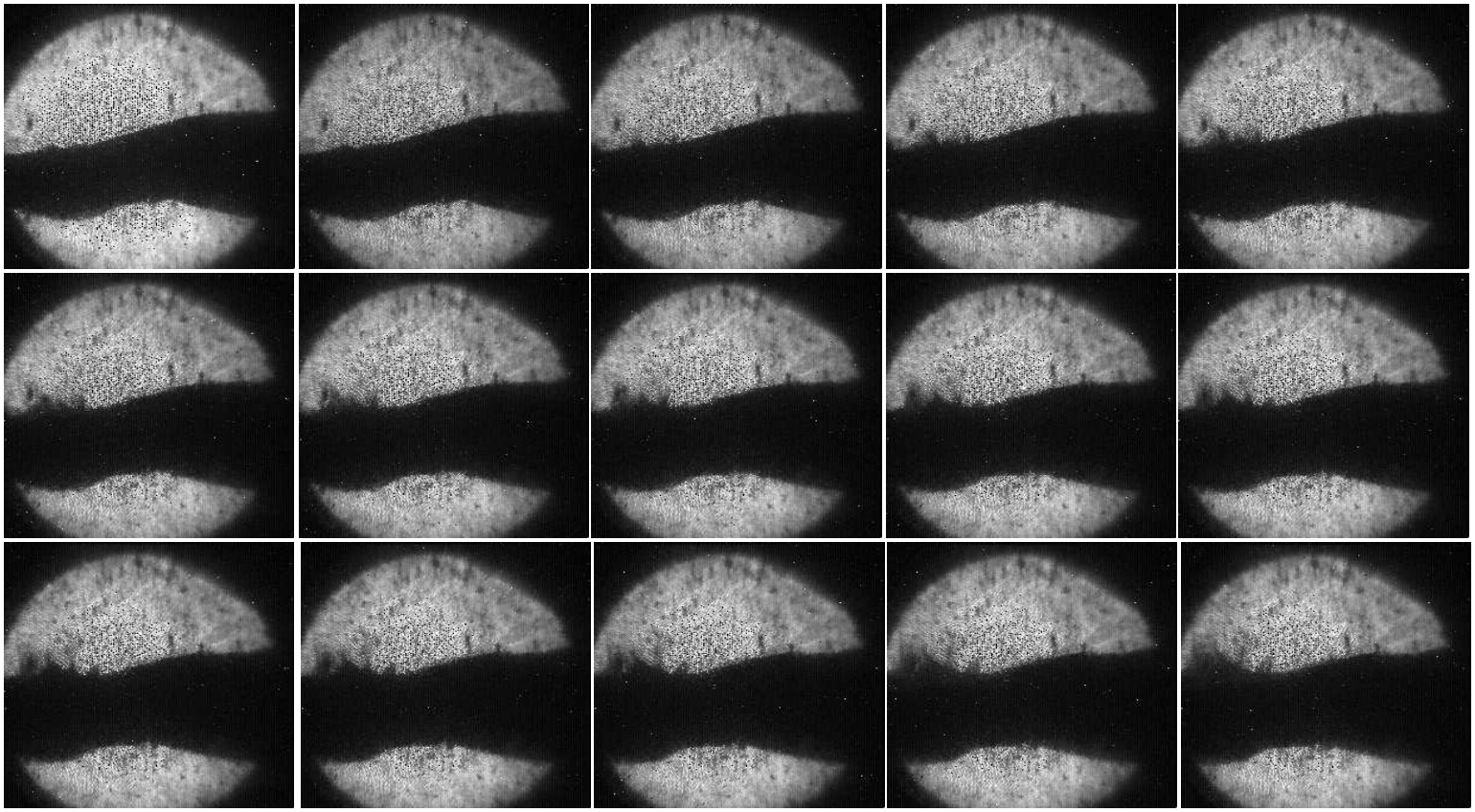

Figure B.5: Shot number is 11010.

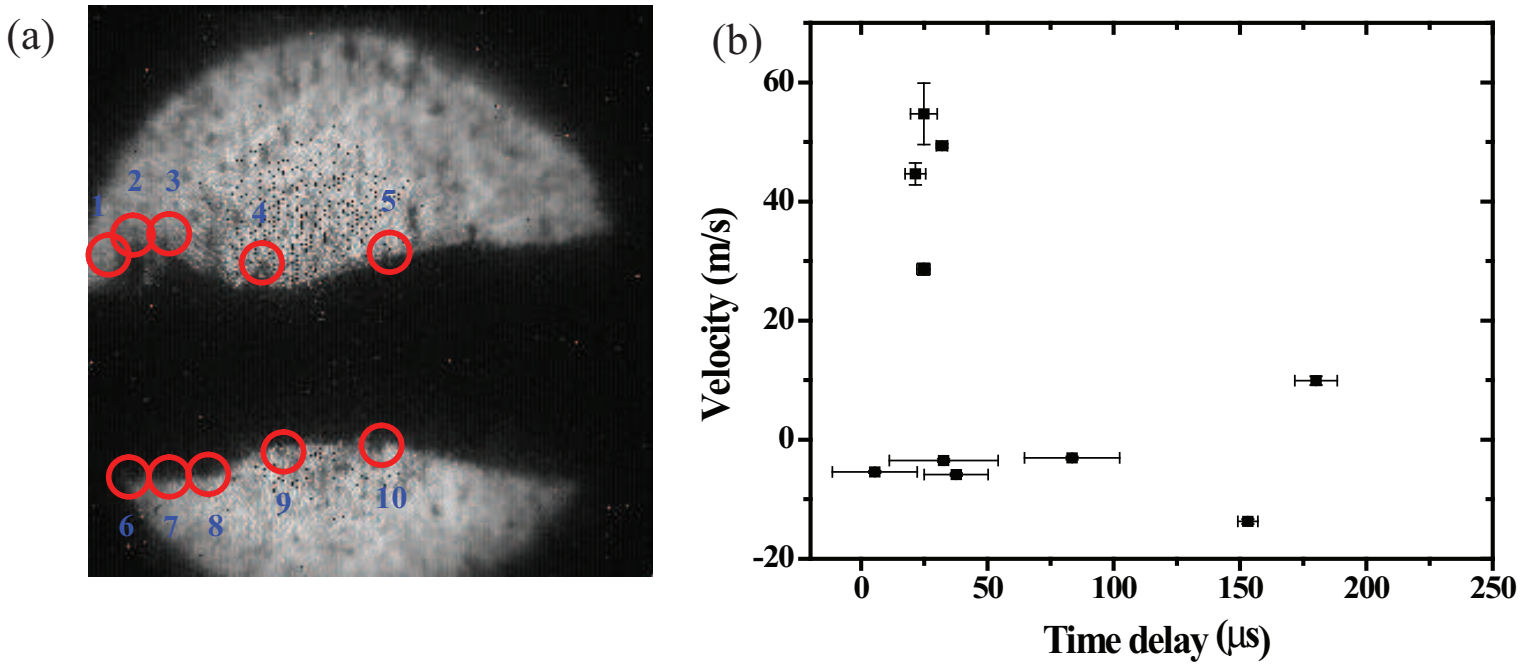

Figure B.6: Shot number is 11010. a.) Illustration of measured filaments. b.) Onset time of measured filament velocity.

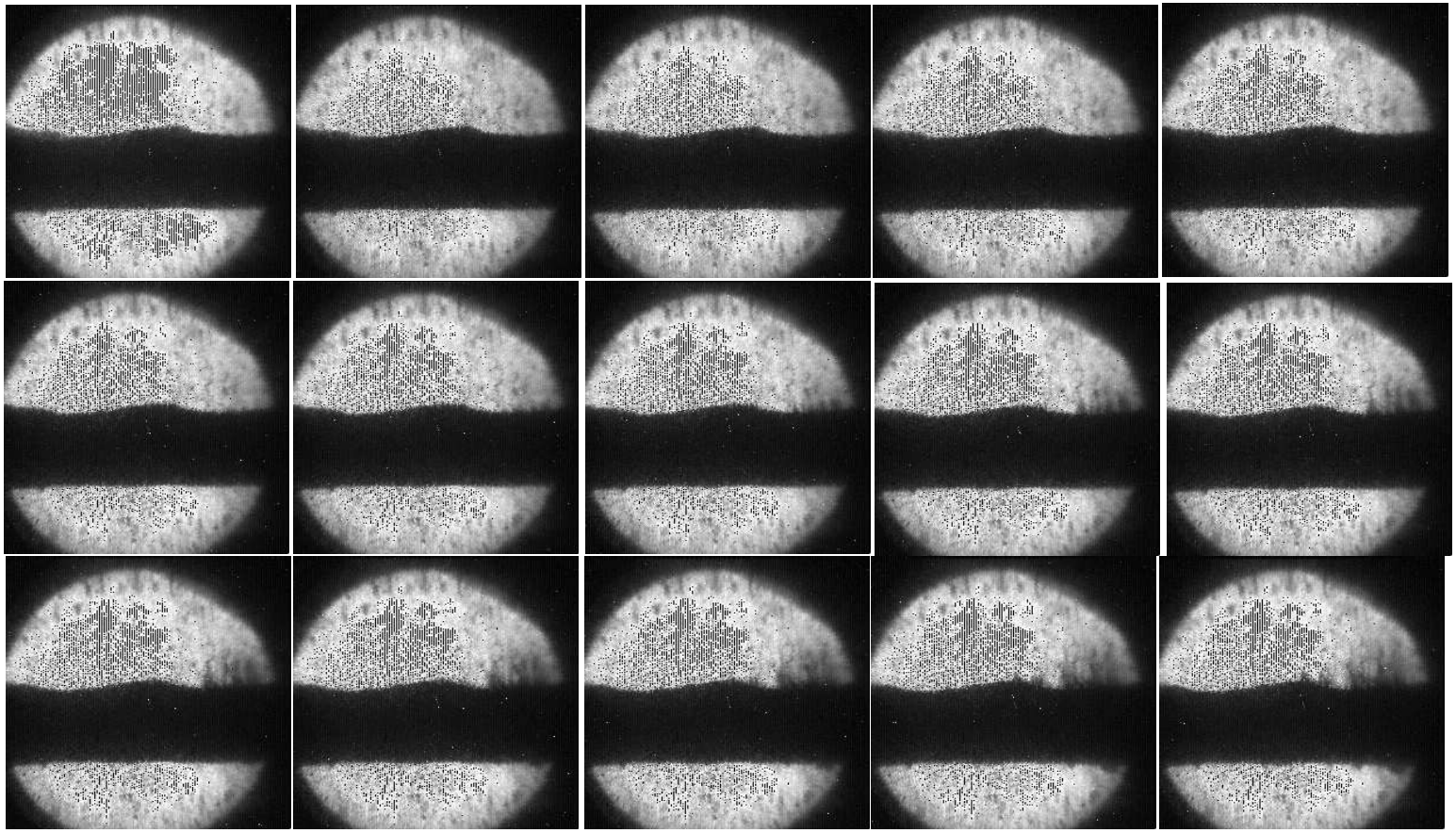

Figure B.7: Shot number is 11021.

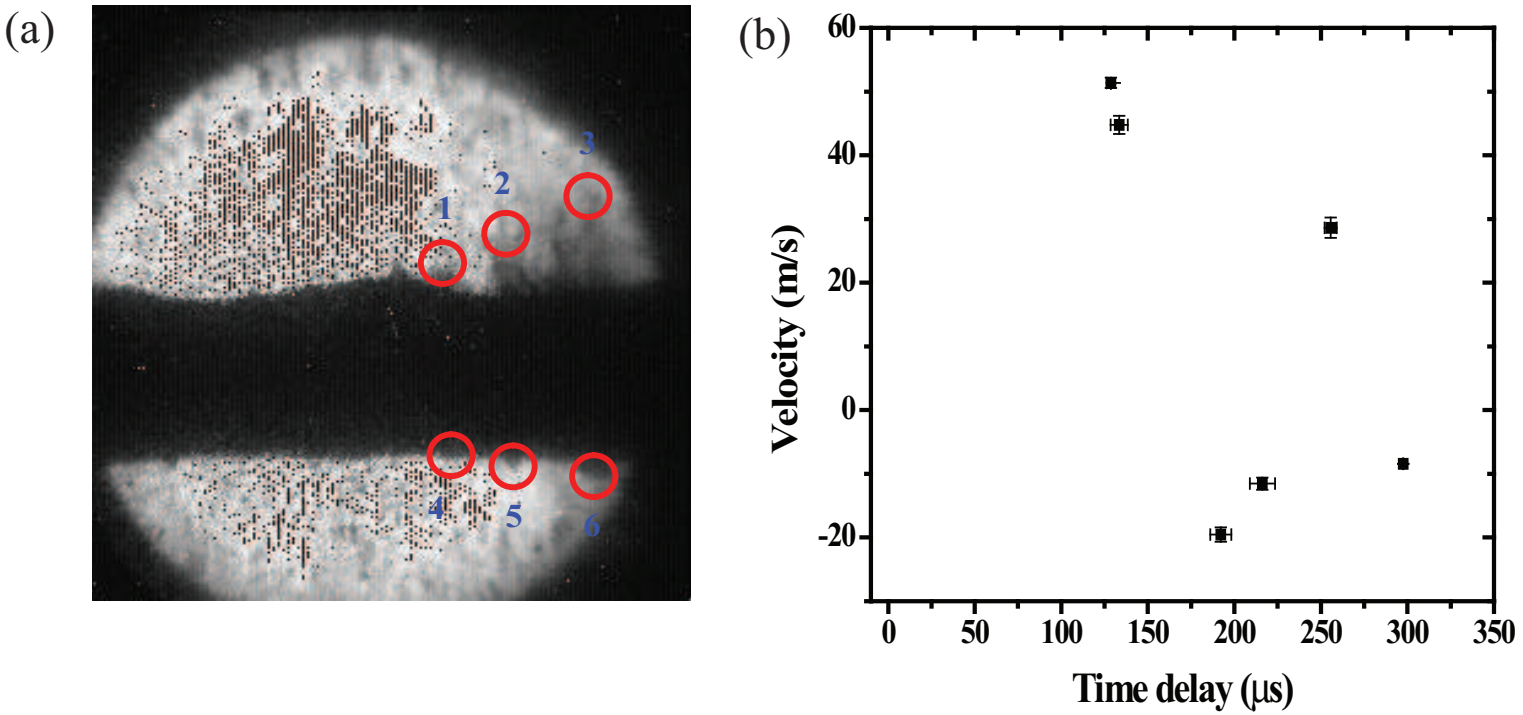

Figure B.8: Shot number is 11021. a.) Illustration of measured filaments. b.) Onset time of measured filament velocity.

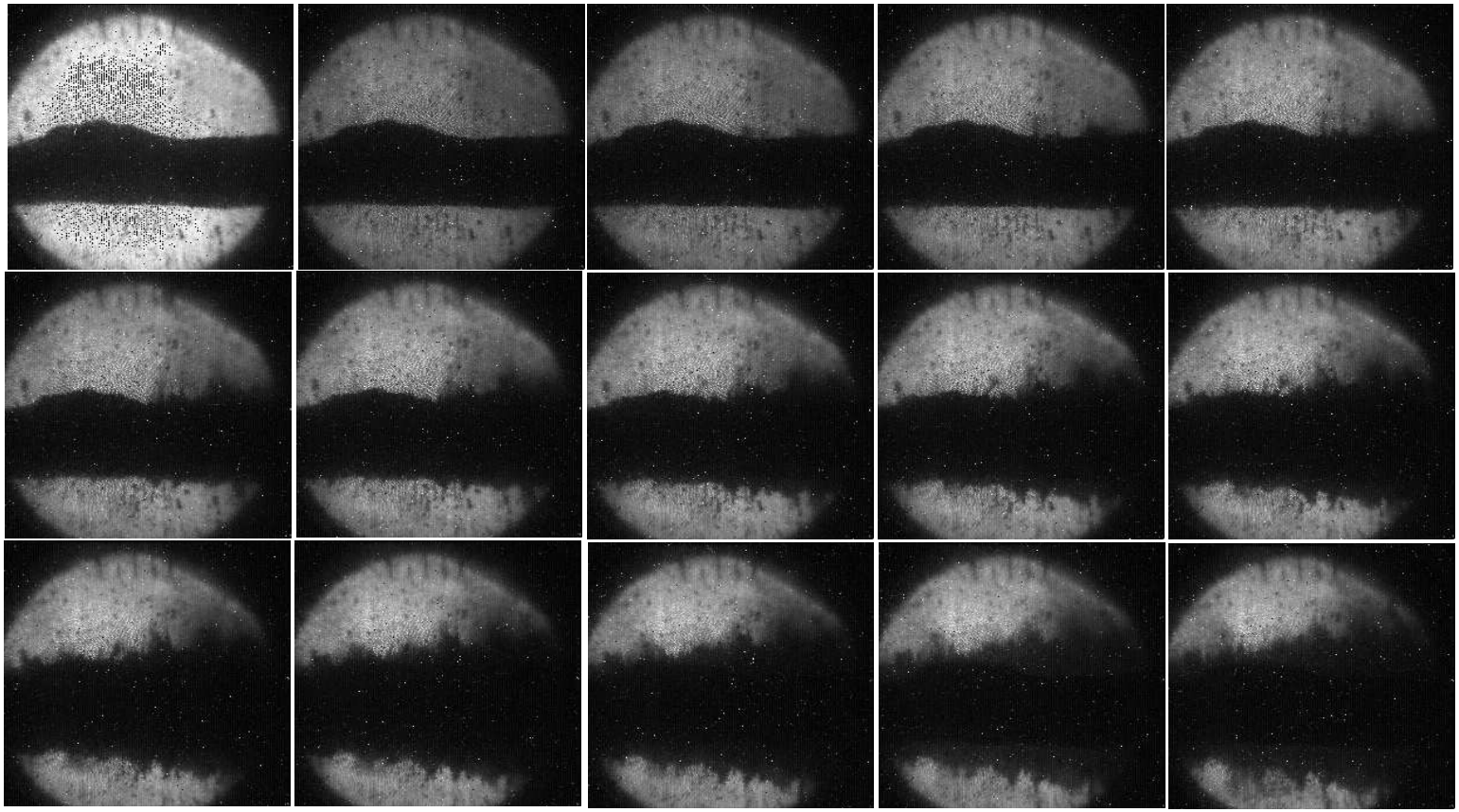

Figure B.9: Shot number is 11032.

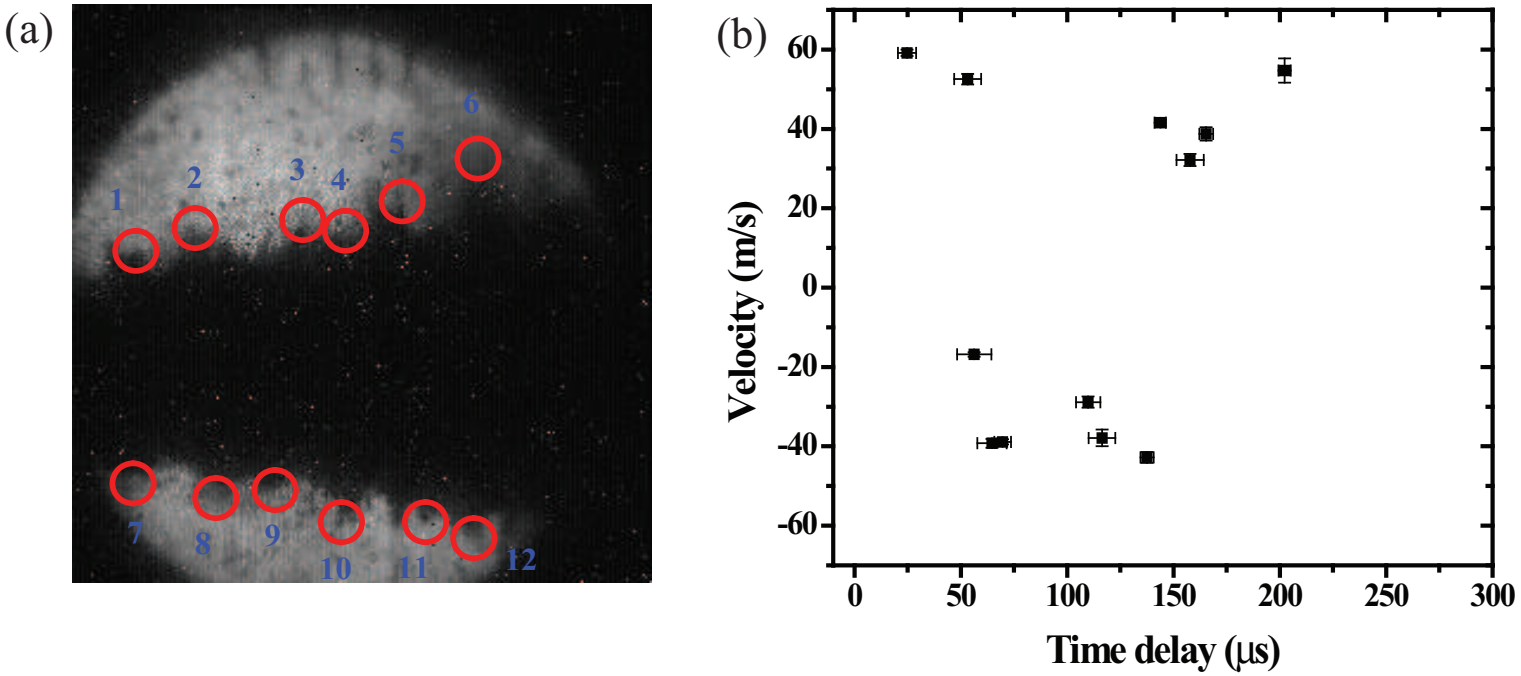

Figure B.10: Shot number is 11032. a.) Illustration of measured filaments. b.) Onset time of measured filament velocity.

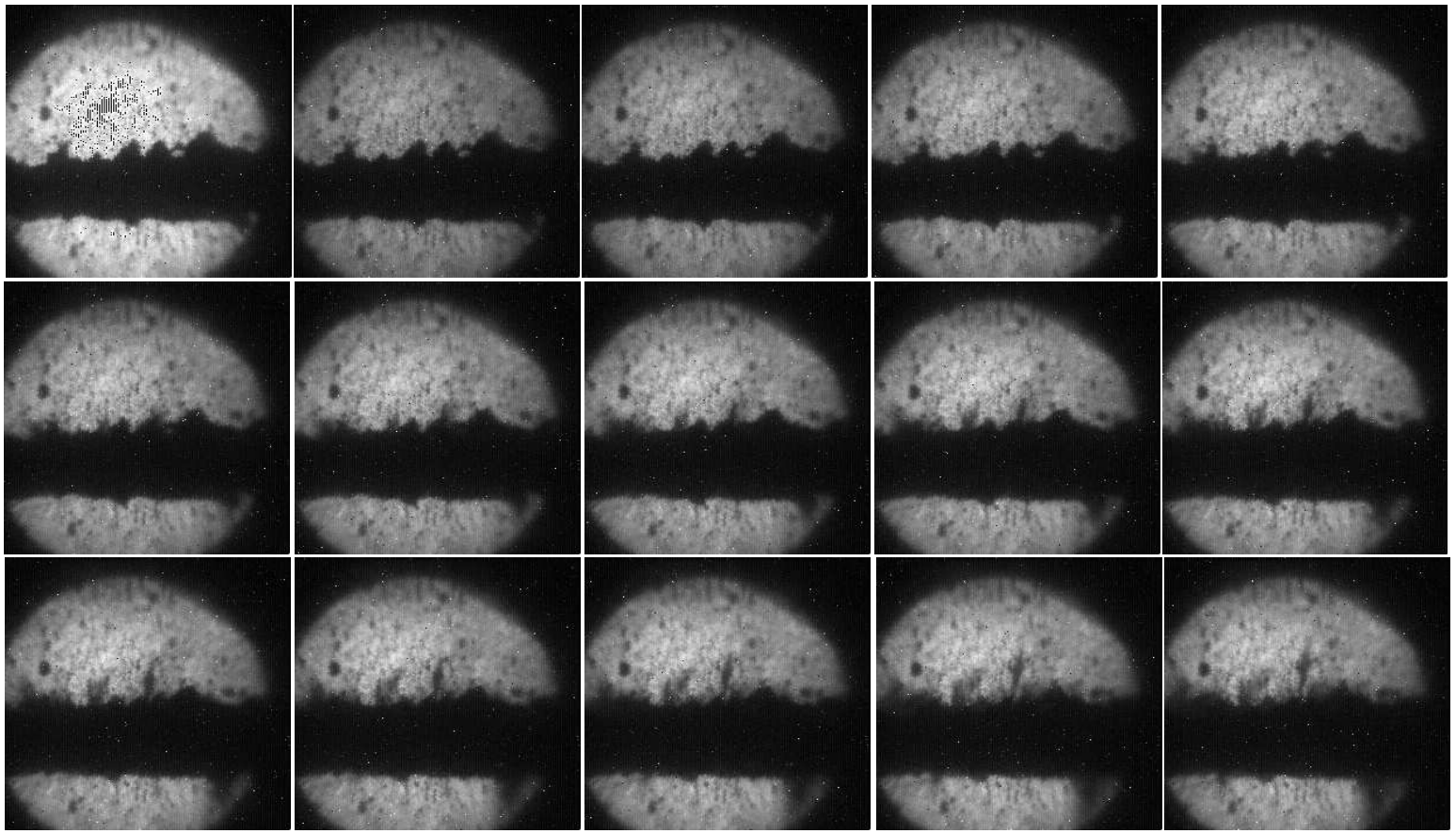

Figure B.11: Shot number is 12031.

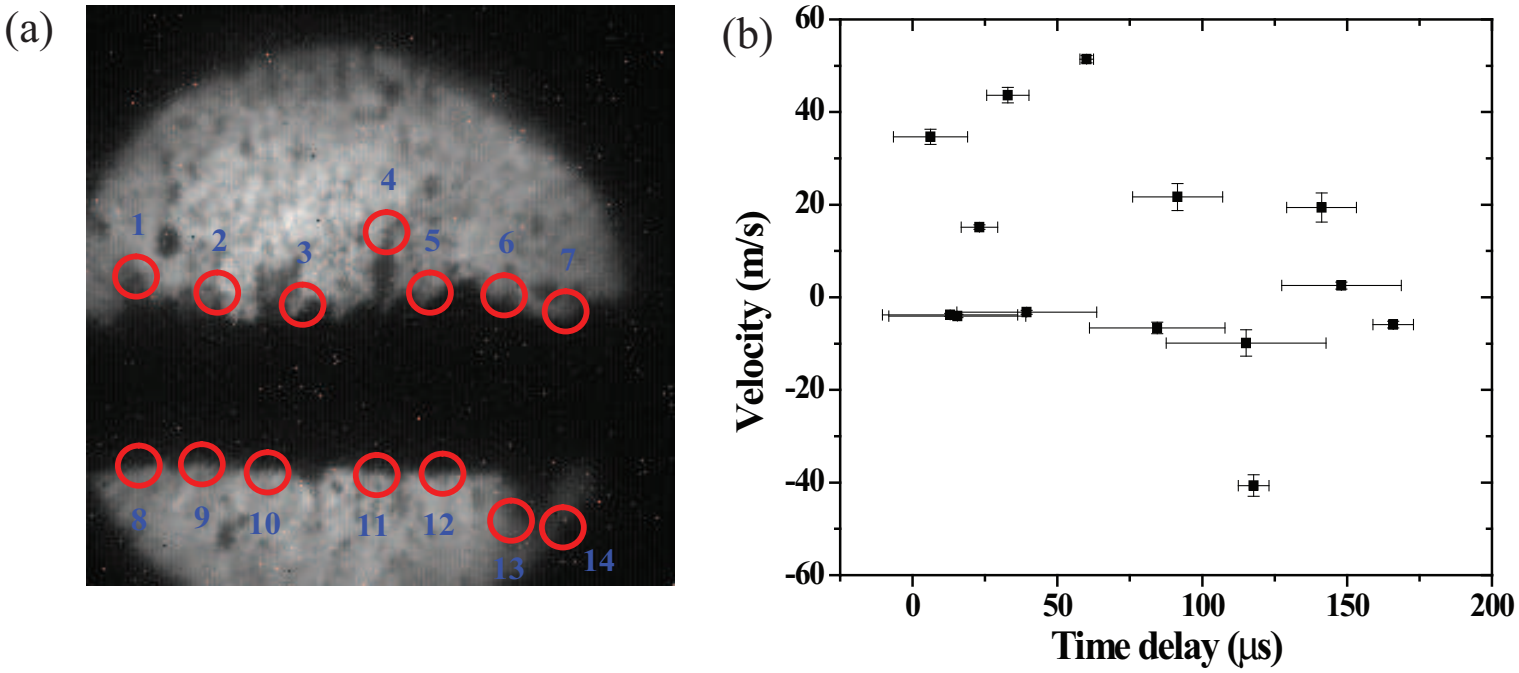

Figure B.12: Shot number is 12031. a.) Illustration of measured filaments. b.) Onset time of measured filament velocity.

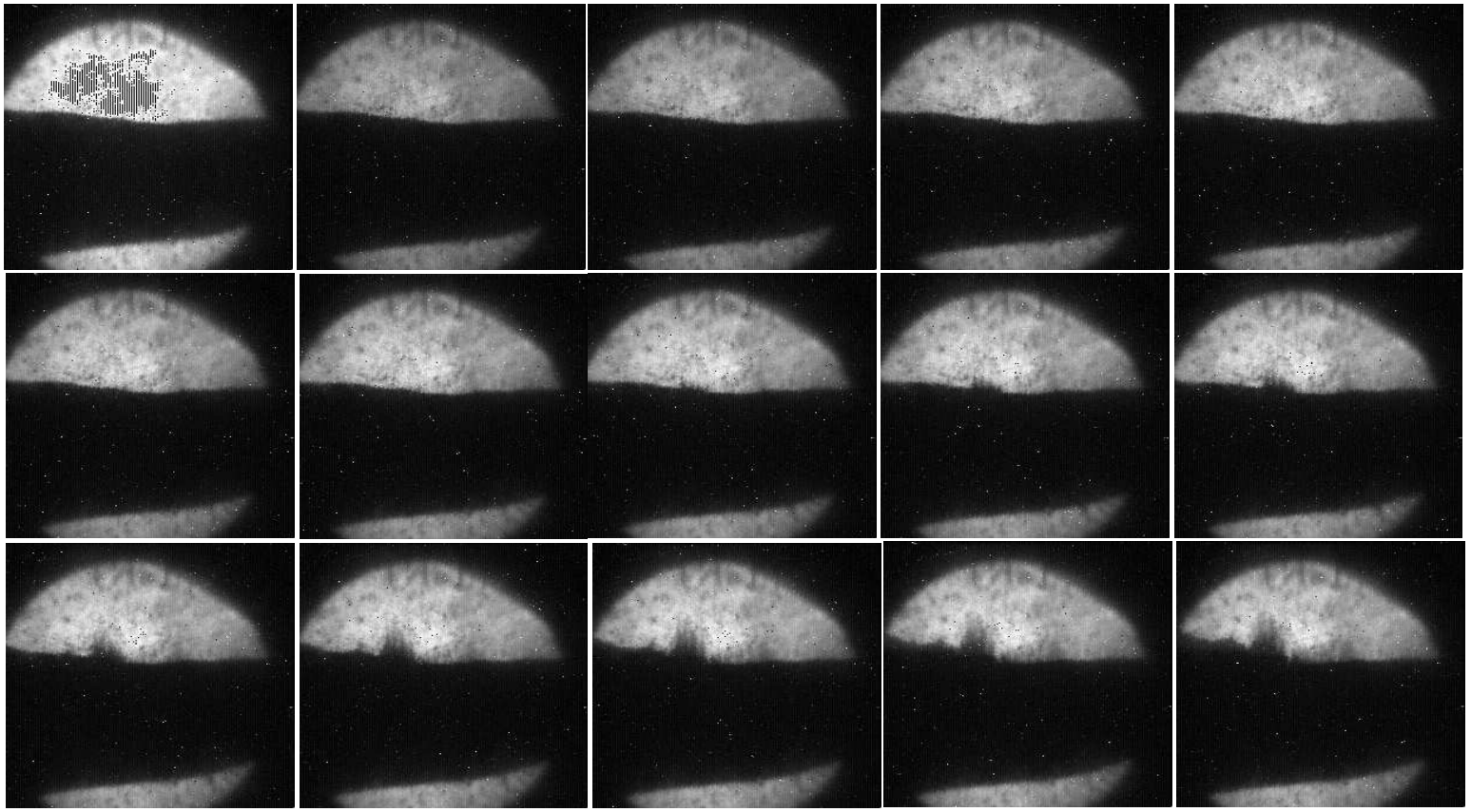

Figure B.13: Shot number is 12032.

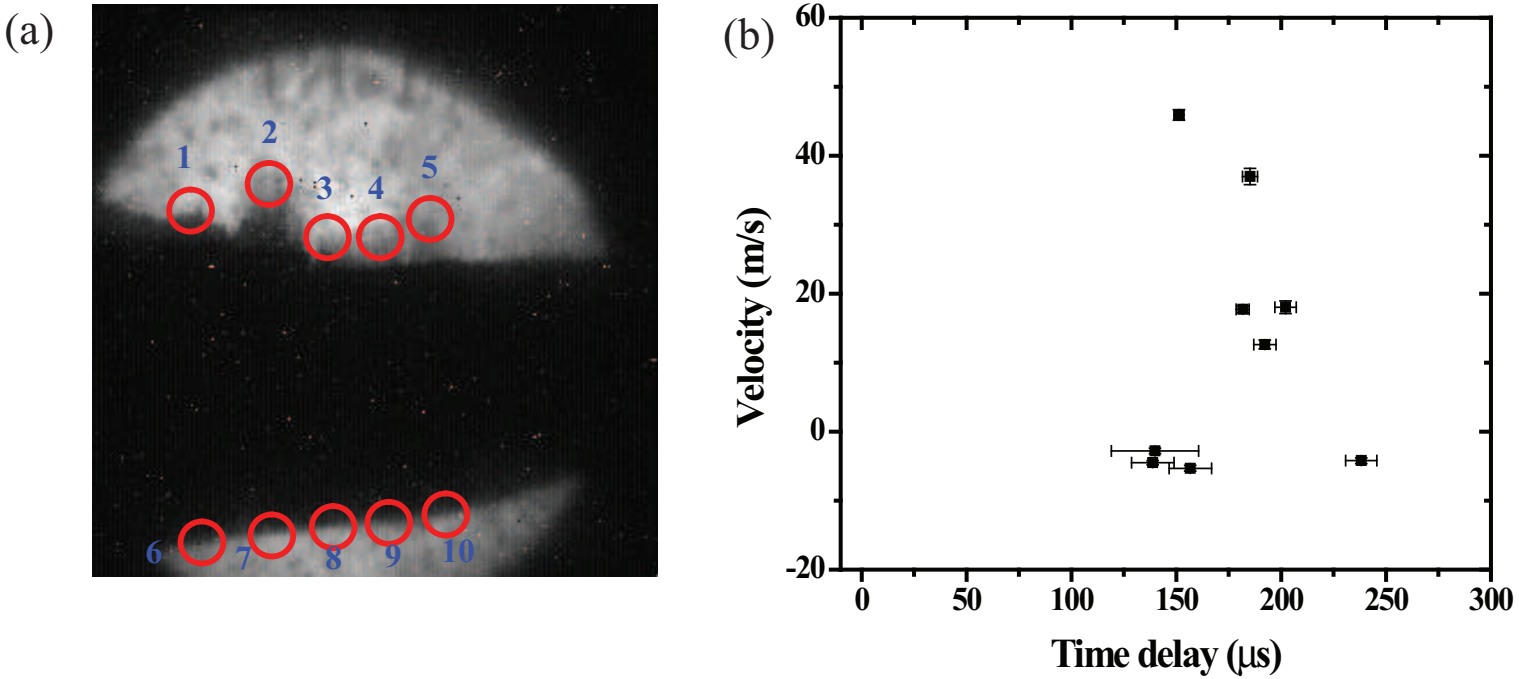

Figure B.14: Shot number is 12032. a.) Illustration of measured filaments. b.) Onset time of measured filament velocity.

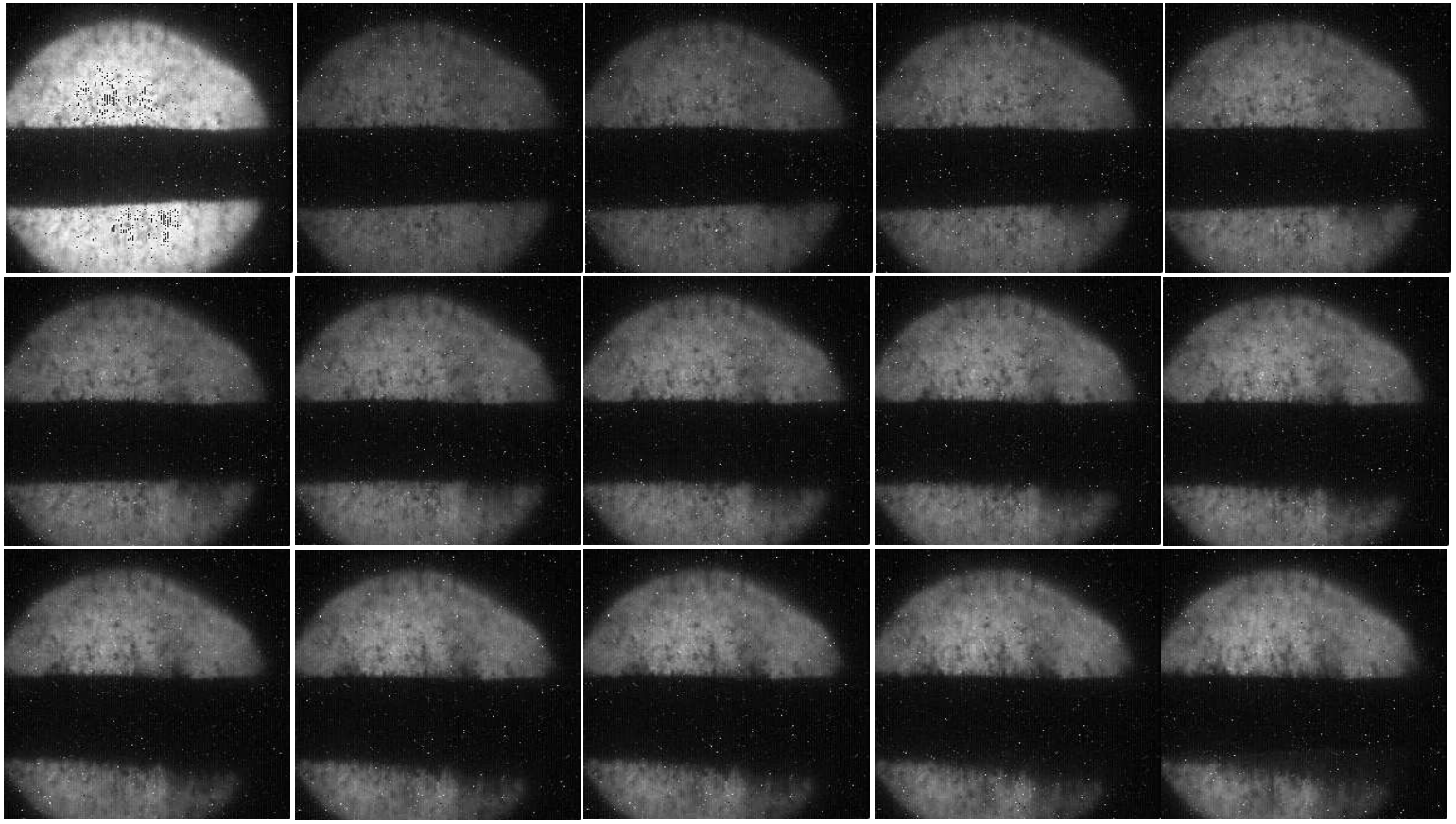

Figure B.15: Shot number is 12033.

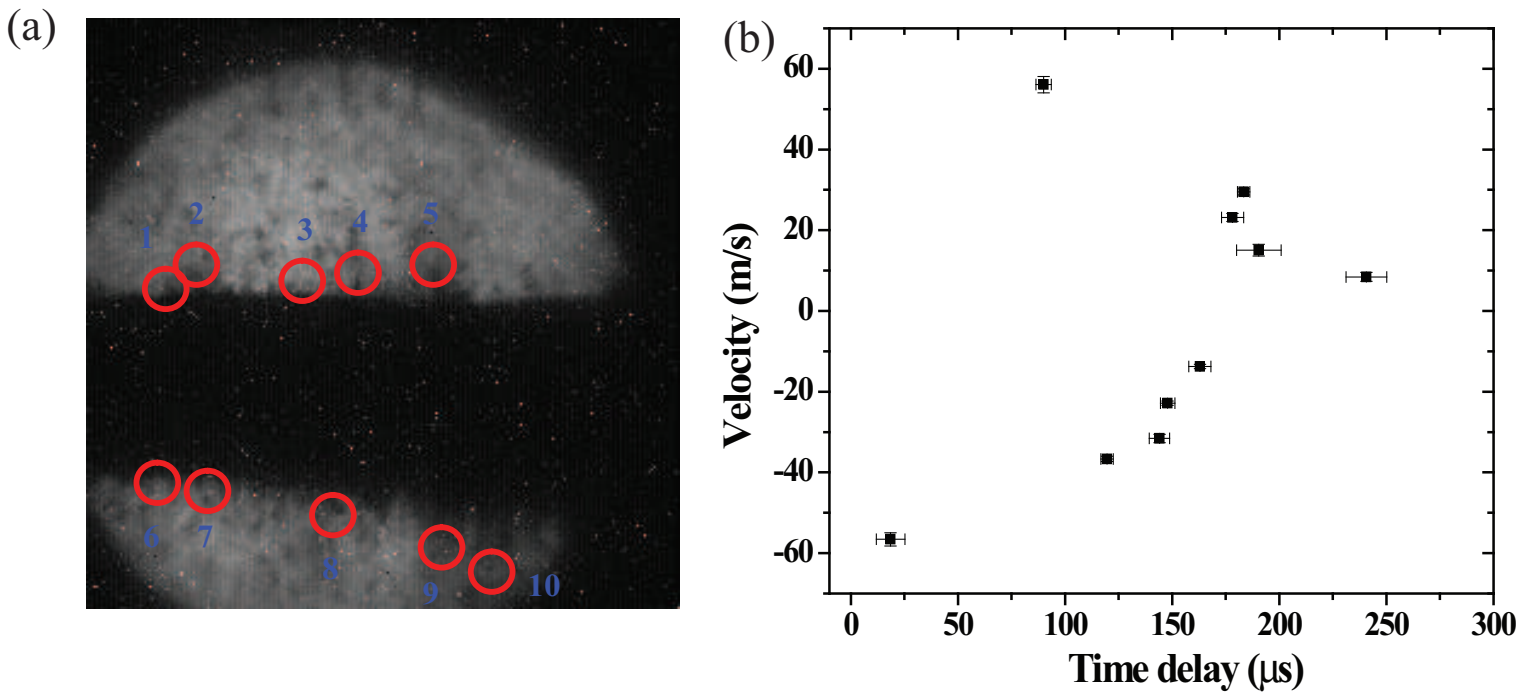

Figure B.16: Shot number is 12033. a.) Illustration of measured filaments. b.) Onset time of measured filament velocity.

Appendix C

Mathematical Derivation for Chapter 2

C.1 Derivation of Rayleigh's Instability at an Interface Separating Two Flows in a Magnetic Field

C.1.1 Kinematic boundary condition at interface

We consider the (x, y, z) coordinate system in Fig. 2.1. A particle of fluid that is at some time on the free surface will always remain on the free surface. Then, since the equation of the free surface is $y - (\xi + a) = 0$, it follows that

$$\frac{D}{Dt}(y - (\xi + a)) = 0 \ . \tag{C.1}$$

Neglecting quadratically small terms, Eqn. (C.1) yields at the interface($y = \pm a$):

$$\frac{\partial \xi}{\partial t} + U_i \frac{\partial \xi}{\partial x} = \frac{\partial \phi_i}{\partial y} \ . \tag{C.2}$$

In the region $(-a < y < a)$, the velocity potential ϕ_i must satisfy $\frac{\partial^2 \phi_1}{\partial x^2} + \frac{\partial^2 \phi_1}{\partial y^2} = 0$, $|\nabla \phi_1|$=finite. In the region $y > a$, $y < -a$, the velocity potential

must satisfy $\frac{\partial^2\phi_2}{\partial x^2}+\frac{\partial^2\phi_2}{\partial y^2}=0$, $|\nabla\phi_2|$=finite. In view of the shape of the interface, the solutions should be trigonometric in x, then the y dependence will be exponential. In view of the finite conditions of velocity potentials, the negative exponential should be rejected for ϕ_1 and the positive exponential should be rejected for ϕ_2. Therefore, the general solutions are

$$\begin{aligned}\phi_1(x,y,t) &= A_1 e^{(2\pi/\lambda)y} e^{i(2\pi/\lambda)(x-ct)} \ , \\ \phi_2(x,y,t) &= A_2 e^{-(2\pi/\lambda)y} e^{i(2\pi/\lambda)(x-ct)} \ . \end{aligned} \tag{C.3}$$

Imposing the kinematic conditions on these solutions, the coefficients are determined at $y=a$ and $y=-a$ respectively as follow:

$$\begin{aligned}\phi_1(x,y,t) &= -i\epsilon(c-U_1) e^{i(2\pi/\lambda)(x-ct)} \ , \\ \phi_2(x,y,t) &= i\epsilon(c-U_2) e^{i(2\pi/\lambda)(x-ct)} \ , \end{aligned} \tag{C.4}$$

where $U_1=U_1(a)$, $U_2=U_2(a)$, and

$$\begin{aligned}\phi_1(x,y,t) &= i\epsilon(c-U_1) e^{i(2\pi/\lambda)(x-ct)} \ , \\ \phi_2(x,y,t) &= -i\epsilon(c-U_2) e^{i(2\pi/\lambda)(x-ct)} \ , \end{aligned} \tag{C.5}$$

where $U_1=U_1(-a)$ and $U_2=U_2(-a)$. Since the perturbed surface at $y=a$ and $y=-a$ are supposed to be symmetric, half of the jet section for the surface stability is considered in the following work.

C.1.2 Hydrodynamic stability in a magnetic field

Substituting the perturbed expressions into the equations of motion, neglecting second order terms in the perturbed quantities, and making use of the fact that U, P satisfy the flow equations and the current density in Lorentz force term can be represented using Ohm's law, one will have the linearized equations governing the motion of disturbance as follows:

$$\begin{aligned}&\frac{\partial v'_{xi}}{\partial t}+U_i\frac{\partial v'_{xi}}{\partial x}+v'_{xi}\frac{dU_i}{dy} \\ &=-\frac{1}{\rho_i}\frac{\partial p'_i}{\partial x}-\frac{\sigma_i}{\rho_i}\mathrm{B}_y^2 v'_{xi}+\frac{\sigma_i}{\rho_i}\mathrm{B}_x\mathrm{B}_y v'_{yi}\end{aligned} \tag{C.6}$$

and

$$\frac{\partial v'_{yi}}{\partial t} + U_i \frac{\partial v'_{yi}}{\partial x} = -\frac{1}{\rho_i}\frac{\partial p'_i}{\partial y} - \frac{\sigma_i}{\rho_i} \mathrm{B}_x^2 v'_{yi} + \frac{\sigma_i}{\rho_i} \mathrm{B}_x \mathrm{B}_y v'_{xi} \ , \tag{C.7}$$

where $p'_i = f_i(c, \lambda, y) e^{i(2\pi/\lambda)(x-ct)}$. The perturbed velocity v'_x, v'_y are given as follow:

$$\begin{aligned} v'_x &= \frac{\partial \phi_1}{\partial x} = i(\frac{2\pi}{\lambda}) A_1 e^{(2\pi/\lambda)y} e^{i(2\pi/\lambda)(x-ct)} \\ v'_y &= \frac{\partial \phi_1}{\partial y} = (\frac{2\pi}{\lambda}) A_1 e^{(2\pi/\lambda)y} e^{i(2\pi/\lambda)(x-ct)} \ . \end{aligned} \tag{C.8}$$

Putting Eqn. (C.8) into Eqn. (C.6) and Eqn. (C.7), equate the hydrodynamic pressures since it is isotropic, which leads to Rayleigh's stability equation for the flow in a magnetic field as follow:

$$\sigma_1 B_x B_y + i\sigma_1 B_x^2 = \sigma_1 B_y^2 i - \sigma_1 B_x B_y + \rho_1 (\frac{\lambda}{2\pi}) \frac{d^2 U_1}{dy^2} \ , \tag{C.9}$$

where $U_1 = U_1(y)$. In the same manner, the Rayleigh's stability equation for the upper flow in magnetic field is derived as follow:

$$\sigma_2 B_x^2 + \sigma_2 B_x B_y i = \sigma_2 B_y^2 - i\sigma_2 B_x B_y - \rho_2 i (\frac{\lambda}{2\pi}) \frac{d^2 U_2}{dy^2} \ , \tag{C.10}$$

where $U_2 = U_2(y)$.

C.1.3 Dynamic boundary condition at interface

The difference of the normal stress must be balanced by the normal stress induced by surface tension at the interface, which is expresses as follow:

$$(P_1 + \frac{\partial P_1}{\partial y}\xi + \frac{\partial^2 P_1}{\partial y^2}\xi + \ldots + p'_1) - (P_2 + \frac{\partial P_2}{\partial y}\xi + \frac{\partial^2 P_2}{\partial y^2}\xi + \ldots + p'_2) + \Gamma \frac{\partial^2 \xi}{\partial x^2} = 0 \ , \tag{C.11}$$

where Γ is surface tension. Considering the gravity force in the free surface waves, Eqn. (C.11) can be rewritten as follow:

$$
\begin{aligned}
&(\rho_2-\rho_1)g\cos\theta+\rho_1(c-U_1)^2(\frac{2\pi}{\lambda})+\rho_2(c-U_2)^2(\frac{2\pi}{\lambda})\\
&+\rho_1(c-U_1)\frac{dU_1}{dy}-\rho_2(c-U_2)\frac{dU_2}{dy}+iB_y^2(\sigma_1(c-U_1)+\sigma_2(c-U_2))\\
&+B_xB_y(\sigma_2(c-U_2)-\sigma_1(c-U_1))-\Gamma(\frac{2\pi}{\lambda})^2=0\ ,
\end{aligned}
\tag{C.12}
$$

where $U_1 = U_1(a),\ U_2 = U_2(a)$. Consider the case that $U_2 = 0, \frac{dU_2}{dy} = 0, \rho_2 = 0, \sigma_2 = 0$. This would correspond to the stationary fluid on the upper and the density and conductivity of the upper fluid are very small compared with these of the lower fluid. The wave velocity is represented as follow:

$$
\begin{aligned}
c=[\ \ &-\rho_1\frac{dU_1}{dy}+B_xB_y\sigma_1-iB_y^2\sigma_1+2(\frac{2\pi}{\lambda})\rho_1U_1\\
&\pm\sqrt{\rho_1^2(\frac{dU_1^2}{dy})+4(\frac{2\pi}{\lambda})\cos\theta g\rho_1^2-2B_xB_y\rho_1\sigma_1\frac{dU_1}{dy}+2iB_y^2\rho_1\sigma_1\frac{dU_1}{dy}}\\
&\overline{+B_x^2B_y^2\sigma_1^2-2iB_xB_y^3\sigma_1^2-B_y^4\sigma_1^2+4(\frac{2\pi}{\lambda})^3\rho_1\Gamma}\ \ ]\times\frac{1}{2(\frac{2\pi}{\lambda})\rho_1}\ .
\end{aligned}
\tag{C.13}
$$

C.2 The Governing Equations of MHD Flow in Cylindrical Coordinates

The momentum equations in the (r, θ, z) coordinates can be written as follows:

$$
\begin{aligned}
&-\rho(v_r\frac{\partial v_r}{\partial r}+\frac{v_\theta}{r}\frac{\partial v_r}{\partial\theta}+v_z\frac{\partial v_r}{\partial z})-\frac{\partial p_t}{\partial r}-\rho g\cos\theta+\eta(\frac{\partial^2v_r}{\partial r^2}+\frac{1}{r}\frac{\partial v_r}{\partial r}+\frac{1}{r^2}\frac{\partial^2v_r}{\partial\theta^2}+\frac{\partial^2v_r}{\partial z^2})\\
&+\frac{1}{\mu}(B_r\frac{\partial B_r}{\partial r}+\frac{B_\theta}{r}\frac{\partial B_r}{\partial\theta}+B_z\frac{\partial B_r}{\partial z})=\rho\frac{\partial v_r}{\partial t}\ ,
\end{aligned}
\tag{C.14}
$$

$$- \rho(v_r\frac{\partial v_\theta}{\partial r} + \frac{v_\theta}{r}\frac{\partial v_\theta}{\partial \theta} + v_z\frac{\partial v_\theta}{\partial z}) - \frac{1}{r}\frac{\partial p_t}{\partial \theta} + \rho g\sin\theta + \eta(\frac{\partial^2 v_\theta}{\partial r^2} + \frac{1}{r}\frac{\partial v_\theta}{\partial r} + \frac{1}{r^2}\frac{\partial^2 v_\theta}{\partial \theta^2} + \frac{\partial^2 v_\theta}{\partial z^2})$$
$$+ \frac{1}{\mu}(B_r\frac{\partial B_\theta}{\partial r} + \frac{B_\theta}{r}\frac{\partial B_\theta}{\partial \theta} + B_z\frac{\partial B_\theta}{\partial z}) = \rho\frac{\partial v_\theta}{\partial t} \ , \tag{C.15}$$

and

$$- \rho(v_r\frac{\partial v_z}{\partial r} + \frac{v_\theta}{r}\frac{\partial v_z}{\partial \theta} + v_z\frac{\partial v_z}{\partial z}) - \frac{\partial p_t}{\partial z} + \eta(\frac{\partial^2 v_z}{\partial r^2} + \frac{1}{r}\frac{\partial v_z}{\partial r} + \frac{1}{r^2}\frac{\partial^2 v_z}{\partial \theta^2} + \frac{\partial^2 v_z}{\partial z^2})$$
$$+ \frac{1}{\mu}(B_r\frac{\partial B_z}{\partial r} + \frac{B_\theta}{r}\frac{\partial B_z}{\partial \theta} + B_z\frac{\partial B_z}{\partial z}) = \rho\frac{\partial v_z}{\partial t} \ , \tag{C.16}$$

where $p_t = p + \frac{\mathbf{B}^2}{2\mu}$. The magnetic induction equation in the (r, θ, z) coordinates can be written as follows:

$$\frac{1}{\mu\sigma}[\frac{\partial^2 B_r}{\partial r^2} + \frac{1}{r}\frac{\partial B_r}{\partial r} + \frac{1}{r^2}\frac{\partial^2 B_r}{\partial \theta^2} + \frac{\partial^2 B_r}{\partial z^2}] + \frac{1}{r}B_r(r\frac{\partial v_r}{\partial r}) + \frac{1}{r}B_\theta\frac{\partial v_r}{\partial \theta} + B_z\frac{\partial v_r}{\partial z}$$
$$- \frac{1}{r}v_r(r\frac{\partial B_r}{\partial r}) - \frac{1}{r}v_\theta\frac{\partial B_r}{\partial \theta} - v_z\frac{\partial B_r}{\partial z} = \frac{\partial B_r}{\partial t} \ , \tag{C.17}$$

$$\frac{1}{\mu\sigma}[\frac{\partial^2 B_\theta}{\partial r^2} + \frac{1}{r}\frac{\partial B_\theta}{\partial r} + \frac{1}{r^2}\frac{\partial^2 B_\theta}{\partial \theta^2} + \frac{\partial^2 B_\theta}{\partial z^2}] + \frac{1}{r}B_r(r\frac{\partial v_\theta}{\partial r}) + \frac{1}{r}B_\theta\frac{\partial v_\theta}{\partial \theta} + B_z\frac{\partial v_\theta}{\partial z}$$
$$- \frac{1}{r}v_r(r\frac{\partial B_\theta}{\partial r}) - \frac{1}{r}v_\theta\frac{\partial B_\theta}{\partial \theta} - v_z\frac{\partial B_\theta}{\partial z} = \frac{\partial B_\theta}{\partial t} \ , \tag{C.18}$$

and

$$\frac{1}{\mu\sigma}[\frac{\partial^2 B_z}{\partial r^2} + \frac{1}{r}\frac{\partial B_z}{\partial r} + \frac{1}{r^2}\frac{\partial^2 B_z}{\partial \theta^2} + \frac{\partial^2 B_z}{\partial z^2}] + \frac{1}{r}B_r(r\frac{\partial v_z}{\partial r}) + \frac{1}{r}B_\theta\frac{\partial v_z}{\partial \theta} + B_z\frac{\partial v_z}{\partial z}$$
$$- \frac{1}{r}v_r(r\frac{\partial B_z}{\partial r}) - \frac{1}{r}v_\theta\frac{\partial B_z}{\partial \theta} - v_z\frac{\partial B_z}{\partial z} = \frac{\partial B_z}{\partial t} \ . \tag{C.19}$$

The Ampère's law can be written as

$$
\begin{aligned}
j_r &= \frac{1}{\mu}\left(\frac{1}{r}\frac{\partial B_z}{\partial \theta} - \frac{\partial B_\theta}{\partial z}\right) , \\
j_\theta &= \frac{1}{\mu}\left(-\frac{\partial B_z}{\partial r} + \frac{\partial B_r}{\partial z}\right) , \\
j_z &= \frac{1}{\mu}\left(\frac{\partial B_\theta}{\partial r} - \frac{1}{r}\frac{\partial B_r}{\partial \theta}\right) .
\end{aligned} \tag{C.20}
$$

The equation of continuity and the solenoidal condition for the magnetic field are

$$
\frac{1}{r}\frac{\partial}{\partial r}(r v_r) + \frac{1}{r}\frac{\partial v_\theta}{\partial \theta} + \frac{\partial v_z}{\partial z} = 0 \tag{C.21}
$$

and

$$
\frac{1}{r}\frac{\partial}{\partial r}(r B_r) + \frac{1}{r}\frac{\partial B_\theta}{\partial \theta} + \frac{\partial B_z}{\partial z} = 0 \ . \tag{C.22}
$$